

**FIRST PRINCIPLES STUDY ON
TRANSITION METAL COMPOUNDS
USING DENSITY FUNCTIONAL THEORY**

**THESIS SUBMITTED FOR THE DEGREE OF
DOCTOR OF PHILOSOPHY (SCIENCE)**

IN

PHYSICS (THEORETICAL)

BY

KARTIK SAMANTA

**DEPARTMENT OF PHYSICS
UNIVERSITY OF CALCUTTA
JULY, 2017**

Dedicated to

My Parents

Acknowledgements

During my Ph.D period I have been supported and accomplished by many people. Here, I take the opportunity to acknowledge all the well wishers who have contributed, influenced and supported directly and indirectly towards the accomplishment of the thesis works.

First of all, I want to express my sincere and humble gratitude to my respected thesis supervisor Prof. Tanusri Saha-Dasgupta. My supervisor gave me the opportunity to involve in different types of projects and collaborations that helped me a lot to increase my experience and knowledge. I have been always benefited from her expertise supervision, brilliant ideas, constant push, endless enthusiasm and limitless passion for science. I would also like to thank all my collaborators Prof. Patrick M. Woodward, Prof. Tapan Chatterji, Prof. Masaki Azuma, Prof. Prabuddha Sanyal, Dr. Satyaki Kar. The discussion that I had with them helped me to understand the subject and to develop my own way to express my understanding of the subject.

I had the pleasure to work with some of the most vibrant group-mates, like Santu-da, Tilak-da, Soumyajit-da, Sudipta-da, Hrishit, Poulami, Dhani, Ransell, Anita, Shreya. I owe my deep gratitude to them, for their prompt response and skilful comments that helped my research career. A special thanks for Tilak-da, for his continuous help and suggestion in any matter at any situation. I have learnt lot of computational things from him. I thank Dr. Badiur Rahaman who always extended his help when ever I stuck in NMTO calculations.

I would like to acknowledge my school days teachers, Surya sir, Shyamal sir, Debasis sir, Vivek sir and college sir Upenda for setting up initial interest in science.

I thank all the academic and non-academic staff of S. N. Bose National Centre for Basic Sciences, Kolkata for providing me such a global platform, excellent research atmosphere and beautiful natural scenery. I am grateful to the Department of Science and Technology, Govt. of India for providing me regular monthly fellowship to carry out my research peacefully.

I am fortunate enough to have a great friend circles, seniors and juniors who stay very close to my heart. Among seniors I would like to thank Joydev-da, Swarup-da, Abhijit-da for their help and suggestion during my Ph.D period. The memory of my daily life during my stay in S. N. Bose are eventful and enjoyable due to the presence of friends like Arindam-da, Sarowar-da, Subrata, Shishir, Krishendu, Souvanik, Debasis, Aslam, Subhadip, Somnath, Suprio. Among juniors I would like to name Ananda, Rakesh, Sudipta. I shall miss all those weekend evenings spend with SNB friends which are not worth mentioning here! I would also like to thank Ashis, Uttam, Rajkumar, Aritra from whom I have been benefited in many way.

I would like to thank my family for their unconditional love and support. I would like to take this opportunity to express my heart-felt gratitude to my family; baba, ma and elder sisters for understanding me and tolerate me. It will be my audacity if I try to express their contribution in my life.

Finally, I would like to thank every body who played important role throughout my journey, as well as I am expressing my apology some one, I forget to mention.

Kartik Samanta
Kolkata, India
July, 2017

Preface

Among the various crystalline materials, transition metal (TM) compounds present a unique class of solids which play a major role in the modern day material science industry. Apart from industrial usage, the transition metal compounds are important also from basic science point of view. They have been studied for long time due to extremely rich physics offered by strongly correlated transition metal d -electrons. The intriguing interplay of charge, orbital and spin degrees of freedom give rise many novel physical phenomena ranging from Mott transition, half-metallicity, colossal magnetoresistance, multiferroicity to high- T_c superconductors *etc.* which are appealing both from application as well as fundamental science aspect.

In this thesis, few different transition metal compounds belonging two broad categories, namely i) low dimensional quantum spin systems ii) double perovskite compounds, have been investigated theoretically using density functional theory (DFT) based approach, often combined with model Hamiltonian approach with an aim to the investigate the microscopic origin of many exciting and intriguing physical properties as well as improve their physical properties, to be useful for technological applications. The first principles DFT based calculations, which is free of any adjustable parameters and takes into account all the structural and chemical aspect of material accurately, fail in some cases to predict the ground state properties, specially for strongly correlated electron materials. On the other hand electron-electron correlation are taken into account in a much more improved way within the many-body model Hamiltonian based approach but the parameters of model Hamiltonian are vastly unknown. Therefore model Hamiltonian approach fails to capture the material specific complexity of the transition metal compounds. Thus for theoretical calculations we combined this two approaches interms of building up a first principles derived model Hamiltonian, followed by the solution of the model Hamiltonian by means of many body techniques.

As electronic and magnetic properties of strongly correlated transition metal systems are mainly governed by the limited of states lying close to the Fermi energy, a crucial step in the model Hamiltonian building is the construction of low energy few band orbitals in a restricted Hilbert space, which has been achieved in terms of highly successful N^{th} order muffin-tin orbital based downfolding method. Many-body techniques like quantum Monte Carlo (QMC) and exact diagonalization (ED) have been used in this thesis to solve first principle derived model Hamiltonian. The theoretical methods that have been used in the present study are described in chapter 2. Hence after result of our studies is presented. Following is a brief description of problems studied in different chapters.

chapter 3: Using combination of first-principles density-functional theory and quantum Monte Carlo (QMC) technique, we described the electronic structure and magnetic behaviour of spin $S=1$ Haldane chain compound $\text{SrNi}_2\text{V}_2\text{O}_8$. We derived a microscopic spin model from parameter free ab initio calculation and solved with QMC technique to understand the individual role of complex longer range interactions and single ion anisotropy in reducing the Haldane spin

gap value from that of an ideal 1D Haldane chain compound. With a motivation of external tuning of ground state magnetic properties of this Haldane chain compound, we also studied the effects of biaxial compressive as well tensile strain.

chapter 4: Magnetic properties of recently synthesized vanadate carbonate compound $\text{K}_2\text{Mn}_3(\text{VO}_4)_2\text{CO}_3$ was discussed in terms of unusual low-spin state of Mn^{2+} . To examine the experimental proposal of unusual low-spin state of Mn^{2+} , as well as to investigate the possible effects of frustration arising from the geometry of Mn^{2+} ions, we carried out electronic structure calculation using first principles calculations. We also derived a microscopic spin model for this compound from ab initio calculation and checked the validity of our proposed model by comparing the computed magnetic susceptibility and magnetization using quantum Monte Carlo technique, with the available experimental data.

chapter 5: With an aim to obtain microscopic understanding on the issue of B and B' cations arrangements in double perovskite compounds of general composition $\text{A}_2\text{BB}'\text{O}_6$, we carried out first principles calculations considering the specific cases of $\text{La}_2\text{CuSnO}_6$ and $\text{La}_2\text{CuIrO}_6$. We studied the relative structural stability of this two compounds between layered and rock-salt ordering considering (a) the band structure effect, (b) the effect of magnetism, (c) effect of spin orbit coupling (SOC). We also studied the magnetic structure of these compounds.

chapter 6: We explored the possibility of driving half-metallicity in $\text{Sr}_2\text{CrOsO}_6$ double perovskite by La/Na doping at Sr sites, maintaining the spectacularly high magnetic transition temperature T_c of parent compound ($\simeq 725$ K). The aim of this work was to search new half-metallic magnetic materials with very high T_c , so that room temperature applications can be made. To explore this possibility we carried out first principles density functional calculation together with exact diagonalization of Cr-Os model Hamiltonian constructed in a first principles Wannier function basis.

chapter 7: We carried out investigation of electronic structure and magnetic properties of two mixed $3d$ - $5d$ ferrimagnetic double perovskites, namely $\text{Ca}_2\text{CoOsO}_6$ and $\text{Ca}_2\text{NiOsO}_6$ in order to understand the issue of local moment formation at $5d$ Os site as well as to provide the critical insight on super-exchange interaction between $3d$ and $5d$ transition metal ions. We developed a comprehensive picture of the local magnetism and magnetic couplings in these compounds using first principles calculations. Theoretical results based on DFT calculations were furtherer corroborated by experimental measurements.

Finally in chapter 8, we present the summary of the results presented in this thesis and the future direction.

List of Publications

1. **Kartik Samanta** and T. Saha-Dasgupta
Spin state of Mn^{2+} and magnetism in vanadate-carbonate compound, $\text{K}_2\text{Mn}_3(\text{VO}_4)_2\text{CO}_3$
Phys. Rev. B **90**, 064420 (2014)*
2. **Kartik Samanta**, Prabuddha Sanyal and T. Saha-Dasgupta
Half-Metallic Behavior in Doped $\text{Sr}_2\text{CrOsO}_6$ Double Perovskite with High Transition Temperature
Sci. Rep. **5**, 15010 (2015)*
3. Tapan Chatterji, Antonio M. dos Santos, Jamie J. Molaison, Thomas C. Hansen, Stefan Klotz, Mathew Tucker, **Kartik Samanta**, and T. Saha-Dasgupta
Anomalous breakdown of Bloch's rule in the Mott-Hubbard insulator MnTe_2
Phys. Rev. B **91**, 104412 (2015)
4. **Kartik Samanta**, Satyaki Kar, and T. Saha-Dasgupta
Magnetic modelling and effect of biaxial strain on the Haldane chain compound $\text{SrNi}_2\text{V}_2\text{O}_8$
Phys. Rev. B **93**, 224404 (2016)*
5. Ryan Morrow, **Kartik Samanta**, Tanusri Saha-Dasgupta, Jie Xiong, John W. Freeland, Daniel Haskel, and Patrick M. Woodward
Magnetism in $\text{Ca}_2\text{CoOsO}_6$ and $\text{Ca}_2\text{NiOsO}_6$: Unraveling the Mystery of Superexchange Interactions between $3d$ and $5d$ Ions
Chem. Mater. **28** (11), pp 3666-3675 (2016)*
6. **Kartik Samanta** and Tanusri Saha-Dasgupta
Rocksalt versus layered ordering in double perovskites: A case study with $\text{La}_2\text{CuSnO}_6$ and $\text{La}_2\text{CuIrO}_6$
Phys. Rev. B **95**, 235102 (2017)*
7. Hajime Hojo, Ryo Kawabe, Keisuke Shimizu, Hajime Yamamoto, Ko Mibu, **Kartik Samanta**, Tanusri Saha-Dasgupta, and Masaki Azuma
Ferromagnetism at Room Temperature Induced by Spin Structure Change in $\text{BiFe}_{1-x}\text{Co}_x\text{O}_3$ Thin Films
Adv. Mater. **1603131**, (2017)

Contents

Table of Contents	xi
List of Figures	xx
List of Tables	xxii
1 Introduction	1
1.1 General introduction about transition metal compounds	1
1.2 Transition metal compounds discussed in thesis	11
1.2.1 Low dimensional quantum spin systems	11
1.2.2 Double perovskite compounds $A_2BB'O_6$	19
1.3 Theoretical method to study transition metal compounds	28
2 Theoretical methods	38
2.1 The many-electron Hamiltonian	38
2.2 The Born-Oppenheimer approximation	39
2.3 Modern Density Functional Theory: way of solving quantum many body problem	41
2.3.1 The Hohenberg-Kohn (HK) theorem	41
2.3.2 The Kohn-Sham (KS) equations	43
2.3.3 Exchange-correlation functional	45
2.4 LDA+U Method	49
2.4.1 The Lichtenstein method	50
2.4.2 The Dudarev method	52
2.5 Basis Set	52
2.5.1 Fixed basis set methods	53

2.5.2	Partial wave methods	53
2.6	Overview of band structure methods	54
2.6.1	Plane wave based pseudopotential method	54
2.6.2	The linear muffin-tin orbital method	58
2.6.3	N^{th} order muffin-tin orbital (NMTO) downfolding method	62
2.6.4	The linearised augmented plane wave + local orbital method	65
2.6.5	The Projector-Augmented-Wave method	67
2.7	Many body technique	70
2.7.1	Stochastic series expansion of quantum Monte Carlo method	71
3	Magnetic modeling and effect of biaxial strain on the Haldane chain compound $\text{SrNi}_2\text{V}_2\text{O}_8^\dagger$	77
3.1	Introduction and motivation	77
3.2	Results and discussion	80
3.2.1	Crystal structure	80
3.2.2	Electronic structure of $\text{SrNi}_2\text{V}_2\text{O}_8$	83
3.2.3	Understanding of dominant exchange path: NMTO downfolding calculation	85
3.2.4	Magnetic-exchange interaction and single-ion anisotropy	87
3.2.5	Magnetic model	89
3.2.6	Calculation of thermodynamic quantities	90
3.3	Summary and conclusions	96
4	Spin state of Mn^{2+} and magnetism in vanadate-carbonate compound, $\text{K}_2\text{Mn}_3(\text{VO}_4)_2\text{CO}_3^\dagger$	100
4.1	Introduction and motivation	100
4.2	Results and discussion	103
4.2.1	Crystal structure	103
4.2.2	Electronic structure and spin state of Mn^{2+} ions	105
4.2.3	Estimation of magnetic exchange interactions	110
4.2.4	Magnetic structure	116
4.2.5	Calculation of thermodynamic properties	117
4.3	Summary and conclusions	119

5	Rock-salt versus Layered Ordering in Double Perovskites: A Case Study with $\text{La}_2\text{CuSnO}_6$ and $\text{La}_2\text{CuIrO}_6^\dagger$	123
5.1	Introduction and motivation	123
5.2	Computational details	125
5.3	Results and discussion	127
5.3.1	Crystal structure	127
5.3.2	Consideration of different structures to study structural stability	128
5.3.3	Structural stability in terms of energetics	129
5.3.4	Microscopic analysis	134
5.3.5	Electronic structure of magnetic $\text{La}_2\text{CuSnO}_6$	140
5.3.6	Electronic structure of magnetic $\text{La}_2\text{CuIrO}_6$	141
5.4	Summary and conclusions	143
5.5	Structural stability of $\text{La}_2\text{CuMnO}_6$ (LCMO)	144
6	Half-Metallic Behavior in Doped $\text{Sr}_2\text{CrOsO}_6$ Double Perovskite with High Transition Temperature[†]	148
6.1	Introduction and motivation	148
6.2	Computational details	150
6.3	Results and discussion	151
6.3.1	Results for parent compound $\text{Sr}_2\text{CrOsO}_6$	151
6.3.2	DFT electronic and magnetic structure of doped compounds	153
6.3.3	Exact diagonalization study of DFT derived model Hamiltonian	157
6.4	Summary and conclusions	163
7	Magnetism in $\text{Ca}_2\text{CoOsO}_6$ and $\text{Ca}_2\text{NiOsO}_6$: Unraveling the Mystery of Superexchange Interactions between $3d$ and $5d$ Ions[†]	167
7.1	Introduction and motivation	167
7.2	Results	170
7.2.1	Crystal structure	170
7.2.2	DFT electronic structure calculation	171
7.2.3	DFT calculated local moments	174
7.2.4	Calculation of magnetic exchange interaction	175

7.3	Experimental results	178
7.3.1	DC electrical conductivity measurements	178
7.3.2	Magnetic hysteresis loop measurements	179
7.3.3	XAS and XMCD measurements	179
7.4	Discussion	181
7.5	Conclusions	185
8	Conclusion and outlook	189
8.1	Conclusion	189
8.2	Outlook	194

List of Figures

1.1	Symmetry and corresponding crystal field splitting of d levels in a regular octahedral coordination. Δ represents strength of crystal field splitting.	2
1.2	Panel (a): Schematic diagram showing covalency contribution to crystal field splitting for transition metal e_g electrons (σ bonding) due to p - d hybridization. Panel (b): Schematic diagram showing covalency contribution to crystal field splitting for transition metal t_{2g} electrons (π bonding) due to p - d hybridization.	3
1.3	Schematic diagram showing the origin of the crystal field splitting due to p - d covalency. d and p represent five-fold degenerate d -levels of transition metal ions and p level of oxygen ions, respectively. b and a stand for bonding and antibonding levels.	4
1.4	Splitting of d levels due to tetragonal distortion of TM-O ₆ octahedra for tetragonal elongation (a) and compression (c). Panel (b): splitting of d levels due to crystal field of regular TM-O ₆ octahedra.	4
1.5	Splitting of d levels due to trigonal distortion of TM-O ₆ octahedra for trigonal elongation (a) and contraction (c). Panel (b): splitting of d levels due to crystal field of regular TM-O ₆ octahedra.	5
1.6	Dependence of the energy levels as a function of distortion u [see Eq. 1.4]. It shows the lifting of doubly degenerate energy levels (at $u=0$) for finite distortion u_0	6
1.7	Schematic diagram showing (a) high-spin (HS) and (b) low-spin (LS) states for transition metal ions with d^4 electron occupation within the crystal field of regular octahedra.	7
1.8	Symmetry and corresponding crystal field splitting of d levels for two regular MO _{n} polyhedra, namely (a) tetrahedra, (b) trigonal by-pyramid.	8

1.9	Schematic diagram showing the energy band in the Hubbard model as a function of the strength of electron-electron repulsion (Hubbard U) for a lattice of N sites with one electron per site. Left hand side shows the conventional band picture which gives rise metallic solution at half-filling. The two bands on the right side represent the Hubbard (sub)bands for a critical value of (U/t) . For a lattice with one electron per site, lower (shaded) Hubbard band is completely filled with N electrons and upper (unshaded) Hubbard band is completely empty and U represents the approximate energy gap between these two Hubbard (sub)bands. Fig. is taken from Ref. [1].	10
1.10	Panel (a): Spin $S=1/2$ chain with uniform antiferromagnetic exchange coupling. Panel (b): Schematic representation of singlet ground state of the dimerized lattice below the spin-Peierls transition, which leads to alternation of the exchange interaction.	13
1.11	Schematic representation of valence bond solid model, showing (a) Spin $S=1$ chain with uniform antiferromagnetic exchange coupling (b) decomposition of each spin $S=1$, into two $S=1/2$ spin degrees of freedom, (c) formation of singlet state by pairing adjacent spins, (d) symmetrization of the two $S=1/2$ spins at each side to restore the original spin $S= 1$, (e) the introduction of a spin vacancy which breaks two valence bonds and liberates two $S= 1/2$ degrees of freedom on the neighbouring sites.	15
1.12	The simplest two chain spin ladder model. J and J_R represent the exchange coupling along the spin chain and along the rung of the ladder, respectively. . . .	16
1.13	Schematic diagram of the Shastry-Sutherland model. J is the nearest-neighbour antiferromagnetic exchange interaction and J_1 is the selected antiferromagnetic bond interactions.	18
1.14	Schematic representation of three different ordering of BO_6 and $\text{B}'\text{O}_6$ octahedra, possible in a double perovskite structure. The BO_6 and $\text{B}'\text{O}_6$ octahedra are marked with two different colors. From left to right, the figure shows the columnar, layered and rock-salt ordering.	20
1.15	Ideal rock-salt ordered cubic structure of double perovskite, $\text{A}_2\text{BB}'\text{O}_6$	21
1.16	Schematic diagram showing the hybridization induced negative spin polarization of Mo bands for $\text{Sr}_2\text{FeMoO}_6$. The shaded semicircular density of states represent the spin split Fe bands. The semicircular density of states, marked in solid red lines, represent Mo bands before switching on the hybridization while that after switching on the hybridization is shown by red dashed lines. E_f marks the position of Fermi energy. Fig. is taken form Ref [76].	26
1.17	Schematic representation of half-metal showing insulating behaviour in up spin channel and metallic behaviour in down spin channel.	26
1.18	Schematic diagram showing the combined approaches of DFT and many body calculations.	29
1.19	Basic procedure of extracting model Hamiltonian parameters from NMTO down-folding method.	30

2.1	Schematic diagram presenting the relationship between the real many body system (left hand side) and the non-interacting system of Kohn-Sham density functional theory (right hand side) Fig. is taken from Ref. [12].	44
2.2	DFT self consistent cycle.	46
2.3	In presence of U parameter, shifting of the occupied and unoccupied LDA orbitals with respect to each other.	50
2.4	Schematic diagram showing the basic idea of pseudopotential. Fig. is taken from web: http://en.wikipedia.org/wiki/Pseudopotential	57
2.5	Upper panel: Schematic diagram of potential inside real crystal considered in LMTO method. Lower panel: Schematic diagram of approximated potential considered in LMTO method. In the vicinity of core atomic region potential is rapidly varying . In the interstitial region <i>i.e.</i> away from atom core region, the actual potential is approximated as a constant potential.	59
2.6	Constituents of Kink partial wave (KPW), ϕ , ϕ_0 , φ	64
2.7	The N^{th} order approximation to the energy dependence of a partial wave for a discrete (Lagrange) mesh.	64
2.8	Schematic diagram showing the division of a unit cell in muffin tin regions and the interstitial region (IS) for a case of two atoms. The origin of the axis is set at centre of S_α atom.	66
3.1	(a) Crystal structure of $\text{SrNi}_2\text{V}_2\text{O}_8$, showing the three-dimensional network. Various atoms including the inequivalent oxygens are marked. Sr atoms are not shown for clarity. (b) Projection of the crystal structure onto the ab plane, showing the four screw chains. For clarity only the atoms and bonds are shown without polyhedra.	80
3.2	GGA spin-polarized total and partial density of states of $\text{SrNi}_2\text{V}_2\text{O}_8$, as obtained from FLAPW calculation. The zero of the energy is set at GGA Fermi energy. Top panel shows the total density of states, while the middle and bottom panels show density of states projected to Ni d (black shaded area), V d (cyan solid line), and O p (black shaded area) states.	83
3.3	(a) Left panel shows overlap of Ni1 and Ni2 effective x^2-y^2 Wannier functions placed at two nearest-neighbour intrachain Ni sites. The two oppositely signed lobes of the wave functions at site 1 (2), are coloured differently as black (blue) and white (orange). Plotted are the constant value surfaces. Right panel shows same as in left panel, but plotted for Ni $3z^2-r^2$ Wannier functions. (b) The network of edge-sharing nearest-neighbour Ni octahedra, connected through two paths, one through edge-sharing oxygens and another through path involving V atom. The V, O, and Ni atoms are marked.	86

- 3.4 The magnetic lattice created by Ni spins, projected to the plane perpendicular to the chain direction (left panel), and that in the plane of the chain (right panel). Four dominant magnetic interactions are shown here. The magnetic exchange interactions J_1 and J_2 are nearest and next-nearest-neighbour intrachain interactions and J_3 and J_4 are two interchain interactions. 89
- 3.5 Temperature dependence of magnetic susceptibility for the unstrained $\text{SrNi}_2\text{V}_2\text{O}_8$. The circles correspond to experimental data [17] and the solid line corresponds to QMC calculated susceptibility based on the first-principles derived J_1 - J_2 - J_3 - J_4 spin model, together with easy-axis anisotropy, in presence of a magnetic field of 1 T. 91
- 3.6 Evolution of magnetization as a function of magnetic field applied parallel to chain direction, for the various spin models. 93
- 3.7 Temperature dependence of the theoretical spin susceptibility for the unstrained $\text{SrNi}_2\text{V}_2\text{O}_8$ (black solid line), compressive strained (black dashed line), and tensile strained (gray line) compounds. Inset shows the plot zoomed at low temperature to focus on the spin-gap behaviour. 94
- 3.8 Evolution of magnetization as a function of magnetic field applied parallel to chain direction for the unstrained (black solid line), tensile strained (gray line), and compressive strained (dashed line) compounds. The inset shows the variation of the calculated spin gap, estimated from critical field, as a function of the in-plane lattice constant. L_0 , $L_0(1-0.02)$ and $L_0(1+0.02)$ denote the in-plane lattice constants of the unstrained compound, compressive strained, and tensile strained compounds, respectively. The line is to guide the eye. The data point shown by the asterisk corresponds to the estimate obtained from experimentally measured critical field 95
- 4.1 (a) Experimentally measured temperature dependence of the magnetic susceptibility plots. The right inset shows the inverse magnetic susceptibility. The dashed lines indicates the slopes of this curve at low ($T < 100$ K) and high ($T > 100$ K) temperature. The left inset shows the temperature dependence of the magnetic susceptibility measured at $B = 0.1$ T. (b) Experimentally measured field dependence of the magnetization at $T = 2$ K. The insets show the crystal-field splitting of d level in Mn1 and Mn2 sites. Figures are taken from Ref. [6] 101
- 4.2 Crystal structure of $\text{K}_2\text{Mn}_3(\text{VO}_4)_2\text{CO}_3$. (a) The basic structural units VO_4 , CO_3 , Mn_2O_5 , and edge-sharing Mn_1O_6 octahedra (from top to bottom). The inequivalent oxygens have been marked. (b) The layered sublattices of Mn1 (bottom panel) and Mn2 (top panel). (c) The connected, three-dimensional network. 103
- 4.3 Spin-polarized GGA density of states, projected onto Mn1 d (black solid line), Mn2 d (green solid line), O p (black shaded area), V d (brown solid line) and C p (orange shaded area) states. The zero of the energy is set at GGA Fermi energy. 106
- 4.4 Energy plotted as a function of the fixed total magnetic moment in the unit cell, consisting of four Mn1 and two Mn2 ions. The solid and dashed lines correspond to calculations within GGA and GGA+U, respectively. 108

- 4.5 (a) Spin-polarized GGA density of states, projected onto octahedral crystal field splits Mn1 t_{2g} (cyan solid line) and e_g states (black solid line). The zero of the energy is set at GGA Fermi energy. (b) Spin-polarized GGA density of states, projected onto crystal field splits Mn2 d states. (c) Energy-level positions of Mn1 d states and their occupancies. The distortion in Mn1O₆ octahedra gives rise to small splitting of t_{2g} states into e_g^π and a_{1g} states. (d) Energy-level positions of Mn2 d states and their occupancies. 109
- 4.6 NMTO downfolded Mn d only bands, shown in black, solid lines, in comparison to Mn1 d (the fatness, shown as red, vertical lines) and Mn2 d (the fatness, shown as blue, vertical lines) projected states of the full band structure. The energies E0 and E1 represent energy about the expansion were carried out in NMTO calculation. 111
- 4.7 The dominant Mn-Mn effective hopping interactions, in the Mn1 layer (right top), Mn2 layer (right bottom), and that between Mn1 and Mn2 layers (left). The Mn1 and Mn2 sites are shown as green and blue balls, respectively. The fatness of the connecting bonds, connecting two sites, are proportional to the corresponding hopping strength. 113
- 4.8 Plot of Wannier functions placed at two interacting nearest neighbour Mn1 sites, corresponding to strongest interaction t_1 . The two oppositely signed lobes of the wavefunctions at site $i(j)$ are coloured differently as black (blue) and white (orange). 113
- 4.9 (a) Plot of Wannier functions placed at two interacting nearest neighbour Mn2 sites. (b) Plot of Wannier functions placed at two nearest neighbour Mn1 and Mn2 site, which connect the two layers. The two oppositely signed lobes of the wavefunctions at site $i(j)$ are coloured differently as black (blue) and white (orange). 114
- 4.10 Labeling of Mn1 and Mn2 sites, forming alternate layers in the $1 \times 2 \times 1$ supercell, considered for total-energy calculations. The Mn1 and Mn2 atoms are coloured differently as pink and light gray, respectively. The connections corresponding to J_1, J_2, J_3, J_4 and J_5 are indicated. 115
- 4.11 (a) The lowest-energy spin structure of Mn1 spins in Mn1 layer, as given in DFT calculation. (b) The lowest energy spin structure of Mn2 spins in Mn2 layer. . . 117
- 4.12 Temperature dependence of magnetic susceptibility. The solid line and circle correspond to calculated susceptibility based on ab initio-derived spin model and experimental data [6], respectively. Inset shows the calculated susceptibility based on only Mn1-Mn1 interactions *i.e.* J_1 - J_2 - J_3 118
- 4.13 The magnetic-field dependence of magnetization. The left and right panels correspond to calculation based on ab initio-derived spin model and experimental data [6], respectively. In the left panel, the stars mark the calculated data while the line is a spline fit through the data points. 119

- 5.1 Panel (A): Crystal structures of $\text{La}_2\text{CuIrO}_6$ in $\text{P}\bar{1}$ space group, showing the rock-salt ordering of CuO_6 (brown color) and IrO_6 (light grey color) octahedra. Panel (B): Crystal structures of $\text{La}_2\text{CuSnO}_6$ in $\text{P}2_1/\text{m}$ space group, showing the layered ordering of CuO_6 (brown color) and SnO_6 (light grey color) octahedra. Two inequivalent CuO_6 , IrO_6 and SnO_6 octahedra are labelled in both the structures. The La ions sitting the void created by the corner-shared octahedra are not shown for clarity. 127
- 5.2 The non spin-polarized total energy of LCIO (circles) and LCSO (squares), in the optimized rock-salt ordered $\text{P}\bar{1}$ symmetry structure (black symbols) and layered ordered $\text{P}2_1/\text{m}$ symmetry (red symbols) structure. The positive value of ΔE indicates stability of $\text{P}2_1/\text{m}$ symmetry over $\text{P}\bar{1}$ symmetry. 130
- 5.3 The various considered AFM magnetic structures. Panels I, II, are for rock-salt ordered, $\text{P}\bar{1}$ and layered ordered, $\text{P}2_1/\text{m}$ structured of LCIO, respectively while panels III and IV are for rock-salt ordered, $\text{P}\bar{1}$ and layered ordered, $\text{P}2_1/\text{m}$ structured of LCSO, respectively. The Cu and Ir sites are shown as blue and yellow coloured balls, while Sn sites are shown as pink coloured balls. The spins at Cu and Ir sites are as arrows. 132
- 5.4 The comparison of GGA+U total energy of LCIO (circles) and LCSO (squares) between the rock-salt and layer ordered structures, considering different magnetic structures. See Fig. 5.3 for the considered magnetic structures. Plotted are the total energy differences (ΔE) for the optimized $\text{P}2_1/\text{m}$ symmetry (red symbols) structure and the $\text{P}\bar{1}$ symmetry structure (black symbols). See text for details. The positive value of ΔE for LCSO and LCIO indicates stability of $\text{P}2_1/\text{m}$ symmetry over $\text{P}\bar{1}$ symmetry, and of $\text{P}\bar{1}$ symmetry over $\text{P}2_1/\text{m}$ symmetry, respectively. The open symbols in case of LCIO represent results corresponding to GGA+U+SO calculations 133
- 5.5 Panel (A): Non spin-polarized band structure and density of states of LCSO in the rock-salt ordered $\text{P}\bar{1}$ symmetry. Panel (B): Non spin-polarized band structure and density of states of LCSO in the layer ordered $\text{P}2_1/\text{m}$ symmetry. Band structure is plotted along the high-symmetry k-points of the triclinic (for $\text{P}\bar{1}$ symmetry) BZ and the monoclinic (for $\text{P}2_1/\text{m}$ symmetry) BZ. The zero of the energy is set at Fermi energy (E_F). The dominant orbital characters of the states are shown by side. 134
- 5.6 Panel (A): Non spin-polarized band structure and density of states of LCIO in the rock-salt ordered $\text{P}\bar{1}$ symmetry. Panel (B): Non spin-polarized band structure and density of states of LCIO in layer ordered $\text{P}2_1/\text{m}$ symmetry. Band structure is plotted along the high-symmetry k-points of the triclinic (for $\text{P}\bar{1}$ symmetry) BZ and the monoclinic (for $\text{P}2_1/\text{m}$ symmetry) BZ. The zero of the energy is set at Fermi energy (E_F). The dominant orbital characters of the states are shown by side. 135
- 5.7 Wannier functions of effective Cu $d_{x^2-y^2}$ of LCSO for the rock-salt [panel (A)] and layer ordered [panel (B)] structures. Plotted are the constant value surfaces, with positive and negative lobes of the wavefunctions coloured differently. 136

- 5.8 Left panel: dominant hopping path for rock-salt ordered $P\bar{1}$ symmetry structure. B1(B2) represent Ir1(Ir2) for LCIO and Sn1(Sn2) for LCSO. Right panel: dominant hopping path for layered ordered $P2_1/m$ symmetry structure. 137
- 5.9 Wannier functions of effective Cu $d_{3z^2-r^2}$ for the rock-salt [panel (A)] and Cu $d_{3z^2-r^2}$ for layer ordered [panel (B)] structures of LCIO. Plotted are the constant value surfaces, with positive and negative lobes of the wavefunctions coloured differently 139
- 5.10 The band structure and density of states of LCSO in magnetically ordered ground state of AFM-2D in layer ordered $P2_1/m$ symmetry within GGA+U scheme of calculation. Band structure is plotted along the high-symmetry k-points of the monoclinic BZ. The zero of the energy is set at E_F . The dominant orbital characters of the states are shown by side, with Cu $d_{x^2-y^2}$ (a)/(b) denoting the minority/majority spin bands. 140
- 5.11 The band structure and density of states of LCIO in magnetically ordered state of AFM-C in rock-salt ordered $P\bar{1}$ symmetry within GGA+U [panel (A)] and GGA+U+SOC [panel (B)] scheme of calculations. Band structure is plotted along the high-symmetry k-points of the triclinic BZ. The zero of the energy is set at E_F . The dominant orbital characters of the states are shown by side. Cu $d_{x^2-y^2}$ (a)/(b) denotes the minority/majority spin bands, while Cu- d_{z^2} (c)/(v) denotes the UHB and LHB bands of Cu $d_{3z^2-r^2}$ 141
- 5.12 experimental determined magnetic structure of LCIO, stabilized in a $2 \times 1 \times 2$ supercell of $P\bar{1}$ symmetry. The Cu and Ir sites are shown as blue and yellow coloured balls. 142
- 5.13 Panel I: Crystal structure of Fm-3m space group of LCMO, showing the rock-salt ordering of CuO_6 (green color) and MnO_6 (pink color) octahedra. Panel II: (left side) The non spin-polarized total energy difference (ΔE) of LCMO between the optimized Fm-3m symmetry structure (black symbol) and $P2_1/m$ symmetry (red symbol) structure. The positive value of ΔE indicates stability of $P2_1/m$ symmetry over Fm-3m symmetry. Right side: The comparison of GGA+U total energy between the rock-salt and layer ordered structures, considering different magnetic structures. Plotted are the total energy differences (ΔE) for the optimized $P2_1/m$ symmetry (red symbols) structure and the Fm-3m symmetry structure (black symbols). The positive value of ΔE indicates stability of Fm-3m symmetry over $P2_1/m$ symmetry. 145
- 6.1 The cubic structure of $\text{Sr}_2\text{CrOsO}_6$ in Fm-3m space group. The small red balls represent O atoms. 151
- 6.2 GGA+U+SOC density states of parent compound, $\text{Sr}_2\text{CrOsO}_6$, projected onto Cr d (black solid lines), Os d (cyan solid lines) and O p (brown shaded area). Zero of the energy is set at E_F 153

- 6.3 Panel I: left side shows the A sublattice with eight Sr atoms. Right side shows the A sublattice with one of eight Sr atoms substituted by La/Na. The substituted atom is shown as yellow ball. Panel II.: The A sublattice with two out of eight Sr atoms substituted by Na/La, in various inequivalent positions. Panel III.: The A sublattice with three out of eight Sr atoms substituted by Na/La, in various inequivalent positions. 154
- 6.4 Left panel: GGA+U+SOC density of states of the parent compound, and the Na doped compounds. From top to bottom, the various panels refer to parent compound, $\text{Sr}_{1.875}\text{Na}_{0.125}\text{CrOsO}_6$, $\text{Sr}_{1.75}\text{Na}_{0.25}\text{CrOsO}_6$, $\text{Sr}_{1.625}\text{Na}_{0.375}\text{CrOsO}_6$ compounds respectively. The zero of the energy is set at E_F . The black, cyan, orange shaded area represent the states projected onto Cr d , Os d and O p states, respectively. Right panel: Same as left panel, but shown for parent and La doped compounds. From top to bottom, the various panels refer to parent compound, $\text{Sr}_{1.875}\text{La}_{0.125}\text{CrOsO}_6$, $\text{Sr}_{1.75}\text{La}_{0.25}\text{CrOsO}_6$, $\text{Sr}_{1.625}\text{La}_{0.375}\text{CrOsO}_6$ compounds respectively. The dashed, vertical lines in each panel mark the positions of Fermi level. 155
- 6.5 Panel I: Calculated M_S and M_L at Cr site for the parent and six different doped compounds as a function of Os t_{2g} filling (N). The circle denotes the parent compound, while the diamond and squares represent Na doped and La doped compounds. Panel II: Same as panel I, but shown for that at Os site. Panel III: The net magnetic moment per formula unit plotted as a function of Os t_{2g} filling 156
- 6.6 The downfolded, tight-binding band structure of $\text{Sr}_2\text{CrOsO}_6$ in effective Cr-Os t_{2g} basis (in red lines) in comparison with full band structure (in green lines). Zero of the energy is set at Fermi energy. The energies, E0 and E1 represent the energy points about the expansion were carried out in NMTO calculation. 159
- 6.7 The energy difference between PM and FM arrangement of Cr spins, plotted as a function of Os t_{2g} filling (N), shown as black solid line. The vertical lines mark the filling corresponding to the parent (solid, magenta) and various Na (red-solid, orange-dashed and brown- dot-dashed for $\text{Sr}_{1.875}\text{Na}_{0.125}\text{CrOsO}_6$, $\text{Sr}_{1.75}\text{Na}_{0.25}\text{CrOsO}_6$, $\text{Sr}_{1.625}\text{Na}_{0.375}\text{CrOsO}_6$, respectively) and La doped compounds (green-solid, green-dashed and indigo-dot-dashed for $\text{Sr}_{1.875}\text{La}_{0.125}\text{CrOsO}_6$, $\text{Sr}_{1.75}\text{La}_{0.25}\text{CrOsO}_6$, $\text{Sr}_{1.625}\text{La}_{0.375}\text{CrOsO}_6$, respectively) studied in present work. Both the Na-doped and La-doped compounds are half-metallic, while the parent compound with electron count of three, is insulating. . 160
- 6.8 The spin polarization, plotted as a function of Os t_{2g} filling (N), shown as black solid line. The vertical lines mark the filling corresponding to the parent (solid, magenta) and various Na (red-solid, orange-dashed and brown- dot-dashed for $\text{Sr}_{1.875}\text{Na}_{0.125}\text{CrOsO}_6$, $\text{Sr}_{1.75}\text{Na}_{0.25}\text{CrOsO}_6$, $\text{Sr}_{1.625}\text{Na}_{0.375}\text{CrOsO}_6$, respectively) and La doped compounds (green-solid, green-dashed and indigo-dot-dashed for $\text{Sr}_{1.875}\text{La}_{0.125}\text{CrOsO}_6$, $\text{Sr}_{1.75}\text{La}_{0.25}\text{CrOsO}_6$, $\text{Sr}_{1.625}\text{La}_{0.375}\text{CrOsO}_6$, respectively) studied in present work. Both the Na-doped and La-doped compounds are half-metallic, while the parent compound with electron count of three, is insulating 163

7.1	Crystal structure of $\text{Ca}_2\text{CoOsO}_6$ (left panel) and $\text{Ca}_2\text{NiOsO}_6$ (right panel), showing the three dimensional network. Various atoms including the inequivalent oxygens are marked. Ca atoms are not shown for clarity.	170
7.2	Total density of states of $\text{Ca}_2\text{CoOsO}_6$ and $\text{Ca}_2\text{NiOsO}_6$ as obtained within GGA, GGA+U and GGA+U+SOC scheme of calculations. The zero of the energy in each panel is set at Fermi energy. The insets in the bottom panels highlights the region near the Fermi energy revealing a small gap.	172
7.3	Density of states of $\text{Ca}_2\text{CoOsO}_6$ and $\text{Ca}_2\text{NiOsO}_6$ projected onto the Co/Ni (black line) and Os- d (brown shaded area) states, as obtained within GGA, GGA+U and GGA+U+SOC scheme of calculations. The zero of the energy in each panel is set at Fermi energy. The insets in the bottom panels highlights the region near the Fermi energy revealing a small gap.	173
7.4	The relevant magnetic exchange pathways.	176
7.5	Temperature dependence of the electrical conductivity of $\text{Ca}_2\text{CoOsO}_6$ and $\text{Ca}_2\text{NiOsO}_6$ shown on a linear temperature scale. (reproduced from Ref. [25]). . .	178
7.6	Field dependence of the magnetization measured at 5 K. (reproduced from Ref. [25]).	179
7.7	XAS and XMCD spectra of $\text{Ca}_2\text{CoOsO}_6$ (a, c) and $\text{Ca}_2\text{NiOsO}_6$ (b, d). The data have been normalized to a 2:1 L_3 to L_2 step size. Arbitrary y-axis units are used for all spectra. (reproduced from Ref. [25]).	180
7.8	Potential superexchange interactions between the Os t_{2g} orbitals and the Co e_g orbitals (upper row), and the Co t_{2g} orbitals (lower row).	183
7.9	Overlap of the Os xy effective Wannier functions in $\text{Ca}_2\text{CoOsO}_6$ obtained from NMTO-downfolding calculations, keeping active only the Os t_{2g} states in the basis. The plot shows the overlap of Wannier functions at two Os sites connected through diagonal hopping. Plotted are the constant value surfaces with positive and negative lobes of the wavefunctions coloured differently at two different Os sites. The red small and green medium balls denote the positions of the O and Co. The Ca atom sits in the middle of the square, covered by the lobes of the Wannier functions.	184

List of Tables

1.1	Cation ordered found in different double perovskite compounds. Taken from Ref. [51].	20
3.1	The theoretically optimized atomic positions compared to the experimentally determined data. During the optimization the parameters of the tetragonal ($I4_1cd$) unit cell is kept fixed at the experimentally measured value, $a=12.16 \text{ \AA}$ and $c=8.32 \text{ \AA}$	81
3.2	Theoretically optimized crystal structure of 2% biaxially strained $\text{SrNi}_2\text{V}_2\text{O}_8$. During the optimization tetragonal ($I4_1cd$) symmetry of the unit cell is kept fixed. Lattice constant for 2% tensile and compressive strain, are $a=12.40 \text{ \AA}$, $c=8.21 \text{ \AA}$ and $a=11.92 \text{ \AA}$, $c=8.41 \text{ \AA}$ respectively.	82
3.3	Selected bond lengths and bond angles for optimised unstrained as well as 2% biaxially strain applied compounds.	82
3.4	Calculated GGA and GGA+U magnetic moments (in μ_B)	84
3.5	Ni-Ni effective hopping interactions. Each hopping interaction is a 2×2 matrix involving two e_g orbitals of Ni.	85
3.6	Calculated magnetic interactions of the unstrained and biaxially strained compounds. For the unstrained compound, the experimental estimates [24] are also shown for comparison.	88
4.1	The theoretically optimized atomic positions compared to the experimentally measured data. During the optimization the parameters of the hexagonal unit cell are fixed at the experimentally measured values, $a = 5.201 \text{ \AA}$ and $c = 20.406 \text{ \AA}$	104
4.2	Comparison of selected bond lengths for experimental as well as theoretical optimized structure.	105
4.3	Magnetic moment at V, Mn1, Mn2, and inequivalent O sites (in μ_B) as calculated in GGA and GGA+U scheme of calculation, considering measured as well as theoretically optimized crystal structures. The moment at C sites being vanishingly small has not been shown.	107

4.4	Effective hopping interactions (in eV) between two Mn sites which can be either Mn1 or Mn2 (see third column), connected through the connecting vector, as given in the first column, and separated by a distance, as given in the fourth column of the table. The number of neighbours for a given pair of Mn sites is indicated in the second column. Each hopping interaction is a 5×5 matrix, $h_{m,m'}$ with $m, m' = d_{xy}, d_{yz}, d_{3z^2-r^2}, d_{xz}$, and $d_{x^2-y^2}$	112
4.5	Magnetic configurations of the Mn ions in the supercell for the states used to determine the magnetic interactions. The numbering of the Mn sites are as shown in Fig. 4.8. The last column gives the relative GGA+U energies in eV.	116
5.1	Structural parameters and selected bond length for fully relaxed LCIO and LCSO structures in both rock-salt ordered $P\bar{1}$ and layered $P2_1/m$ symmetry.	128
5.2	Calculated magnetic moments (in μ_B) of Cu, Ir in LCIO and of Cu, Sn in LCSO for the lowest energy magnetic structures within $P2_1/m$ and $P\bar{1}$ symmetry	131
5.3	Dominant hopping integrals (in eV), as obtained from NMTO-downfolding calculation, for LCSO in $P\bar{1}$ and $P2_1/m$ symmetry. The large hoppings are marked in bold.	137
5.4	Dominant hopping integrals (in eV), as obtained from NMTO-downfolding calculation, for LCIO in $P\bar{1}$ and $P2_1/m$ symmetry. The large hoppings are marked in bold	138
5.5	Calculated magnetic (spin and orbital) moments (in μ_B) of Cu and Ir in LCIO for experimentally determined magnetic structure of $P\bar{1}$	143
6.1	Structural parameters and selected bond lengths of experimentally measured parent compound Sr_2CrOsO_6	151
6.2	Calculated magnetic moments (in μ_B) of parent compound Sr_2CrOsO_6	152
6.3	Model Hamiltonian estimated transition temperature T_c of six doped compounds with respect to parent compound	161
7.1	Structural parameters, selected bond lengths and bond angles of experimentally measured Ca_2CoOsO_6 and Ca_2NiOsO_6 double perovskites.	171
7.2	DFT calculated the spin (m_s), orbital (m_l) and total (m_{tot}) magnetic moments within GGA+U+SOC.	175
7.3	Computed values of the relevant magnetic exchange interactions in meV unit. Negative and positive values of J signify, anti-ferromagnetic and ferromagnetic coupling respectively.	177
7.4	The spin (m_s) and orbital (m_l) moments obtained from X-ray magnetic circular dichroism measurements (XMCD)	180

Chapter 1

Introduction

1.1 General introduction about transition metal compounds

Transition metal (TM) compounds present a unique class of materials exhibiting a variety of structure and physical properties. Transition metal compounds specially the oxides have been studied for long time due to their outstanding range of electronic and magnetic properties offered by strongly correlated transition metal d -electrons which are appealing both from application as well as from fundamental science aspect.

The basic structural unit of transition metal oxides is metal(M)-oxygen(O) polyhedra (MO_n , where M is transition atom, and n is an integer number) such as octahedra, trigonal bipyramid, square pyramid, tetrahedra, square planar, *etc.* Isolated transition metal atoms have spherical symmetry but when put in a crystal, the spherical symmetry is violated and the resulting symmetry depends on the coordination of oxygen polyhedra. The surrounding charge distribution of oxygens produces an anisotropic static electric field around the transition metal ion, known as crystal field, which breaks the degeneracies of d orbitals of transition metal ion. This results into lifting of five-fold degenerate d levels ($l=2$; $l^z = -2, -1, 0, 1, 2$). The strength and nature of this splitting, known as crystal field splitting depend on the following factors.

- Oxidation state of transition metal ions. Higher oxidation state leads to a larger splitting.
- The arrangement of the oxygen around the metal ion *i.e.* the symmetry of oxygen cage.

- Strength of transition metal (TM) and oxygen (O) covalency.

The most common geometry in transition metal oxides is the octahedral geometry where six oxygens form an octahedron around the metal ion, as shown in left side of Fig. 1.1. In the cubic

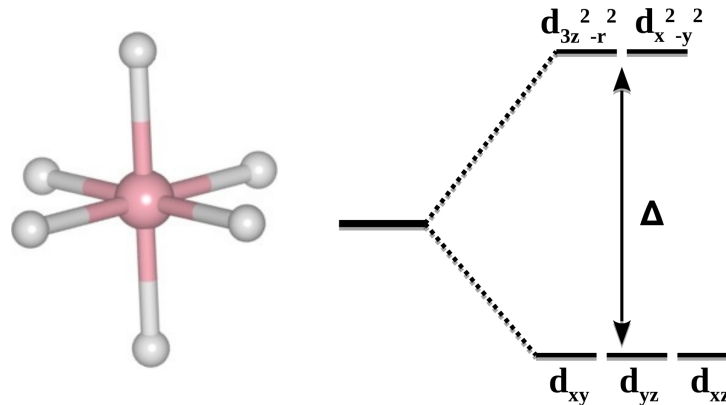


Figure 1.1: Symmetry and corresponding crystal field splitting of d levels in a regular octahedral coordination. Δ represents strength of crystal field splitting.

crystal field of regular octahedron, the d -orbitals split into a higher energy level of two-fold (four-fold including spin) degenerate e_g and a lower energy level of three fold (six-fold including spin) degenerate t_{2g} orbitals. This notation comes from group theory and subscript g from German *gerade* which means even, due to the fact that base function are even with respect to spatial inversion $\mathbf{r} \rightarrow -\mathbf{r}$ [1,2]. For a cubic crystal field of regular octahedron, the lobes (electron densities) of the e_g orbitals, formed by $d_{x^2-y^2}$ and $d_{3z^2-r^2}$ orbitals are pointed directly toward the oxygen ions surrounding the TM ion and therefore e_g electrons experience strong Coulomb repulsion from the negatively charged oxygen ions. On the other hand the lobes of t_{2g} orbitals, constituted by d_{xy} , d_{yz} and d_{xz} orbitals are directed in between two oxygen atoms, therefore t_{2g} electrons experience weak Coulomb repulsion from oxygen ions and consequently the energy of t_{2g} levels is lower than that of e_g one [cf. Fig. 1.1]. This contribution to the crystal field splitting is known as point-charge contribution, as the negatively charged oxygen ions are assumed to be point-charge in this description. Apart from point-charge contribution, the covalency between d -electrons and surrounding oxygens is very important to determine the type and magnitude of the crystal-field splitting. The wave-functions of d -orbitals of TM ion have non-zero overlap with that of surrounding $2p$ orbitals of oxygens. In the case of e_g electrons, for example the $d_{x^2-y^2}$ orbital, one can see from the Fig. 1.2(a) that this $d_{x^2-y^2}$ orbital has strong overlap

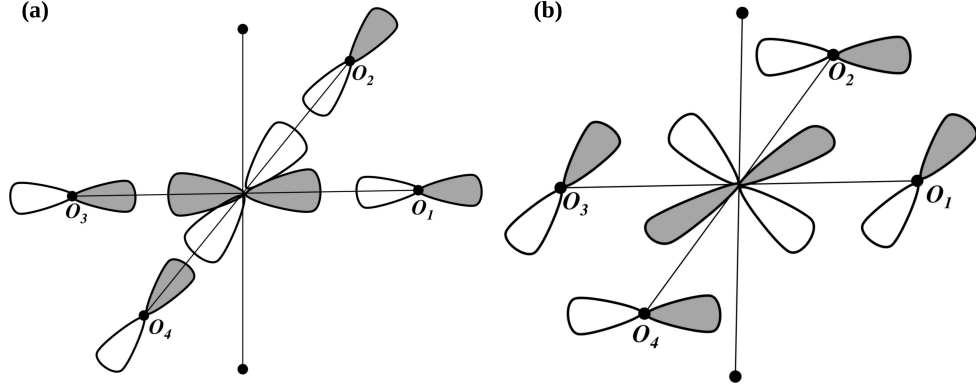


Figure 1.2: Panel (a): Schematic diagram showing covalency contribution to crystal field splitting for transition metal e_g electrons (σ bonding) due to p - d hybridization. Panel (b): Schematic diagram showing covalency contribution to crystal field splitting for transition metal t_{2g} electrons (π bonding) due to p - d hybridization.

with p_x orbitals of oxygen O_1 and O_3 and with p_y orbitals of O_2 and O_4 . Consequently, there will be large hopping matrix elements between this d orbitals and the respective p orbital of oxygens. This type of hybridization where lobes of d orbital are pointed directly toward the oxygen orbitals, gives rise strong overlap, is called σ hybridization, denoted as $t_{pd\sigma}$. In normal situation the oxygen p levels ϵ_p lie much lower in energy than the d levels ϵ_d but as a result of the strong p - d hybridization, the d and p levels are mixed and repelled each others, resulting into splitting of energy levels. This splitting of energy levels can be written as [1],

$$\epsilon_{\pm} = \frac{\epsilon_d + \epsilon_p}{2} \pm \sqrt{\frac{(\epsilon_d - \epsilon_p)^2}{4} + t_{pd\sigma}^2} \quad (1.1)$$

where, ϵ_+ and ϵ_- correspond to energies of bonding(b) and anti-bonding(a) levels for e_g orbitals [cf. Fig. 1.3] and in the limit $t_{pd} \ll \epsilon_d - \epsilon_p$, one can obtain the following equations,

$$\begin{aligned} \epsilon_b &= \epsilon_p - \frac{t_{pd\sigma}^2}{\epsilon_d - \epsilon_p} \\ \epsilon_a &= \epsilon_d + \frac{t_{pd\sigma}^2}{\epsilon_d - \epsilon_p} \end{aligned} \quad (1.2)$$

On the other hand for t_{2g} -electrons, for example the d_{xy} orbital is orthogonal to p orbitals as shown in Fig. 1.2(b), resulting very weak non-zero overlap and hybridization with the p orbitals. These p orbitals directed perpendicular to the TM-O bonds are called π orbitals and the corresponding hoping matrix element is denoted $t_{pd\pi}$. The $t_{pd\pi}$ is much smaller than the

$t_{pd\sigma}$, therefore the bonding-antibonding splitting will be smaller for t_{2g} orbitals than that of e_g orbitals [cf. Fig. 1.3].

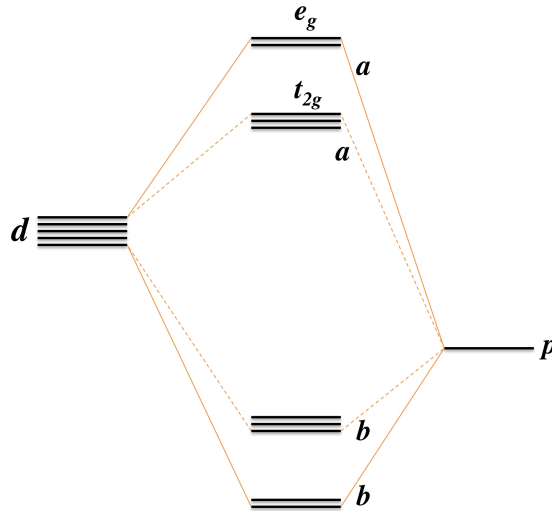


Figure 1.3: Schematic diagram showing the origin of the crystal field splitting due to p - d covalency. d and p represent five-fold degenerate d -levels of transition metal ions and p level of oxygen ions, respectively. b and a stand for bonding and antibonding levels.

The d -orbitals can further split with possible effect of symmetry reduction due to the distortion of the oxygen and octahedron. For example, consider the deformation of the MO_6

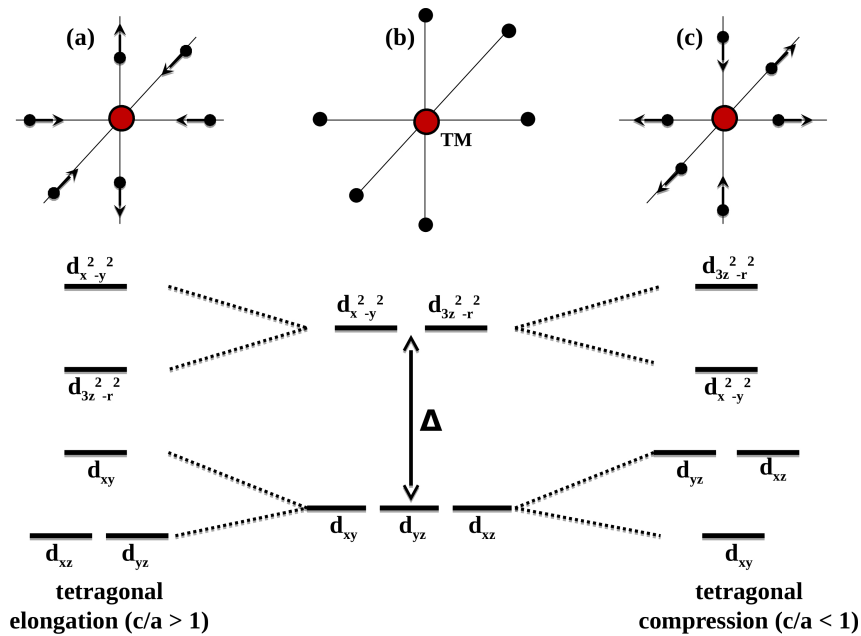


Figure 1.4: Splitting of d levels due to tetragonal distortion of TM-O_6 octahedra for tetragonal elongation (a) and compression (c). Panel (b): splitting of d levels due to crystal field of regular TM-O_6 octahedra.

octahedron as shown in Fig. 1.4 that is a tetragonal elongation [cf. Fig. 1.4(a)] and contraction [cf. Fig. 1.4(c)] in the z -direction, in which the coordinates of oxygens change as $z \rightarrow z \pm 2\delta$, $x \rightarrow x \mp \delta$, $y \rightarrow y \mp \delta$, so that corresponding volume $V \sim xyz$ remains unchanged. For tetragonal elongation ($\delta > 0$), due to the shortening of TM-O distance in the xy -plane, the strong d - p hybridization with the in-plane oxygens would push up the $d_{x^2-y^2}$ level stronger than that of d_{z^2} level. Similarly for t_{2g} levels, energy of d_{xy} orbital would increase and that of the d_{xz} and d_{yz} would go down, as shown in Fig. 1.4(a). To preserve the centre of gravity, the shift of singlet d_{xy} will be twice as large than that of the doublet(d_{xz} , d_{yz}) levels. On the other hand, for tetragonal compression($\delta < 0$), the splitting of t_{2g} and e_g levels would be opposite [cf. Fig. 1.4(c)] compared to tetragonal elongation.

Also the trigonal distortion (elongation or contraction of MO_6 octahedral along one of the [111] axis) splits the t_{2g} levels. The splitting is shown in Fig. 1.5. The trigonal distortion splits the t_{2g} levels into a singlet a_{1g} and doublet e_g^π but e_g levels remain unchanged [cf. Fig. 1.5]. The corresponding wave-function can be written in the following form [1],

$$\begin{aligned} |a_{1g}\rangle &= \frac{1}{\sqrt{3}}[|xy\rangle + |yz\rangle + |xz\rangle] \\ |e_{g\pm}^\pi\rangle &= \pm \frac{1}{\sqrt{3}}[|xy\rangle + e^{\pm 2\pi i/3}|yz\rangle + e^{\mp 2\pi i/3}|xz\rangle] \end{aligned} \quad (1.3)$$

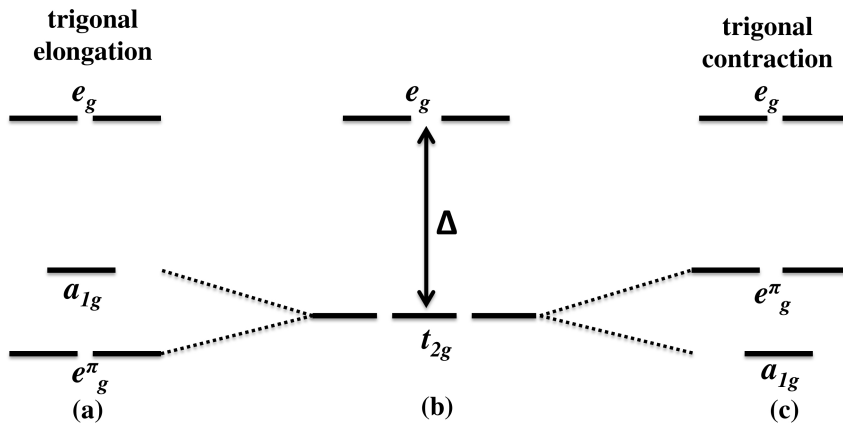


Figure 1.5: Splitting of d levels due to trigonal distortion of TM-O_6 octahedra for trigonal elongation (a) and contraction (c). Panel (b): splitting of d levels due to crystal field of regular TM-O_6 octahedra.

In connection with geometric distortion of the metal-oxygen polyhedra MO_n , the Jahn-Teller effect is an important concept which gives rise to many intriguing properties in transition metal

oxides. According to the Jahn-Teller theorem [3], only degeneracy allowed in the ground state for non-linear molecular system is the spin (Kramers) degeneracy, connected to invariance with respect to time reversal. All other degenerate state would be unstable and system will undergo spontaneous distortion to form a system of lower symmetry and lower energy, to remove the degeneracy. Considering the crystal field splitting in the cubic crystal field of regular octahedron

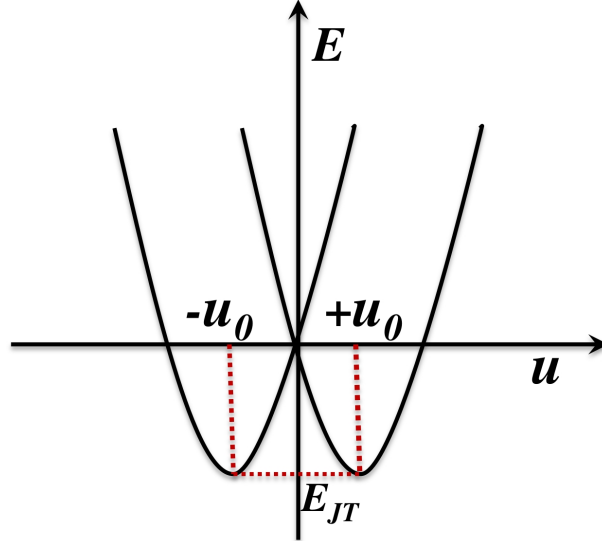


Figure 1.6: Dependence of the energy levels as a function of distortion u [see Eq. 1.4]. It shows the lifting of doubly degenerate energy levels (at $u=0$) for finite distortion u_0 .

[cf. Fig 1(b)], if the degenerate e_g orbitals are occupied partially, as in the case of $\text{Mn}^{3+}(d^4)$ and $\text{Cu}^{2+}(d^9)$, then besides the double-spin degeneracy (spin of the electron for Mn^{3+} or hole for Cu^{2+} can be \downarrow or \uparrow), there will be an extra double orbital degeneracy. So according to Jahn-Teller theorem, the system will undergo distortion of the regular MO_6 octahedron such as in the cases of tetragonal or orthorhombic distortion, to reduce the symmetry and to lift the degeneracy of e_g levels [cf. Fig. 1.4]. The electronic energy gain due to Jahn-Teller effect can be calculated by simple consideration. Consider the situation where Jahn-Teller effect leads to small distortion u which splits the e_g levels as $\pm\lambda u$ where λ is the electron-phonon coupling constant. This distortion will cost an elastic energy of $\frac{1}{2}Bu^2$, where B is the Bulk modulus. So the total energy of the ground state as a function of distortion will be ,

$$E = \pm\lambda u + \frac{1}{2}Bu^2 \quad (1.4)$$

Energies of two levels are degenerate at $u = 0$, as shown in Fig. 1.6. From Fig. 1.6 one can see that minimum energy would correspond to a certain finite distortion u_0 , which can be obtained by minimizing Eq. 1.4 ,

$$\frac{\delta E}{\delta u} = 0 \Rightarrow u_0 = \pm \frac{\lambda}{B}$$

The electronic energy gain, $E_0 = E_{JT} = -\frac{\lambda^2}{2B}$, due to the distortion overcompensate the elastic energy loss. So essence of the Jahn-Teller effect is following: the symmetric situation would lead to extra degeneracy which is always unstable and finite distortion lifts this degeneracy and stabilize the ground state energy.

When transition metal ions have several d -electrons, the filling of d -levels depends on the relative strength of crystal field (Δ) and Hund's rule coupling energy (J_H). For example, consider the case of d^4 ion in the cubic crystal field of regular octahedron. In this case, first three electrons will occupy the three lowest t_{2g} levels with parallel spin but the fourth electron can occupy the either e_g levels or half-filled t_{2g} levels. If the fourth electron occupy the e_g levels then gain of

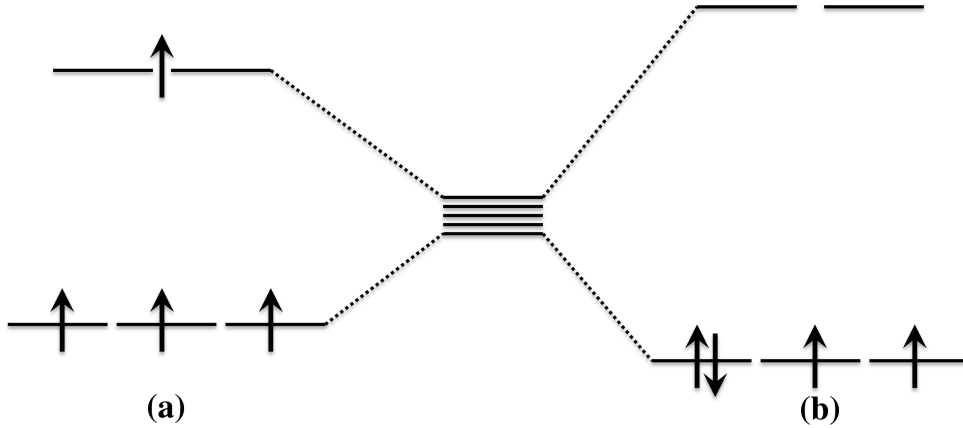


Figure 1.7: Schematic diagram showing (a) high-spin (HS) and (b) low-spin (LS) states for transition metal ions with d^4 electron occupation within the crystal field of regular octahedra.

Hund's rule energy is $E_{Hund} = -3J_H$ but since electron occupy higher lying energy levels, cost of energy equals to crystal field splitting Δ . If $\Delta < 3J_H$, it is energetically favourable to put this fourth electron onto the e_g levels [cf. Fig. 1.7(a)- high spin state] otherwise on the t_{2g} levels with opposite spin [cf. Fig. 1.7(b)- low spin state]. For most of $3d$ -ions in TM oxides, the crystal field splitting is small, therefore electrons would be in high spin (HS) state. Low spin (LS) states are sometimes realized in $3d$ oxides, for example La_2CoO_3 , but they are very rare. Low spin

(LS) states are more common for $4d$ or $5d$ compounds owing to the larger extent of $4d$ and $5d$ orbitals which leads to strong $p-d$ hybridization and strong crystal field splitting compared to $3d$ ions. The spin state of $3d$ Mn^{2+} ions in vanadate-carbonate compound, $\text{K}_2\text{Mn}_3(\text{VO}_4)_2\text{CO}_3$ is one of major issue, discussed in chapter 4.

Another most common geometry of MO_n polyhedra is tetrahedra. In the regular tetrahedral coordination, the d -levels split into a e doublet and t_2 triplet, but e orbitals are energetically more stabilized than t_2 , as shown in right panel of Fig. 1.8(a). Ordering of t_2 - e levels is exactly

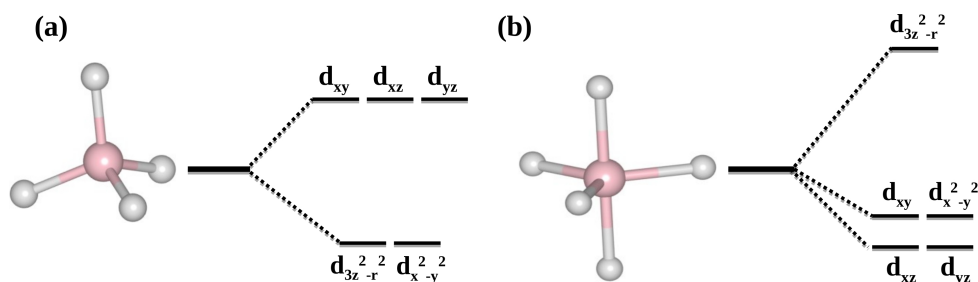


Figure 1.8: Symmetry and corresponding crystal field splitting of d levels for two regular MO_n polyhedra, namely (a) tetrahedra, (b) trigonal by-pyramid.

opposite compared to the case of regular octahedral crystal field splitting. Splitting pattern of d orbitals in the crystal field of regular tetrahedra can be explained by an analogous line of reasoning as explained for octahedral symmetry. The t_2 - e splitting is much less in this case than that in octahedral case because of the fact that none of the d orbitals are exactly directed towards the ligand atoms. The distortions in the regular tetrahedra can also lead extra splitting of d -levels, similar to octahedral cases. The extension of tetrahedral geometry is trigonal bipyramid, which can be visualized as two tetrahedra glued together across a common face (see left panel of Fig. 1.8(b)). The crystal field splitting in that case is shown in right panel of Fig. 1.8(b).

Transition metal d orbitals possess a strong intra-atomic Coulomb interaction (H_{int}) which supports local magnetic moment. On the other hand, as the direct overlap between TM d orbitals is negligibly small, the electrons can only hop through hybridization with oxygen $2p$ orbitals. This strong hybridization leads to formation of delocalized band (H_{band}). The celebrated Hubbard Model [4] is the simplest many body Hamiltonian which demonstrates these opposing

tendencies. One-band Hubbard model can be written as,

$$\begin{aligned} H &= -t \sum_{\langle ij \rangle, \sigma} (c_{i\sigma}^\dagger c_{j\sigma} + c_{j\sigma}^\dagger c_{i\sigma}) + U \sum_i n_{i\uparrow} n_{i\downarrow} \\ &= H_{band} + H_{int} \end{aligned} \quad (1.5)$$

where $c_{i\sigma}^\dagger$ ($c_{i\sigma}$) is creation (annihilation) operator of electrons at site i with spin σ , t is the hopping matrix element and U is onsite Coulomb repulsion between electrons sharing the same orbital i . $n_{i,\sigma} = c_{i,\sigma}^\dagger c_{i,\sigma}$ represents the occupation number operator. To understand the essence of two terms presented in Eq. 1.5, let us consider a state with one electron per site. To create a charge carrying excitations, take one electron from a given site, say i site and transfer it to another site j . This will create a hole at site i and extra electron at site j which already had an electron, leading to doubly occupied site. To create such doubly occupied site, it would cost an energy of Coulomb repulsion (U) of two electron at site j . On the other hand in this processes, one can gain the kinetic energy of both electron and hole when they start to move through the crystal. This would lead to formation of an energy band, with bandwidth $W=2zt$, where z is the number of nearest neighbours. Therefore total energy gain from such charge carrying excitations would be $W=2zt$ and the energy loss would be onsite Coulomb repulsion energy U . So, there will be a competition between these two terms. Thus, for system with one electron per site and for small electron hopping t , inclusion of onsite Coulomb repulsion U , can make the system insulating if $U \geq U_{crit} \sim W = 2zt$, in contrast with conventional band picture which would have been lead to the metallic solution. Such electron-electron correlation driven insulators are called Mott-Hubbard insulators. The essence of Mott-Hubbard insulators is schematically shown in Fig. 1.9. In the limit of $U=0$ (non-interacting electrons), the energy band are half-filled and for large enough U , $(U/t) > (U/t)_{crit} \sim W=2zt$, the energy band splits into two subbands with an energy gap between them given by $E_g \sim U - W = U - 2zt$. Thus if one start from non-interacting electrons (*i.e.* $U=0$) for which system is definitely metallic and increase U (or U/t), there should occur a metal-insulator transition for a critical value of U/t . This transition from metal to Mott-Hubbard insulator is called Mott-Hubbard transition. For system with one electron per site, the lower subband (called lower Hubbard band) will be occupied and upper

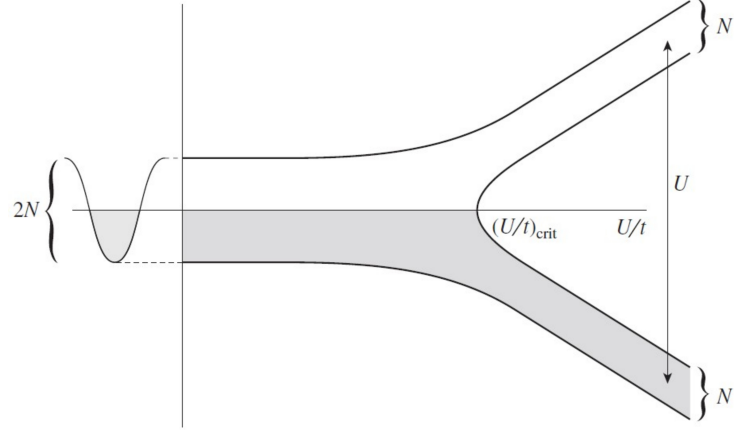


Figure 1.9: Schematic diagram showing the energy band in the Hubbard model as a function of the strength of electron-electron repulsion (Hubbard U) for a lattice of N sites with one electron per site. Left hand side shows the conventional band picture which gives rise metallic solution at half-filling. The two bands on the right side represent the Hubbard (sub)bands for a critical value of (U/t) . For a lattice with one electron per site, lower (shaded) Hubbard band is completely filled with N electrons and upper (unshaded) Hubbard band is completely empty and U represents the approximate energy gap between these two Hubbard (sub)bands. Fig. is taken from Ref. [1].

one (upper Hubbard band) empty. The above described general introduction about transition metal compounds is primarily based on Ref. [1]. For details see the Ref. [1].

In the Hubbard model, four configurations are possible at each site, such as singly occupied by one electron with spin up or down, doubly occupied site by two electron with opposite spin or empty. Last two configurations lead to charge fluctuation. In the restricted Hilbert space eliminating fluctuations (double occupancies) in strong U limit, leads to an effective model, called t - J model, which conserves the double occupancies and holes. t - J model represents a generic model for the interplay of spin and charge degrees of freedom. In the limit of half-filled lattice *i.e.* one electron per site ($n=1$) and a large U limit, this effective t - J model reduces to effective Heisenberg Hamiltonian,

$$H_{eff} = J \sum_{ij} S_i \cdot S_j \quad (1.6)$$

where, exchange term $J = \frac{2t^2}{U}$, S_i is the spin operator at site i , and other symbols have their usual meaning. It describes the situation where charge degrees of freedom are bound to atomic position and only spin degrees of freedom remain active. This Heisenberg model is used in this thesis to study the spin systems.

1.2 Transition metal compounds discussed in thesis

In this thesis, we have used DFT calculations combined with many body approach to compute, understand as well as to improve the physical properties of transition metal compounds belonging to two broad categories, namely (1) Low dimensional quantum spin systems, (2) Double perovskite based transition metal oxides. Descriptions of these two class of materials and their general properties are given below.

1.2.1 Low dimensional quantum spin systems

Quantum spin systems form a fascinating branch of theoretical physics, as they demonstrate surprisingly rich physics. Particularly, low dimensional systems in 2D, specially in 1D, have been attractive because exact solution can be found for these cases, which provide information of the ground state and excited states, possible new phases, phase transitions, arising due to interplay of thermal and quantum fluctuation [5]. The low energy excitations of these low dimensional quantum systems are primarily due to the spin degree of freedom. Therefore, in such systems, the Heisenberg Hamiltonian (Eq. 1.6) is a good starting point for describing the magnetic properties. Heisenberg model can be represented as a combination of Ising ($S_i^z.S_j^z$), and spin flip terms, as given in the following,

$$H = J \sum_{i,j} [S_i^z.S_j^z + \frac{1}{2}(S_i^+S_j^- + S_i^-S_j^+)]$$

where S_i^z is the z component of spin operator at the lattice site i , $S_i^+(S_i^-)$ is the spin raising(lowering) operator and J denotes the strength of the exchange interaction. For anti-ferromagnetic Heisenberg model, strict antiferro alignment of spins, leads to gain in energy only from the Ising part ($S^z.S^z$) of the Heisenberg interaction (the energy value is $-JS^2$, where J is coupling strength and S is spin operator). On the other hand to get the true ground state, one needs to let the spins to fluctuate, so that the system can gain energies also from spin flip (or x - y) terms. The extra energy gain from this spin fluctuation part is $-JS$, which has purely quantum mechanical origin. Thus for two site case, ratio of the quantum correction to the classical z - z energy is $\frac{-JS}{-JS^2} = \frac{1}{S}$. For lattice case, quantum effects are of order of $\frac{1}{zS}$,

where z is the coordination number. Therefore quantum fluctuation is more stronger for small spin and low dimensionality (small z value). This strong quantum fluctuation effect gives rise to a number of unusual magnetic properties that exhibit by low dimensional spin systems. In the 1980's when it was realized that magnetism can play an important role to understand the high T_c superconductivity in cuprates [6], a variety of quantum spin model has been studied. This strongly motivated large number of theoretical and experimental studies of quantum spin systems with exotic properties. A comprehensive reviews on magnetism in the low dimensions can be found in Ref. [7,8]. Though these materials are structurally three dimensional, the magnetic interactions and directional nature of chemical bonding between different atoms, reduce the effective dimensionality of the underlying spin system to less than three.

In this thesis we have considered special class of low dimensional quantum spin systems that exhibit gap in their excitation spectra. This gap is related to the singlet formation of pair of spins. The magnitude of gap is difference between a singlet and triplet excited states and proportional to the strongest exchange interaction (J) between two magnetic ions. As this gap is originated purely from spin degree of freedom, it is conventionally called spin-gap. Primarily, the presence of the spin-gap (Δ) can be confirmed from the experimentally measured macroscopic properties like susceptibilities χ , which goes to zero exponentially at low temperature (T) as,

$$\chi \sim \exp(-\Delta/K_B T) \quad (1.7)$$

Some well known examples of spin gap (SG) AFMs in 1D and 2D are given below.

Spin-gap systems in one dimension

I. Spin-Peierls(SP) systems: A spin-Peierls system is an one-dimensional Heisenberg antiferromagnetic spin chain of half-integer spin on an elastic lattice, in which magneto-elastic coupling is found to be strong enough. Due to the magneto-elastic coupling, below a certain transition temperature, T_{SP} , the distance between neighbouring spins along the chain no longer remains uniform but alternates and this leads to the alteration of exchange coupling. Each pair of stronger-coupled spins forms a spin-singlet, as presented in Fig. 1.10. The ground state structure of the spin-Peierls system is thus a stacking of spin-singlet pairs. This so-called dimerization

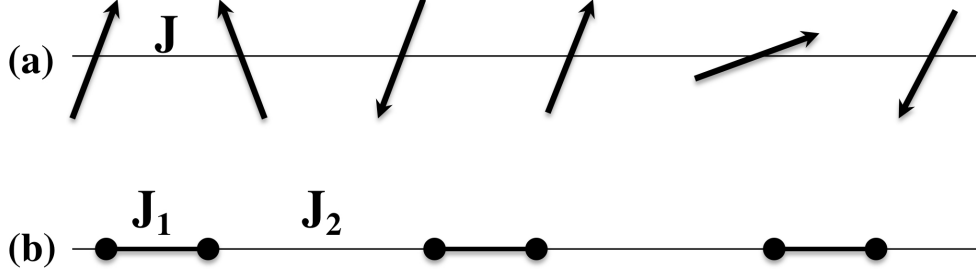


Figure 1.10: Panel (a): Spin $S=1/2$ chain with uniform antiferromagnetic exchange coupling. Panel (b): Schematic representation of singlet ground state of the dimerized lattice below the spin-Peierls transition, which leads to alternation of the exchange interaction.

helps to gain the magnetic energy which overcompensates the loss of elastic energy arising from the alternating structural distortion along the spin chains. This dimerized spin chain also leads to an energy gap between the singlet ground state and low lying band of triplet excited states. The magnitude of the gap is related to the degree of dimerization and hence to the degree of lattice distortion. The critical temperature below which the spin-Peierls transition takes place, is given by $T_{SP} \sim |J| \exp(-1/\lambda)$, where J is the exchange interaction between adjacent spins and λ is the electron-phonon coupling.

In 1970s, the spin-Peierls transition was widely studied both experimentally and theoretically. Experimentally observed first spin-peierls were organic compounds like TTF-CuBDT [9, 10], TTF-CuS₄C₄(CF₃)₄ [11, 12], MEM-(TCNQ)₂ [13]. Discovery of such transition in inorganic transition metal oxide based system, CuGeO₃ [14] extended the horizon of this field. Later many inorganic compounds have been found, such as NaV₂O₅ [15], TiOBr and TiOCl [16] *etc.* which show spin-Peierls like (combined with charge or orbital ordering) transition.

II. System with competing antiferromagnetic interactions: Sufficient frustration due to nearest neighbour (J_1) and next-nearest-neighbour (J_2) antiferromagnetic exchange interaction in one dimensional spin-chain, can lead to spin-gap behaviour. The $S=1/2$, antiferromagnetic Heisenberg J_1 - J_2 model in 1D is called Majumdar-Ghosh (MG) chain [17]. The Hamiltonian with periodic boundary condition is given by,

$$H_{MG} = J_1 \sum_{i=1}^N S_i \cdot S_{i+1} + J_2 \sum_{i=1}^N S_i \cdot S_{i+2} \quad (1.8)$$

Majumdar and Ghosh [17] showed that when next nearest exchange accounts for exactly half of the nearest neighbour exchange *i.e.* $J_2/J_1=0.5$, the Heisenberg model is exactly solvable and ground state is two-fold degenerate singlet state.

III. Haldane-chain compounds: In the above mentioned two cases the singlet bond between two particular spins is formed due to geometric reasons. However in the case of Haldane-chain compounds, the origin of the spin-gap character of the ground state, lies in the integer spin-value. In 1931, from the exact solution of 1D chain of $S=1/2$ Heisenberg antiferromagnetic (HAFM) model, H. A. Bethe [18] showed that,

- (i) ground state is a many-body spin singlet.
- (ii) ground state has no energy-gap to the excited states.
- (iii) spin-spin correlations decay slowly as a power law of distance.

The absence of the spin-gap had been proved in the ‘Lieb-Shultz-Mattis theorem’ [19] for Heisenberg antiferromagnetic half-odd integer spin chain in an infinite chain length limit. Contrary to this expectation, in 1983 F. D. M. Haldane based on his analysis of the nonlinear σ model mapping of the large spin (S) HAFM Hamiltonian in 1D conjectured [20,21] that the ground state of the Heisenberg model strongly depends on the value of S . He predicted that half-odd-integer spin systems preserve the features of the $S=1/2$ spin-chain, but integer spin chains have the following features:

- (i) ground state is unique.
- (ii) there exists a large energy gap (called Haldane gap) between the ground state and the excited states.
- (iii) spin-spin correlation function quickly decays as an exponential function.

The Haldane’s conjecture has now been verified both theoretically and experimentally. Affleck *et al.* proposed the valence-bond-solid model [22], which is currently the best and also well-established approximation of the ground state of a realistic $S=1$ spin-chains. This model correctly predicted the singlet nature of ground state, the spin gap to the first excited state

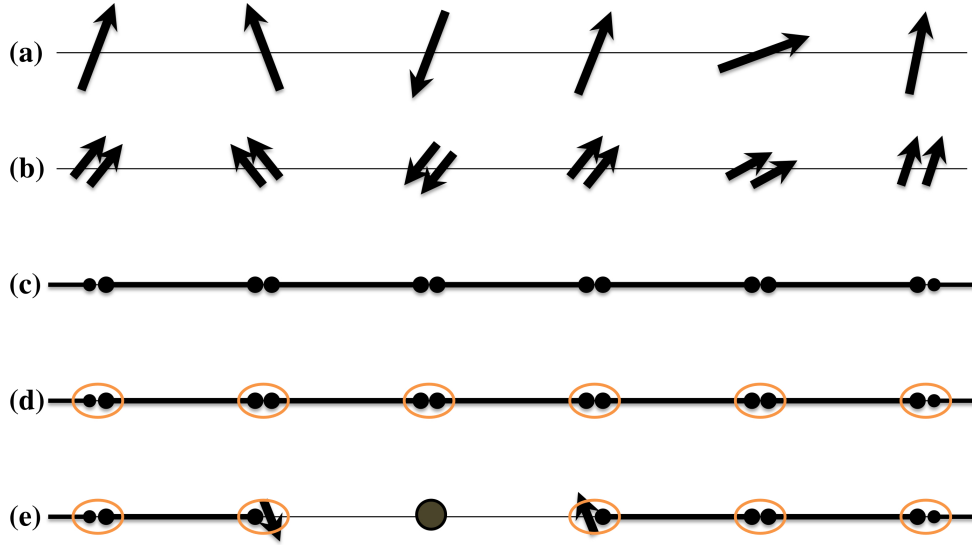


Figure 1.11: Schematic representation of valence bond solid model, showing (a) Spin $S=1$ chain with uniform antiferromagnetic exchange coupling (b) decomposition of each spin $S=1$, into two $S=1/2$ spin degrees of freedom, (c) formation of singlet state by pairing adjacent spins, (d) symmetrization of the two $S=1/2$ spins at each side to restore the original spin $S=1$, (e) the introduction of a spin vacancy which breaks two valence bonds and liberates two $S=1/2$ degrees of freedom on the neighbouring sites.

as well as short range exponential decaying spin-spin correlations by considering two valence bonds emerging from each site and terminating in the two neighbouring sites. Here each valence bond contracts two of the $S=1/2$ variables to form a singlet, as illustrated in Fig. 1.11. This valence-bond-solid ground state is only an approximation of the realistic ground state for $S=1$ spin chain with only nearest neighbour exchange coupling [23]. It is an exact solution of the following Hamiltonian,

$$H = J \sum_i [S_i \cdot S_{i+1} + \frac{1}{3} (S_i \cdot S_{i+1})^2] \quad (1.9)$$

The Haldane gap was first observed in the CsNiCl_3 system and it shows Neél order below T_N ($\simeq 4.9$ K) [24, 25]. The another Haldane chain compound is $[\text{Ni}(\text{C}_2\text{H}_8\text{N}_2)_2(\text{NO}_2)]\text{ClO}_4$, which shows a spin-gap but no Neél ordering [26]. Various other Haldane chain systems have been reported on oxide materials, such as Y_2BaNiO_5 [27] and $\text{Tl}_2\text{Ru}_2\text{O}_7$ [28] with the last one being $\text{PbNi}_2\text{V}_2\text{O}_8$ [29–31] and $\text{SrNi}_2\text{V}_2\text{O}_8$ [32–34] spiral-chain systems. From the exact diagonalization of the Haldane Hamiltonian for ideal one dimensional $S=1$ chain, the Haldane gap is estimated to be $\Delta = 0.41J$ [35], where J is the isotropic nearest neighbour intra-chain exchange. Due to quantum many body effects [36] the Haldane gap can be suppressed with respect to ideal

Haldane chain spin-gap value of $\Delta = 0.41J$ for $S=1$. The possible mechanism for the suppression of Haldane gap in $\text{SrNi}_2\text{V}_2\text{O}_8$ compound is one of the topics of this thesis and discussed in chapter 3.

Spin-gap systems in quasi 2D and 2D

I. Spin-ladder systems: The spin-ladder systems serve as a bridge between one and two dimensional spin systems. The spin ladder system is an $S=1/2$ antiferromagnetic square lattice with finite width and infinite length. The simplest ladder system consists of two chains coupled by rungs, as shown in Fig. 1.12. In the spin ladder systems, the exchange coupling of spins along

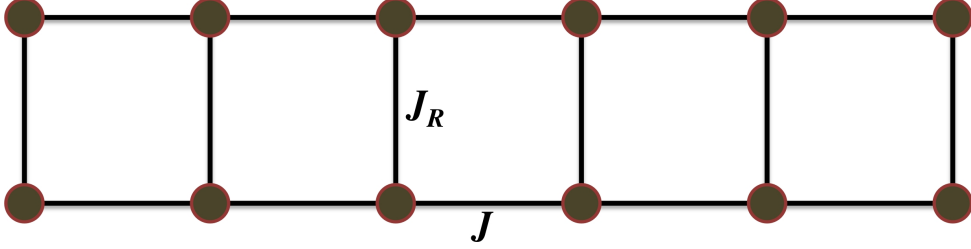


Figure 1.12: The simplest two chain spin ladder model. J and J_R represent the exchange coupling along the spin chain and along the rung of the ladder, respectively.

rungs, J_R approximately equal or larger than the nearest neighbour intra-chain interactions, J . $J_R=0$ corresponds to decoupled AFM spin chains for which the excitation spectrum is known to be gapless. For all $J_R/J > 0$, the ground state is composed of singlets, formed on the rungs with a gap in the spin excitation spectrum [37]. This is easy to understand in the limit $J_R/J \gg 0$. In this limit, intra-chain interaction can be treated as perturbation. For, $J=0$, exact ground state is product state of singlets along the rungs, which is given by

$$|\psi_s\rangle = (|\uparrow\downarrow\rangle - |\downarrow\uparrow\rangle)/\sqrt{2} \quad (1.10)$$

As the total spin $S=0$ for singlet state, correction to the ground state energy is zero. $S=1$ excitation can be created by promoting one of the rung singlets to the $S=1$ triplet states,

$$|\psi_t\rangle = [|\uparrow\uparrow\rangle, (|\uparrow\downarrow\rangle + |\downarrow\uparrow\rangle)/\sqrt{2}, |\downarrow\downarrow\rangle] \quad (1.11)$$

The weak coupling along the chains gives rise to a propagating $S=1$ magnon with the following dispersion relation,

$$\omega(k) = J_R + J \cos k \quad (1.12)$$

where k is the momentum vector and spin-gap is given by $\Delta = \omega(\pi) \simeq J_R - J$. The significant interest in the spin-ladder systems is due to the unconventional properties of the CuO_2 planes in doped cuprates, which exhibit high temperature superconductivity in an appropriate range of dopant concentration. Doped ladder models are toy model of strongly correlated systems, in which some of the issues related to strong correlation can be addressed in a rigorous manner. CaV_2O_5 [38] is recently synthesized two leg ladder system in which intra chain interaction is small compared to inter chain interaction. The interesting feature associated with ladder systems is that, the ladders with an even number of legs have a spin gap and ground state has true spin-liquid nature [39], while odd-leg ladders are gapless and exhibit a powerlaw decay of the spin correlation functions [40]. First experimentally realized series of even and odd-legs ladder is $\text{Sr}_{n-1}\text{Cu}_{n+1}\text{O}_{2n}$ compound which consists of planes of weakly coupled ladders of $(n+1)/2$ chains [41, 42]. $n=3$ and 5 of this series provide two chain and three chain ladder compounds SrCu_2O_3 and $\text{Sr}_2\text{Cu}_3\text{O}_5$. The first compound is spin gap AFM ladder system while $\text{Sr}_2\text{Cu}_3\text{O}_5$ compound is gapless. This observation is consistent with the theoretical prediction that in n -chains ladder the excitation spectrum is gapped(gapless) when n is even(odd) [37].

II. Topology or frustration driven spin gap systems: In the literature, very few two-dimensional systems are known which exhibit the spin-gap because only few special mechanisms lead to gapped excitation spectrum in 2D. The first possible root leading to the gapped excitation spectrum in two-dimensions is modified exchange topology. A prominent example of this is, 1/5-depleted square lattice of the CaV_4O_9 which shows two-dimensional arrangement of plaquette singlet units of four V^{4+} ions, possessing spin $S=1/2$ [43].

The second possible root is sufficient geometrical frustration which may lead to spin-gap. Geometrical frustration leads to the conflict in minimizing the exchange interaction energy associated with different spin-pairs. The presence of frustration enhances the quantum fluctuations in a spin systems. The geometrical frustration is quite large in the Kagome lattice. The Shastry-

Sutherland (SS) model [44], on a square lattice with selected diagonal bonds are shown in Fig. 1.13, is an example of a frustrated spin-gap AFMs in 2D. The $\text{SrCu}_2(\text{BO}_3)_2$ system was recog-

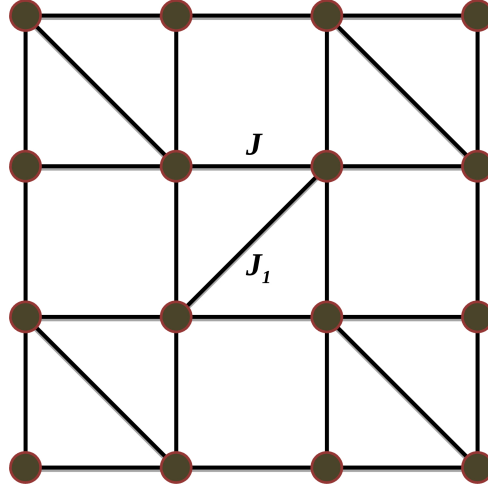


Figure 1.13: Schematic diagram of the Shastry-Sutherland model. J is the nearest-neighbour antiferromagnetic exchange interaction and J_1 is the selected antiferromagnetic bond interactions.

nized to be topologically equivalent to the two-dimensional Shastry-Sutherland lattice [45, 46].

Though experimental techniques such as neutron scattering experiments can provide the information of magnetic ground state and the excitation spectrum, such as presence or the absence of the singlet and triplet gap (spin-gap), a quantitative description of the magnetic properties require the knowledge of the microscopic spin Hamiltonian, in which key parameters are the magnetic exchange couplings. Magnetic exchange couplings can be derived from first principles electronic structure calculations in an efficient manner. In this thesis, we have considered two quantum spin system namely

- (a) $S=1$ Haldane chain compound, $\text{SrNi}_2\text{V}_2\text{O}_8$.
- (b) $S=5/2$, Vanadate-Carbonate compound, $\text{K}_2\text{Mn}_3(\text{VO}_4)_2\text{CO}_3$.

Details of calculations for these two spin-system compounds are discussed in chapter-3 and chapter-4.

1.2.2 Double perovskite compounds $A_2BB'O_6$

Double perovskite compounds have general formula $A_2BB'O_6$ where A is rare earth or alkaline earth cations and B, B' are transition metal ions. As the $A_2BB'O_6$, consists of two times the perovskite structure (ABO_3), this type of structure is usually called double perovskite. Compounds crystallizing in the double perovskite structure are one of the most intensely studied material in solid state chemistry and physics due to their interesting chemical and physical properties like half-metallicity, magneto-dielectric effect, colossal magneto-resistance, multiferroicity, superconductivity *etc.* This wide range of interesting properties arise mainly due to the exceptional structural and composition flexibility of double perovskite compounds. The special interest in double perovskites is due to the possibility of combining $3d$ and $4d/5d$ elements at two B sites. Crystal structure and some intriguing physical properties of double perovskite compounds are discussed below.

Crystal structure

One of the crucial issue in double perovskite compounds is the ordering of B and B' cations. In absence of this, the compounds becomes a disordered perovskite compound with no doubling of the perovskite cell. The main factors affecting the B-site cation ordering is the difference in B and B' cation's oxidation state, $\Delta Z_B = |Z_B - Z_{B'}|$ and in ionic radius difference, $\Delta r_B = |r_B - r_{B'}|$. Broadly speaking, with $\Delta Z_B < 2$ compounds are disordered and with $\Delta Z_B > 2$ compounds are ordered [47–49]. Galasso and Darby [50] suggested that a difference in radii Δr_B , higher than 7-17 % would be enough to cause ordering. Summary of B site cation ordering found in different double perovskite compounds are summarized in Table 1.1. In the ordered double perovskite structure, B and B' cations can order in three different ways like [cf. Fig. 1.14],

- (i) **Rock-salt like ordered structure:** maximum ordered double perovskites are found to be rock-salt like ordering where the B site cations alternate in all three dimension creating rock-salt like arrangement.
- (ii) **Layered ordered structure:** here B and B' cations alternate only in one directions. This type of B-site cation ordering has only been found in few ordered double-perovskite

Table 1.1: Cation ordered found in different double perovskite compounds. Taken from Ref. [51].

ΔZ_B	Compound	Ordering
0	$A_2^{2+}B^{4+}B'^{4+}O_6$	Disordered for $\Delta r_B < 0.17 \text{ \AA}$, Ordered otherwise
	$A_2^{3+}B^{3+}B'^{3+}O_6$	Disordered
2	$A_2^{1+}B^{2+}B'^{4+}O_6$	Ordered
	$A_2^{2+}B^{3+}B'^{5+}O_6$	Disordered, partially ordered or ordered with increasing Δr_B
	$A_2^{3+}B^{2+}B'^{4+}O_6$	Most compounds at least partially ordered
4	$A_2^{2+}B^{2+}B'^{6+}O_6$	Mostly highly ordered
	$A_2^{3+}B^{1+}B'^{5+}O_6$	Ordered
6	$A_2^{2+}B^{1+}B'^{7+}O_6$	Ordered

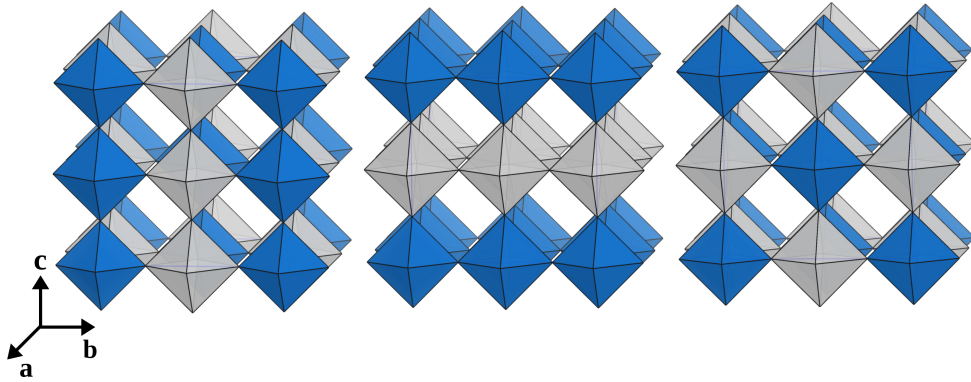


Figure 1.14: Schematic representation of three different ordering of BO_6 and $B'O_6$ octahedra, possible in a double perovskite structure. The BO_6 and $B'O_6$ octahedra are marked with two different colors. From left to right, the figure shows the columnar, layered and rock-salt ordering.

compounds such as, La_2CuSnO_6 [52], and $R_2CuB'O_6$ where $B' = Sn$ or Zn and $R = Nd, Pr$ or Sm [53, 54].

- (iii) **Columnar ordered structure:** here two different B-site cations alternate in two directions. This type of ordering has only been found when A site is also occupied by two different elements and only in rare cases this type of ordering take place [48].

Crystal structure of rock-salt ordered structure is shown in Fig. 1.15, where corner sharing BO_6 and $B'O_6$ octahedra alternate along three crystallographic axis and 12 coordinated A cations sit in the void formed by the octahedra. The divalent (2+) and trivalent (3+) A cations allow for a large range of oxidation state combination for the two B site cations. In this thesis work we have considered B^{3+}/B'^{5+} and B^{2+}/B'^{6+} oxidation state combination in case of an A^{2+} cations and B^{2+}/B'^{4+} in case of an A^{3+} cations. Crystal structure of ideal rock-salt ordered double perovskites are cubic (well described within $Fm-3m$ space group). However it can undergo

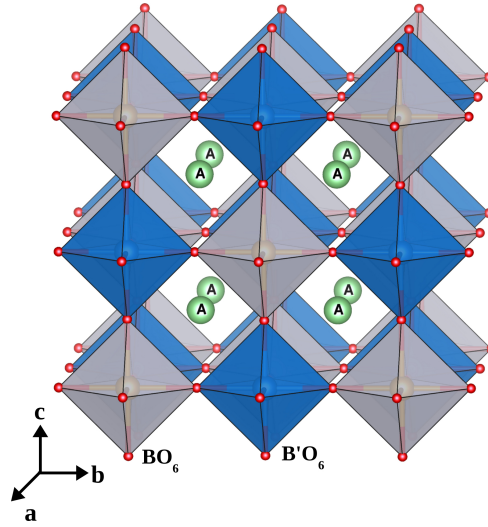


Figure 1.15: Ideal rock-salt ordered cubic structure of double perovskite, $A_2BB'O_6$.

symmetry lowering due to structural distortion. The source of distortion can be of different origins, such as,

- (i) Due to mismatch of the relative ionic radii of A and B/B' site cations. In order to quantify this A and B/B' site cation size mismatch, one can define a tolerance factor (f) as,

$$f = \frac{r_A + r_O}{\sqrt{2}(\frac{r_B + r_{B'}}{2} + r_O)} \quad (1.13)$$

where r_i is the effective ionic radius of the i atom ($i=A, B, B'$ and O), as for example tabulated by Shannon [55]. When $f < 1 (> 1)$, the A site cation radius is smaller (larger) than ideal and the strain caused by cation size mismatch compensates by tilting the B/B'O₆ octahedra. Depending on the value of tolerance factor f , it is observed that the following condition generally holds true for the whole double-perovskite family: Hexagonal structure is adopted for $f > 1.05$, in between $1.05 > f > 1.00$ the compound becomes cubic within the Fm-3m space group, for $1.00 > f > 0.97$ most likely structure corresponds to the tetragonal space group and for small values of $f < 0.97$ compounds become monoclinic [56].

- (ii) The distortion of the BO₆ octahedra due to electronic instabilities such as Jahn-Teller (JT) effect, can effect the crystal structure of double perovskites. Most prominent JT active ions are Cu²⁺ and Mn³⁺. Almost, all of the Mn³⁺ ion based compounds are disordered. Such disordered compounds do not show cooperative JT distortion [57]. However

$\text{Sr}_2\text{MnB}'\text{O}_6$ with $\text{B}' = \text{Nb}, \text{Ta}$ or Sb show a low degree of cation ordering, thus cooperative JT distortion is active in these compounds. Sr_2CuWO_6 (roc-salt ordered), $\text{Sr}_2\text{CuMoO}_6$ (rock-salt ordered), R_2CuSnO_6 with $\text{R} = \text{La}, \text{Nd}, \text{Pr}$ or Sn (layered ordered) are example of Cu^{2+} ions based JT active compounds.

- (iii) Cationic displacement due to ferroelectric distortion can effect the crystal structure of the double perovskite. Particularly Pb^{2+} or Bi^{3+} at the A site of double perovskites can cause ferroic distortions, due to the presence of $6s^2$ lone electron pair in these ions.

Properties of double perovskites

As discussed earlier, double perovskite compounds exhibit many interesting and intriguing properties both from the fundamental and the application point of view. Some of the important properties are discussed below.

I. Electronic properties: The electronic properties of double perovskites are mainly controlled by B site cations. The compounds with most intriguing electronic properties are those which contain combined $3d$ and $4d/5d$ elements at two B sites. Broadly speaking, the electronic properties of solid are mainly governed by two factors, the electronic band width (W), and the intra atomic electron-electron interactions (U). With partially occupied conduction band, when $W < U$, the electrons are localized and itinerant when $W > U$.

In case of double perovskites, band-width W largely depends on spatial orbital overlap between different elements. In addition to spatial overlap, energetic overlap and symmetry of orbitals of two B-site cations should be taken into account to understand the electronic behaviour of double perovskite compounds as there are some notable characteristic difference between $3d$ and $4d/5d$ transition metal elements. $3d$ metals have large intra-atomic electron-electron repulsion energies (U) compared to crystal field splitting (Δ), as a consequence they are usually found in high spin state. On the other hand $4d/5d$ metal have higher crystal field splitting and weak inter-electronic repulsion and mostly they are found in low-spin state. $4d/5d$ elements in $\text{A}_2\text{BB}'\text{O}_6$ double perovskites tend to be found in high oxidation states [51], which means there are fewer d electrons. Thus the relevant electrons in the low spin $4d/5d$ elements are found in the t_{2g}

orbitals, where as for the high spin $3d$ elements, the relevant electrons are often in e_g orbitals, which some cases hinder orbital overlap due to their different symmetries. Also, in the $4d/5d$ metals spin-orbit coupling (SOC) is very strong compared to $3d$ metals [58, 59]. This strongly enhanced SOC, can cause notable changes to the electronic structure specially in the case of Ir^{4+} and Ir^{5+} compound, where SOC can split the otherwise degenerate t_{2g} orbitals [60]. However structural distortion can lift the orbital-degeneracy, quenched orbital moment and allow for some σ - π interaction [61–63]. Therefore crystal structure plays an important role to govern the electronic structure of double-perovskite compounds.

II. Magnetic properties: Due to various possibility of combining different paramagnetic cations at all of three cation sites, double perovskite compounds $\text{A}_2\text{BB}'\text{O}_6$, offer a great playground for wide range of magnetic properties. Magnetic properties of solids are primarily governed by sign and relative strength of different possible super-exchange path between magnetic ions. So knowledge of super-exchange interactions is very important to understand the magnetic ground state. In case of single paramagnetic B site cation in $\text{A}_2\text{BB}'\text{O}_6$ double perovskites, most important super-exchange paths are 90° B-O-B'-O-B nearest neighbour (NN) interactions and 180° B-O-B'-O-B next nearest neighbour (NNN). Strength of this two interactions can often be of same order or can compete with each others [64, 65]. The relative strength of these interactions depends on the nature of paramagnetic ions. For example, in some Ru based compounds [66], 90° B-O-B'-O-B interactions are stronger compared to 180° B-O-B'-O-B.

In case of two magnetic B-site cations specially combined $3d$ and $4d/5d$ elements, things are bit more complicated due to different characteristic feature of $3d$ and $4d/5d$ elements as discussed earlier. In this case short range super-exchange interactions B-O-B', as well as long range super-exchange interactions, B-O-B'-O-B and B'-O-B-O-B' play a crucial role in predicting the magnetic ground state. One can expect that short range B-O-B' would be the strongest interaction in the system, dominating the magnetic ordering. However in $\text{A}_2\text{BB}'\text{O}_6$ double perovskite compounds, the B-O-B'-O-B and B'-O-B-O-B' super-exchange interactions sometimes are found to be stronger than that of B-O-B' interactions due to weaker energetic orbital overlap of two different B site cations. Such cases are found in tetragonal, Sr_2BOsO_6 (B = Fe, Co, Ni and Cu) double perovskites [67–71]. However in some of double perovskite compounds like as

$\text{Sr}_2\text{FeMoO}_6$ [72] magnetic properties are not simply caused by super-exchange mechanism but are governed by hybridization driven mechanism. Hybridization driven mechanism in double perovskites is reminiscent of a generalized double exchange mechanism [73,74]. Ordered double perovskites with nonmagnetic B' site, superexchange coupling between the B magnetic moments is small and the primary magnetic interaction arises from electron delocalization in the B-O- B' network. Main physical ingredients for generalized double exchange mechanism are: a large S core spin at the B site, strong coupling on the B site between the core spin and the itinerant electron, and delocalization of the itinerant electron on the B- B' network [75]. A comprehensive reviews on magnetism in double perovskites can be found in Ref. [56,76].

Magnetic properties depend on the overlap of the different ions and several factors can effect this overlap such as, (i) orbital energy of transition metal decreases as one moves to the right side in the periodic table due the increase in nuclear charge, (ii) crystal field splitting decreases moving right in the periodic table due to decrease in ionic radius and which leads to decrease in bond covalency, and (iii) in additions, some notable different characteristic feature of $3d$ and $4d/5d$ orbitals as discussed in previous sections. Moreover the structural distortion strongly effect the energetic overlap of different ions, in which the magnetic properties depend on. Strong structural distortion can lead to the large energetic orbital overlap of the two B-site cations and therefore short range B-O- B' interaction becomes strongest in system, dominating the magnetic ordering as found in the monoclinic Ca_2BOsO_6 (B= Fe, Co, Ni and Cu) double perovskite compounds [68, 70, 77, 78].

Spin-orbit coupling (SOC) and spin delocalization by bond covalency are much stronger in $4d/5d$ orbitals compared to $3d$ orbitals. Thus magnetic moment of the $4d/5d$ elements are found to be notably reduced from the spin-only values in many compounds like Ru, Re, Os, specially in the Ir compound where strong SOC are comparable to crystal field splitting or inter-electronic interactions [60,79]. The effect of SOC can be quenched by structural distortions, as in case of Sr_2YIrO_6 [60].

In the literature, ordered $\text{A}_2\text{BB}'\text{O}_6$ compounds are reported to have mainly three types of magnetic ordering, anti-ferromagnetic (AFM), ferri-magnetic (FiM) and ferromagnetic (FM).

- **Anti-ferromagnetic double perovskites:** most of the double perovskite compounds are found to have antiferromagnetic ordering. In the literature one or other form of AFM order has been reported for over 200 double perovskites [51]. Along with antiferromagnetism, weak ferromagnetism also often has been found in many compounds, such as $\text{La}_2\text{MgIrO}_6$, $\text{La}_2\text{ZnIrO}_6$ *etc.* [80]. In most cases this weak FM behaviour results due to the presence of Dzyaloshinsky-Moriya interactions [81,82] and canting of spins [83].
- **Ferrimagnetic double perovskites:** for ferrimagnetic ordering, two magnetic cations with different moment need to be aligned antiferromagnetically, which results to a net magnetic moment. There are nearly 30 compounds reported to have ferrimagnetic ordering with high values of $T_c > 300\text{K}$ [51], some of these are Sr_2CrWO_6 , $\text{A}_2\text{BB}'\text{O}_6$ with $\text{A}=\text{Ca}$, Sr or Ba , $\text{B}=\text{Cr}$ or Fe and $\text{B}'=\text{Mo}$, Re or Os [61]. Most of the ferri-magnetic double perovskites are half-metallic or nearly half-metallic compounds.
- **Ferro-magnetic double perovskites:** double perovskite compounds with two different B-site cations allow for different possible combinations where superexchange FM can happen between neighbouring cations. Most of the cases, the double perovskite compounds that are reported to be FM, are various $\text{R}_2\text{B}'\text{MnO}_6$ with $\text{B}'=\text{Co}$, Ni . In this cases, FM ordering appears due to the combinations of partially filled $\text{Co}^{2+}/\text{Ni}^{2+}$ e_g orbitals and empty Mn^{4+} e_g orbitals [84,85]. Hybridization driven mechanism which is reminiscent of a generalized double exchange mechanism, can also lead to the FM ordering in double perovskite compounds, as found in $\text{Sr}_2\text{FeMoO}_6$ [72], $\text{Sr}_2\text{CrMoO}_6$ [86], *etc.* Basic Mechanism for hybridization driven FM ordering in $\text{Sr}_2\text{FeMoO}_6$ is schematically shown in Fig. 1.16. Spin splitting of Fe d levels is quite high and Mo t_{2g} energy levels are placed energetically within the spin split energy levels of Fe d . Mo t_{2g} energy levels attain a negative spin polarization due to the hybridization between Mo t_{2g} and Fe t_{2g} . This helps to stabilize parallel alignment of spins in Fe sublattice *i.e.* FM ordering of Fe spins.

III. Half metallicity and magnetoresistance: Perhaps the most intriguing property of double perovskites, is the half-metallicity and the magneto-resistance. Half-metallicity is characterized by metallic behaviour in one spin channel and insulating behaviour in other spin channel[cf. Fig. 1.17]. So in an ideal case electron transport is completely spin-polarized for

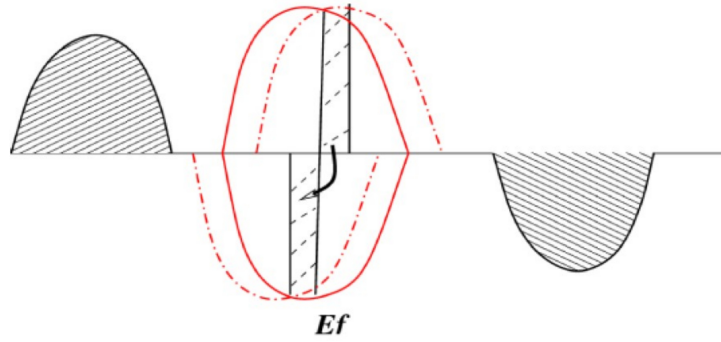


Figure 1.16: Schematic diagram showing the hybridization induced negative spin polarization of Mo bands for $\text{Sr}_2\text{FeMoO}_6$. The shaded semicircular density of states represent the spin split Fe bands. The semicircular density of states, marked in solid red lines, represent Mo bands before switching on the hybridization while that after switching on the hybridization is shown by red dashed lines. E_f marks the position of Fermi energy. Fig. is taken from Ref [76].

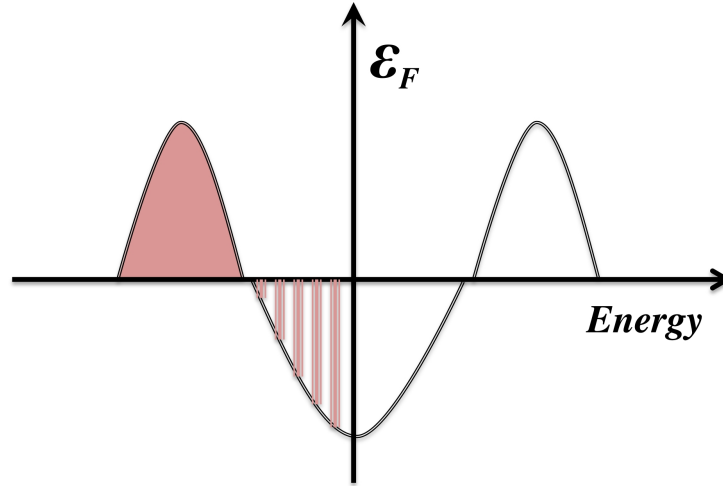


Figure 1.17: Schematic representation of half-metal showing insulating behaviour in up spin channel and metallic behaviour in down spin channel.

half-metal. Typically half-metals should be metallic with integer spin moment at $T=0$ K [87]. Half-metals have potential application possibility in the field of spintronics. A comprehensive reviews on the properties of half-metallic double perovskite compounds can be found in Ref. [56,61].

Magnetoresistance (MR) is defined as the change of electrical resistance of a materials in presence of magnetic field. It is defined as ,

$$MR = [\rho(H) - \rho(0)]/\rho(0) = [\Delta\rho/\rho(0)] \quad (1.14)$$

where $\rho(H)$ and $\rho(0)$ are resistivity in presence and in absence of magnetic field, H respectively. The first observation of magnetoresistance was made Lord Kelvin in 1951 [88]. Later discovery of high negative MR ($\sim 80-90\%$), usually called as colossal magnetoresistance, in the mixed valent oxide of manganese, close to the magnetic transition temperature T_c [89] at a field of few Tesla, provided lot of attention to search new high MR materials due to their rich fundamental physics and great potential application in spintronics.

Perhaps the most studied materials of double perovskite compounds is $\text{Sr}_2\text{FeMoO}_6$, which has very high ferromagnetic transition temperature. The compound is found to be half-metallic with high metallic conductivity and notable negative tunnelling magnetoresistance (TMR) behaviour even at room temperature, which triggered lot of interest in this materials. The unusually high ferromagnetic transition temperature in $\text{Sr}_2\text{FeMoO}_6$ was explained [72, 90] in terms of kinetic-energy driven mechanism which produces a negative spin polarization at otherwise non-magnetic Mo site. A_2FeMoO_6 compounds with $A=\text{Ca}, \text{Sr}, \text{Ba}$ studied most thoroughly and all of the compounds are found to half-metallic with notable negative TMR [56, 61]. Best properties are found with either $A=\text{Ca}$ or Sr . Sr_2CrWO_6 is also found to be half-metallic and shows similar MR effect to $\text{Sr}_2\text{FeMoO}_6$. It is observed that cation disorder can destroy the half-metallic nature of these compounds and lower the TMR effect [91, 92]. Also spin-orbit coupling (SOC) has strong effect on the half-metallicity. Though $\text{Sr}_2\text{FeReO}_6$ appears to be similar to $\text{Sr}_2\text{FeMoO}_6$, it is found that strong SOC of Re compared to that of Mo destroys the half metallic nature in $\text{Sr}_2\text{FeReO}_6$ compound [93, 94].

IV. Superconductivity: High T_c superconducting behaviour in perovskite related cuprate layered compounds is linked to the Cu-O layers. In the $\text{A}_2\text{BB}'\text{O}_6$ double perovskites, similar Cu-O layers are found in case of the layered $\text{La}_2\text{CuSnO}_6$ compound. Thus this compound is expected to show superconductivity as well, but unfortunately they do not. This is due to the positioning of the Cu orbitals in this compound, as discussed by Anderson *et al.* [95]. However superconducting properties with $T_c \simeq 30-40$ K, have been reported for some rock-salt ordered compounds, such as $\text{Sr}_2\text{Y}(\text{Ru}_{1-x}\text{Cu}_x)\text{O}_6$ with small amount of $x \simeq 0.05-0.2$ [96, 97].

1.3 Theoretical method to study transition metal compounds

In order to explain the physical properties of transition metal compounds, understanding of the underlying electronic structure is necessary which is complex in general and difficult to calculate due to simultaneous presence of localized electrons and itinerant band states, as discussed above. On the theoretical front to study such complex transition metal compounds, we have mainly used two approaches,

- (i) Density functional theory based ab initio calculation takes into account all the structural and chemical aspect of material accurately. The DFT is based on single particle approximation, where electron-electron correlation is treated in a mean field manner within local density approximation (LDA) [98]. It is fully free of any adjustable parameters.
- (ii) Many-body model Hamiltonian based approaches (like Hubbard and Heisenberg model) where electron-electron correlation is taken into account in an improved way but parameters of model Hamiltonian are vastly unknown. The major problem of the model Hamiltonian approach is correct choice of model parameters.

Both the approaches have made tremendous progress in last decade. The DFT calculations, within local density approximation in which the correlation as well as exchange interaction of the Coulomb interactions is treated by means of local density of real system, is found to be unexpectedly highly successful approach in describing physical properties of many materials. Sometimes the conventional LDA fails in describing the ground state properties of many materials where electron-electron correlation is strong, such as transition metal compounds. One of the crucial reason for this failure is that problem of self-interaction (interaction of electrons with the field it generates) is treated in an average way within LDA. Effect of self-interaction is severe for transition metal compound with partially occupied d -states. Extension like addition of partially screened Coulomb interaction (Hubbard U), in DFT+ U [99–101] or hybrid functional [102, 103] which partly correct the self-interaction error by introducing certain portion of exact exchange, significantly improved the localized description of the d electrons in transition metal compounds. But, in the DFT+ U method, absence of Coulomb interactions, screening effect which leads to strong overestimation of effective Coulomb parameter U and the

dependence on the adjustable parameters in the hybrid functional approaches, remain a serious concern. A parameter free ground state approach beyond the LDA is the GW approximation (GWA) [104,105] where problem of screening is addressed in an rigorous way. The GW approach is based on many body perturbation theory (MBPT), in which first order term of a systematic expansion in MBPT is retained. It is more accurate method for description of quasi particle band structure in moderately correlated solids. The main problem of this method is that it is computationally very heavy and it can't describe properly strongly correlated metals where higher order terms in W need to be included. Electronic and magnetic properties of strongly

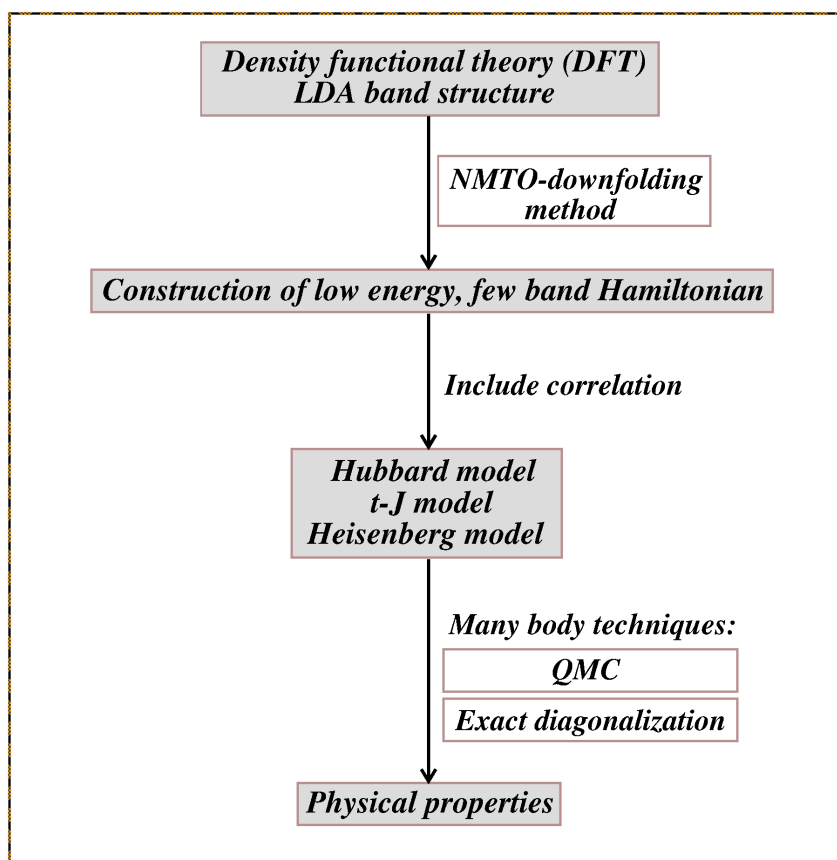


Figure 1.18: Schematic diagram showing the combined approaches of DFT and many body calculations.

correlated transition metal systems are mainly governed by the limited of states lying close to the Fermi energy and well isolated from rest of the states. This helps to explore the possibility of combining the DFT based first principles electronic structure calculations with many body models such a way that it retains the best of both the approaches. The basic idea of combing the two approaches is that first construct the model Hamiltonian entirely from the DFT based first

principles calculations and make it free of any adjustable parameters. Then by using modern many-body method solve the model Hamiltonian. Such a construction is expected to describe the effect that are not captured by LDA. The basic procedure of combing the two approaches are summarized by the flow chart given in Fig. 1.18.

The crucial step is the construction of one-electron part of the model Hamiltonian in a restricted Hilbert space, which would pick up only those state that are primarily responsible for the physics of the considered phenomena. In this regard the N^{th} order muffin tin orbital

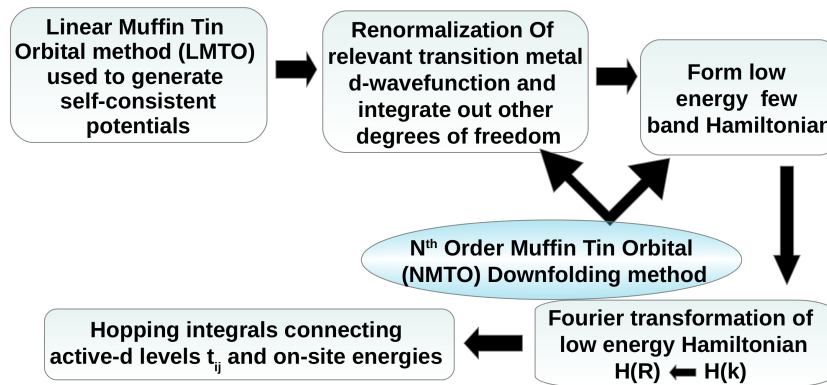


Figure 1.19: Basic procedure of extracting model Hamiltonian parameters from NMTO down-folding method.

(NMTO) based down-folding technique [106] is found to be highly successful method to derive low energy few orbital Hamiltonian by an energy selective down-folding processes that integrates out higher energy degrees of freedom from a complicated full LDA Hamiltonian. By construction this effective orbitals that define the low energy Hamiltonian, serve as Wannier-like orbitals [107]. The parameters for the many body Hamiltonian are then extracted from real space representation of the few band low energy down-folded Hamiltonian. Basic procedure of extracting model Hamiltonian parameters from NMTO down-folding method is shown in Fig. 1.19. Many-body technique like quantum Monte Carlo [108–110] method and exact diagonalization (ED) have been used in this thesis to solve many body Hamiltonian. A detail description of these theoretical methods involved in such theoretical approaches is given in chapter-2.

Crystal structures shown in this chapter and in all the subsequent chapters are produced using software package, VESTA [111].

Bibliography

- [1] D. Khomskii, "Transition Metal Compounds", Cambridge University Press, Cambridge, England, (2014).
- [2] Patrik Fazekas, "Lecture notes on electron correlation and magnetism" (Series in Modern Condensed Matter Physics) World Scientific Publishing Company (1999).
- [3] H. A. Jahn, E. Teller, Proc. R. Soc. A. 161 (A905): 220-235 (1937).
- [4] J. Hubbard, "Electron Correlations in Narrow Energy Bands". Proceedings of the Royal Society of London. 276 (1365): 238-257 (1963).
- [5] J. B. Parkinson, D. J. J. Farnell, "An Introduction to Quantum Spin Systems, Lect. Notes", Phys. 816 , Springer, Berlin Heidelberg, (2010).
- [6] J. G. Bednorz, K. A. Müller, Z. Phys. B 64, 189 (1986).
- [7] P. Lemmens, G. Güntherodt, C. Gros, Phys. Rep. 375, 1 (2003).
- [8] K. Katsumata, J. Phys.: Condens. Matter 12, R589 (2000).
- [9] J. W. Bray, H. R. Hart, L. V. Interrante, I. S. Jacobs, J. S. Kasper, G. D. Watkins, S. H. Wee, J. C. Bonner, Phys. Rev. Lett. 35, 744 (1975).
- [10] I. S. Jacobs, J. W. Bray, H. R. Hart, L. V. Interrante, J. S. Kasper, G. D. Watkins, D. E. Prober, J. C. Bonner, Phys. Rev. B 14, 3036 (1976).
- [11] J. W. Bray, H. R. Hart Jr., L. V. Interrante, I. S. Jacobs, J. S. Kasper, G. D. Watkins, S. H. Wee and J. C. Bonner, Phys. Rev. Lett. 35, 744 (1975).

-
- [12] I. S. Jacobs, J. W. Bray, H. R. Hart Jr., L. V. Interrante, J. S. Kasper, G. D. Watkins, D. E. Prober and J. C. Bonner, *Phys. Rev. B* 14, 3036 (1976).
- [13] S. Huizinga, J. Kommandeur, G.A. Sawatzky, B.T. Thole, K. Kopinga, W.J.M. de- Jonge, J. Roos, *Phys. Rev. B* 19, 4723 (1979).
- [14] M. Hase, I. Terasaki, and K. Uchinokura, *Phys. Rev. Lett.* 70, 3651 (1993); J. P. Pouget, L. P. Regnault, *et al. ibid.* 72, 4037 (1994).
- [15] M. Isobe, Y. Ueda, *J. Phys. Soc. Japan* 65, 1178 (1996).
- [16] J. P. Clancy, B. D. Gaulin, and F. C. Chou, *Phys. Rev. B* 81, 024411 (2010).
- [17] C. K. Majumdar and D. Ghosh, *J. Math. Phys.* 10, 1388 (1969).
- [18] H. A. Bethe, *Z. phys.* 71, 205 (1931).
- [19] E. Lieb, T. D. Schultz and D. C. Mattis, *Ann. Phys.* 16, 407 (1961).
- [20] F. D. M. Haldane, *Phys. Rev. Lett.* 50, 1153 (1983).
- [21] F. D. M. Haldane, *Phys. Lett. A* 93, 464 (1983).
- [22] I. Affleck, T. Kennedy, E. H. Lieb, H. Tasaki, *Phys. Rev. Lett.* 59, 799 (1987).
- [23] M. Hagiwara, K. Katsumata, I. Affleck, B. I. Harpelin, J. P. Renard, *Phys. Rev. Lett.* 65, 3181 (1990).
- [24] W. J. L. Buyers, R. M. Morra, R. L. Armstrong, M. J. Hogan, P. Gerlach, and K. Hirakawa, *Phys. Rev. Lett.* 56, 371 (1986);
- [25] R. M. Morra, W. J. L. Buyers, R. L. Armstrong, and K. Hirakawa, *Phys. Rev. B* 38, 543 (1988).
- [26] J. P. Renard, M. Verdaguer, L. P. Regnault, W. A. C. Erkelens, J. Rossat-Mignod, and W. G. Stirling, *Europhys. Lett.* 3, 945 (1987).
- [27] J. F. Di Tusa, S. -W. Cheong, J. -H. Park, G. Aeppli, C. Broholm, and C. T. Chen, *Phys. Rev. Lett.* 73, 1857 (1994).

- [28] S. Lee, J.-G. Park, D. T. Adroja, D. Khomskii, S. Streltsov, K. A. McEwen, H. Sakai, K. Yoshimura, V. I. Anisimov, D. Mori, *et al.* Nature Materials 5, 471 (2006).
- [29] N. Tsujii, O. Suzuki, H. Suzuki, H. Kitazawa, and G. Kido, Phys. Rev. B 72, 104402 (2005).
- [30] Y. Uchiyama, Y. Sasago, I. Tsukada, K. Uchinokura, A. Zheludev, T. Hayashi, N. Miura, and P. Böni, Phys. Rev. Lett. 83, 632 (1999).
- [31] A. I. Smirnov, V. N. Glazkov, T. Kashiwagi, S. Kimura, M. Hagiwara, K. Kindo, A. Y. Shapiro, and L. N. Demianets, Phys. Rev. B 77, 100401 (2008).
- [32] A. Zheludev, T. Masuda, I. Tsukada, Y. Uchiyama, K. Uchinokura, P. Boni, and S.-H. Lee, Phys. Rev. B 62, 8921 (2000).
- [33] A. Zheludev, T. Masuda, K. Uchinokura, and S. E. Nagler, Phys. Rev. B 64, 134415 (2001).
- [34] A. K. Bera, B. Lake, A. T. M. N. Islam, B. Klemke, E. Faulhaber, and J. M. Law, Phys. Rev. B 87, 224423 (2013).
- [35] S. R. White and I. Affleck, Phys. Rev. B 77, 134437 (2008).
- [36] T. Sakai and M. Takahashi, Phys. Rev. B 42, 4537 (1990).
- [37] E. Dagotto and T. M. Rice, Science, 271, 618 (1996).
- [38] Yutaka Ueda, Chem. Mater. 10, 2653-2664 (1998)
- [39] T. Barnes, E. Dagotto, J. Riera, and E. S. Swanson, Phys. Rev. B, 47, 3196, (1993).
- [40] S. Gopalan, T. M. Rice, and M. Sigrist, Phys. Rev. B, 49, 8901, (1994).
- [41] T. M. Rice, S. Gopalan and M. Sigrist, Europhys. Lett. 23, 445 (1993).
- [42] Z. Hiroi, M. Azuma, M. takano and Y. Bando, J. Solid State Chem. 95, 230 (1991).
- [43] S. Taniguchi, T. Nishikawa, Y. Yasui, Y. Kobayashi, M. Sato, T. Nishioka, M. Kontani, and K. Sano, J. Phys. Soc. Jpn. 64, 2758 (1995).
- [44] B. S. Shastry and B. Sutherland, Physica B, 108, 1069 (1981).
- [45] H. Kageyama, K. Yoshimura, R. Stern, *et al.* Phys. Rev. Lett. 82, 3168 (1999).

- [46] S. Miyahara, and K. Ueda, Phys. Rev. Lett., 82, 3701 (1999).
- [47] M. T. Anderson, K. B. Greenwood, G. A. Taylor, K. R. Poeppelmeier, Prog. Solid State Chem. 22, 197 (1993).
- [48] G. King, P. M. Woodward, J. Mater. Chem. 20, 5785 (2010).
- [49] P. M. Woodward, R. D. Hoffmann, A. Sleight, J. Mater. Res. 9, 2118 (1994).
- [50] F. Galasso, W. Darby, J. Phys. Chem. 66, 131 (1962).
- [51] S. Vasala, M. Karppinen, Prog. in Solid State Chem. 43, 1-36 (2015).
- [52] M. T. Anderson, K. R. Poeppelmeier, Chem. Mater. 3, 476 (1991).
- [53] M. Azuma, S. Kaimori, M. Takano, Chem. Mater. 10, 3124 (1998).
- [54] S. Kaimori, S. Kawasaki, M. Azuma, M. Takano, J. Jpn. Soc., 44-127 (1997).
- [55] R. D. Shannon, Acta Crystallogr. A, 32 751 (1976).
- [56] D. Serrate, J. M. De Teresa and M. R. Ibarra, J. Phys.: Condens. Matter. 19, 023201 (2007).
- [57] M. W. Lufaso, P. M. Woodward, Acta Crystallogr. Sect. B Struct. Sci., 60-10 (2004).
- [58] B. C. Jeon, C. H. Kim, S. J. Moon, W. S. Choi, H. Jeong, Y. S. Lee, *et al.* J. Phys. Condens. Matter. 22, 345602 (2010).
- [59] J. H. Choy, D. K. Kim, J. Y. Kim, Solid State Ionics 108, 159 (1998).
- [60] G. Cao, T. F. Qi, L. Li, J. Terzic, S. J. Yuan, L. E. DeLong, *et al.* Phys. Rev. Lett. 112, 56402 (2014).
- [61] J. B. Philipp, P. Majewski, L. Alff, A. Erb, R. Gross, T. Graf, *et al.* Phys. Rev. B 68, 144431 (2003).
- [62] H. Kato, T. Okuda, Y. Okimoto, Y. Tomioka, K. Oikawa, T. Kamiyama, *et al.* Phys. Rev. B 69, 184412 (2004).

- [63] P. A. Kumar, R. Mathieu, R. Vijayaraghavan, S. Majumdar, O. Karis, P. Nordblad, *et al.* Phys. Rev. B 86, 94421 (2012).
- [64] G. Blasse, Philips, Res. Rep. 20, 327 (1965).
- [65] R. P. Singh, C. V. Tomy, Phys. Rev. B 78, 24432 (2008).
- [66] P. D. Battle, G. R. Blake, T. C. Gibb, J. F. Vente, J. Solid State Chem. 145, 541 (1999).
- [67] A. K. Paul, M. Reehuis, V. Ksenofontov, B. Yan, A. Hoser, D. M. Tobbens, P. M. Abdala, M. Jansen, C. Felser, P. Adler, Phys. Rev. Lett. 111, 167205 (2013).
- [68] R. Morrow, J. W. Freeland, P. M. Woodward, Inorg. Chem. 53, 7983-7992 (2014).
- [69] R. Morrow, R. Mishra, O. R. Restrepo, M. R. Ball, W. Windl, S. Wurmehl, U. Stockert, B. Büchner, P. M. Woodward, J. Am. Chem. Soc. 135, 18824-18830 (2013).
- [70] R. Macquart, S. J. Kim, W. R. Gemmill, J. K. Stalick, Y. Lee, T. Vogt, H. C. Zur Loye, Inorg. Chem. 44, 9676-9683 (2005).
- [71] M. W. Lufaso, W. R. Gemmill, S. J. Mugavero, S. J. Kim, Y. Lee, T. Vogt, H. C. zur Loye, J. Solid State Chem. 181, 623-627 (2008).
- [72] D. D. Sarma, P. Mahadevan, T. Saha-Dasgupta, S. Ray, and A. Kumar, Phys. Rev. Lett. 85, 2549 (2000).
- [73] L. Brey, M. J. Calderon, S. Das Sarma, and F. Guinea, Phys. Rev. B 74, 094429 (2006).
- [74] P. Sanyal and P. Majumdar, Phys. Rev. B 80, 054411 (2009).
- [75] P. Sanyal, Phys. Rev. B, 89, 115129 (2014).
- [76] T. Saha-Dasgupta, J. Supercond. Nov. Magn. 26, 1991-1995 (2013).
- [77] H. L. Feng, M. Arai, Y. Matsushita, Y. Tsujimoto, Y. Guo, C. I. Sathish, X. Wang, Y. Yuan, M. Tanaka, K. Yamaura, J. Am. Chem. Soc. 136, 3326-3329 (2014).
- [78] R. Morrow, J. Q. Yan, M. A. McGuire, J. W. Freeland, D. Haskel, P. W. Woodward, Phys. Rev. B 92, 094435 (2015).

- [79] B. J. Kim, H. Jin, S. J. Moon, J. Y. Kim, B. G. Park, C. S. Leem, J. Yu, T. W. Noh, C. Kim, S. J. Oh, J. H. Park, V. Durairaj, G. Cao, E. Rotenberg, *Phys. Rev. Lett.* 101, 076402 (2008).
- [80] G. Cao, A. Subedi, S. Calder, J. Q. Yan, J. Yi, Z. Gai, L. Poudel, D. J. Singh, M. D. Lumsden, A. D. Christianson, B. C. Sales, D. Mandrus, *Phys. Rev. B* 87, 155136 (2013).
- [81] I. Dzyaloshinskii, *Journal of Physics and Chemistry of Solids* 4, 241 (1958).
- [82] T. Moriya, *Physical Review* 120, 91 (1960).
- [83] Q. Lin, M. Greenblatt, M. Croft, *J. Solid State Chem.* 178-1356 (2005).
- [84] R. I. Dass, J. B. Goodenough, *Phys. Rev. B*, 67-14401 (2003).
- [85] R. Mishra, J. R. Soliz, P. M. Woodward, W. Windl. *Chem. Mater.* 24, 2757 (2012).
- [86] P. Sanyal, A. Halder, Liang Si, M. Wallerberger, K. Held and T. Saha-Dasgupta, *Phys. Rev. B.* 94, 035132 (2016).
- [87] J. M. D. Coey, M. Venkatesan, *J. Appl. Phys.* 91, 8345 (2002).
- [88] William Thomson (Lord Kelvin), *Proc. Royal Soc. London* 8, 546-550 (1857).
- [89] *Colossal Magnetoresistive Oxides*, ed. Y. Tokura (Gordon and Breach, Amsterdam, 2000).
- [90] J. Kanamori and K. Terakura, *J. Phys. Soc. Jpn.* 70, 1433 (2001).
- [91] D. D. Sarma, E. V Sampathkumaran, S. Ray, R. Nagarajan, S. Majumdar, A. Kumar, *et al.* *Solid State Commun.* 114, 465 (2000).
- [92] M. Garcia-Hernandez, J. L. Martinez, M. J. Martinez-Lope, M. T. Casais, J. A. Alonso, *Phys. Rev. Lett.* 86, 2443 (2001).
- [93] J. M. De Teresa, J. M. Michalik, J. Blasco, P. A. Algarabel, M. R. Ibarra, C. Kapusta C, *et al.*, *Appl. Phys. Lett.* 90, 252514(2007).
- [94] M. Sikora, C. Kapusta, M. Borowiec, C. J. Oates, V. Prochazka, D. Rybicki, *et al.* *Appl. Phys. Lett.* 89, 62503 (2006).

-
- [95] M. T. Anderson, K. R. Poeppelmeier, S. A. Gramsch, J. K. Burdett, *J. Solid State Chem.*, 102, 164 (1993).
- [96] S. M. Rao, J. K. Srivastava, M. K. Wu, B. H. Mok, C. L. Chen, M. C. Ling, *et al.* *Nov. Magn.* 24, 1249 (2011).
- [97] G. Long, M. DeMarco, D. Coffey, M. K. Toth, M. S. Torikachvili, *Phys. Rev. B* 87, 24416 (2013).
- [98] W. Kohn and L. J. Sham, *Phys. Rev.* 140, A1133-A1138 (1965).
- [99] V. I. Anisimov, J. Zaanen and O. K. Andersen, *Phys. Rev. B* 44, 943 (1991).
- [100] V. I. Anisimov *et al.* *Phys. Rev. B* 48, 16929 (1993).
- [101] A. I. Lichtenstein *et al.*, *Phys. Rev. B* 52, R5467 (1995).
- [102] A. D. Becke, *The Journal of Chemical Physics* 98, 1372-1377 (1993).
- [103] J. Heyd, G. E. Scuseria, and M. Ernzerhof, *The Journal of Chemical Physics* 118, 8207-8215 (2003).
- [104] L. Hedin, *Phys. Rev.* 139, A796 (1965).
- [105] L. Hedin and S. Lundqvist, *Solid State Physics* vol 23, ed H. Ehrenreich, F. Seitz and D. Turnbull (New York: Academic) p:1 (1969).
- [106] O. K. Andersen and T. Saha-Dasgupta, *Phys. Rev. B* 62, R16219 (2000).
- [107] G. H. Wannier, *Phys. Rev.* 52, 191 (1937).
- [108] A. W. Sandvik, *Phys. Rev. B* 59, R14157 (1999).
- [109] A. Dorneich and M. Troyer, *Phys. Rev. E* 64, 066701 (2001).
- [110] K. Louis and C. Gros, *Phys. Rev. B* 70, 100410(R) (2004).
- [111] K. Momma and F. Izumi, *Journal of Applied Crystallography* 44, 1272-1276 (2011).

Chapter 2

Theoretical methods

In this chapter we describe the theoretical methods which are used in this thesis to study different transition metal compounds. The theoretical study carried out in this thesis is primarily based on density functional theory (DFT), description of which is given in section 2.3. In some of the projects, we combined the density functional theory based electronic structure calculations with many body model Hamiltonian approach as have been mentioned in the introductory chapter 1. To calculate the single particle part of correlated many body Hamiltonian, such as hopping integrals, on site energies, we used N^{th} order muffin-tin orbital method which is discussed in the section 2.6.3. Finally to solve the DFT derived correlated Heisenberg spin Hamiltonian, many body technique like stochastic series expansion (SSE) of quantum Monte Carlo method has been used in this thesis which is described in section 2.7.1. Description of different theoretical methods are given below.

2.1 The many-electron Hamiltonian

When atoms are put together to form a three dimensional material, it can be thought of as collection of heavy positively charged particles (nuclei) and lighter negatively charged particles (electrons). If such a solid system consists of N atoms having atomic number Z , then we have to deal with the problem of $(N + N \times Z)$ electromagnetically interacting particles. The

corresponding exact many-particle total Hamiltonian for such system can be written as,

$$\begin{aligned}
 H &= -\frac{\hbar^2}{2} \sum_I \frac{\nabla_{\mathbf{R}_I}^2}{M_I} - \frac{\hbar^2}{2} \sum_i \frac{\nabla_{\mathbf{r}_i}^2}{m_e} - \frac{1}{4\pi\epsilon_0} \sum_{I,i} \frac{e^2 Z_I}{|\mathbf{R}_I - \mathbf{r}_i|} \\
 &\quad + \frac{1}{4\pi\epsilon_0} \sum_{i>j} \frac{e^2}{|\mathbf{r}_i - \mathbf{r}_j|} + \frac{1}{4\pi\epsilon_0} \sum_{I>J} \frac{e^2 Z_I Z_J}{|\mathbf{R}_I - \mathbf{R}_J|} \\
 &= T_N(\mathbf{R}) + T_e(\mathbf{r}) + V_{Ne}(\mathbf{R}, \mathbf{r}) + V_{ee}(\mathbf{r}) + V_{NN}(\mathbf{R})
 \end{aligned} \tag{2.1}$$

Where Z_I and M_I are charge and mass of the nucleus and mass of electron is m_e . The nuclear coordinates are given by \mathbf{R}_I and electronic coordinates are given by \mathbf{r}_i . The first two terms are the kinetic energy operators for the nuclei and the electrons, respectively. The last three terms represent the electron-nucleus, electron-electron, and nucleus-nucleus Coulomb interactions, respectively. The Hamiltonian given by Eq. 2.1, is easy to write, can not be solved exactly due to many body nature of Coulomb interaction, except for simple systems, such as an isolated hydrogen atom [1, 2]. One needs to make approximations at different level in order to solve the Schrödinger equation, given by the above Hamiltonian for realistic systems.

2.2 The Born-Oppenheimer approximation

The first step towards the simplification of the above many-body Hamiltonian is the Born-Oppenheimer approximation (1927) [3]. This approximation leads to the separation of the electronic and nuclear degrees of freedom. Electronic mass is significantly smaller compared to the nuclei and therefore, motion of nuclei is much slower than that of the electron. As a consequence, one can consider nuclei to be static at fixed position and the electrons to be almost in the instantaneous equilibrium with the nuclei. Because the nuclei are fixed, their kinetic energy can be neglected and the potential energy due to nucleus-nucleus interactions (last term in Eq. 2.1) is assumed to be constant. Thus, under the Born-Oppenheimer approximation the many body Hamiltonian given in the Eq. 2.1 is reduced to the following electronic Hamiltonian,

$$H_{el} = T_e(\mathbf{r}) + V_{Ne}(\mathbf{r}; \mathbf{R}_a) + V_{ee}(\mathbf{r}) + V_{NN}(\mathbf{R}_a) \tag{2.2}$$

where the constant nucleus-nucleus interaction term $V_{NN}(\mathbf{R}_a)$ is called Madelung energy and is calculated classically. The solution of the Schrödinger equation with H_{el} gives the electronic wave function ψ_{el} and the electronic energy E_{el} . ψ_{el} explicitly depends on the electron's coordinates, while the nuclear's coordinates enter only parametrically in the Eq. 2.2. The total energy E_{tot} , of the whole system can be written as the sum of an electronic term E_{el} and constant nuclear term E_{nuclei} , is given by

$$E_{tot} = (E_{el} + E_{nuclei})$$

In Eq. 2.2, the attractive Coulomb interaction between electron and nucleus $V_{Ne}(\mathbf{r}; \mathbf{R}_a)$ is also termed as the external potential, $V_{ext}(\mathbf{r}; \mathbf{R}_a)$ and this external potential is not necessarily limited to the effect of nuclear field on electrons, but may include external magnetic and/or electric fields.

Even after this simplification with Born-Oppenheimer approximation, Eq. 2.2 represents a very complicated many-electron eigenvalue problem and further approximations are needed to solve it. Different approaches are made to transform this many-electron eigenvalue value problem to an effective single-particle picture, in which the system of interacting electrons can be mapped onto a system of non-interacting quantum mechanical particles that approximates the behaviour of original system. Two distinct approaches have been put forward in this direction, (a) wave function based approaches like Hartree [4], Hartree-Fock [5] and configuration-interaction [6] *etc* (b) density functional theory based approaches [7–9]. In the wave functional theory based approaches huge computational resources are needed even for a simple system for capturing the detailed wave function which is function of $3N$ variables. As system grows, such approaches become quickly computationally prohibitive. On the other hand DFT is computationally much simpler than wave functional theory based approaches which is primarily used in this thesis for theoretical calculations. Details description of density functional theory is given below.

2.3 Modern Density Functional Theory: way of solving quantum many body problem

Density Functional theory (DFT) is one of highly successful approach in describing structural and electronic properties in a vast class of materials, ranging from atoms and molecules to simple crystals to complex materials. In the DFT one ignores the precise details of many body wave function $\Psi(\mathbf{r}, \mathbf{r}_2 \dots \mathbf{r}_N)$ which is function of $3N$ variables and consider only the diagonal element of the first order density matrix, namely the charge density of electrons,

$$\rho(\mathbf{r}) = N \int \Psi(\mathbf{r}, \mathbf{r}_2 \dots \mathbf{r}_N) \Psi^*(\mathbf{r}, \mathbf{r}_2 \dots \mathbf{r}_N) d\mathbf{r}_2 d\mathbf{r}_3 \dots d\mathbf{r}_N \quad (2.3)$$

as a basic variable. Central idea of DFT is that ground state properties of many electron system are uniquely determined by its electron density, which is only function of 3 variables. Hence DFT is computationally much simpler than wave function based methods like Hartree and Hartree-Fock. Nowadays DFT has become a common tool in first-principles calculations to describe or even to predict the physical properties of molecular and condensed matter systems. One of the earlier tractable density functional approach was proposed by Thomas-Fermi (1927) [10, 11] to solve the many body problem but the theory suffered from various drawback. The main source of error was in the presentation of kinetic energy, followed by the error in the exchange energy. The Thomas-Fermi model completely ignored the electrons correlation and it did not predict bonding between atoms. In 1964 Hohenberg and Kohn proposed and proved the two theorems [7] which are back-bone of modern DFT.

2.3.1 The Hohenberg-Kohn (HK) theorem

Theorem I: first theorem of HK states that, there is an one to one correspondence between external potential V_{ext} and ground state electron density $\rho(\mathbf{r})$, *i.e.* the external potential is uniquely determined by the electron density of a system. So ground state expectation value of any observable \hat{A} is unique functional of the ground-state electron density,

$$\langle \Psi | \hat{A} | \Psi \rangle = A[\rho]$$

Hohenberg and Kohn [7] gave a straightforward proof of this theorem in their original paper. Let us consider two N -electron systems, characterised by two different external potentials (differs by more than an additive constant), $V_1(\mathbf{r})$ and $V_2(\mathbf{r})$. Let us assume that corresponding two wave-functions Ψ_1 and Ψ_2 , yield the same electron density $\rho(\mathbf{r})$. Using variation principle one can obtain the energy,

$$\begin{aligned} E_1 &= \langle \Psi_1 | H_1 | \Psi_1 \rangle < \langle \Psi_2 | H_1 | \Psi_2 \rangle \\ &= \langle \Psi_2 | H_2 | \Psi_2 \rangle + \langle \Psi_1 | [H_1 - H_2] | \Psi_1 \rangle \\ &< E_2 + \int dr \rho(\mathbf{r}) [V_1(\mathbf{r}) - V_2(\mathbf{r})] \end{aligned} \quad (2.4)$$

On interchange of suffixes, one can obtain

$$E_2 < E_1 + \int dr \rho(r) [V_2(\mathbf{r}) - V_1(\mathbf{r})]$$

Summation of two inequalities leads to the contradiction,

$$E_1 + E_2 < E_2 + E_1$$

Hence the assumption of identical density arising from two different external potentials is wrong. So a given charge density $\rho(\mathbf{r})$ uniquely determines the external potential and thus the Hamiltonian, since Hamiltonian is specified by the external potential and the total number of electrons, N which can be computed from the density simply by integration over all space. So in principle, given the charge density, the Hamiltonian operator can be determined uniquely and thus the wave functions Ψ (of all states) and therefore all material properties.

Theorem II: let us consider \hat{A} to be many-electron Hamiltonian $\hat{H} = \hat{T} + \hat{V} + \hat{V}_{ext}$ where \hat{T} is the kinetic energy, \hat{V} the electron-electron interaction, and \hat{V}_{ext} the external potential with ground state wave-function Ψ . If $\rho(\mathbf{r})$ is the charge density, then total energy takes the form,

$$\begin{aligned} E[\rho(\mathbf{r})] &= \underbrace{\langle \Psi | \hat{T} + \hat{V} | \Psi \rangle}_{F_{HK}[\rho(\mathbf{r})]} + \langle \Psi | \hat{V}_{ext} | \Psi \rangle \\ &= F_{HK}[\rho(\mathbf{r})] + \int \rho(\mathbf{r}) V_{ext}(\mathbf{r}) d\mathbf{r} \end{aligned} \quad (2.5)$$

where $F_{HK}[\rho(\mathbf{r})]$ is a universal functional of the charge density $\rho(\mathbf{r})$ (and not of $V_{ext}(\mathbf{r})$) for any many electron system. For this functional a variational principle holds. The Hohenberg-Kohn variational theorem states that if the functional $E[\rho(\mathbf{r})]$ is varied with respect to any positive definite trial density $\rho(\mathbf{r})$, such that $\int \rho(\mathbf{r})d\mathbf{r} = N$, then energy functional takes it's minimum value when trial density is equal to correct ground state density, $\rho_0(\mathbf{r})$, *i.e.*

$$E[\rho(\mathbf{r})] = \langle \Psi | \hat{H} | \Psi \rangle \geq E_0[\rho_0(\mathbf{r})]$$

This theorem restricts density functional theory to study the ground state properties only. In this way DFT exactly reduces the N body problem to the determination of a 3-dimensional function $\rho(\mathbf{r})$ which minimizes the functional $E[\rho(\mathbf{r})]$. Unfortunately this is of little uses as exact analytical form of universal functional $F_{HK}[\rho(\mathbf{r})]$ is not known which consists of all many body effects.

2.3.2 The Kohn-Sham (KS) equations

One year later, (1965) Kohn and Sham (KS) [8] reformulated the problem in a more familiar form to approximate the kinetic and electron-electron functional. They mapped the system of interacting electrons on to an auxiliary system of non-interacting electrons having the same ground state charge density $\rho(\mathbf{r})$. A cartoon representing this relationship is shown in the Fig. 2.1. For a system of non-interacting electrons the ground-state charge density can be represent as a sum over one-electron orbitals (the KS orbitals) ϕ_i , *i.e.*

$$\rho(\mathbf{r}) = \sum_i^N |\phi_i|^2 \quad (2.6)$$

In this system of non-interacting electrons, the universal functional $F_{KH}[\rho(\mathbf{r})]$ can be written as,

$$F_{HK}[\rho(\mathbf{r})] = T_s[\rho(\mathbf{r})] + \frac{1}{2} \frac{e^2}{4\pi\epsilon_0} \int \frac{\rho(\mathbf{r})\rho(\mathbf{r}')}{|\mathbf{r} - \mathbf{r}'|} d\mathbf{r}d\mathbf{r}' + E_{xc}[\rho(\mathbf{r})] \quad (2.7)$$

Where, first term $T_s[\rho(\mathbf{r})]$ represents kinetic energy of non-interacting electrons and second term is the classical electrostatic contribution (Hartree term). The last term $E_{xc}[\rho(\mathbf{r})]$ is the

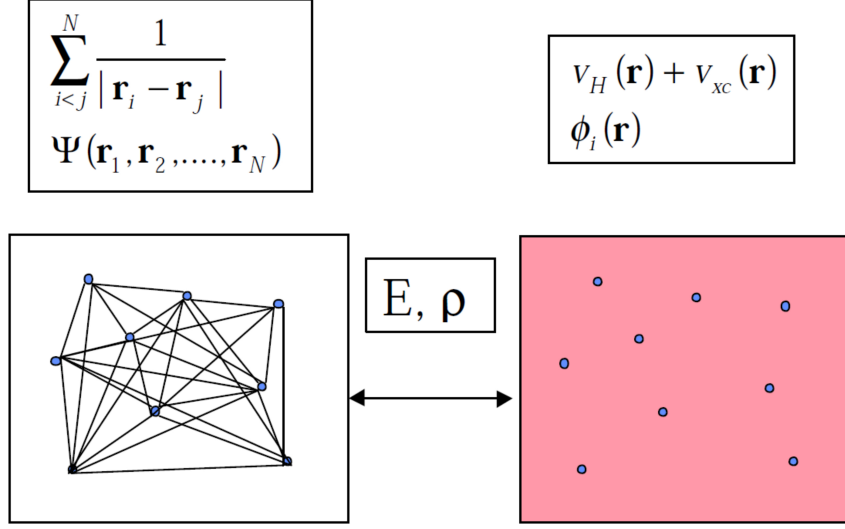


Figure 2.1: Schematic diagram presenting the relationship between the real many body system (left hand side) and the non-interacting system of Kohn-Sham density functional theory (right hand side) Fig. is taken from Ref. [12].

exchange-correlation energy, which can be written as

$$E_{xc}[\rho(\mathbf{r})] = (T[\rho] - T_s[\rho]) + (V_{ee}[\rho] - V_H[\rho]) \quad (2.8)$$

Thus, $E_{xc}[\rho(\mathbf{r})]$ is simply the sum of the error made in using a non-interacting kinetic energy and the error made in treating the electron-electron interaction classically. The energy functional takes the following form:

$$E_{KS}(\rho) = T_s[\rho(\mathbf{r})] + \int V_{ext}(\mathbf{r})\rho(\mathbf{r})d\mathbf{r} + \frac{1}{2} \frac{e^2}{4\pi\epsilon_0} \int \frac{\rho(\mathbf{r})\rho(\mathbf{r}')}{|\mathbf{r} - \mathbf{r}'|} d\mathbf{r}d\mathbf{r}' + E_{xc}[\rho(\mathbf{r})] \quad (2.9)$$

The corresponding KS Hamiltonian can be written as,

$$H_{KS} = \frac{-\hbar^2}{2m} \nabla^2 + V_{eff} \quad (2.10)$$

where

$$\begin{aligned} V_{eff}(\mathbf{r}) &= V_{ext}(\mathbf{r}) + \frac{1}{2} \frac{e^2}{4\pi\epsilon_0} \int \frac{\rho(\mathbf{r}')}{|\mathbf{r} - \mathbf{r}'|} d\mathbf{r}' + \frac{\delta E_{xc}}{\delta \rho(\mathbf{r})} \\ &= V_{ext} + V_{Hartree} + V_{xc} \end{aligned} \quad (2.11)$$

Applying the normalised condition of charge density $\int \rho(\mathbf{r})d\mathbf{r} = N$, variational equation leads to the following equation,

$$\delta[E[\rho] - \mu \int (\rho(\mathbf{r})d\mathbf{r} - N)] = 0 \quad (2.12)$$

where μ is the Lagrange multiplier. Using Eq. 2.9 one can find that the single particle orbitals ϕ_i , which minimize the energy, satisfy the following set of single particle Schrödinger-like equations;

$$\left[-\frac{\hbar^2}{2m}\nabla^2 + V_{eff}(\mathbf{r}; \rho)\right]\phi_i(\mathbf{r}) = \varepsilon_i\phi_i(\mathbf{r}) \quad (2.13)$$

This set of nonlinear equations (the Kohn-Sham equations) describe the behaviour of non-interacting electrons in an effective local potential. Since Hartree part and exchange-correlation term depend on the density $\rho(\mathbf{r})$, which depends on Kohn-Sham orbitals ϕ_i , which in turn depend on $V_{ext}(\mathbf{r})$, the Kohn-Sham equations can't be solved in a straight-forward way. The Kohn-Sham equations are to be solved by using a self-consistent iterative numerical method *i.e.*, start with an initial guess for charge density $\rho(\mathbf{r})$, calculate the corresponding $V_{eff}(\mathbf{r} : \rho)$ and then solve the differential equation (Eq. 2.13) for ϕ_i . From these ϕ_i calculate the new charge density and repeat the process until it converges (see the flow chart given in Fig. 2.2).

2.3.3 Exchange-correlation functional

Although the Kohn-Sham theory is exact in principle, the main problem of this theory, lies in the fact that exact expression for the exchange-correlation(*xc*) energy and potential are not known and hence approximations are needed to find the *xc* functional to some known form. Among the various approximate methods, the local density approximation and generalized gradient approximation are two common methods used for this purpose.

Local density approximation (LDA): One of simplest and commonly used approximation for estimating the exchange-correlation (*xc*) energy is the local density approximation (LDA). It was introduced by Kohn and Sham in their 1965 paper [8], although the basic idea existed in the theory by Thomas-Fermi-Dirac [10, 11, 13]. The basic idea employed here is that exchange-correlation energy is a function of only the local value of the electron density $\rho(\mathbf{r})$. Within LDA

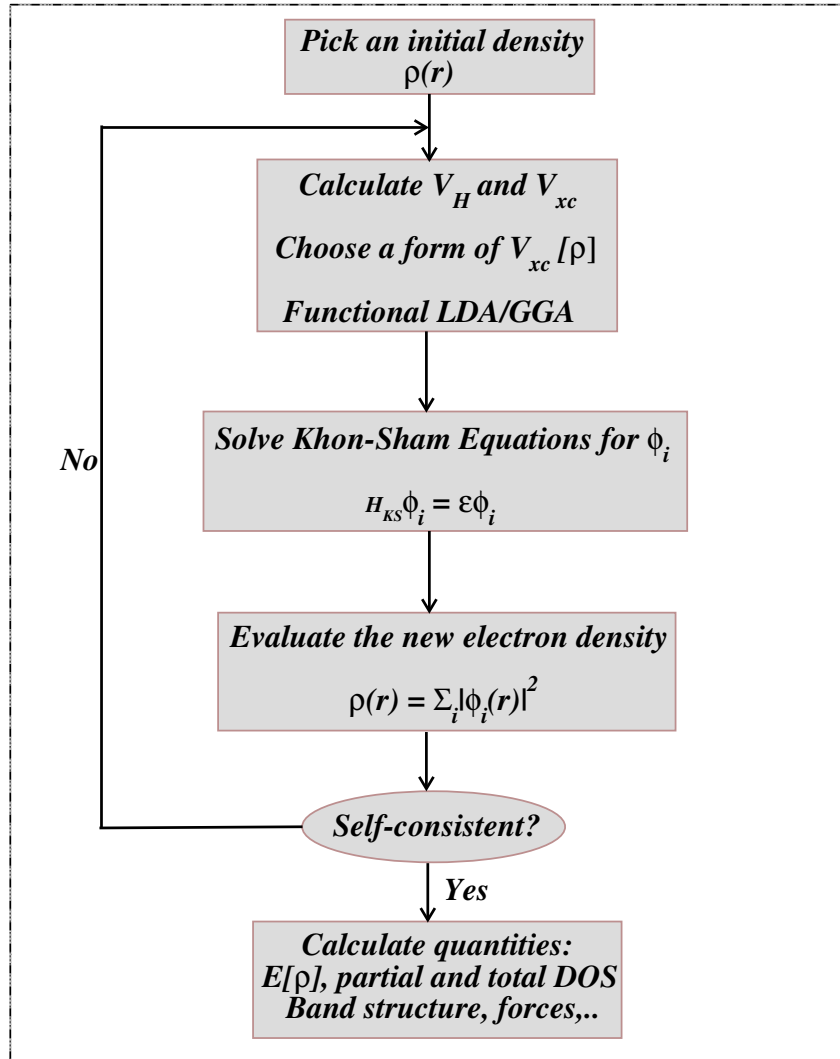


Figure 2.2: DFT self consistent cycle.

the exchange-correlation functional can be written as following form,

$$E_{xc}[\rho(\mathbf{r})] = \int \epsilon_{xc}^{LDA}[\rho(\mathbf{r})] \rho(\mathbf{r}) d\mathbf{r} \quad (2.14)$$

Under the LDA, an obvious choice is to take $\epsilon_{xc}[\rho(\mathbf{r})]$ to be the exchange and correlation energy density of the homogeneous electron gas of density $\rho(\mathbf{r})$. In practice ϵ_{xc} can be written as a sum of individual exchange and correlation contribution,

$$\epsilon_{xc}^{LDA}[\rho(\mathbf{r})] = \epsilon_x^{LDA}[\rho(\mathbf{r})] + \epsilon_c^{LDA}[\rho(\mathbf{r})] \quad (2.15)$$

For homogeneous electron gas, the exchange energy is exactly given by Dirac's expression:

$$\epsilon_x^{LDA} = -\frac{3}{4}\left(\frac{3}{\pi}\right)^{1/3}\rho^{1/3} = -\frac{3}{4}\left(\frac{9}{4\pi^2}\right)^{1/3}\frac{1}{r_s} = -\frac{0.058}{r_s} \quad (2.16)$$

where $r_s = (3/4\pi\rho)^{1/3}$ is the mean inter-electronic distance.

The functional form for the correlation energy density, $\epsilon_c[\rho(\mathbf{r})]$ is unknown and in 1980 Ceperly and Alder [14] estimated the most accurate result by the numerical quantum Monte Carlo calculation for homogeneous electron gas which yields essentially exact result with numerical accuracy. Later it has been parametrized by Perdew and Zunger (1981) [15], John P. Perdew and Yue Wang [16] *etc.*

One can expect that LDA would work well for the system in which the electronic charge density is varying slowly, but surprisingly it yields good result also in the case of highly inhomogeneous systems [17] for which this approximation hardly look appropriate. The reasons for such a surprising work lie in the following two facts,

- (i) There are significant error in the exchange and correlation energies calculation within LDA but as exchange energy is generally underestimated and the correlation energy overestimated, these two errors tend to cancel each others.
- (ii) Electron-electron interaction can be written in terms of pair density $P(\mathbf{r}, \mathbf{r}')$ as,

$$V_{ee} = \frac{1}{2} \int P(\mathbf{r}, \mathbf{r}') \frac{1}{|\mathbf{r} - \mathbf{r}'|} d\mathbf{r} d\mathbf{r}' \quad (2.17)$$

where the pair density $P(\mathbf{r}, \mathbf{r}') = N(N-1) \int d\mathbf{r}_3 \dots d\mathbf{r}_N |\Psi(\mathbf{r}, \mathbf{r}', \dots, \mathbf{r}_N)|^2$ interpreted as the probability of finding an electron in $d\mathbf{r}$ around \mathbf{r} , and a second electron in $d\mathbf{r}'$ around \mathbf{r}' . It contains information on the correlations among electrons. Thus pair density can be written as,

$$P(\mathbf{r}, \mathbf{r}') = \rho(\mathbf{r})[\rho(\mathbf{r}') + \rho_{xc}(\mathbf{r}, \mathbf{r}')]]$$

where $\rho(\mathbf{r})$ is the charge density defined in Eq. 2.3, and $\rho_{xc}(\mathbf{r}, \mathbf{r}')$ is the exchange correlation hole. The quantity $\rho_{xc}(\mathbf{r}, \mathbf{r}') d\mathbf{r}'$ interpreted as the conditional probability of finding

an electron in $d\mathbf{r}'$ around \mathbf{r}' given that there is an electron in $d\mathbf{r}$ around \mathbf{r} . Therefore Eq. 2.17, can be written as,

$$V_{ee} = \frac{1}{2} \int \frac{\rho(\mathbf{r})\rho(\mathbf{r}')}{|\mathbf{r} - \mathbf{r}'|} d\mathbf{r}d\mathbf{r}' + \frac{1}{2} \int \frac{\rho_{xc}(\mathbf{r}, \mathbf{r}')}{|\mathbf{r} - \mathbf{r}'|} \rho(\mathbf{r}) d\mathbf{r}d\mathbf{r}' \quad (2.18)$$

First term in Eq. 2.18 is simply Hartree electrostatic energy, U and second term is defined as exchange correlation energy U_{xc} , arises due to the Coulomb interaction between the charge density and its surrounding exchange correlation hole. Substitution of $\mathbf{u} = \mathbf{r} - \mathbf{r}'$ yields,

$$U_{xc} = \frac{1}{2} \int \rho(\mathbf{r}) d\mathbf{r} \int_0^\infty 4\pi u^2 \left[\int \frac{\rho_{xc}(\mathbf{r}, \mathbf{r} + \mathbf{u})}{u} \frac{d\Omega_u}{4\pi} \right] du \quad (2.19)$$

Thus the electron-electron interaction depends only on the spherical average of the exchange correlation hole, not on the local position of exchange correlation hole.

Generalized Gradient Approximation(GGA): The next step towards the improvement of LDA xc energy is to take into account the spatial variation of charge density $\rho(\mathbf{r})$ (*i.e.* inhomogeneities) in the functional. In the generalized gradient approximation, the energy functional depends on both the density and its gradient but the analytic properties of the exchange correlation hole are retained as in the LDA. Within the GGA, the xc energy can be expressed as,

$$\begin{aligned} E_{xc}^{GGA}[\rho(r)] &= \int \epsilon_{xc}[\rho(\mathbf{r}), |\nabla\rho(\mathbf{r})|] \rho(\mathbf{r}) d\mathbf{r} \\ &= \int \epsilon_{xc}[\rho(r)] F_{xc}[\rho(\mathbf{r}), \nabla\rho(\mathbf{r})] \rho(\mathbf{r}) d\mathbf{r} \end{aligned} \quad (2.20)$$

where the functional F_{xc} is called an enhancement factor. Depending on the choice of the functional form of enhancement factor F_{xc} , there are many forms of GGAs available which are being used over the years. One of the most widely used functional form of F_{xc} was given by Perdew-Wang (PW91) [18] in 1990 obtained from ab-initio calculations. Later on in 1996, Perdew-Burke-Ernzerhof [19] simplified the derivation of PW91 with minor changes of important

features of PW91 and introduced simple functional form, which is famously known as PBE. Calculations presented in this thesis are mostly done with this functional.

Although, GGA works significantly better than LDA to yield the binding energy, total energy of system and many physical properties like structural and magnetic properties of materials but the systematic improvement is not obvious. For examples, it overestimates the electric polarization for polar system [20] and also it cannot describe the long-range behaviour ($1/R^6$) of the Van Der waals interaction. It often fails to correctly describe the strongly correlated system where local electron-electron correlation is very strong and plays significant role to describe many properties. In both the LDA and GGA, electron-electron correlation is treated in an average way. For LDA and GGA functional, the self-interaction (the interaction of electron with the field it generates) term is not exactly cancelled by the exchange and correlation functional. Self-interaction strongly effects the system containing localized electronic state like d and f orbital and its effects is vanishingly small for delocalized extended states. So for such a strongly correlated system, a more accurate treatment of strong correlation effect is required.

2.4 LDA+U Method

One of highly successful method in describing the correlated system is the LDA+U method [21–23]. In the LDA+U method strong on-site Coulomb repulsion (generally term as U) is directly added to strongly localized orbitals such as d and f orbitals along with the LDA or GGA functional. The magnitude of the added interaction is determined by the parameter U . Let us consider a system with fluctuating number of d electrons, but total number of electron $N = \sum_i n_i$ is constant. Within the LDA+U method total energy can be written as

$$E = E^{LDA} + \frac{1}{2}U \sum_{i \neq j} n_i n_j - U \frac{N(N-1)}{2} \quad (2.21)$$

Hubbard term (second term of Eq. 2.21) is explicitly added in Eq. 2.21 which is already included in the LDA functional. Thus in order to avoid double contribution the third term is subtracted.

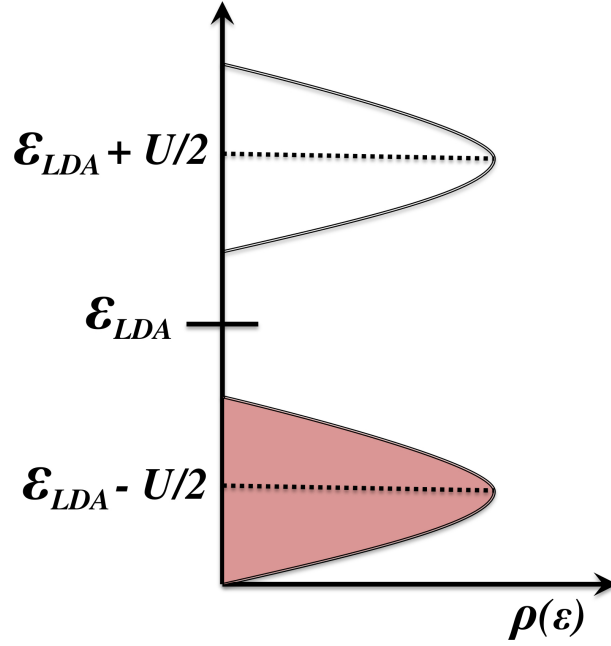


Figure 2.3: In presence of U parameter, shifting of the occupied and unoccupied LDA orbitals with respect to each other.

The orbital energy is given by,

$$\epsilon_i = \frac{\delta E}{\delta n_i} = \epsilon^{LDA} + U\left(\frac{1}{2} - n_i\right) \quad (2.22)$$

One can see that for occupied orbital in which $n_i=1$, LDA orbital energy shifts by $(-U/2)$ and an amount of $(+U/2)$ for unoccupied orbital with $n_i=0$ [cf. Fig. 2.3]. So LDA+U orbital dependent potential gives rise to upper and lower Hubbard bands with an energy separation between them equal to Coulomb parameter U . Hence this method qualitatively reproduces the essential physics of strongly correlated system. In connection with LDA+U method, there exist two popular approaches in which rotationally invariant multi-band Hubbard model is used. They are:

2.4.1 The Lichtenstein method

This was proposed by A. I. Liechtenstein, V. I. Anisimov, and J. Zaanen in 1995 [23]. The generalized LDA+U functional for multi-orbital situations can be defined as:

$$E^{LDA+U}[\rho^\sigma(\mathbf{r}), n^\sigma] = E^{LDA/GGA}[\rho(r)] + E^U[n_m^\sigma] - E_{dc}[n^\sigma] \quad (2.23)$$

Where n_m^σ are orbital occupancies for atom experiencing the on-site Hubbard interactions, m the magnetic quantum number, σ the spin index and $n^\sigma = \sum_m n_m^\sigma$. The last term is subtracted to correct for the double counting. A rotationally invariant form of Hartree-Fock like term $E^U[n_m^\sigma]$ was introduced by Liechtenstein *et. al.*, given by:

$$\begin{aligned} E^U[n_m^\sigma] &= \frac{1}{2} \sum_{m,\sigma} \langle m_1 m_3 | V_{ee} | m_2 m_4 \rangle n_{m_1 m_2}^\sigma n_{m_3 m_4}^{-\sigma} \\ &- (\langle m_1 m_3 | V_{ee} | m_2 m_4 \rangle - \langle m_1 m_3 | V_{ee} | m_4 m_2 \rangle) n_{m_1 m_2}^\sigma n_{m_3 m_4}^\sigma \end{aligned} \quad (2.24)$$

Where V_{ee} are the screened Coulomb interactions among the electrons in nl quantum states. The matrix elements can be expressed in terms of complex spherical harmonics and effective Slater integrals F^k [24], as:

$$\langle m_1 m_3 | V_{ee} | m_2 m_4 \rangle = \sum_k a_k(m_1, m_2, m_3, m_4) F^k \quad (2.25)$$

where $0 \leq k \leq 2l$ and

$$a_k(m_1, m_2, m_3, m_4) = \frac{4\pi}{2k+1} \sum_{q=-k}^k \langle l m_1 | Y_{kq} | l m_2 \rangle \langle l m_3 | Y_{kq}^\dagger | l m_4 \rangle$$

For d electrons one needs F^0 , F^2 and F^4 and these can be expressed interms of two adjustable parameters, as onsite screened Coulomb repulsion, U and exchange parameter, J through the following relations,

$$\begin{aligned} U &= F^0 \\ J &= \frac{F^2 + F^4}{14} \end{aligned}$$

for f electrons the expression for J is:

$$J = \frac{286F^2 + 195F^4 + 250F^6}{6435}$$

with this approach, the double counting term are expressed as,

$$E_{dc}[n^\sigma] = \frac{1}{2} U N(N-1) - \frac{1}{2} J [N^\uparrow(N^\uparrow-1) + N^\downarrow(N^\downarrow-1)] \quad (2.26)$$

where $n^\sigma = \text{Tr}(n_{m_1 m_2}^\sigma)$ and $n = N^\uparrow + N^\downarrow$

2.4.2 The Dudarev method

Later Dudarev *et. al.* [25] proposed a more simplified approach, in which orbital degeneracy of the 3d electrons are taken into account. In this approach the total energy functional can be expressed as:

$$E^{LSDA+U} = E^{LSDA} + \frac{U-J}{2} \sum_{\sigma} \left[\left(\sum_{m_1} n_{m_1 m_2}^{\sigma} \right) - \left(\sum_{m_1 m_2} n_{m_1 m_2}^{\sigma} n_{m_2 m_1}^{\sigma} \right) \right] \quad (2.27)$$

where the summation is performed over projection of orbital momentum ($m_1, m_2 = -2, -1 \dots, 2$ in case of d -electrons). In this approach U and J do not enter separately, only the difference ($U-J$) is used.

So one can see that, the applicability of LDA+U approach mainly depends on the proper choice of values of screened Coulomb interaction U and exchange parameter J . One can obtain the U value from constrained local density approximation (cLDA) approach [26, 27] where the Hubbard U is calculated from the total energy variation with respect to the occupation number of the localized orbitals. Often this approach is found to over estimate the values. Recently, based on random-phase approximation (RPA), a different approach [28–30] was introduced to calculate the Hubbard U systematically from first principles. This approach is computationally very expensive. So one common way to determine the value of U lies in the fact that find a good agreement of calculated properties with experimental results by varying value of U .

2.5 Basis Set

To solve the single-particle Kohn-Sham Eq. 2.13 and to obtain the eigenvalues and eigenfunctions, one needs to choose an appropriate basis set $\psi_{\alpha}(\mathbf{r})$ to expand the single-particle wave-functions $\phi_i(\mathbf{r})$,

$$\phi_i(\mathbf{r}) = \sum_{\alpha} C_{\alpha}^i \psi_{\alpha}(\mathbf{r}) \quad (2.28)$$

For the band structure calculation of solid, several different basis methods have been introduced. Depending on the choice of basis function, different methods can be broadly classified into two categories.

2.5.1 Fixed basis set methods

In these methods, single-particle Kohn-Sham orbitals are expanded in some set of energy independent fixed basis functions, like tight binding method using linear combination of atomic orbitals (LACO) type basis [31], orthogonalized plane wave method within a pseudopotential scheme using plane wave basis [32] set *etc.* Here one has to solve the following eigenvalue equation,

$$(H - \epsilon O).C = 0 \quad (2.29)$$

to determine the eigenvalue ϵ and expansion coefficient C , where O is the overlap matrix. This method is computationally simple but the disadvantage is that basis depends on the ionic positions, so Pulay corrections have to be added to the Hellmann-Feynman forces.

2.5.2 Partial wave methods

In these methods, the Kohn-Sham orbitals are expanded in a set of energy and potential dependent partial wave basis set as in the cellular method [33], the augmented plane wave method [34], and the Korringa-Kohn-Rostoker (KKR) method [35]. Here one has to solve the set of equation of the following form,

$$M(\epsilon).C = 0 \quad (2.30)$$

This kind of approach is quite accurate in the band structure calculation but due the complicated non-linear energy dependence of the secular equation, solution of this kind of equation is computationally very heavy. To overcome this, in 1975 O. K. Andersen [36] first proposed an unified approach considering the positive aspects of fixed basis set method and that of partial wave basis by linearisation of energy dependent of partial waves. Linear augmented plane wave (LAPW) and linear muffin-tin orbital (LMTO) methods are the linearised version of APW and KKR method, respectively.

2.6 Overview of band structure methods

In this thesis, we used three different basis set methods for the general band-structure calculations of various complex transition metal compounds and they are as given below:

- I. Plane wave basis set within projector augmented wave (PAW) [37, 38] potential, as implemented in Vienna ab-initio simulation package (VASP) [39–41].
- II. Tight-binding linear muffin-tin orbital within atomic sphere approximation (TB-LMTO-ASA) method [42] and N^{th} -order linear muffin-tin orbital (NMTO)-downfolding technique [43] as implemented in the Stuttgart code.
- III. All electron linear augmented plane wave (LAPW) [44]+local orbital (lo) [45] method as implemented in WIEN2k code [46].

The brief description of these methods are given below:

2.6.1 Plane wave based pseudopotential method

Choice of the plane wave as basis function to expand the single particle Kohn-Sham orbitals ϕ_i , is one of the common and widely used approach in many first principles method calculations due to the following reasons:

- The basis set is independent of atomic position.
- The Hellmann-Feynman forces acting on the atoms and the stresses on the unit cell can be easily calculated in terms of the expectation value of the Hamiltonian with respect to the ionic coordinates. So no basis set correction to the force is needed.
- With this basis set, it is easy to change from a real-space representation (where the potential energy V has a diagonal representation) to momentum-space (where kinetic energy has diagonal representation) via a Fast Fourier Transform (FFT).

The electronic states of a large number of materials can be separated into two classes, such as, Core states, which are localized in space and deep in energy and Valence or conduction states

which are spread out spatially as well as higher in energy. Since the core electrons are tightly bound to the nucleus and rapidly oscillating due to the orthogonality required with the valence state, a large number of plane waves are required to describe the accurate behaviour of the core state's wave functions. This is the one of major problem of the plane wave basis. To overcome the problem, in 1940 C. Herring introduced the orthogonalized plane wave method [47,48], where he described core states by Bloch sums built from localized orbitals and valence states by plane waves, orthogonalized to the core states. The concept of pseudopotential are originated from the orthogonalized plane wave method. The basic concept of pseudopotential in terms of classical picture is following. When a valence electron moves past the core region, it accelerates toward the positive charge of the ion core and gains large kinetic energy due to the orthogonalization of the valence orbitals to the strongly oscillating core orbital. But the change in total energy (kinetic + potential) should be remained constant throughout the process. Therefore, gain in the kinetic energy cancels the decrease in the potential energy to keep the total energy constant. If one can transform the increase in kinetic energy into an effective repulsive potential and add with the real attractive electrostatic potential, they tend to cancel each other. This cancellation of the effective repulsive and real attractive potentials is not complete and the residual weak potential is called the pseudopotential.

Construction of first-principles pseudopotentials

The general procedure for obtaining the pseudo-potential is following,

- Solve the free atom Kohn-Sham radial equation (see Eq. 2.31) taking into account all the electrons (AE) for a given distribution of electrons in the atomic energy levels. This is generally called the reference configuration:

$$\left[-\frac{1}{2} \frac{d^2}{dr^2} + \frac{l(l+1)}{2r^2} + V_{eff}^{AE}[\rho^{AE}(\mathbf{r})] \right] r R_{nl}^{AE}(r) = \varepsilon_{nl}^{AE}(r) R_{nl}^{AE}(r) \quad (2.31)$$

where R_{nl}^{AE} is the radial part of all electron wave function with angular momentum l and the spherical approximation of Hartree and xc potential is assumed. The effective potential, V_{eff}^{AE}

is given by

$$V_{eff}^{AE}[\rho^{AE}(\mathbf{r})] = -\frac{Z}{r} + V_{Hartree}[\rho^{AE}(\mathbf{r})] + V_{xc}[\rho^{AE}(\mathbf{r})] \quad (2.32)$$

• Next, generate a pseudo-wave function $R_{nl}^{ps}(r)$ corresponding to $R_{nl}^{AE}(r)$ imposing the following conditions,

- (i) Pseudowave function should be node-less inside the core region of certain radius r_c .
- (ii) It should coincide exactly with the true all-electrons (AE) wave function beyond a certain distance *i.e.* $R_{nl}^{AE}(r) = R_{nl}^{ps}(r)$ for $r \geq r_c$.

• Knowing the pseudo wave-function, the pseudo-potential can be obtained by inverting the radial Kohn-Sham equation for the pseudo wave-function and the valence electronic density, given by,

$$V_{l,scr}^{ps} = \varepsilon_l^{ps} - \frac{l(l+1)}{2r^2} + \frac{1}{2rR_l^{ps}(r)} \frac{d^2}{dr^2} [rR_l^{ps}(r)] \quad (2.33)$$

The resulting pseudopotential, $V_{l,scr}^{ps}$, includes screening effect due to the valence electrons. Finally to obtain the pseudopotential one has to subtract the Hartree and xc potential calculated only for the valence electrons. Therefore, considering the screening effect the pseudopotential takes the following form,

$$V_l^{ps} = V_{l,scr}^{ps} - V_{Hartree}[\rho^{ps}] - V_{xc}[\rho^{ps}] \quad (2.34)$$

The basic idea of pseudopotential is shown in Fig. 2.4. The cut-off radius r_c where pseudo and true wave-functions coincide, is not an adjustable pseudo-potential parameter. The outermost nodal surface of the true wave-function gives rise the estimation of smallest possible value of cut-off radius r_c and the pseudo-potential corresponding this cut-off radius close to minimum, is very realistic and same time also very strong. If very large cut-off radius are chosen, the pseudo-potential will be smooth and almost angular momentum independent and same time it will be very unrealistic. A smooth potential leads to a fast convergence of plane-wave basis calculations. So proper choice of cut-off radius is very important to balance between basis-set size and pseudopotential accuracy.

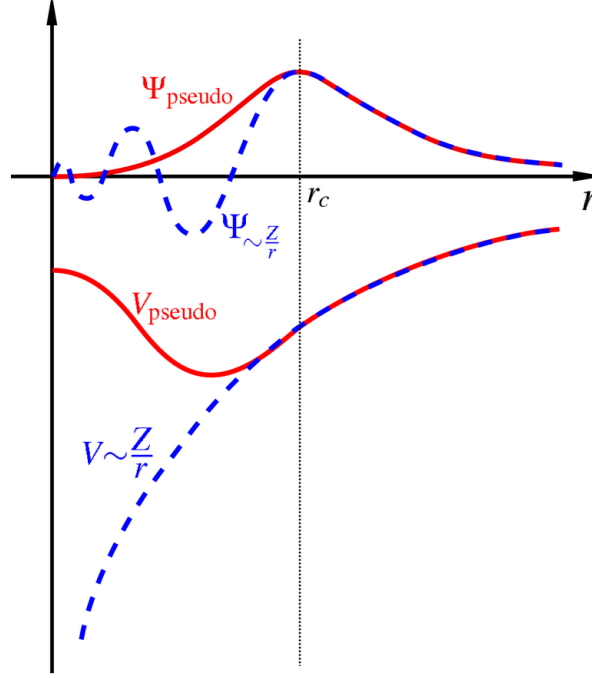


Figure 2.4: Schematic diagram showing the basic idea of pseudopotential. Fig. is taken from web:<http://en.wikipedia.org/wiki/Pseudopotential>.

Several methods have been introduced to generate more accurate as well as more efficient pseudopotentials. Following three kinds of pseudopotentials are widely used in first principle electronic structure calculations in connection to plane wave basis sets.

- **Norm conserving pseudopotential:** In the norm conserving pseudopotential [49], keeping the basic principles the same, an extra constraint is added so that within the cut-off radius r_c the norm of the pseudo wave-function (R_l^{ps}) is the same as the norm of the all electron wave-function (R_l^{AE}) i.e.,

$$\int_0^{r_c} |R_l^{ps}(r)|^2 r^2 dr = \int_0^{r_c} |R_l^{AE}(r)|^2 r^2 dr \quad (2.35)$$

For elements with strongly localized orbitals like first-row $3d$ and rare earth elements, the outermost nodal surface of the true wave-function is close to the nucleus, hence the resulting pseudopotential requires a large plane wave basis set, leading to slow convergence of plane wave basis calculations.

- **Ultra soft pseudopotential:** It is very unrealistic to make the pseudopotential dramatically smooth within the requirement of norm conservation criteria to make fast convergence of plane wave basis calculation. To overcome this issue, a completely new idea was introduced by Vanderbilt [50] where norm conservation constrain was relaxed and atom centred augmentation charge was introduced to make up the charge deficit, where the charge density difference between the AE and pseudowavefunction is termed as augmentation charge. So only for the augmentation charge, small cut-off radius r_c to be used to restore the moments and the charge distribution of the AE wavefunction accurately. One of the problem of this approach is that construction of pseudopotential is much more complex. In the VASP [39–41] and quantum espresso [51] code ultra soft pseudopotentials are implemented.
- **Projector augmented wave (PAW) method:** Later, this method was introduced by Blöchl [37], which is computationally elegant, transferable and accurate method for electronic structure calculation of transition metal and oxides within the plane wave basis. Details of this method are discussed in section 2.6.5

2.6.2 The linear muffin-tin orbital method

Computationally efficient linear Muffin-tin orbital (LMTO) method [42] is a good choice for obtaining microscopic understanding of electronic structure of complex materials. LMTO is based on muffin-tin (MT) approximation in which the actual crystal potential is approximated in the following way [cf. Fig. 2.5]. Within this approximation, the space inside the crystal is divided into two parts, atom-centred MT sphere and the rest region as interstitial. The potential around each atom is assumed to be spherically symmetric within a muffin-tin sphere of certain radius S_R . In the interstitial region, potential varies very slowly, hence considered to be constant (can be taken as zero). Mathematically a single muffin-tin potential can be written as,

$$v_{ext}(\mathbf{r}_R) = \begin{cases} v(r_R) & \text{for } r_R \leq S_R \text{ where } r_R = |\mathbf{r} - \mathbf{R}| \\ -v_0 & \text{for } r_R \geq S_R \end{cases} \quad (2.36)$$

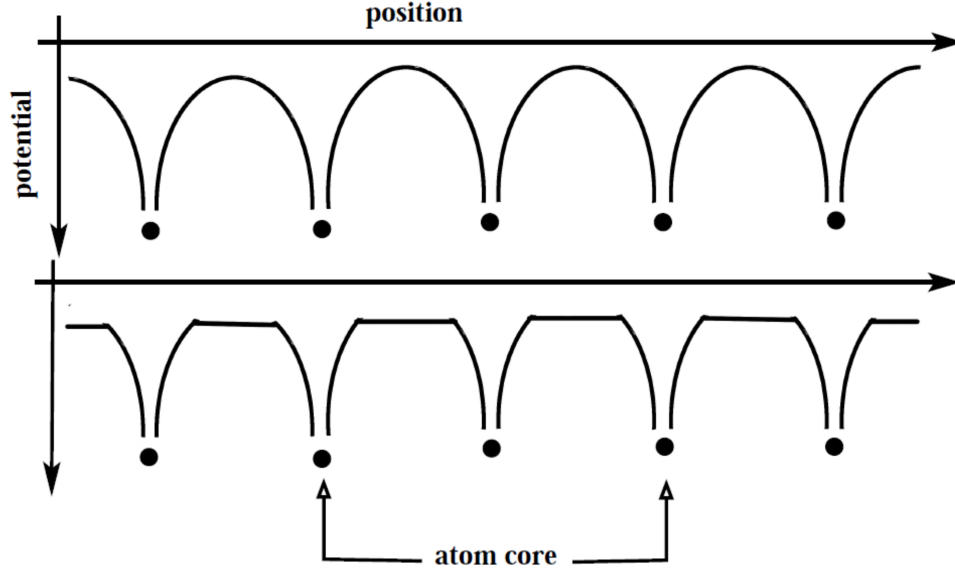


Figure 2.5: Upper panel: Schematic diagram of potential inside real crystal considered in LMTO method. Lower panel: Schematic diagram of approximated potential considered in LMTO method. In the vicinity of core atomic region potential is rapidly varying. In the interstitial region *i.e.* away from atom core region, the actual potential is approximated as a constant potential.

Within the MT sphere, the potential is spherically symmetric, hence the total wave function can be represented by radial solution of Schrödinger equation times spherical harmonics, known as partial wave, given by,

$$\phi_{RL}(\mathbf{r}_R, \epsilon) = \phi_{Rl}(r_R, \epsilon) Y_L(\hat{r}_R)$$

where L denotes the angular momentum labels (l, m) , $Y_L(\hat{r}_R)$ is the spherical harmonics functions and \hat{r}_R is the angular variables associated with the vector \hat{r}_R . $\phi_{Rl}(r_R, \epsilon)$ is the energy dependent solution of the following radial Schrödinger equation inside the muffin-tin sphere at R ,

$$\left[-\frac{\partial^2}{\partial r_R^2} + \frac{l(l+1)}{r_R^2} - v(r_R) - \epsilon \right] r_R \phi_{Rl}(r_R, \epsilon) = 0 \quad (2.37)$$

Outside the MT sphere, since potential is constant ($-v_0$), the total wave function can be written as,

$$\psi_{RL}(\mathbf{r}_R, \epsilon) = R_l(r_R, \epsilon) Y_L(\hat{r}_R)$$

The radial part ($R_l(r_R, \epsilon)$) of total wave function, is a solution of the following radial Schödinger equation,

$$\left[-\frac{\partial^2}{\partial r_R^2} + \frac{l(l+1)}{r_R^2} - \kappa^2 \right] r_R R_l(r_R, \epsilon) = 0 \quad (2.38)$$

where $\kappa^2 = \epsilon - v_0$. Solution of Eq. 2.38 can be written as combination of spherical Bessel, $j_l(\kappa r_R)$ and Neumann functions, $\eta_l(\kappa r_R)$ where they are given by,

$$j_L(\kappa \mathbf{r}_R) = j_l(\kappa r_R) Y_L(\hat{r}_R) \propto r^l$$

$$\eta_L(\kappa \mathbf{r}_R) = \eta_l(\kappa r_R) Y_L(\hat{r}_R) \propto \frac{1}{r^{l+1}}$$

The wave functions outside and inside the muffin-tin sphere must be continuous and differentiable at the muffin-tin sphere boundary S_R . In order to augment (continue) a general function f continuously and differentiable at $r = r_0$, into a linear combination of two functions f_1 and f_2 , the function f has to behave following way, as r approaching to r_0 .

$$f(r) \mapsto \frac{[f, f_2]|_{r=r_0} f_1(r) - [f, f_1]|_{r=r_0} f_2(r)}{[f_1, f_2]} \quad (2.39)$$

With this general statement, one can write the continuity condition for the radial function $\phi_{RL}(r_R, \epsilon)$ at S_R (taking $j_l(\kappa r_R)$ as f_1 and $\eta_l(\kappa r_R)$ as f_2):

$$N_{RL}(\epsilon, \kappa) \phi_{RL}(r_R, \epsilon) \mapsto \eta_l(\kappa r_R) - P_{RL}(\epsilon, \kappa) j_l(\kappa r_R) \quad (2.40)$$

Where the potential function is given by,

$$P_{RL}(\epsilon, \kappa) = \frac{[\eta_l(\kappa r_R), \phi_{RL}(r_R, \epsilon)]}{[j_l(\kappa r_R), \phi_{RL}(r_R, \epsilon)]} \Big|_{r=S_R}$$

and the normalization function is given by,

$$N_{RL}(\epsilon, \kappa) = \frac{\omega}{2} \frac{1}{[\phi_{RL}(r_R, \epsilon), j_l(\kappa r_R)]} \Big|_{r=S_R}$$

This condition sets the starting point for the definition of the muffin-tin orbitals. Now, consider an array of ion-cores, the total wave functions for the system can be expressed as linear

combination of muffin-tin orbitals, $\psi_{RL}(\mathbf{r}_R, \epsilon)$ centred at various R ,

$$\Psi(\mathbf{r}_R, \epsilon) = \sum_{RL} C_{RL}(\epsilon) \psi_{RL}(\mathbf{r}_R, \epsilon) \quad (2.41)$$

These muffin-tin orbitals can be expressed in terms of partial waves as,

$$\psi_{RL}(\mathbf{r}_R, \epsilon) = \begin{cases} N_{RL}(\epsilon, \kappa) \phi_{RL}(\mathbf{r}_R, \epsilon) + P_{RL}(\epsilon, \kappa) j_L(\mathbf{r}_R \kappa) & \text{for } r_R \leq S_R \\ \eta_L(\kappa \mathbf{r}_R) & \text{for } r_R \geq S_R \end{cases} \quad (2.42)$$

The MTO is smooth in all regions and disappears at $r \mapsto \infty$.

One can expand the envelope $\eta_L(\kappa \mathbf{r}_R)$ outside its personal sphere *i.e.* $R \neq R'$ in the following way,

$$\eta_L(\kappa \mathbf{r}_R) = - \sum_{L'} S_{RL, R' L'}^\alpha(\kappa) j_{L'}^\alpha(\kappa \mathbf{r}'_R) \quad r_R \geq S_R (R' \neq R) \quad (2.43)$$

to ensure that the linear combination of muffin-tin orbitals is a solution of the schrödinger equation. Where the coefficient $S_{RL, R' L'}^\alpha(\kappa)$ is called structure constant, can be obtained from multi-pole expansion and the superscript α represent the screening constant which control the range of MTO. So, for an array of ion-cores, MTO can be expressed as,

$$\psi_{RL}(\mathbf{r}_R, \epsilon) = \begin{cases} N_{RL}^\alpha(\epsilon, \kappa) \phi_{RL}(\mathbf{r}_R, \epsilon) + P_{RL}^\alpha(\epsilon, \kappa) j_L^\alpha(\kappa \mathbf{r}_R) & \text{for } r_R \leq S_R \\ - \sum_{L'} S_{RL, R' L'}^\alpha(\kappa) j_{L'}^\alpha(\kappa \mathbf{r}'_R) & \text{for } r_R \geq S_R (R' \neq R) \\ \eta_L^\alpha(\kappa \mathbf{r}_R) & \text{for } r_R \geq IS \end{cases} \quad (2.44)$$

Where IS is the interstitial region.

In the muffin-tin sphere centre at R , $N_{RL}^\alpha(\epsilon, \kappa) \phi_{RL}(\mathbf{r}_R, \epsilon)$ is the solution of Eq. 2.37 but since $P_{RL}^\alpha(\epsilon, \kappa) j_L^\alpha(\kappa \mathbf{r}_R)$ is not a solution of Eq. 2.37, the tail at $R' \neq R$, where the envelope $\eta_L(\mathbf{r}_R)$ is expanded, should cancel the term. This condition is called the tail cancellation theorem. This leads to the Korringa-Kohn-Rostoker(KKR) equation in the atomic sphere approximation (ASA). The KKR system of equations have a non-trivial solution when the following condition is fulfilled,

$$\det |P_{RL}^\alpha(\epsilon, \kappa) \delta_{RL, R' L'} - S_{RL, R' L'}^\alpha| = 0 \quad (2.45)$$

The structure constant $S_{RL,R'L'}^\alpha$, only depends on the crystal structure, and P_{Rl}^α is a local potential term since it depends on individual ASA sphere. The KKR-ASA secular equation has complicated non-linear energy dependence. To bypass the energy dependence of the KKR-ASA equation, following the Andersen's approach of linearisation [36], the LMTO basis function can be expressed as,

$$\chi_{RL}^\alpha(\mathbf{r}_\mathbf{R}) = \phi_{RL}(\mathbf{r}_\mathbf{R}) + \sum_{R'L'} \dot{\phi}_{R'L'}^\alpha(\mathbf{r}_{R'}) h_{RL,R'L'}^\alpha \quad (2.46)$$

The dot ($\dot{}$) represents derivative with respect to energy and the function $\dot{\phi}_{R'L'}^\alpha(\mathbf{r}_{R'})$ is the linear combination of ϕ and $\dot{\phi}$, as given by,

$$\dot{\phi}_{R'L'}^\alpha = \dot{\phi}_{R'L'} + \phi_{R'L'} O^\alpha$$

where, O^α is the non-diagonal overlap matrix. The matrix h^α is given by,

$$h^\alpha = C^\alpha - \epsilon_\nu + (\Delta^\alpha)^{1/2} S^\alpha (\Delta^\alpha)^{1/2} \quad (2.47)$$

Where, C^α and Δ^α are the diagonal potential matrices. They depend on the potential inside the muffin-tin sphere, screening parameter α and on the sphere radii. The band centre parameter C^α is given by,

$$C^\alpha = \epsilon_\nu - \frac{P_{Rl}^\alpha(\epsilon_\nu)}{\dot{P}_{Rl}^\alpha(\epsilon_\nu)}$$

and the band width is given by,

$$\sqrt{(\Delta^\alpha)} = \frac{1}{\dot{P}_{Rl}^\alpha(\epsilon_\nu)}$$

2.6.3 N^{th} order muffin-tin orbital (NMTO) downfolding method

One needs to construct low energy, few band Hamiltonian out of the full correlated Hamiltonian, to extract the single particle part of the many body Hamiltonian, namely the hopping integrals or onsite terms. This can be achieved through the downfolding technique. In this technique, the space of a full DFT basis set is considered to be separated into two subsets, lower $|l\rangle$ and higher $|h\rangle$. In this down-folding technique, the reduction of the full Hamiltonian H into lower subset Hamiltonian \hat{H}_{ll} , is carried out in such a way that lowest l eigenvalue of H and \hat{H}_{ll} are

same. Construction of the \hat{H}_{ll} introduces additional energy dependence and can be express as,

$$\hat{H}_{ll}(\epsilon) = H_{ll} - H_{lh}(H_{hh} - \epsilon)^{-1}H_{hl} \quad (2.48)$$

In LMTO method this procedure is implemented in the KKR equation and this is done via transformation of the structure matrix S^α . Additional energy dependence is taken care of by the linearisation procedure in construction of LMTO. Though, implementation of down-folding procedure in LMTO helps to overcome the problem of ghost bands, it is does not provide an accurate way to do a massive downfolding, where the downfolded bands span in a very narrow energy window. The shortcomings of LMTO method in general are given by,

- The basis is complete to $(\epsilon - \epsilon_\nu)$ (*i.e.* 1^{st} order) inside the sphere while it is only complete to $(\epsilon - \epsilon_\nu)^0 = 1$ (O^{th} order) in the interstitial, which is inconsistent. This inconsistency can be corrected by removing the interstitial region through introduction of ASA.
- Introduction of non-ASA corrections (combined correction) for the open-system, make the formalism computationally heavy and basis need to be increased by multi-panel calculations.
- The expansion of the Hamiltonian H in the orthogonal representation as a power series in the two centred tight-binding Hamiltonian h :

$$\langle \phi | H - \epsilon_\nu | \phi \rangle = h - hoh + \dots \quad (2.49)$$

is obtained only within ASA and excluding downfolding.

In order to avoid all these shortcomings a more improved and sophisticated method, based on N^{th} order muffin-tin orbital (NMTO) [43] method was introduced. This is more consistent formalism, in which one can describe the downfolded band structure with better accuracy within a chosen energy range. In this formalism interstitial region was treated accurately. In this formalism within atomic sphere where potential was approximated as a spherical, the energy dependent partial wave, $\phi_{RL}(\epsilon, r_R)$ was retained as a solution but in the interstitial region (IS), instead of Neumann function, screen spherical wave (SSW) was introduced. The screening technique that

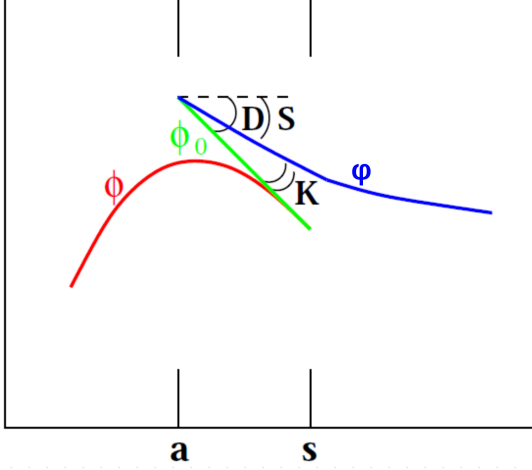


Figure 2.6: Constituents of Kink partial wave (KPW), ϕ , ϕ_0 , φ .

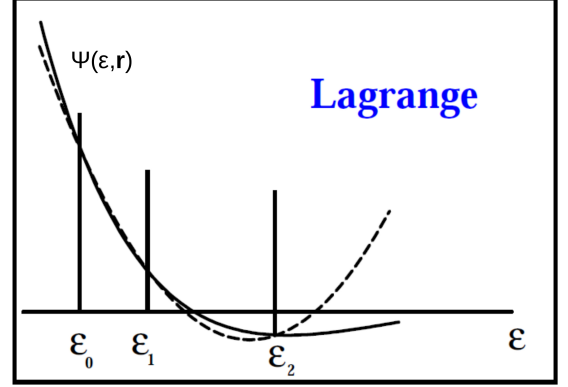


Figure 2.7: The N^{th} order approximation to the energy dependence of a partial wave for a discrete (Lagrange) mesh.

has been adopted is described briefly, as follows.

It introduces a hard sphere of radius a and a phase shifted partial wave solution $\phi_{RL}^{\alpha 0}$ (green line in Fig. 2.6), which matches the value and slope of ϕ at S_R , but their curvatures differ. At the hard sphere, $\phi_{RL}^{\alpha 0}$ is joined continuously but with a kink to the SSW, φ_{RL}^{α} , shown by blue line in Fig. 2.6. The combined form of these contribution is known as the Kink Partial Wave (KPW), which can be written as,

$$\psi_{RL}^{\alpha}(\epsilon, r_R) = [\phi_{RL}^{\alpha}(\epsilon, r_R) - \phi_{RL}^{\alpha 0}(\epsilon, r_R)]Y_L(\hat{r}_R) + \varphi_{RL}^{\alpha}(\epsilon, r_R) \quad (2.50)$$

The numbers of the NMTO basis set $\chi_{R'L'}^N$ is constructed by Lagrange interpolation of $\psi_{RL}^{\alpha}(\epsilon, r_R)$, evaluated at the energy points $\epsilon_0, \epsilon_1, \dots, \epsilon_N$ [cf. Fig. 2.7],

$$\chi_{R'L'}^{(N)} = \sum_{n=0}^N \sum_{RL \in A} \psi_{RL}^{\alpha}(\epsilon_n, r_R) L_{n,RL,R'L'}^N \quad (2.51)$$

Therefore the constructed basis set is energy selective as well as localized in nature. Due to this energy selective nature of basis set, one can select a narrow energy window from full DFT band structure more accurately. In this procedure due to the integrated out of the irrelevant orbital from full DFT Hamiltonian, one naturally needs to take into account the the re-normalization effect. This re-normalized effective few orbitals, defining the low energy Hamiltonian in the downfolded representation, serve as Wannier like orbitals. The real space representation of the

down-folded Hamiltonian in the basis of downfolded NMTO provides information of effective hopping, onsite energy of desired relevant orbitals.

2.6.4 The linearised augmented plane wave + local orbital method

Though the pseudo-potential method is extremely useful for electronic structure calculation but it may not be the primary choice if one is interested in information that is inherently contained in the region near the nucleus (for example hyperfine splitting or core level excitation). In such cases augmented plane wave (APW) basis set can be more useful. In the region far away from the nucleus, the electrons behave as more or less free particle and can be described by plane waves. But close to the nucleus, the localised electron can be described efficiently by atomic like functions. Therefore the space can be separated into two regions, like we discussed for LMTO method in the section 2.6.2. Around each atom a sphere of radius R_α is considered and such sphere is usually refereed as muffin-tin spheres (S_α). The remaining space outside the spheres is called the interstitial region (IS). One augmented plane wave (APW) used in the expansion of $\phi_{\mathbf{G}}^{\mathbf{k}}$ is defined as:

$$\phi_{\mathbf{G}}^{\mathbf{k}}(\mathbf{r}, \epsilon) = \begin{cases} \frac{1}{\sqrt{\Omega}} e^{i(\mathbf{k}+\mathbf{G})\cdot\mathbf{r}} & \text{for } \mathbf{r} \in IS \\ \sum_{l,m} A_{lm}^{\alpha,\mathbf{k}+\mathbf{G}} \varphi_l^\alpha(\mathbf{r}, \epsilon) Y_m^l(\theta', \phi') & \text{for } \mathbf{r} \in S_\alpha. \end{cases} \quad (2.52)$$

The symbols \mathbf{k} , \mathbf{G} , \mathbf{r} have their usual meaning and Ω represents the volume of the unit cell. Each atom inside the unit cell is labelled by α [cf. Fig. 2.8]. The position inside the spheres, which is given with respect to the center of each sphere is given by $\mathbf{r}' = \mathbf{r} - \mathbf{r}_\alpha$. φ_l^α , is the solution of radial schödinger equation for an isolated atom α at the energy ϵ . One can expand the plane wave in terms of spherical harmonics about the origin of the sphere of atom α in the following way,

$$\frac{1}{\sqrt{\Omega}} e^{i(\mathbf{k}+\mathbf{G})\cdot\mathbf{r}} = \frac{4\pi}{\sqrt{\Omega}} e^{i(\mathbf{k}+\mathbf{G})\cdot\mathbf{r}_\alpha} \sum_{l,m} i^l j_l(|\mathbf{k} + \mathbf{G}|, \mathbf{r}') Y_m^{l'}(\mathbf{k} + \mathbf{G}) Y_m^l(\theta', \phi') \quad (2.53)$$

where j_l is the Bessel function of order l . The wave-function $\phi_{\mathbf{G}}^{\mathbf{k}}(\mathbf{r}, \epsilon)$ is considered to be well-behaved throughout the unit cell when the plane wave outside the sphere matches the function

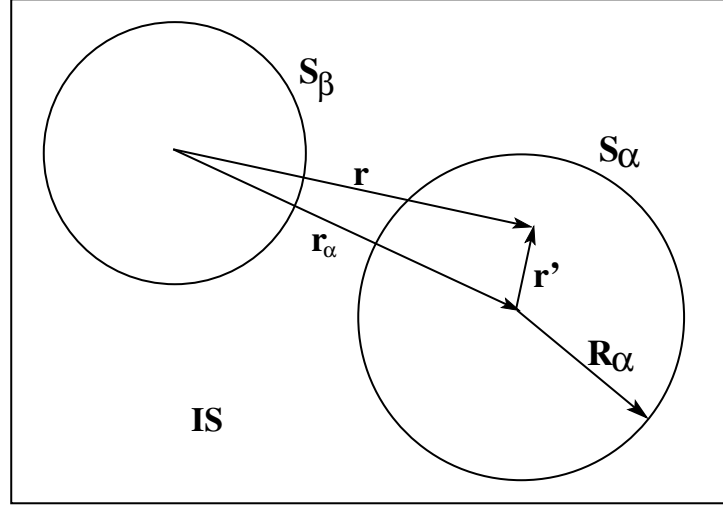


Figure 2.8: Schematic diagram showing the division of a unit cell in muffin tin regions and the interstitial region (IS) for a case of two atoms. The origin of the axis is set at centre of S_α atom.

inside the sphere over the complete surface of the sphere (in value, not in slope). With this boundary condition one can uniquely determine the coefficient $A_{lm}^{\alpha, \mathbf{k}+\mathbf{G}}$. In principle there are infinite number of terms in Eq. 2.53 and one can find infinite number of $A_{lm}^{\alpha, \mathbf{k}+\mathbf{G}}$ to create a good matching between the two functions. In practice one have to truncate at some value of l_{max} . Practically used reasonably accurate condition is $R_\alpha G_{max} = l_{max}$, where G_{max} is the cut-off for plane waves. This condition allows for a good estimation of l_{max} for a given G_{max} . Though a finite value for l_{max} does not ensure the exact matching of each APW at the sphere boundaries, but it is sufficient enough to work with. For details see the Ref. [52].

The basis set functions have non-linear complicated energy dependence, so it is difficult to solve. Following the Andersen's linearisation approach [36], the linearised version of Augmented Plane wave (LAPW) basis can be expressed as:

$$\phi_{\mathbf{G}}^{\mathbf{k}}(\mathbf{r}, \epsilon) = \begin{cases} \frac{1}{\sqrt{\Omega}} e^{i(\mathbf{k}+\mathbf{G}) \cdot \mathbf{r}} & \text{for } \mathbf{r} \in IS \\ \sum_{l,m} \left(A_{lm}^{\alpha, \mathbf{k}+\mathbf{G}} \varphi_l^\alpha(\mathbf{r}', \epsilon_\nu) + B_{lm}^{\alpha, \mathbf{k}+\mathbf{G}} \dot{\varphi}_l^\alpha(\mathbf{r}', \epsilon_\nu) \right) Y_m^l(\theta', \phi') & \text{for } \mathbf{r} \in S_\alpha \end{cases} \quad (2.54)$$

where the two coefficients $A_{lm}^{\alpha, \mathbf{k}+\mathbf{G}}$ and $B_{lm}^{\alpha, \mathbf{k}+\mathbf{G}}$ can be determined by matching the above two solutions in magnitude and slope at MT sphere boundary.

The core states, (for example $1s$ of Cu) extremely well bound to the nucleus, do not participate in the chemical bonding. So they can be treated as in the free atoms subject to the potential due to the valence states. The problem arises in order to treat the semi core states properly, which lie in between the core and valence state. For example, due to hybridization, Fe atom in bcc lattice have a non-negligible amount of $4p$ -character in its valence states that are about $0.2 Ry$ below the Fermi level. But the $3p$ -states that are $4.3 Ry$ below the Fermi level are not entirely confined in the core region. So, it is not clear how $\epsilon_{l=1}^{Fe}$ should be chosen: close to $3p$, close to $4p$, or at an intermediate value? To get rid of this problem another type of basis function can be added to the LAPW basis set, called local orbital (LO) [45] which is defined for a particular l, m and atom α . A local orbital is defined as:

$$\begin{aligned} \phi_{lm}^{\alpha(LO)}(\mathbf{r}, \epsilon) = & \sum_{l,m} [A_{lm}^{\alpha,LO} \varphi_l^{\alpha}(\mathbf{r}', \epsilon_{\nu 1,l}) + B_{lm}^{\alpha,LO} \dot{\varphi}_l^{\alpha}(\mathbf{r}', \epsilon_{\nu 1,l}) \\ & + C_{lm}^{\alpha,LO} \varphi_l^{\alpha}(\mathbf{r}', \epsilon_{\nu 2,l})] Y_m^l(\theta', \phi') \end{aligned} \quad (2.55)$$

The local orbital is zero in the interstitial region and in the muffin-tin sphere of other atoms, justifying its name as local orbital. The three coefficients $A_{lm}^{\alpha,LO}$, $B_{lm}^{\alpha,LO}$, $C_{lm}^{\alpha,LO}$ are determined by the conditions that the LO is normalized, and has zero value and zero slope at the muffin tin boundary *i.e.* it does not leak out of the muffin tin sphere. $\epsilon_{\nu 1,l}^{\alpha}$ is the linearisation energy value suitable for the state with higher l value among the two valence state and the lower valence state which is much more free-atom like, is sharply peaked at an energy $\epsilon_{\nu 2,l}^{\alpha}$. Though adding the local orbitals slightly increases the LAPW basis set size, hence the computational time, still they are always used due to the fact that local orbitals offer much better accuracy. The LAPW based computer code that has been used extensively in present study, is WIEN2k [46].

2.6.5 The Projector-Augmented-Wave method

In the 1994 P. E. Blöchl [37] introduced the projector-augmented wave (PAW) method to achieve simultaneously the computational efficiency of the pseudopotential method as well as the accuracy of the full-potential linearised augmented-plane-wave (FLAPW) method. Due to the combination of these unique features, this method is computationally elegant and accurate for electronic structure calculations. In the PAW approach, the all-electron (AE) valence wave func-

tion Ψ_n is reconstructed from the pseudo (*ps*) wave functions by means of a linear transformation and can be expressed as following way:

$$|\Psi_n^{AE}\rangle = |\Psi_n^{ps}\rangle + \sum_a \sum_i (|\phi_{i,a}^{AE}\rangle - |\phi_{i,a}^{ps}\rangle) \langle p_i^{ps} | \Psi_n^{ps} \rangle \quad (2.56)$$

The first term, $|\Psi_n^{ps}\rangle$ (n is the band index) at the right-hand side of Eq. 2.56 is the pseudo wave function which is variational quantities and is expanded in plane waves. This pseudo function is identical to the all-electron single-particle Kohn-Sham wave function, except inside the augmentation spheres, a . The remaining terms at the right hand side of Eq. 2.56 is the difference between AE partial wave and *ps* partial wave. The index i is shorthand for the reference energy, the angular momentum quantum numbers, and the atomic coordinates R_i . In the PAW approach the relation between the all-electron and pseudo wave function can be expressed via transformation operators τ^a , given as,

$$|\Psi_i^{AE}\rangle = \left(1 + \sum_a \tau^a \right) |\Psi_i^{ps}\rangle \quad (2.57)$$

How these operators will look like, is fully determined by the choice of the three terms as defined in the Eq. 2.56.

1. **All-electron partial wave $\phi_{i,a}^{AE}$:** These are basis functions in which the all-electron wave function can be expanded. As this expansion only be needed within the augmentation spheres, a , the radial solutions of the Schrödinger equation for the free atom can be chosen as basis function. The pseudo partial waves $\phi_{i,a}^{ps}$ can be constructed from the all-electron partial waves via same transformation operator τ^a

$$|\phi_{i,a}^{ps}\rangle = (1 + \tau^a) |\phi_{i,a}^{AE}\rangle \quad (2.58)$$

As *ps* partial wave is due to specific atom, there is no sum over atoms. So form the Eq. 2.58 the transformation operator τ^a can be defined as,

$$\tau^a |\phi_{i,a}^{ps}\rangle = (\phi_{i,a}^{AE} - \phi_{i,a}^{ps})$$

One can see that the action of τ^a is fully defined as soon as the all-electron partial waves and pseudo partial waves are chosen. For the pseudo partial waves a different choice is made inside and outside the augmentation spheres:

2. **Pseudo partial waves $\phi_{i,a}^{ps}$ (outside augmentation spheres):** The pseudo partial waves are chosen to be identical to the all-electron partial waves outside the augmentation spheres.
3. **Projector functions $p_{i,a}^{ps}$ (pseudo partial waves inside augmentation spheres):** With the help of projector operator, the pseudo partial wave can be chosen in such a way that they form a basis for the pseudo wave function within the augmentation sphere *i.e.*

$$|\Phi_n^{ps}\rangle = \sum_i C_{ni}^a |\phi_{i,a}^{ps}\rangle$$

Also Ψ_n^{AE} can be expanded in the $\phi_{i,a}^{AE}$ by exactly the same coefficients C_{ni}^a . If one choose a set of projector functions such that they are orthonormal to the pseudo partialwave *i.e.* $\langle p_{i,a}^{ps} | \phi_{j,a}^{ps} \rangle = \delta_{ij}$, then the coefficients C_{ni}^a turn out to be the dot product between the projector function and the pseudo wave function, *i.e.*

$$\langle p_{i,a}^{ps} | \Psi_n^{ps} \rangle = C_{ni}^a$$

Eq. 2.56 can be explicitly written down with these three specified ingredients. Re-arranging the Eq. 2.56 one can write as following:

$$\begin{aligned} |\Psi_n^{AE}\rangle &= |\Psi_n^{ps}\rangle + \sum_a \left(\sum_i \langle p_{i,a}^{ps} | \Psi_n^{ps} \rangle |\phi_{i,a}^{AE}\rangle \right) - \sum_a \left(\sum_i \langle p_{i,a}^{ps} | \Psi_n^{ps} \rangle |\phi_{i,a}^{ps}\rangle \right) \\ &= |\Psi_n^{ps}\rangle + \sum_a \Psi_{n,a}^{AE} - \sum_a \Psi_{n,a}^{ps} \end{aligned} \quad (2.59)$$

The all-electron single-particle Kohn-Sham wave function $|\Psi_n^{AE}\rangle$ can be written as the sum of a pseudo wave function $|\Psi_n^{ps}\rangle$ that is smooth everywhere, to which is added a steep function $|\Psi_{n,a}^{AE}\rangle$ that is defined only within each augmentation sphere, and from which is smooth part, $|\Psi_{n,a}^{ps}\rangle$ subtracted only within the spheres. For details see the Ref. [52]. We have used extensively the PAW method, as implemented in VASP [39–41].

2.7 Many body technique

The conventional DFT approach is based on single particle approximation, where electron-electron correlation is treated in the mean field manner within local density approximation. Sometimes strong electron-electron correlation effect is very important in describing the system properties. This electron-electron correlation effect can be taken into account in an improved way by the many body model Hamiltonian approach. One-band Hubbard model [53], which has been already mentioned (see Eq. 1.5) in section 1.1 of introductory chapter 1, was originally introduced in order to model electronic correlation in narrow energy bands. In the Hubbard model, four configurations are possible at each site, such as singly occupied by one electron with spin up or down, doubly occupied site by two electron with opposite spin or empty. Last two configurations lead to charge fluctuation. In the limit of $t/U \ll 1$, ground state to be chose in such that it minimized the interaction energy. Eliminating fluctuations (double occupancies) in strong U limit, leads to an effective model, called t - J model, which conserves the double occupancies and holes. t - J model represents a generic model for the interplay of spin and charge degrees of freedom. In the limit of half-filled lattice *i.e.* one electron per site ($n=1$) and a large U limit, this effective t - J model reduces to effective Heisenberg Hamiltonian,

$$H_{eff} = J \sum_{\langle ij \rangle} S_i \cdot S_j \quad (2.60)$$

where, exchange term $J = \frac{2t^2}{U}$, S_i is the spin operator at site i , and other symbols have their usual meaning. It describes the situation where charge degrees of freedom are bound to atomic position and only spin degrees of freedom remain active. In this thesis, to solve the DFT derived Heisenberg spin-model Hamiltonian, many body technique like stochastic series expansion technique of quantum Monte Carlo method has been used, as discussed below.

2.7.1 Stochastic series expansion of quantum Monte Carlo method

One can calculate the expectation value of some operator A at temperature T for some model Hamiltonian H , with the following expression,

$$\langle A \rangle = \frac{1}{Z} \text{Tr}[A \exp(-\beta H)], \quad (2.61)$$

where β is the inverse temperature ($\beta = \frac{1}{k_B T}$) and Z is the partition function written as, $Z = \text{Tr}[\exp(-\beta H)]$. This partition function Z is the central quantity to be sampled in the Quantum Monte Carlo (QMC) simulation. In the stochastic series expansion (SSE) method [54–56] of QMC, Z can be expressed as;

$$Z = \sum_{\alpha} \sum_{n=0}^{\infty} \frac{\beta^n}{n!} \langle \alpha | (-H)^n | \alpha \rangle \quad (2.62)$$

where exponential part is taken care of by the Taylor series expansion and the trace is expressed as sum over a complete set of states in a suitable basis α . Hamiltonian can be written as,

$$H = - \sum_{a,b} H_{a,b}$$

where indices a refer to operator class *i.e.* diagonal for $a=1$ and off-diagonal for $a=2$ in the chosen basis and b is the bond connecting a pair of interacting lattice sites $i(b), j(b)$. One can write power of the Hamiltonian as a sum over all possible product (string) of the operator H_{ab} ;

$$(-H)^n = \sum_{H_{ab}} \prod_{p=1}^n H_{a(p),b(p)}$$

In practice the Taylor expansion should be truncated at some cut-off value, let's say L . Introducing the unit operator $H_{0,0} = 1$ which is used to augment all strings with $L > n$ and allowing the all possible placements of unit operator in strings the partition function (Z) can be written as

$$Z = \sum_{\alpha} \sum_{S_L} \frac{\beta^n (L-n)!}{L!} \langle \alpha | \prod_{p=1}^{p=L} |H_{a(p),b(p)}| \alpha \rangle \quad (2.63)$$

where S_L denotes a sequence of operator indices; $S_L = [a_1, b_1], [a_2, b_2], \dots, [a_L, b_L]$. In the quantum Monte Carlo simulation, the SSE terms $\{\alpha, S_L\}$ are sampled according to the weight in the above partition function summation. Let us consider two configuration $\{\alpha, S_L\}$ and $\{\alpha', S'_L\}$ for which there is an update (with finite weight $W(\alpha, S_L)$) that can change them into each other. If the probability of selecting $\{\alpha', S'_L\}$ when this is in $\{\alpha, S_L\}$ is not the same as selecting $\{\alpha, S_L\}$ when this is in $\{\alpha', S'_L\}$, one can write the acceptance probability using the detailed balance condition as following,

$$P_{accept}[\{\alpha, S_L\} \rightarrow \{\alpha', S'_L\}] = \min \left[\frac{W(\alpha', S'_L)P_{select}(\alpha', S'_L \rightarrow \alpha, S_L)}{W(\alpha, S_L)P_{select}(\alpha, S_L \rightarrow \alpha', S'_L)}, 1 \right] \quad (2.64)$$

Selection probability (P_{select}) is not always the same when updating an SSE configuration, in contrast to classical Monte Carlo simulation where P_{select} is always same with $1/N$. We use the "operator loop update" scheme, as proposed by Sandvik [54], which consist of two steps:

- (i) Local update of single diagonal operator, $[0,0] \leftrightarrow [1,b]_p$
- (ii) Change the operator type, diagonal to off-diagonal, for any number of diagonal and off-diagonal operators, $[1,b]_{p_1}, [1,b]_{p_2}, \dots, [1,b]_{p_m} \leftrightarrow [2,b]_{p_1}, [2,b]_{p_2}, \dots, [2,b]_{p_m}$

Details on the "operator loop update" technique can be found in the Ref. [54–56].

Bibliography

- [1] B. H. Bransden and C. J. Joachain, *Physics of Atom and Molecules* 2nd Edn., Pearson Education (2003).
- [2] N. W. Ashcroft and N. D. Mermin, *Solid State Physics* (Thomson Learning, Toronto, 1976).
- [3] M. Born and J. R. Oppenheimer, *Ann. Physik* 84, 457 (1927).
- [4] D. R. Hartree, *Mathematical Proceedings of the Cambridge Philosophical Society* 24, 426-437 (1928).
- [5] V. Fock, *Z. Phys.* 61 (1930).
- [6] C. D. Sherrill and H. F. S. III, "The Configuration Interaction Method: Advances in Highly Correlated Approaches," in *The Configuration Interaction Method: Advances in Highly Correlated Approaches*, Vol. 34 of *Advances in Quantum Chemistry*, M. C. Z. Per-Olov Lowdin, John R. Sabin and E. Brandas, eds., (Academic Press, 1999), pp. 143-269.
- [7] P. Hohenberg and W. Kohn, *Phys. Rev.* 136, B864-B871 (1964).
- [8] W. Kohn and L. J. Sham, *Phys. Rev.* 140, A1133-A1138 (1965).
- [9] R. M. Dreizler and E. K. U. Gross, *Density Functional Theory* (Springer, Berlin, 1990).
- [10] L. H. Thomas (1927). "The calculation of atomic fields". *Proc. Cambridge Phil. Soc.* 23 (5): 542548.
- [11] E. Fermi "Un Metodo Statistico per la Determinazione di alcune Priopriet dell'Atomo". *Rend. Accad. Naz. Lincei* 6: 602607 (1927).

-
- [12] N. H. Harrison, An Introduction to Density Functional Theory.
- [13] P. A. M. Dirac The Quantum Theory of the Electron, Proceedings of the Royal Society A : Mathematical, Physical and Engineering Sciences 117(778), 610(1928).
- [14] D. M. Ceperley and B.J. Alder, Phys. Rev. Lett. 45, 566 (1980).
- [15] J. P. Perdew and A. Zunger, Phys. Rev. B 23, 5048 (1981).
- [16] J. P. Perdew, Y. Wang, Phys. Rev. B, 45, 13244 (1992).
- [17] R. O. Jones and O. Gunnarsson. The density functional formalism, its applications and prospects, Rev. Mod. Phys. 61, 689 (1989).
- [18] J. P. Perdew, in Electronic Structure of Solids 91, edited by P. Ziesche and H. Eschrig (Akademie Verlag, Berlin, 1991), p. 11.
- [19] J. P. Perdew, K. Burke and M. Ernzerhof, Phys. Rev. Lett. 77, 3865 (1996).
- [20] Y. Umeno, B. Meyer, C. Elsasser, and P. Gumbsch, Phys. Rev. B 74, 060101(R) (2006).
- [21] V. I. Anisimov, J. Zaanen and O. K. Andersen, Phys. Rev. B 44, 943 (1991).
- [22] V. I. Anisimov *et al.* Phys. Rev. B 48, 16929 (1993).
- [23] A. I. Liechtenstein, V. I. Anisimov, and J. Zaanen, Phys. Rev. B 52, R5467 (1995).
- [24] B. R. Judd 1963 Operator Techniques in Atomic Spectroscopy (New York: McGraw- Hill).
- [25] S. L. Dudarev, G. A. Botton, S. Y. Savrasov, C. J. Humphreys and A. P. Sutton, Phys. Rev. B 57, 1505 (1998).
- [26] O. Gunnarsson, O. K. Andersen, O. Jepsen, and J. Zaanen, Phys. Rev. B 39, 1708 (1989); O. Gunnarsson, *ibid.* 41, 514 (1990); V. I. Anisimov and O. Gunnarsson, *ibid.* 43, 7570 (1991).
- [27] J. Kunes, V. I. Anisimov, A. V. Lukoyanov, and D. Vollhardt, Phys. Rev. B 75, 165115 (2007).
- [28] M. Springer and F. Aryasetiawan, Phys. Rev. B 57, 4364 (1998).

- [29] T. Kotani, *J. Phys: Condens. Matter* 12, 2413 (2000).
- [30] F. Aryasetiawan, K. Karlsson, O. Jepsen, and U. Schönberger, *Phys. Rev. B* 74, 125106 (2006).
- [31] J. C. Slater and G. F. Koster, *Phys. Rev.* 94, 1498-1524 (1954).
- [32] J. C. Phillips and L. Kleinman, *Phys. Rev.* 116, 287-294 (1959).
- [33] E. Wigner and F. Seitz, *Phys. Rev.* 46, 509-524 (1934).
- [34] T. L. Loucks, *Augmented plane wave method* (W.A. Benjamin, New York, 1967).
- [35] J. Koringa, *Physica* 13, 392 (1947); J. Koringa, *Phys. Rev.* 238, 341 (1994).
- [36] O. K. Andersen, *Phys. Rev. B* 12, 3060 (1975), and *The Electronic Structure of Complex Systems* (Plenum, New York, 1984); H. L. Skriver, *The LMTO Method* (Springer, New York, 1984).
- [37] P. E. Blöchl, *Phys. Rev. B* 50, 17953 (1994).
- [38] G. Kresse and D. Joubert, *Phys. Rev. B* 59, 1758 (1999).
- [39] G. Kresse and J. Hafner, *Phys. Rev. B* 47, 558 (1993).
- [40] G. Kresse and J. Hafner, *Phys. Rev. B* 49, 14251 (1994).
- [41] G. Kresse and J. Furthmüller, *Phys. Rev. B* 54, 11169 (1996).
- [42] O. K. Andersen and O. Jepsen, *Phys. Rev. Lett.* 53, 2571-2574 (1984).
- [43] O. K. Andersen and T. Saha-Dasgupta, *Phys. Rev. B* 62, R16219-R16222 (2000).
- [44] O. Jepsen, J. Madsen, and O. K. Andersen, *Phys. Rev. B* 18, 605-615 (1978).
- [45] D. Singh, *Phys. Rev. B* 43, 6388-6392 (1991).
- [46] P. Blaha, K. Schwarz, G. K. H. Masden, D. Kvasnicka, and J. Luitz, in *Wien2k, An Augmented PlaneWave+Local Orbitals Program for Calculating Crystal Properties*, edited by K. Schwarz (Technische Universitat Wien, Vienna, 2001).

-
- [47] W. C. Herring, Phys. Rev. 57, 1169 (1940); W. C. Herring and A. G. Hill, Phys. Rev. 58, 132 (1940).
- [48] J. C. Phillips and L. Kleinman, Phys. Rev. 116, 287 (1959).
- [49] D.R. Hamann, M. Schluter and C. Chiang, Phys. Rev. Lett. 43, 1494 (1979).
- [50] D. Vanderbilt, Phys. Rev. B 41, 7892 (1985).
- [51] P. Giannozzi, *et al.*, J. Phys.: Condens. Matter, 21, 395502 (2009).
- [52] S. Cottenier, ISBN 978-90-807215-1-7, (*2nd* edition), (2002-2013).
- [53] J. Hubbard, (1963). "Electron Correlations in Narrow Energy Bands". Proceedings of the Royal Society of London. 276 (1365): 238-257.
- [54] A. W. Sandvik, Phys. Rev. B 59, R14157 (1999).
- [55] A. Dorneich and M. Troyer, Phys. Rev. E 64, 066701 (2001).
- [56] K. Louis and C. Gros, Phys. Rev. B 70, 100410(R) (2004).

Chapter 3

Magnetic modeling and effect of biaxial strain on the Haldane chain compound $\text{SrNi}_2\text{V}_2\text{O}_8^\dagger$

3.1 Introduction and motivation

Low dimensional quantum spin systems (QSS) form an active field of research in condensed matter physics [1, 2], as they demonstrate surprisingly rich physics, dominated by quantum fluctuation effects. Different aspects of low dimensional quantum spin systems and possible origin of spin-gap in their excitation spectrum have been already discussed in the section 1.2.1 of chapter 1. In the context of low dimensional spin-gapped quantum systems, the spin $S = 1$ Heisenberg antiferromagnetic (HAFM) chains, also famously known as Haldane chain, is a special class of quantum magnets which are of current research interest due to their novel magnetic properties [3, 4]. Haldane based on his analysis of nonlinear σ model mapping of large spin (S) HAFM Hamiltonian in 1D, conjectured that [5, 6], ground state of 1D antiferromagnetic

[†] This chapter is based on publication, Kartik Samanta, Satyaki Kar and T. Saha-Dasgupta, Phys. Rev. B 93, 224404 (2016).

integer spin chains, have a unique ground state and gapped magnon ($S=1$) excitation with a large energy gap (Haldane gap) between ground and triplet excited state. This is in marked contrast with $S = 1/2$ Heisenberg antiferromagnetic chains which exhibit a gapless continuum of spinon with algebraic decay of spin-spin correlation [7, 8].

For spin-gapped systems, applied magnetic field which serves as chemical potential splits the triplet states due to the Zeeman effect [9–11] and one of the triplet states is driven to the ground state when applied magnetic field crosses a critical value H_c . At this critical field, the Zeeman splitting closes the spin gap causing a phase transition from a nonmagnetic spin-singlet to a magnetically ordered state. Thus, attention has been paid to the field induced magnetic transition in spin-gapped systems, specially Haldane chain compounds [12], which by conjecture are expected to exhibit spin-gap behavior [13]. The original conjecture of Haldane considered strictly 1D, HAFM chain, but real compounds show finite interchain interaction as well as finite single-ion anisotropy. With anisotropy, the triplet state splits into a singlet and a doublet and as a result two separate gaps are produced [14]. It gets further split to three branches with applied magnetic field. A theoretical work by Sakai and Takahashi [15] predicted a complete phase diagram in D - J' space for the ground state of Haldane chain systems, where D is the single-ion anisotropy and J' is the ratio of interchain (J_\perp) to nearest-neighbour (NN) intrachain interactions (J_1). Their predicted phase diagram suggests that phase transition from a spin-gapped solution with a nonmagnetic spin singlet ground state to a three-dimensionally ordered AFM state is achievable beyond the critical value of single-ion anisotropy, and/or interchain interaction. Thus, presence of non negligible single-ion anisotropy, D and interchain interaction in real Haldane chain compound, can even suppress the Haldane gap and significantly modify the nature of magnetic field induced transition. In this respect, one can expect that external perturbation like biaxial strain applied on Haldane chain compounds can influence the values of D and J_1 , J_\perp , thereby tuning the magnetic field induced transition.

In this present study, we considered experimentally reported $S=1$, Haldane chain compound, $\text{SrNi}_2\text{V}_2\text{O}_8$, which is of special interest due to the presence of substantial interchain interactions and single-ion anisotropy, D [16]. Static magnetic susceptibility, inelastic neutron scattering, as well as high-field magnetization measurements were carried out on a single crystal of $\text{SrNi}_2\text{V}_2\text{O}_8$ [17] to investigate the magnetic properties. Concerning the nature of the magnetic ground

state of $\text{SrNi}_2\text{V}_2\text{O}_8$, contradictory reports [16, 18, 19] exist in the literature. However, neutron scattering measurement on the single-crystal [17], confirmed that the ground state of $\text{SrNi}_2\text{V}_2\text{O}_8$ to be a non-magnetic spin singlet, with a gap between singlet and triplet excited states. From the high field magnetization measurement, the critical field H_c for the magnetic transition from the non-magnetic singlet ground state to magnetic state was observed to be smaller compared to the $0.41J_1$, the value corresponding to an ideal 1D Haldane chain compound [20, 21]. It was argued that the finite interchain interactions together with finite single-ion anisotropy cause this reduction of Haldane gap value.

Thus, in order to understand the nature of complex interchain interactions and single ion anisotropy in the $S=1$, Haldane chain compound $\text{SrNi}_2\text{V}_2\text{O}_8$, we carried out DFT based first principles calculations. We derived a microscopic spin model for this compound, from parameter free ab initio calculations and computed thermodynamic properties like static susceptibility and high field magnetization by Quantum Monte Carlo (QMC) technique to investigate the individual role of complex interchain interactions and single ion anisotropy in reducing the Haldane gap value, as well as in determining the magnetic properties. The goodness of ab initio derived spin model has been cross checked by comparing computed data with available experimental data. With a motivation of external tuning of the ground-state magnetic properties of this $S=1$, Haldane chain compound, $\text{SrNi}_2\text{V}_2\text{O}_8$, we also studied the effects of both compressive as well as tensile biaxial strain, applied perpendicular to the chain direction and computed thermodynamic properties by QMC technique. The application of biaxial strain was found to modify the spin gap properties significantly opening up the possibility of strain induced engineering of magnetic properties of the compound.

3.2 Results and discussion

3.2.1 Crystal structure

$\text{SrNi}_2\text{V}_2\text{O}_8$ crystallizes in the tetragonal space group of $I4_1cd$, with lattice constants, $a = 12.16 \text{ \AA}$ and $c = 8.32 \text{ \AA}$ [22]. Sr atoms occupy the 8a Wyckoff positions while Ni, V, and O atoms occupy the 16b Wyckoff positions. The basic structural units of this compound, are VO_4 tetrahedra and edge-shared NiO_6 octahedra. The NiO_6 (VO_4) units show a small distortion, both in Ni-O (V-O) bond lengths and O-Ni-O (O-V-O) bond angles, deviating slightly from ideal octahedral (tetrahedral) structure. The edge-shared NiO_6 (Ni^{2+} ; $3d^8$, $S=1$) octahedrons form spin chains along c axis and these screw chains are connected each other by non-magnetic VO_4 (V^{5+} ; $3d^0$, $S=0$) tetrahedra [cf. Fig. 3.1(a)]. One unit cell of $\text{SrNi}_2\text{V}_2\text{O}_8$ contains four screw chains which are centred around $(1/4, 1/4)$, $(1/4, 3/4)$, $(3/4, 1/4)$, and $(3/4, 3/4)$ in the ab plane [cf. Fig. 3.1(b)]. Each of these screw chains is fourfold and contains four Ni ions along the c axis within one unit cell. The two diagonal chains rotate clockwise, while the other two chains rotate counter-clockwise when propagating along the c axis which provides multiple interchain interactions.

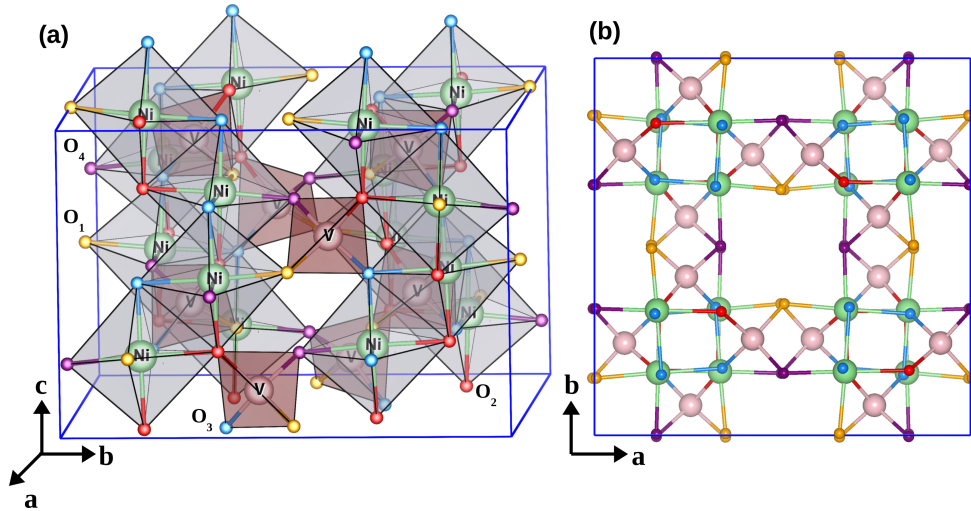


Figure 3.1: (a) Crystal structure of $\text{SrNi}_2\text{V}_2\text{O}_8$, showing the three-dimensional network. Various atoms including the inequivalent oxygens are marked. Sr atoms are not shown for clarity. (b) Projection of the crystal structure onto the ab plane, showing the four screw chains. For clarity only the atoms and bonds are shown without polyhedra.

Since the atomic positions of light atoms are often not well characterized by X-ray diffraction, we carried out structural optimization relaxing the internal positions of all atoms and keeping the lattice constant fixed at experimentally measured values [22]. Experimental measured atomic positions and optimized atomic positions are listed in Table 3.1. After structural optimization various bond length and bond angles are found to change by less than a percentage. All the results reported in this chapter are based on the theoretically optimized structure.

Table 3.1: The theoretically optimized atomic positions compared to the experimentally determined data. During the optimization the parameters of the tetragonal ($I4_1cd$) unit cell is kept fixed at the experimentally measured value, $a=12.16 \text{ \AA}$ and $c=8.32 \text{ \AA}$.

Atom	Site	Measured position			Optimized position		
		x	y	z	x	y	z
Sr	8a	0.0000	0.0000	0.0000	0.0000	0.0000	0.0000
Ni	16b	0.3315	0.3326	0.2261	0.3310	0.3337	0.2316
V	16b	0.2571	0.0798	0.0966	0.2555	0.0796	0.1046
O1	16b	0.1587	0.4964	0.0134	0.1515	0.4953	0.0055
O2	16b	0.3470	0.6712	0.4909	0.3369	0.6721	0.4950
O3	16b	0.1639	0.6768	0.7259	0.1605	0.6777	0.7174
O4	16b	0.3289	0.5026	0.2099	0.3355	0.4966	0.2077

For, 2% biaxial compressive and tensile strained compounds, the atomic coordinates as well as the out-of-plane lattice constant were completely relaxed. The structural optimization calculations were carried out using the plane wave basis with projector-augmented wave (PAW) potentials, as implemented in VASP. During the structural optimization of the strained compounds, keeping the symmetry of the crystal unchanged, atomic positions of the structures as well as the out of plane lattice were relaxed completely towards equilibrium until the Hellman-Feynman forces became less than 0.001 eV/\AA . We considered the exchange correlation functional to be that of generalized gradient approximation (GGA), implemented following the Perdew-Burke-Ernzerhof (PBE) prescription. The optimized structural data for the 2% compressive and tensile strained compounds, are listed in Table 3.2. Selected bond lengths and bond angles for optimized unstrained and strained compounds of $\text{SrNi}_2\text{V}_2\text{O}_8$ are listed in Table 3.3. From Table 3.3, we find that upon application of 2% tensile strain, the volume of the NiO_6 octahedra gets expanded by an amount of 7%, and contracted slightly upon application of compressive strain by an amount of 0.7%. This expansion of average Ni-O bond length upon application of tensile strain has important effects on the nearest-neighbour intrachain Ni-Ni interaction, which will be

Table 3.2: Theoretically optimized crystal structure of 2% biaxially strained $\text{SrNi}_2\text{V}_2\text{O}_8$. During the optimization tetragonal ($I4_1cd$) symmetry of the unit cell is kept fixed. Lattice constant for 2% tensile and compressive strain, are $a=12.40 \text{ \AA}$, $c=8.21 \text{ \AA}$ and $a=11.92 \text{ \AA}$, $c=8.41 \text{ \AA}$ respectively.

Atom	Site	2% tensile strain			2% compressive strain		
		x	y	z	x	y	z
Sr	8a	0.0000	0.0000	0.0147	0.0000	0.0000	0.0062
Ni	16b	0.3299	0.3336	0.2311	0.3314	0.3352	0.2315
V	16b	0.2588	0.0792	0.1024	0.2588	0.0825	0.1028
O1	16b	0.1477	0.4948	0.0104	0.1471	0.4970	0.0041
O2	16b	0.3389	0.6713	0.4902	0.3364	0.6640	0.4901
O3	16b	0.1582	0.6812	0.7199	0.1596	0.6738	0.7208
O4	16b	0.3300	0.4961	0.2013	0.3305	0.4999	0.2104

Table 3.3: Selected bond lengths and bond angles for optimised unstrained as well as 2% biaxially strain applied compounds.

	optimized structure	2% tensile strain	2% compressive strain
Ni-O distance (\AA)			
Ni-O1	2.016	2.073	1.994
Ni-O2	1.972	2.009	2.011
Ni-O2	2.078	2.141	2.047
Ni-O3	1.967	1.995	1.994
Ni-O3	2.080	2.140	2.052
Ni-O4	1.992	2.032	1.971
avg. Ni-O distance (\AA)	2.017	2.065	2.011
Volume of NiO_6 (\AA^3)	10.87	11.65	10.80
V-O distance (\AA)			
V-O1	1.735	1.740	1.724
V-O2	1.782	1.761	1.756
V-O3	1.780	1.761	1.754
V-O4	1.726	1.719	1.704
avg. V-O distance (\AA)	1.755	1.745	1.735
Volume of VO_4 (\AA^3)	2.77	2.71	2.66
$\angle\text{Ni-O1-V}$	125.07^0	124.79^0	124.15^0
$\angle\text{Ni-O2-V}$	133.92^0	134.20^0	131.59^0
$\angle\text{Ni-O3-V}$	133.51^0	133.61^0	131.29^0
$\angle\text{Ni-O4-V}$	127.83^0	130.75^0	128.73^0

discussed later. On the other hand, the volume of the VO_4 octahedra is found to be contracted by application of both tensile and compressive strain by 2-4%. The distortions of NiO_6 and VO_4 octahedra are found to be not much effected by the strain. Application of compressive strain affects the zigzagness of the Ni chain, changing the $\angle\text{Ni1-Ni2-Ni3}$ by 1^0 compared to that of

the unstrained structure, where Ni1, Ni2, and Ni3 are three consecutive Ni atoms in the chain. Also the $\angle\text{Ni-O-V}$ gets reduced by $2\text{-}3^\circ$ compared to that of the unstrained structure. This helps to modulate the strength of the next-nearest-neighbour intrachain Ni-Ni interaction, will be discussed later. On the other hand, corresponding changes are found to be minimal for tensile strain.

3.2.2 Electronic structure of $\text{SrNi}_2\text{V}_2\text{O}_8$

In Fig. 3.2, we show the spin-polarized GGA density of states (DOS) of atomic optimized structure of $\text{SrNi}_2\text{V}_2\text{O}_8$, computed using full potential linearised augmented plane wave (FLAPW) as implemented in the Wien2k code. For the self-consistent calculation in LAPW, we used 164

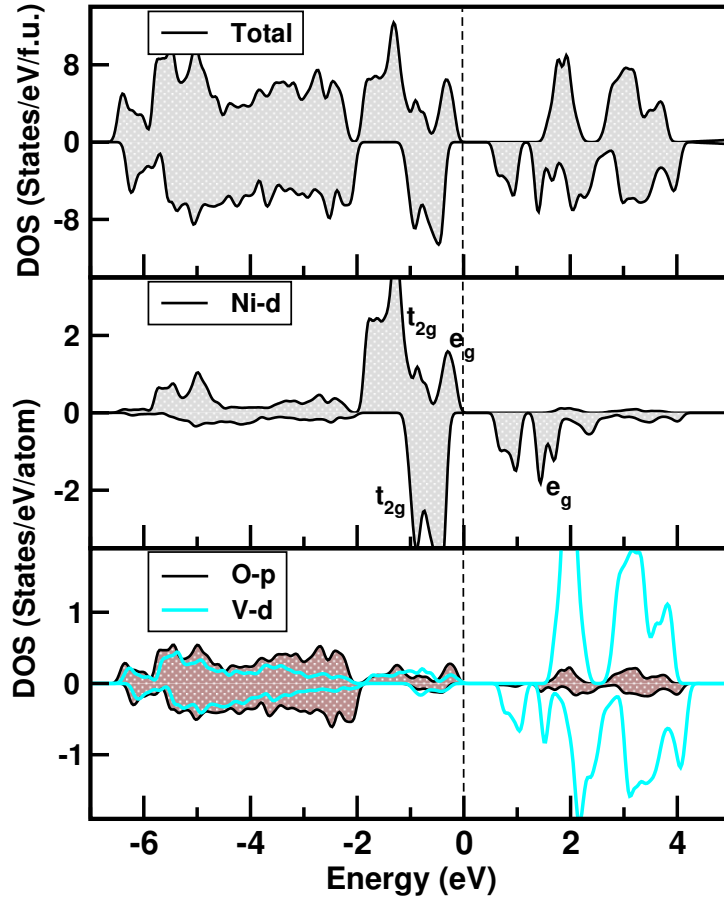


Figure 3.2: GGA spin-polarized total and partial density of states of $\text{SrNi}_2\text{V}_2\text{O}_8$, as obtained from FLAPW calculation. The zero of the energy is set at GGA Fermi energy. Top panel shows the total density of states, while the middle and bottom panels show density of states projected to Ni d (black shaded area), V d (cyan solid line), and O p (black shaded area) states.

k-points in the irreducible part of Brillouin zone. The wave functions were expanded in plane waves with a cut-off $R_{MT}k_{max} = 7.0$, where R_{MT} is the smallest muffin-tin sphere radius and k_{max} is the magnitude of the largest k vector in the plane wave expansion.

We find ground state to be insulating in nature within the GGA scheme of calculation. Repeating the calculation within GGA +U scheme of calculation, it is found that the basic electronic structure remains unchanged between GGA and GGA+U calculations, only the value of the insulating gap increases with increasing value of U, as expected. The GGA density of states, projected onto Ni d , V d and O p states, are shown in the middle and bottom panels of Fig. 3.2. As is evident from the projected DOS, the states close to Fermi level (E_F) are dominated by Ni d states. Ni is in octahedral environment of oxygen ions. Within the crystal field of octahedral, Ni d levels split into approximately degenerate t_{2g} and e_g states. The octahedral crystal-field-split Ni t_{2g} states are completely filled in both spin channels, while Ni e_g states are completely filled in the majority spin channel and empty in the minority spin channel, in conformity with the nominal valence of Ni²⁺ (d^8 ; S=1). Ni d states show some finite mixing with the O p states, which is expected. But the presence of V d character in the energy range of Ni d dominated states, is interesting and unexpected, as V⁵⁺ is in d^0 configuration. This indicates to finite mixing between V d and Ni d states which has an important implication in defining the Ni-Ni exchange paths, will be discussed later, in the context of Wannier function plots. Table 3.4 shows the computed magnetic moments within GGA and GGA+U scheme of calculation, with choice of $U(\text{Ni}) = 7$ eV and $J_H = 0.8$ eV. From the constraint DFT calculations [23], we estimated value of Hubbard U for the SrNi₂V₂O₈ compound. We find net moment per Ni atom

Table 3.4: Calculated GGA and GGA+U magnetic moments (in μ_B)

Site	GGA	GGA+U
Ni	1.508	1.647
V	0.130	0.108
O1	0.054	0.035
O2	0.080	0.047
O3	0.081	0.046
O4	0.054	0.031
Total/Ni	2.00	2.00

in the unit cell to be $2.0\mu_B$, in agreement with formal S=1 state of Ni²⁺ (high spin d^8). Due to the presence of finite Ni-O covalency, a significant fraction of this moment resides on O sites. A

large part of moment resides on V^{5+} (d^0 ; $S=0$) sites, which is unusual, indicates the importance of $V d$ - $Ni d$ covalency. This fact was also stressed in the study in Ref. [24].

3.2.3 Understanding of dominant exchange path: NMTO downfolding calculation

In the next stage, we carried out NMTO-downfolding calculations to understand the dominant exchange paths connecting the magnetic Ni ions. Thus, we constructed Ni e_g only low energy 2×2 Hamiltonian by integrating out other degrees of freedom like Ni t_{2g} , V d , Sr s and O p states, starting from the full non spin-polarized band structure of $SrNi_2V_2O_8$. This defines the effective Ni e_g Wannier functions. From the real-space representation of this low-energy 2×2 Hamiltonian defined in the effective Ni e_g Wannier function basis, we computed the values of the on-site energies of the effective Ni e_g levels, as well as the effective hopping interactions connecting two Ni sites. Table 3.5 shows the various effective hopping interactions, as obtained from the NMTO downfolding calculations. Our computed hopping interactions quite well match with that

Table 3.5: Ni-Ni effective hopping interactions. Each hopping interaction is a 2×2 matrix involving two e_g orbitals of Ni.

Distance (\AA)	$3z^2 - r^2 \leftrightarrow 3z^2 - r^2$ meV	$3z^2 - r^2 \leftrightarrow x^2 - y^2$ meV	$x^2 - y^2 \leftrightarrow 3z^2 - r^2$ meV	$x^2 - y^2 \leftrightarrow x^2 - y^2$ meV
2.888	-99	-125	100	236
5.034	27	32	-30	8
6.392	17	2	10	-5
6.395	2	0	4	-5
4.997	-28	31	16	8
5.850	8	-6	5	3
5.766	-17	0	0	65

presented in Ref. [24]. From the Table 4.5 we notice that the dominant hopping interactions connecting Ni sites to be the nearest-neighbour intrachain interaction (t_1), next-nearest-neighbour intrachain interaction (t_2), and two interchain interactions (t_3 , t_4). These dominant interactions in the context of corresponding magnetic interactions, namely two intrachain interactions, J_1 and J_2 and two interchain interactions, J_3 and J_4 are shown in Fig. 3.4

In left panel of Fig. 3.3(a), we show the overlap of two Ni x^2-y^2 effective Wannier function and overlap of two Ni $3z^2-r^2$ effective Wannier function in the right panel of Fig. 3.3(a), placed at two nearest neighbour (NN) Ni sites within the chain. The central part of these wannier functions are shaped according to the Ni $3z^2-r^2$ or x^2-y^2 symmetry while tail parts are shaped according to integrated out orbitals like O p and V d that have significant mixing with Ni d states. These two NN Ni being part of the neighbouring edge sharing octahedra, they are connected

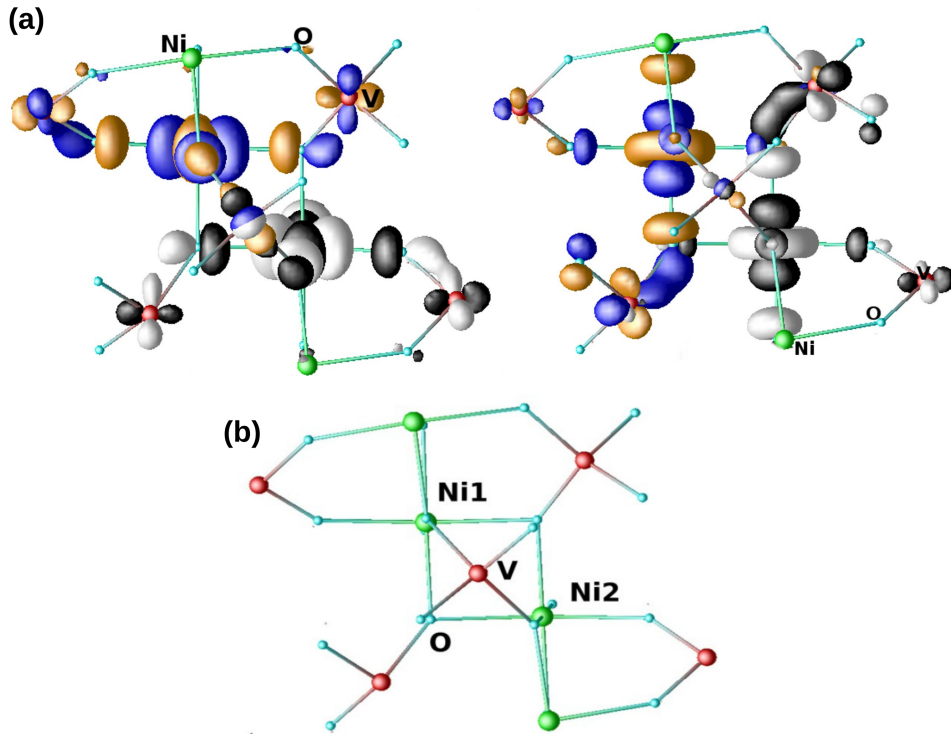


Figure 3.3: (a) Left panel shows overlap of Ni1 and Ni2 effective x^2-y^2 Wannier functions placed at two nearest-neighbour intrachain Ni sites. The two oppositely signed lobes of the wave functions at site 1 (2), are coloured differently as black (blue) and white (orange). Plotted are the constant value surfaces. Right panel shows same as in left panel, but plotted for Ni $3z^2-r^2$ Wannier functions. (b) The network of edge-sharing nearest-neighbour Ni octahedra, connected through two paths, one through edge-sharing oxygens and another through path involving V atom. The V, O, and Ni atoms are marked.

by two sharing oxygens. Additionally they are connected also through the path involving the V atom, as shown in Fig. 3.3(b). From the site projected DOS [cf. Fig. 3.2], we found that there is significant Ni d-V d covalency, which makes the exchange path through O-V-O important. This is further evidenced in the plots of Wannier functions, shown in Fig. 3.3(a). The presence of pronounced tail shaped of the two Ni Wannier functions at the V site connecting two Ni sites indicates that the O-V-O pathway is the crucial exchange pathway. The tail shaped of

the two Ni Wannier functions at the edge-sharing oxygens, on the other hand, is found to be minimal. The importance of the V atom mediated path also makes the next-nearest-neighbour Ni-Ni intrachain interaction non-negligible. This observation is in agreement with the finding of Ref. [24].

3.2.4 Magnetic-exchange interaction and single-ion anisotropy

From the knowledge of above computed hopping interactions, we can calculate the magnetic exchange interactions employing the super-exchange formula [25]. However, as these exchange pathways involve complicated superexchanges, the estimation of the numerical values of magnetic exchanges will not be appropriate using simple superexchange formula. We therefore followed an alternative approach where we carried out total energy calculation of different magnetic arrangement of Ni spins within the GGA+U framework and mapped DFT total energy onto the underlying Ising model to extract dominant magnetic exchange J . The total-energy approach has been followed in various studies in the literature [26] and found to be successful. We used the information of the computed hopping interactions as a guide to dominant exchange pathways. For the GGA+U total-energy calculation, we considered $U(\text{Ni}) = 7.0$ eV and $J_H = 0.8$ eV. It is to be noted that exchange couplings are in order of only a few meV, and being inversely proportional to the U value, the numerical values do depend on the inclusion of the U effect. We thus also calculated total energy of different spin configurations by varying the U value within a range of 6-8 eV, and good agreement with experimental results is obtained for a calculated U value of 7 eV. Though the U value significantly influenced the numerical values of exchange couplings, we found it has only marginal influence on the ratios of various exchanges.

For the GGA+U total-energy calculations, we considered five different magnetic configurations of Ni spins. The energy differences of all the antiferromagnetic (or ferrimagnetic) configurations with respect to the ferromagnetic configuration turned out to be negative indicating the dominance of antiferromagnetic interaction. Mapping onto the effective Ising model, all the dominant magnetic exchange J 's are extracted. We found, the strongest magnetic interaction to be the nearest-neighbour intrachain interaction, J_1 , having a value of 10 meV. The other dominant interactions turned out to be about an order of magnitude smaller. DFT estimated

dominant magnetic exchange interactions are listed in Table 3.6. The corresponding exchange

Table 3.6: Calculated magnetic interactions of the unstrained and biaxially strained compounds. For the unstrained compound, the experimental estimates [24] are also shown for comparison.

	Unstrained (present study)	Unstrained experimental	2% compressive strain	2% tensile strain
J_2/J_1	0.028	0.017	0.006	0.031
J_3/J_1	0.021	0.033	0.023	0.018
J_4/J_1	0.050	0.037	0.052	0.048
J_1 (meV)	9.91	8.70	9.90	7.52

pathways are shown in Fig. 3.4. Our estimated ratios of J 's are in extremely good agreement with that obtained by analysis of the neutron-scattering data presented in Ref. [24]. The experimentally all the exchanges, intrachain as well as interchain exchanges, were determined to be antiferromagnetic [24] which is also the case in our DFT calculated results.

We have already discussed in the section 3.2.1 that application of compressive and tensile biaxial strain changes the structural parameters, and thus it can influence the dominant exchange interactions. Therefore, we calculated magnetic exchanges for 2% compressive and tensile biaxial strained compounds of $\text{SrNi}_2\text{V}_2\text{O}_8$, which are shown in Table 3.6. Table 3.6 shows that the 2% tensile strain influences most the value of the strongest nearest-neighbour interaction J_1 , while the ratios of other dominant interactions remain more or less the same. On the other hand the application of 2% compressive strain keeps the value of J_1 more or less unchanged but it influences the next-nearest-neighbour intrachain interaction J_2 strongly.

Next, we computed the strength of the single-ion anisotropy. In order to do so, in presence of spin-orbit coupling, we calculated total energy considering the spin quantization axis pointed along the chain direction, *i.e.*, the c direction, and pointed perpendicular to it. This calculation was carried out in linear augmented plane wave (LAPW) basis, as implemented in Wien2k. Spin-orbit coupling has been included in the calculation as a perturbation to the original Hamiltonian and was dealt using the second variational scheme. In presence of spin-orbit coupling interaction, we found that the total energy is lower with magnetization axis pointed along the chain direction, compared to the other, suggestive of easy-axis single-ion anisotropy. This finding is in complete agreement with the experimental conclusion [17]. The calculated orbital moment at the Ni site

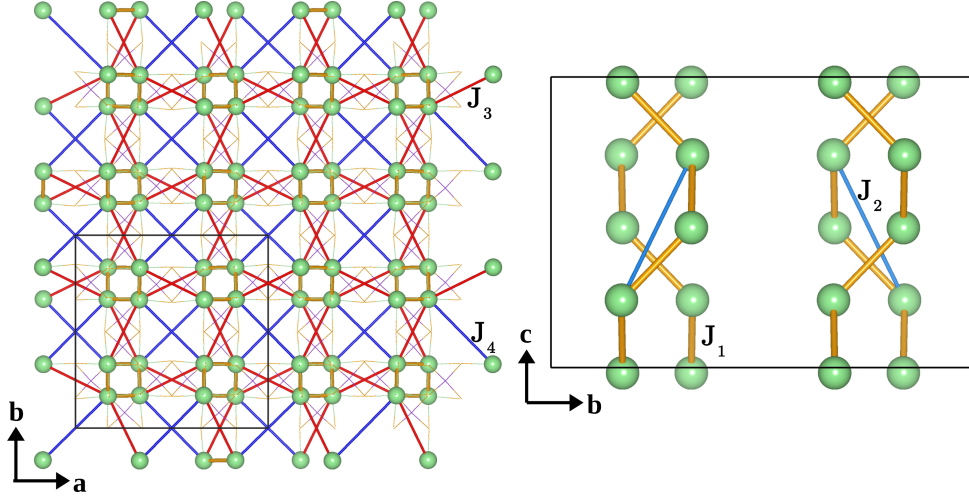


Figure 3.4: The magnetic lattice created by Ni spins, projected to the plane perpendicular to the chain direction (left panel), and that in the plane of the chain (right panel). Four dominant magnetic interactions are shown here. The magnetic exchange interactions J_1 and J_2 are nearest and next-nearest-neighbour intrachain interactions and J_3 and J_4 are two interchain interactions.

is found to be substantial ($\approx 0.14 \mu_B$). From the total energy difference between different orientation of the spin quantization axis we calculated the value of single-ion anisotropy, which turned out to be 0.56 meV, also in rather good agreement with the experimental estimated value [17]. The single-ion anisotropy is found to be remained more or less unchanged (within 1-2%) with application of tensile as well as compressive strain.

3.2.5 Magnetic model

DFT electronic structure calculation, estimated values of exchange interactions and single-ion anisotropy, suggest that $\text{SrNi}_2\text{V}_2\text{O}_8$ can be represented as a spin $S=1$, J_1 - J_2 - J_3 - J_4 model together with the easy-axis single-ion anisotropy, D . The secondary magnetic couplings J_2 , J_3 and J_4 , though small in comparison with the strongest coupling J_1 , have an appreciable effect to manifest the features of quasidimensionality and frustration in the compound. Using Quantum Monte Carlo (QMC) simulation we solved this DFT derived model to calculate thermodynamic quantities.

3.2.6 Calculation of thermodynamic quantities

Considering the J_1 - J_2 - J_3 - J_4 model, the general Hamiltonian with magnetic field H ($= hJ_1$), applied parallel to the c axis, and easy-axis anisotropy D ($= D_0 J_1$) can be written as,

$$H = \sum_b \left[\sum_{a=1}^4 J_a S_{1,b_a}^z S_{2,b_a}^z + \frac{J_1}{2} (S_{1,b_a}^+ S_{2,b_a}^- + h.c.) \right] - hJ_1 \sum_i S_i^z - D_0 J_1 \sum_i [S_i^z]^2 \quad (3.1)$$

To solve this DFT derived spin model of $\text{SrNi}_2\text{V}_2\text{O}_8$, we employed the stochastic series expansion (SSE) technique of the quantum Monte Carlo (QMC) simulation [27–29]. In the SSE-QMC formalism, Eq. 3.1 can be rewritten as sum of bond operators, as following [30],

$$H = J_1 \left[\sum_{a=1}^4 \sum_{b_a} [H_{1b_a} + H_{1b_a}] + \sum_{a=1}^4 N_{b_a} C_a \right] \quad (3.2)$$

Where

$$H_{1,b_a} = C_a - \Delta_a S_{1,b_a}^z S_{2,b_a}^z + h/Z (S_{(1,b_a)}^a + S_{(2,b_a)}^b) + D_0/Z ([S_{1,b_a}^z]^2 + [S_{2,b_a}^z]^2)$$

and $H_{2,b_a} = \frac{t_a}{2} (S_{1,b_a}^+ S_{2,b_a}^- + h.c.)$ represent diagonal and off-diagonal Hamiltonian operators respectively with $\Delta_a = J_a/J_1$ and $t_a = \Delta_a \delta_{a,1}$. Here, b_a denotes bond with interaction of type a and $(1,b_a)$ and $(2,b_a)$ indicate the two sites corresponding to the bond b_a . N_{b_a} is total number of bond for interaction type a and $C_a = \Delta_a S^2 + 2hS/Z$ (Z is the coordination number) is the constant term. S_i^z , S_i^+ , and S_i^- represent the usual z component of the spin operator, and spin raising and spin lowering operators respectively at the site i . The last term in Eq. 3.2 just adds a constant to the Hamiltonian.

For secondary magnetic couplings *i.e.* J_2 , J_3 and J_4 , we considered only Ising-type interactions to avoid the sign problem. To simulate the system we used operator loop updates scheme [27]. In the following section reported thermodynamic properties like magnetic susceptibility and magnetization are calculated on a lattice of dimension $4 \times 4 \times 16$. We have checked our calculation with different lattice size also, but the results were found to be remained unchanged.

Magnetic susceptibility of unstrained $\text{SrNi}_2\text{V}_2\text{O}_8$

In SSE-QMC, the spin susceptibility is measured as $\chi_{th} = \beta J_1 \langle S_z^2 - \langle S_z \rangle^2 \rangle$ where, $\beta = \frac{1}{k_B T}$.

This is related to the experimentally observed molar susceptibility as follows,

$$\chi_{exp} = 0.375 \times S(S+1)g^2 \frac{\chi_{th}}{T_J}$$

Where T_J is the temperature corresponding to the strongest interaction, J_1 . For unstrained

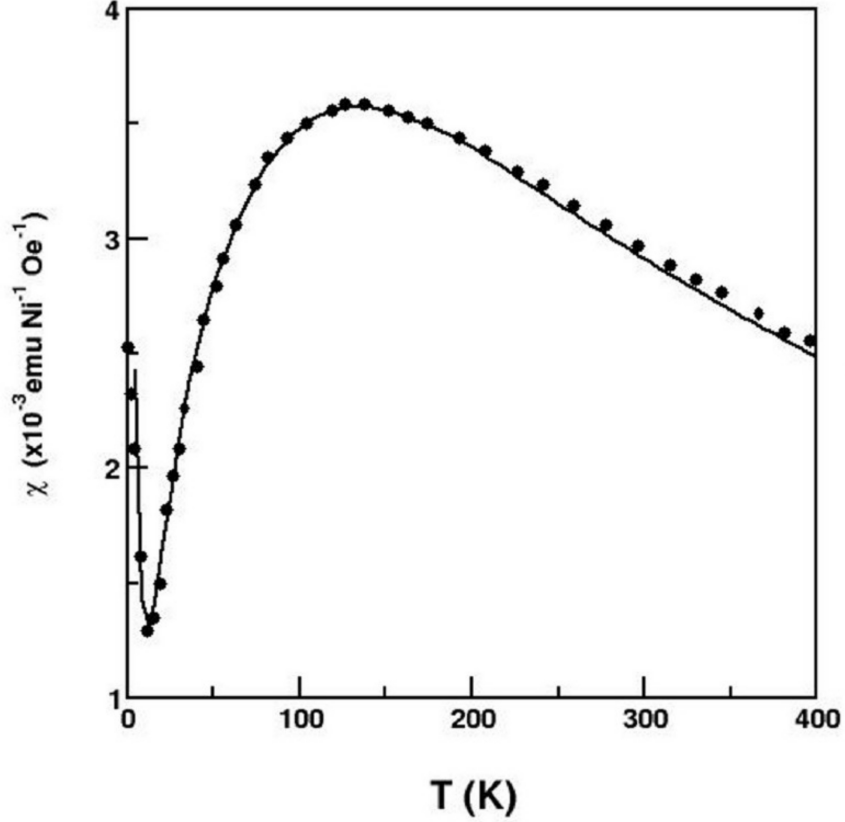


Figure 3.5: Temperature dependence of magnetic susceptibility for the unstrained $\text{SrNi}_2\text{V}_2\text{O}_8$. The circles correspond to experimental data [17] and the solid line corresponds to QMC calculated susceptibility based on the first-principles derived J_1 - J_2 - J_3 - J_4 spin model, together with easy-axis anisotropy, in presence of a magnetic field of 1 T.

$\text{SrNi}_2\text{V}_2\text{O}_8$, to simulate the low temperature part of experimentally measured susceptibility data, we add an impurity term C/T , so that overall susceptibility becomes $\chi_{exp} = 0.375 \times S(S+1)g^2 \frac{\chi_{th}}{T_J} + C/T$. The strongest interaction J_1 and the ratios of the other interactions to J_1 are kept fixed at DFT estimated values (cf. Table 3.6). The calculation are done for applied

magnetic field of $h=0.017$ that corresponds to 1 Tesla, as $h = g\mu_B \sqrt{S(S+1)}B/J_1$ where B is magnetic field in Tesla, the value which are used in the experiment [17]. Keeping the strongest interaction J_1 and the ratios of the other interactions to J_1 fixed, at DFT estimated values, we found a good match of calculated susceptibility with experimentally measured susceptibility data with a choice of $g=2.06$ and $C = 0.012$ [cf. Fig. 3.5].

The features of board maxima, followed by an exponential drop in the susceptibility, indicates the low-dimensional behaviour of the spin model, and existence of a spin gap in the ground state. In the absence of impurity term, we calculated the value of spin gap by fitting the low-temperature behaviour of the susceptibility to the form $\exp(-\Delta/K_B T)$ and value of the spin gap turned out to be $0.315J_1$. This is in good agreement with the estimate obtained from the high-field magnetization, to be described in next section.

Magnetization of unstrained $\text{SrNi}_2\text{V}_2\text{O}_8$

In order to understand the field-induced transition of magnetic behaviour and to observe the evolution of the magnetization upon changing magnetic field, we study the effect of the applied magnetic field along the easy-axis direction (c axis) at a sufficiently low temperature of $\beta = 80$. In Fig. 3.6, we show the evolution of the magnetization upon applied magnetic field along c-axis. Fig. 3.6, shows that, the magnetization develops only beyond a critical field, H_c characterizing closing of the spin gap by Zeeman splitting [9–11]. Anisotropy splits the triplet states into a singlet (corresponds to $S^z=0$ component of triplet) and doublet states (corresponds to $|S^z|=1$ component of triplet), producing two separate gaps [14]. Furthermore, the applied magnetic field parallel to the c axis splits this doublet corresponding the $|S^z|=1$ components of triplet and one of the $|S^z|=1$ components undergoes a level crossing with the ground singlet state at the critical field strength while the $S^z = 0$ component of the triplet remains unchanged in energy [14,31]. The strength of the critical field is found to be about $0.32J_1$ which is much smaller than the value ($0.41J_1$) obtained for a 1D Heisenberg spin chain or equivalently for Haldane chain [20,21]. This value is close to the critical field value of 20.8 T, obtained experimentally [17]. The longer-range interactions, beyond the nearest-neighbour intrachain interaction, both of interchain and intrachain type, can influence the nature of this transition. Thus, to probe the

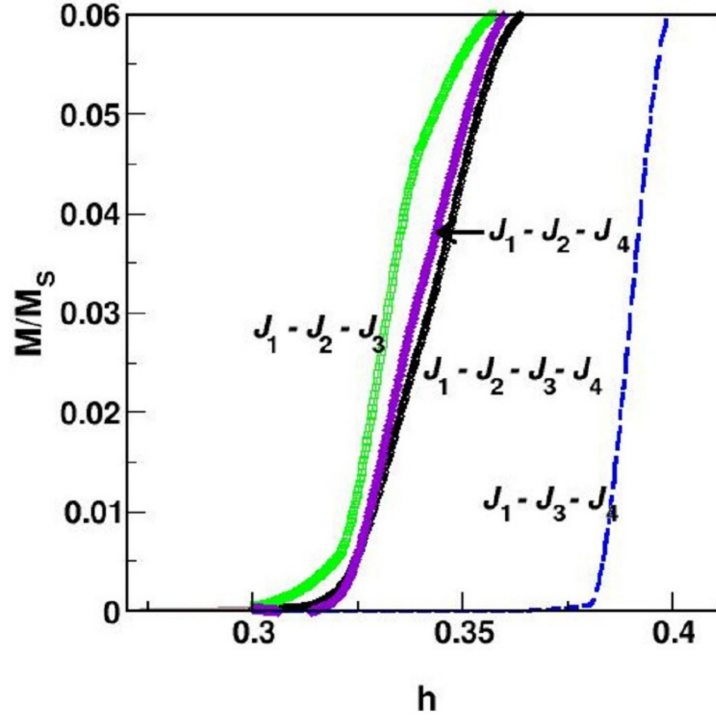


Figure 3.6: Evolution of magnetization as a function of magnetic field applied parallel to chain direction, for the various spin models.

effect of the longer-range interactions individually, we first considered the full model (*i.e.*, J_1 - J_2 - J_3 - J_4) and compared with the behaviour of J_1 - J_2 - J_3 , J_1 - J_2 - J_4 , and J_1 - J_3 - J_4 models, as shown in the Fig. 3.6. As can be seen from Fig. 3.6, the J_2 has the strongest effect in reducing the spin-gap value to $0.32J_1$, compared to the $0.41J_1$ value for an ideal 1D Haldane chain. Thus our study suggest that observed spin-gap quenching effect contributed by the long-range interaction arises primarily from the next- nearest-neighbour intrachain AFM interaction rather than due to the quasi-one-dimensionality of the system [32] described by J_3 and J_4 . It is interesting to note at this point that the presence of diagonal interaction was strongly evident in the experimentally measured magnetic excitation spectra [24]. It was conjectured to be contributed by a combination of in-plane diagonal interchain interaction, which is J_4 , and the next-nearest-neighbour intrachain AFM interaction, which is J_2 [24]. It was further argued that J_4 alone cannot give rise to continuous propagation, unless helped by J_2 due to the peculiar crystal structure. The importance of J_2 has thus been recognized.

Magnetic susceptibility and magnetization of strained compounds of $\text{SrNi}_2\text{V}_2\text{O}_8$

Good agreement between the calculated and the measured susceptibility of unstrained $\text{SrNi}_2\text{V}_2\text{O}_8$ compound [cf. Fig. 3.5], confirmed the effectiveness of the DFT derived spin model to capture the magnetic behaviour of the compound accurately. Thus, considering the same

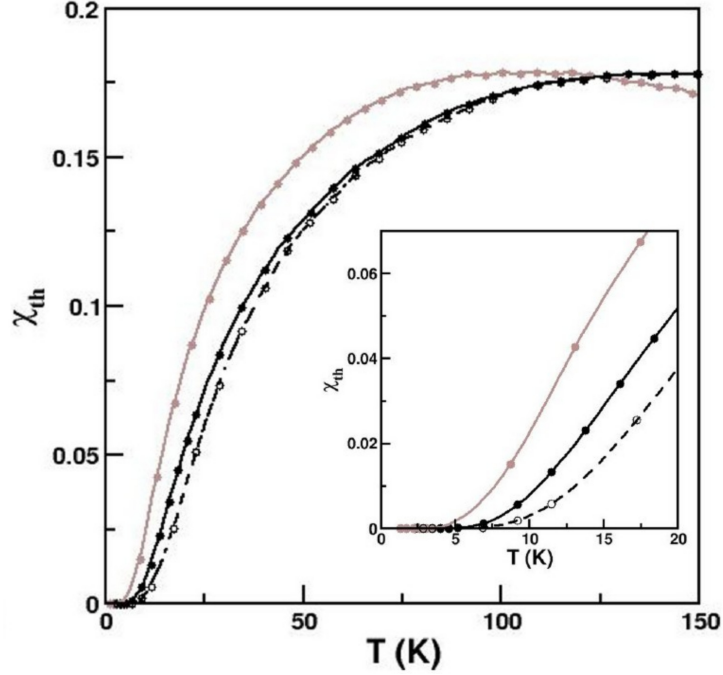


Figure 3.7: Temperature dependence of the theoretical spin susceptibility for the unstrained $\text{SrNi}_2\text{V}_2\text{O}_8$ (black solid line), compressive strained (black dashed line), and tensile strained (gray line) compounds. Inset shows the plot zoomed at low temperature to focus on the spin-gap behaviour.

spin-model, we investigated the effect of biaxial strain on the magnetic behaviour of $\text{SrNi}_2\text{V}_2\text{O}_8$ compounds. In Fig. 3.7, we show the theoretically calculated susceptibility (χ_{th}) plotted as a function of temperature for the strained as well as for the unstrained compounds. From Fig. 3.7, one can see that the general features of the susceptibility which consist of a broad maximum, followed by exponential drop at low temperature remain unchanged between all three compounds. This suggests that the low-dimensional quantum spin behaviour with spin-gapped ground state is applicable for the strained compounds too. The position of the broad maximum and the high-temperature behaviour of the spin susceptibility primarily depend on the value of the dominant AFM interaction J_1 . From the estimated values of magnetic exchanges of strained compounds [cf. Table 3.6], we found that J_1 remains same for the unstrained and compressive

strained compounds, 9.91 and 9.90 meV respectively. Thus a little difference is found between the high-temperature susceptibility data of the compressive strained and unstrained compounds. On the other hand, a significant change is observed in value of J_1 in the case of a tensile strained compound, which causes a large shift in the position of the broad maximum as well as an appreciable change in the high-temperature behaviour of the susceptibility, compared to the unstrained compound. In inset, we show the view zoomed at low temperature, which reveals the spin gap to be largest for the compressive strained compound, followed by the unstrained and tensile strained compounds. In Fig. 3.8 we show, the computed field induced evolutions

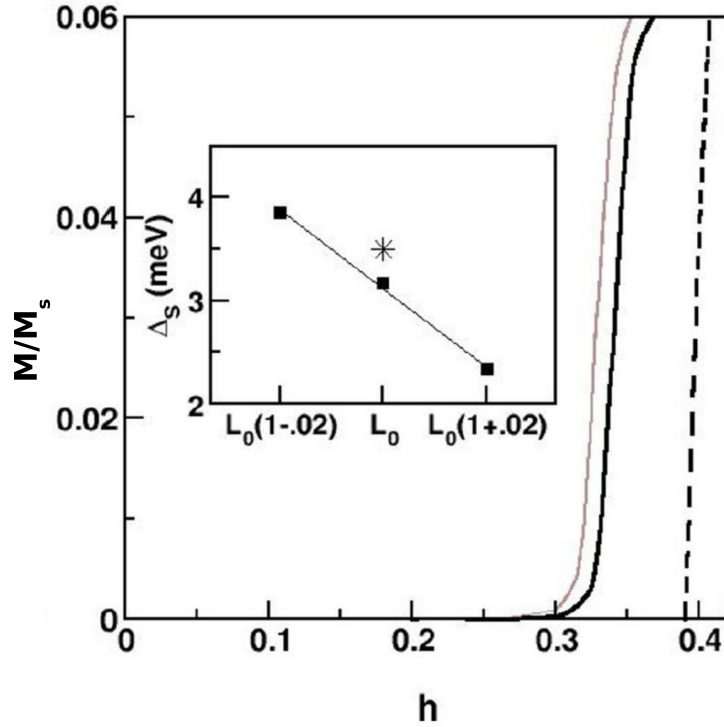


Figure 3.8: Evolution of magnetization as a function of magnetic field applied parallel to chain direction for the unstrained (black solid line), tensile strained (gray line), and compressive strained (dashed line) compounds. The inset shows the variation of the calculated spin gap, estimated from critical field, as a function of the in-plane lattice constant. L_0 , $L_0(1-0.02)$ and $L_0(1+0.02)$ denote the in-plane lattice constants of the unstrained compound, compressive strained, and tensile strained compounds, respectively. The line is to guide the eye. The data point shown by the asterisk corresponds to the estimate obtained from experimentally measured critical field

of the magnetization of the strained compounds as well as unstrained compounds. As is seen from the plot, the behaviour of magnetization upon changing magnetic field for the compressive strained compound is rather different from the unstrained compound. This is caused due to the significant change in value of J_2/J_1 compared to unstrained compound which has a significant

effect, as we discussed before [cf. Fig. 3.6]. The behaviour for the tensile strained compound on the other hand is very similar to that of the unstrained compound, though the absolute value of the critical magnetic field needed to close the gap is decreased due to reduction in the strength of J_1 itself. Inset of Fig 3.8 shows the computed spin gap from the critical field for strained as well as unstrained compounds along with the experimentally observed spin gap value. We observe a monotonic decrease of the spin gap upon tensile strain *i.e.* increasing the in-plane lattice constant. This observed trend suggests that a tensile strain of 7-8% should enable to close the spin gap, resulting into a magnetic transition from the spin-liquid ground state to the ordered state.

3.3 Summary and conclusions

Using first principles density functional theory (DFT) and Quantum Monte Carlo (QMC) technique, we investigated the electronic and magnetic properties of the spin S=1, Haldane chain compound $\text{SrNi}_2\text{V}_2\text{O}_8$. Our DFT based parameter-free first-principles calculation suggested that S=1 spin chain compound $\text{SrNi}_2\text{V}_2\text{O}_8$ can be described by a J_1 - J_2 - J_3 - J_4 model, together with easy axis single-ion anisotropy, where J_1 is the strongest nearest neighbour intrachain coupling, J_2 is the next-nearest-neighbour intrachain coupling, and J_3 and J_4 are two interchain couplings. Site projected density of states and Wannier function plots, revealed that nonmagnetic V atom plays a crucial role in mediating the super-exchange interactions between two nearest neighbour Ni sites, similar to what was pointed out in Ref. [24]. We solved the ab initio derived spin model using stochastic series expansion (SSE) technique of QMC simulation to compute the thermodynamic quantities like static magnetic susceptibility and magnetization. Calculated magnetic susceptibility confirmed the spin-gapped ground state of the compound and very good agreement with the experimentally measured data gave confidence for the ab initio derived model. Calculation of the field induced evolution of magnetization showed the closing of the gap at a critical field, which provided an estimate of the spin gap. The estimated spin gap ($0.32 J_1$) from the estimate of the critical field is found to be much reduced compared to $0.41 J_1$ [20,21] value of an ideal 1D Haldane chain. Our analysis showed next-nearest-neighbour intrachain coupling, J_2

has the strongest effect to reduce the spin gap value from that of the ideal 1D Haldane chain's spin gap value.

With the motivation of external tuning of the ground state properties, we further investigated the influence of 2% biaxial tensile and compressive strain on the magnetic behaviour of $\text{SrNi}_2\text{V}_2\text{O}_8$. Application of 2% compressive strain, made the spin gap increased compared to its value at unstrained condition due to the significant change in the J_2/J_1 ratio. On the other hand application of 2% tensile strain, helped to reduce the spin gap compared to its value at unstrained condition due to the reduction on the strength of strongest coupling J_1 . A monotonic decrease of the absolute value of the spin gap, upon increasing tensile strain suggested that a tensile strain of 7-8% should enable to drive the quantum phase transition from spin-gapped ground state to an ordered state. This finding can be validated experimentally. We hope that our computational study will encourage experimental investigations in this direction.

Bibliography

- [1] P. Lemmens, G. Guntherodt, and C. Gros, *Phys. Rep.* 375, 1 (2003).
- [2] K. Katsumata, *J. phys.: Condens. Matter* 12, R589 (2000).
- [3] I. Affleck, *J. Phys. Condens. Matter* 1, 3047 (1989).
- [4] A. Smirnov and V. Glazkov, *J. Exp. Theor. Phys.* 105, 861 (2007).
- [5] F. D. M. Haldane, *Phys. Rev. Lett.* 50, 1153 (1983).
- [6] F. D. M. Haldane, *Phys. Lett. A* 93, 464 (1983).
- [7] H. A. Bethe, *Z. phys.* 71, 205 (1931).
- [8] I. Affleck, T. Kennedy, E. H. Lieb, and H. Tasaki, *Phys. Rev. Lett.* 59, 799 (1987).
- [9] P. Zeeman, *Phil. Mag.* 43, 226 (1897).
- [10] P. Zeeman, *Phil. Mag.* 44 (266)(1897).
- [11] P. Zeeman, *Nature.* 55 (1424), 347 (1897).
- [12] T. M. Rice, *Science* 298, 760 (2002).
- [13] Y. Maeda, C. Hotta, and M. Oshikawa, *Phys. Rev. Lett.* 99, 057205 (2007).
- [14] O. Golinelli, Th. Jolicoeur, and R. Lacaze, *J. Phys.: Condens. Matter* 5, 7847 (1993).
- [15] T. Sakai and M. Takahashi, *Phys. Rev. B* 42, 4537 (1990).
- [16] A. Zheludev, T. Masuda, I. Tsukada, Y. Uchiyama, K. Uchinokura, P. Boni, and S.-H. Lee, *Phys. Rev. B* 62, 8921 (2000).

-
- [17] A. K. Bera, B. Lake, A. T. M. N. Islam, B. Klemke, E. Faulhaber, and J. M. Law, *Phys. Rev. B* 87, 224423 (2013).
- [18] B. Pahari, K. Ghoshray, R. Sarkar, B. Bandyopadhyay, and A. Ghoshray, *Phys. Rev. B* 73, 012407 (2006).
- [19] A. K. Bera and S. M. Yusuf, *Phys. Rev. B* 86, 024408 (2012).
- [20] S. R. White and I. Affleck, *Phys. Rev. B* 77, 134437 (2008).
- [21] V. A. Kashurnikov, N. V. Prokofev, B. V. Svistunov, and M. Troyer, *Phys. Rev. B* 59, 1162 (1999).
- [22] R. Wichmann and Hk. Muller-Buschbaum, *Rev. Chim. Miner.* 23, 1 (1986).
- [23] V. I. Anisimov, J. Zaanen, and O. K. Andersen, *Phys. Rev. B* 44, 943 (1991).
- [24] A. K. Bera, B. Lake, A. T. M. N. Islam, O. Janson, H. Rosner, A. Schneidewind, J. T. Park, E. Wheeler, and S. Zander, *Phys. Rev. B* 91, 144414 (2015).
- [25] K. I. Kugel and D. I. Khomskii, *Sov. Phys. Usp.* 25, 231 (1982).
- [26] C. S. Hellberg, W. E. Pickett, L. L. Boyer, H. T. Stokes, and M. J. Mehl, *J. Phys. Soc. Jpn.* 68, 3489 (1999).
- [27] A. W. Sandvik, *Phys. Rev. B* 59, R14157 (1999).
- [28] A. Dorneich and M. Troyer, *Phys. Rev. E* 64, 066701 (2001).
- [29] K. Louis and C. Gros, *Phys. Rev. B* 70, 100410(R) (2004).
- [30] O. F. Syljuasen, *Phys. Rev. E* 67, 046701 (2003).
- [31] Z. Wang, M. Schmidt, A. K. Bera, A. T. M. N. Islam, B. Lake, A. Loidl, and J. Deisenhofer, *Phys. Rev. B* 87, 104405 (2013).
- [32] K. Wierschem and P. Sengupta, *J. Phys. Conf. Ser.* 400, 032112 (2012); *Phys. Rev. Lett.* 112, 247203 (2014).

Chapter 4

Spin state of Mn^{2+} and magnetism in vanadate-carbonate compound, $\text{K}_2\text{Mn}_3(\text{VO}_4)_2\text{CO}_3^\dagger$

4.1 Introduction and motivation

Spin state is an important concept when describing the transition metal (TM) compounds, which refers to spin configurations of the transition metal's d electrons, for a given polyhedral environment of surrounding ligand atoms. When transition metal ions have several d electrons, specially the d occupancies between 4 and 7, depending on the filling of d states, the spin states can be either high-spin or low-spin configurations. Thus, considering the Mn^{2+} ion with d^5 configuration, one may expect that it can exist in two possible spin states, high-spin state with $S = 5/2$ state and low-spin state with $S = 1/2$ state. At molecular level, stabilization of a specific spin state primarily depends on the competition between the crystal field splitting and the Hund's rule coupling, the latter favouring high-spin (HS) configuration, through maximization

[†]This chapter is based on publication, Kartik Samanta and T. Saha-Dasgupta, Phys. Rev. B 90, 064420 (2014).

of total spin, and the former favouring low-spin (LS) configuration, as the high-spin configuration involves transfer of electron from lower energy states to higher energy states [1,2]. As, the Hund's rule coupling energy is a characteristic energy of the transition metal ion, it shows only mild variation. On the other hand, for a choice of given TM in a specific compound, the crystal field splitting primarily depends on the nature of crystal field and strength of TM and ligands covalency (see the introductory chapter 1). The relative stability of HS or LS states not only depends on the competition between relative strength of crystal field splitting and Hund's rule coupling, but also on the number of d electrons as Hund's rule energy is given by the number of pairs of parallel spins [3]. Thus following this discussion, the existence of low-spin state of $\text{Mn}^{2+}(d^5)$, is unexpected as half filled d levels would lead to the large Hund's rule stabilization. Therefore, it is a debatable issue, whether $\text{Mn}^{2+}(d^5)$ ion can exhibit spin-state bistability, as observed [4,5] in the case of Fe^{2+} or Co^{3+} .

Recently synthesized vanadate-carbonate compound, $\text{K}_2\text{Mn}_3(\text{VO}_4)_2\text{CO}_3$, represents a novel structure type [6]. Two different polyhedral environment of Mn^{2+} ions gives rise to two inequivalent Mn^{2+} ions in the unit cell, one in octahedral coordination of oxygen atoms (Mn1) and another in trigonal-bipyramidal environment of oxygen atoms (Mn2). The measured magnetic susceptibility and field dependence of magnetization data [cf. Fig. 4.1], were explained, considering the high-spin state of Mn1 and low-spin state of Mn2, in two different local environments in the compound [6]. The proposal of the low-spin state of $\text{Mn}^{2+}(d^5)$ in $\text{K}_2\text{Mn}_3(\text{VO}_4)_2\text{CO}_3$ is cu-

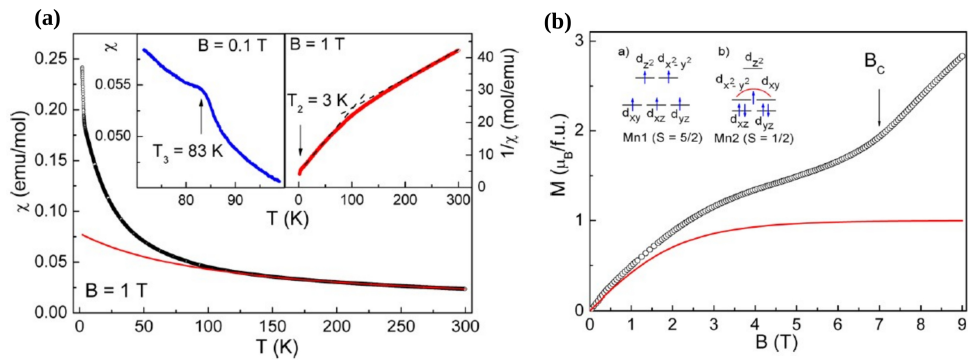


Figure 4.1: (a) Experimentally measured temperature dependence of the magnetic susceptibility plots. The right inset shows the inverse magnetic susceptibility. The dashed lines indicates the slopes of this curve at low ($T < 100$ K) and high ($T > 100$ K) temperature. The left inset shows the temperature dependence of the magnetic susceptibility measured at $B = 0.1$ T. (b) Experimentally measured field dependence of the magnetization at $T = 2$ K. The insets show the crystal-field splitting of d level in Mn1 and Mn2 sites. Figures are taken from Ref. [6]

rious and interesting as there exists, only very few examples of $\text{Mn}^{2+}(d^5)$ in low spin state [7, 8]. Also, the possible effects of frustration [9] in the novel crystal structure of $\text{K}_2\text{Mn}_3(\text{VO}_4)_2\text{CO}_3$, arising from the geometry of the magnetic Mn^{2+} ions, gives rise to further interest in the study of this compound.

Thus, in order to examine the proposal of low-spin state of $\text{Mn}^{2+}(d^5)$ in $\text{K}_2\text{Mn}_3(\text{VO}_4)_2\text{CO}_3$ and possible effect of frustration in magnetic structure, we carried out DFT based first principles calculations. We derived a microscopic spin model for this compound from parameter free ab initio calculations to understand the experimentally measured thermodynamic quantities like magnetic susceptibility and field dependence of magnetization. The derivation of microscopic spin models based on parameter free ab initio calculation, have been found to be very successful for a large number of quantum spin systems including cuprates [10–13], vanadates [14, 15], titanates [16, 17] which established confidence in this approach. We solved this microscopic spin model by quantum Monte Carlo (QMC) technique to compute thermodynamic properties like static susceptibility and field dependence magnetization and compared with experimentally measured data to check the goodness of our DFT derived spin model.

4.2 Results and discussion

4.2.1 Crystal structure

The Vanadate-carbonate compound, $\text{K}_2\text{Mn}_3(\text{VO}_4)_2\text{CO}_3$ crystallizes in the hexagonal space group of $P6_3/m$ (No. 176), with lattice constants, $a = 5.201 \text{ \AA}$ and $c = 22.406 \text{ \AA}$ [6]. There

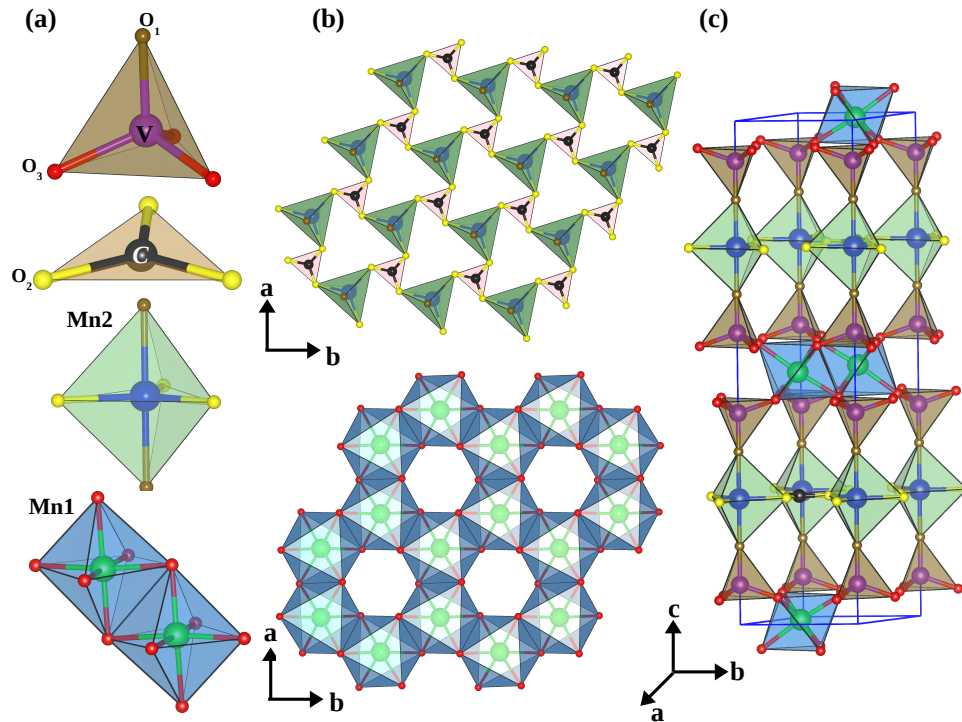


Figure 4.2: Crystal structure of $\text{K}_2\text{Mn}_3(\text{VO}_4)_2\text{CO}_3$. (a) The basic structural units VO_4 , CO_3 , Mn_2O_5 , and edge-sharing Mn_1O_6 octahedra (from top to bottom). The inequivalent oxygens have been marked. (b) The layered sublattices of Mn_1 (bottom panel) and Mn_2 (top panel). (c) The connected, three-dimensional network.

are two inequivalent Mn^{2+} ions, in the unit cell of $\text{K}_2\text{Mn}_3(\text{VO}_4)_2\text{CO}_3$, which arise due to two different polyhedral environment of Mn^{2+} ions. Among these two inequivalent Mn^{2+} , one is in octahedral surrounding of oxygen atoms (Mn_1) and another is in five vertex trigonal-bipyramidal environment of oxygen atoms (Mn_2) [cf. Fig. 4.2(a)]. Apart from Mn_2O_5 trigonal-bipyramid, and Mn_1O_6 edge-shared octahedra, the basic structural units are composed of VO_4 tetrahedra, CO_3 triangle, as shown in Fig. 4.2(a). The Mn_1 and Mn_2 form two types of layers, which alternate along the c -axis of the hexagonal unit cell [cf. Fig. 4.2(b)]. The neighbouring Mn_1O_6 octahedra share edges to form honeycomb layer of Mn_1 ions shown in the bottom panel of Fig.

4.2(b), while Mn_2O_5 trigonal bipyramids are connected to each other via CO_3 triangles, forming a triangular layer, shown in the top panel of Fig. 4.1(b). These two alternating layers are connected via VO_4 tetrahedra through sharing of oxygen vertices's with Mn polyhedra, to form the three-dimensional structure, shown in Fig. 4.2(c). The K^+ ions which are not shown in the figure for clarity, sit in the crisscross channels formed in the structure.

Table 4.1: The theoretically optimized atomic positions compared to the experimentally measured data. During the optimization the parameters of the hexagonal unit cell are fixed at the experimentally measured values, $a = 5.201 \text{ \AA}$ and $c = 20.406 \text{ \AA}$.

Site	Measured position			Optimized position		
	x	y	z	x	y	z
V	0.00000	0.00000	0.07987	0.00000	0.00000	0.07949
Mn1	0.66667	0.33333	0.00457	0.66666	0.33333	0.00427
Mn2	0.00000	0.00000	0.25000	0.00000	0.00000	0.25000
K	0.33333	0.66667	0.15776	0.33333	0.66666	0.15759
C	0.66667	0.33333	0.25000	0.66666	0.33333	0.25000
O1	0.00000	0.00000	0.15520	0.00000	0.00000	0.15626
O2	0.44340	0.06810	0.25000	0.43342	0.06483	0.25000
O3	0.30980	0.98939	0.05494	0.31628	0.99217	0.05337

Since the atomic positions of light atoms are often not well characterized by X-ray diffraction, we carried out structural optimization relaxing the internal positions of all atoms and keeping the hexagonal $\text{P6}_3/\text{m}$ symmetry of the cell as well as lattice constants fixed at experimentally measured values [6]. The structural optimization calculation was carried out using the plane wave basis with projector-augmented wave (PAW) potentials, as implemented in VASP, within non-spin polarized scheme of calculation. During the structural optimization, atomic positions of the structure were relaxed towards equilibrium until the Hellmann-Feynman forces became less than 0.01 eV/\AA . We considered the exchange correlation functional to be that of generalized gradient approximation (GGA), implemented following the Perdew-Burke-Ernzerhof (PBE) prescription. Experimental measured atomic positions and optimized atomic positions are listed in Table 4.1. Table 4.1 shows that the changes of atomic positions upon structural relaxation are not significant. Selected bond lengths for optimized structure are listed in Table 4.2. We find, Mn-O bondlengths get reduced by an amount 1-2% upon optimization, compared to experimentally measured structure. The results reported in this chapter are based on the theoretically optimized structure. We have cross-checked our results considering the experimental measured structure also, but the general conclusions were found to be remained unchanged.

Table 4.2: Comparison of selected bond lengths for experimental as well as theoretical optimized structure.

Unit	Measured Structure	Optimized Structure	
Mn1O ₆	Mn1-O distance in Å		
	Mn1-O3 × 3	2.194	2.166
	Mn1-O3 × 3	2.194	2.166
	avg. Mn1-O distance Å	2.169	2.137
Mn2O ₅	Mn2-O distance in Å		
	Mn2-O1 × 2	2.124	2.100
	Mn2-O2 × 3	2.151	2.106
	avg. Mn2-O distance	2.140	2.104
VO ₄	V-O distance in Å		
	V-O1 × 1	1.688	1.720
	V-O2 × 3	1.732	1.765
	avg. V-O distance	1.721	1.754
CO ₃	C-O distance in Å		
	C-O2 × 3	1.284	1.314

4.2.2 Electronic structure and spin state of Mn²⁺ ions

Electronic structure calculation was carried out using plane wave basis as implemented in the VASP code. For the self-consistent calculation, wave functions were expanded in the plane wave basis with a kinetic energy cut-off of 500 eV. We used the Monkhorst-Pack k-point mesh of $6 \times 6 \times 2$ for reciprocal space integration which was found to provide good convergence of the total energy.

Site projected density of states (DOS)

In Fig. 4.3, we show the spin-polarized GGA density of states (DOS) projected onto Mn1 *d*, Mn2 *d*, V *d*, O *p*, and C states. Fig. 4.3 shows that ground state to be insulating in nature within the GGA scheme of calculation. Repeating the calculation within GGA+U scheme of calculation, it is found that the basic electronic structure remains unchanged between GGA and GGA+U calculations, only the value of the insulating gap increases with increasing value of U, as expected. We notice that the states close to Fermi level, E_F (set at zero in the figure) are dominated by Mn1 *d* states and Mn2 *d* states lie in the energy range between -1.5 to -3.0 eV. *Both the Mn1 and Mn2 d states are completely filled in the majority spin channel and empty in*

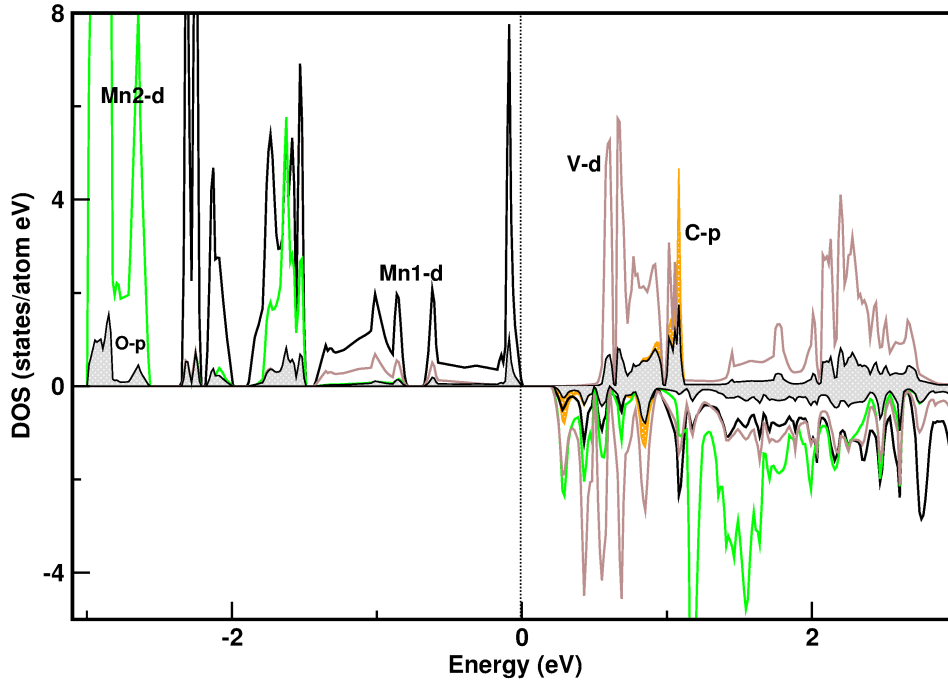


Figure 4.3: Spin-polarized GGA density of states, projected onto Mn1 d (black solid line), Mn2 d (green solid line), O p (black shaded area), V d (brown solid line) and C p (orange shaded area) states. The zero of the energy is set at GGA Fermi energy.

the minority spin channel, indicating both the Mn^{2+} ions to be in high d^5 ($S=5/2$) configuration, in contrary to experimental suggestion that Mn1, (octahedral coordination of oxygens) is in the high-spin state (HS) and Mn2 (trigonal pyramidal environment of oxygens) is in the low spin state (LS). The Mn1 and Mn2 d states show some finite mixing with the O p states, which is expected. But the presence of V d character in the energy range of Mn1 and Mn2 d dominated states, is interesting and unexpected, as V^{5+} is in d^0 configuration. This indicates to finite hybridization of V d states with Mn1 and Mn2 d states which has an important implication in defining the nearest neighbour Mn1-Mn1 exchange paths. This will be discussed later, in the context of Wannier function plot. Small but finite hybridization from C p states also observed. In Table 4.3, we show the computed magnetic moments within GGA and GGA+U scheme of calculation, with choice of $U(Mn) = 4$ eV and $J_H = 0.8$ eV. In order to check the influence of the crystal structure, the magnetic moments computed for the experimental crystal structure are also shown for comparison. As seen from Table 4.3, magnetic moment at Mn1 and Mn2 sites to be around 4.3-4.6 μ_B within GGA, as well as GGA+U scheme of calculations for both the optimized as well as experimental crystal structure. Again, this indicates that both the Mn1

Table 4.3: Magnetic moment at V, Mn1, Mn2, and inequivalent O sites (in μ_B) as calculated in GGA and GGA+U scheme of calculation, considering measured as well as theoretically optimized crystal structures. The moment at C sites being vanishingly small has not been shown.

	measured structure		optimized structure	
	GGA	GGA+U	GGA	GGA+U
V	0.367	0.251	0.490	0.388
Mn1	4.346	4.550	4.276	4.510
Mn2	4.408	4.585	4.366	4.561
O1	0.003	0.001	0.003	0.002
O2	0.012	0.005	0.008	0.003
O3	0.036	0.018	0.031	0.011

and Mn2 are in high-spin states. With application of supplemented Hubbard U, the magnetic moments at Mn sites get increased by $\approx 0.2 \mu_B$, as expected. The total moment in the two-formula unit cell is found to be $30 \mu_B$ corresponding to a moment of $5 \mu_B$ per Mn. A significant fraction of this moment resides on O sites due to the presence of finite Mn-O covalency. A large part of the moment ($\approx 0.2-0.5 \mu_B$) resides on V^{5+} (d^0) sites, which is unusual, indicates once again the importance of V d -Mn d covalency. In order to check the robustness of our conclusion about the HS state of Mn2, which is contradiction with experimental suggestion, we checked the influence of the basis set by carrying out calculations in full potential all electron linear augmented plane wave (LAPW) method as well as in the muffin-tin orbital (MTO) based linear muffin tin orbital method, in addition to the plane wave calculations. Calculations in all three basis sets gave rise to same conclusion of HS state of both Mn1 and Mn2.

Fixed-moment calculation

In order to confirm the spin state of Mn^{2+} , we further carried out fixed-moment calculation, in which one can constrain desirable total magnetic moment in the unit cell. Thus within fixed moment scheme of calculation, varying the total moment in the unit cell of $K_2Mn_3(VO_4)_2CO_3$, over a wide range in both GGA and GGA+U calculation setup, we encompass various possible spin states of Mn. The results are shown in Fig. 4.4. The two formula unit cell of $K_2Mn_3(VO_4)_2CO_3$, contains 4 Mn1 atoms and 2 Mn2 atoms. If both the Mn1 and Mn2 are in HS state (d^5 ; $S=5/2$), then the total magnetic moment in the unit cell to be $30 \mu_B$. While, for the choice of LS state of Mn2 ($S=1/2$) and HS state of Mn1 ($S=5/2$), the total magnetic moment to be $22 \mu_B$ in the

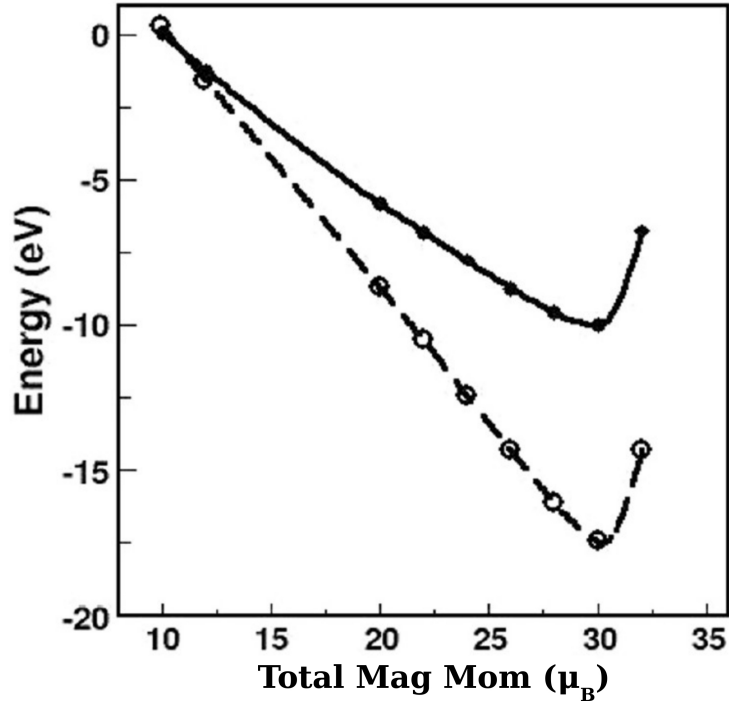


Figure 4.4: Energy plotted as a function of the fixed total magnetic moment in the unit cell, consisting of four Mn1 and two Mn2 ions. The solid and dashed lines correspond to calculations within GGA and GGA+U, respectively.

unit cell, or for the LS states of both Mn ($S=1/2$), it to be $6 \mu_B$. We found in both for GGA as well as GGA+U calculations, the minimum energy is obtained at a total magnetic moment of $30 \mu_B$. This confirms that both the Mn1 and Mn2 are in the high spin state in contrary to experimental suggestion that Mn1 is in HS state and Mn2 is in LS state [6].

Energy level diagram and spin projected DOS

In order to rationalize the high-spin configuration of Mn1 and Mn2, we computed spin-projected DOS as well as the energy-level diagram of Mn d states. Mn1 is in octahedral environment of oxygen ions and Mn2 is in the trigonal bipyramidal environment of oxygen ions. Within the crystal field of octahedron, Mn1 d levels split into approximately degenerate t_{2g} and e_g states, while crystal field of trigonal pyramid, splits the Mn2 d levels into xz/yz , xy/x^2-y^2 and z^2 states. The distortion in Mn1O₆ octahedra leads further splitting of t_{2g} states into doubly state e_g^π and singly state a_{1g} (see the introductory chapter 1). Fig. 4.5(a) and 4.5(b) show the spin projected density of states of Mn1 d and Mn2 d , respectively. The crystal field splitting from the spin

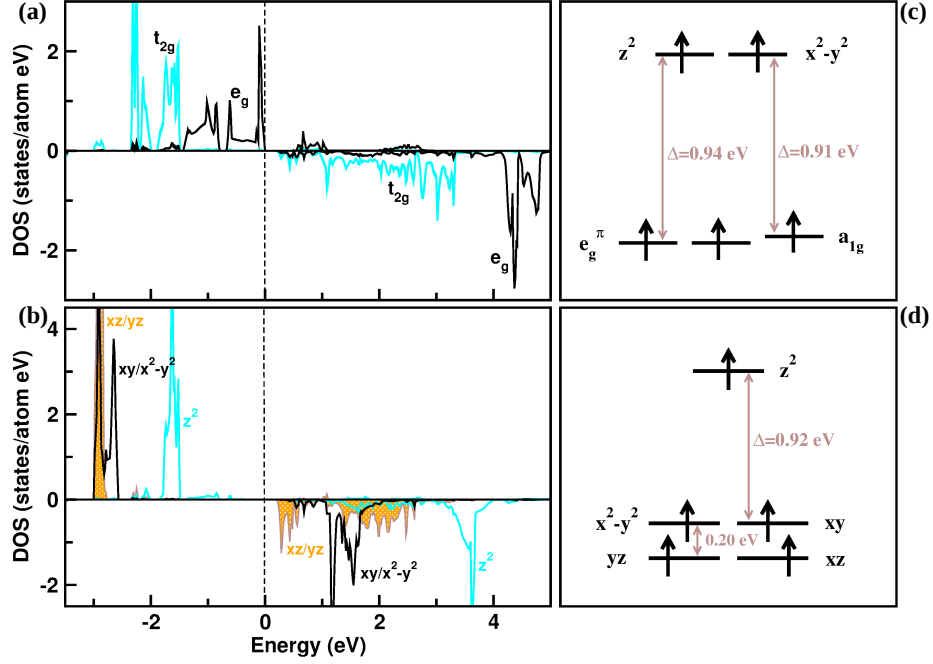


Figure 4.5: (a) Spin-polarized GGA density of states, projected onto octahedral crystal field splits Mn1 t_{2g} (cyan solid line) and e_g states (black solid line). The zero of the energy is set at GGA Fermi energy. (b) Spin-polarized GGA density of states, projected onto crystal field splits Mn2 d states. (c) Energy-level positions of Mn1 d states and their occupancies. The distortion in Mn1O₆ octahedra gives rise to small splitting of t_{2g} states into e_g^π and a_{1g} states. (d) Energy-level positions of Mn2 d states and their occupancies.

projected DOS for both Mn1 and Mn2, is observed to be less than 1 eV approximately. In order to quantify the crystal field splitting precisely, we carried out NMTO downfolding calculation. Using NMTO downfolding procedure we constructed Mn d only low energy Hamiltonian by integrating out all other degrees of freedom starting from the full non spin-polarized GGA band structure. The onsite matrix elements of the real-space representation of this Hamiltonian provide the information of crystal field splitting of d states of Mn1 and Mn2 sites. The onsite energy-level diagrams, for both the Mn1 and Mn2 d states are shown in Fig. 4.5(c) and 4.5(d). Fig. 4.5(c) shows the splitting of d states into approximate degenerate t_{2g} - e_g states for the almost perfect octahedral environment of Mn1 with a splitting of ~ 0.9 eV. Fig. 4.5(d) shows the splitting of d states into double degenerate xz/yz , doubly degenerate $(x^2-y^2)/xy$, and singly degenerate $3z^2-r^2$ for the trigonal bipyramidal environment of Mn2 with a splitting of ~ 0.9 eV between $3z^2-r^2$ and the next-lower-energy level. The splitting between the highest energy state and the next-lower-energy state (~ 0.9 eV) is comparable to Hund's exchange energy which

suggest that the high-spin states of Mn2, as in Mn1, are conceivable, supporting the conclusion, as obtained from the computed site projected DOS as well as values of magnetic moments.

We note that if Mn2 is in the LS (*i.e.* $S=1/2$) state, it would lead to Jahn-Teller active configuration with the unpaired spin residing at doubly degenerate $d_{x^2-y^2}/d_{xy}$ level, leading to distortion of crystal lattice. While the experimental study assigned the anomaly in measured magnetic susceptibility data at $T = 83$ K to be tentatively of Jahn-Teller origin, the same study also reported no indication of this distortion in the specific heat measurements [6], which makes the situation rather undecided. This signature is also not found in the crystal structure data.

4.2.3 Estimation of magnetic exchange interactions

In order to estimate the magnetic exchange interactions between the Mn^{2+} ions which is the key parameters in defining the spin model, we followed two independent routes. One is the NMTO downfolding procedure and another is the total energy calculation approach. Estimation of magnetic exchanges from these two approaches are discussed below.

NMTO downfolding calculation

In the first approach, using NMTO down folding procedure, we constructed Mn1 and Mn2 d only low energy Hamiltonian by integrating out all other degrees of freedom like $V d$, $C p$ and $O p$ *etc.*, starting from the full non spin-polarized GGA band structure. This defines the effective Mn1 and Mn2 d Wannier functions. The low energy Mn1 and Mn2 d only bands in comparison to non-spin-polarized GGA band structure projected onto Mn1 d and Mn2 d characters are shown in Fig. 4.6. From the real-space representation of this low-energy Hamiltonian defined in the effective Mn1 and Mn2 d Wannier function basis, we computed the values of the on-site energies of the effective Mn1 and Mn2 d levels, as presented in the Fig. 4.4(c) and 4.4(d), as well as the effective hopping interactions connecting two Mn sites. Various effective hopping interactions between Mn sites are presented in Table 4.4. We find, strongest hopping interactions to be that connecting nearest-neighbour (NN) Mn1 sites in the Mn1 layer, t_1 , followed by two more, second and third NN interactions in the Mn1 layer, t_2 and t_3 . The interaction connecting

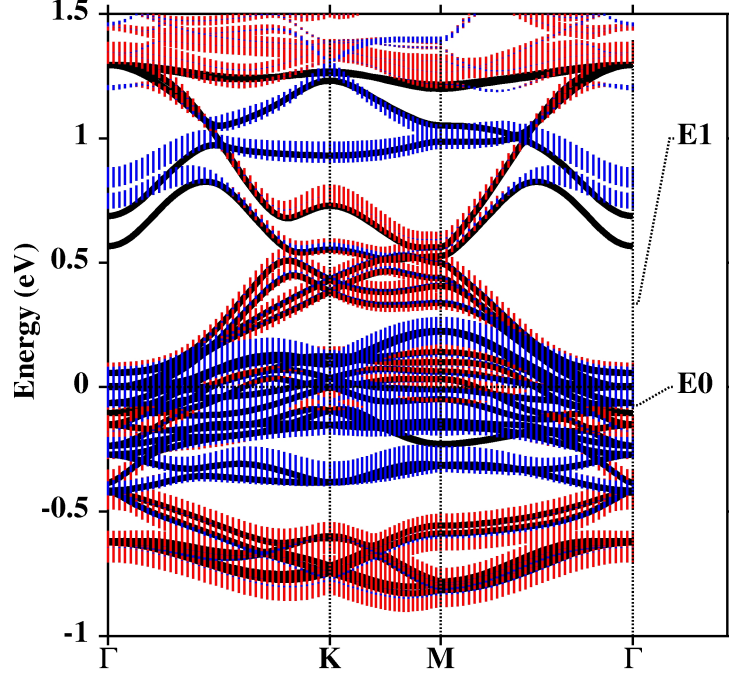


Figure 4.6: NMTO downfolded Mn d only bands, shown in black, solid lines, in comparison to Mn1 d (the fatness, shown as red, vertical lines) and Mn2 d (the fatness, shown as blue, vertical lines) projected states of the full band structure. The energies E0 and E1 represent energy about the expansion were carried out in NMTO calculation.

NN Mn2 sites in Mn2 layer (t_4) is nonnegligible but smaller than the strongest Mn1-Mn1 NN hopping interaction while the hopping interaction connecting Mn1 and Mn2 (t_5) between the two layers is very small. The dominant effective Mn-Mn hopping interactions in the sublattice of Mn ions are marked in Fig. 4.7. From the knowledge of hopping interactions and onsite energies, we estimated the values of magnetic exchange interactions by employing the super exchange formula [18], given as,

$$\sum_{m,m'} \frac{2(t_{m,m'}^{ij})^2}{\Delta_{m,m'}^{ij} + U} \quad (4.1)$$

Where, t is the hopping interactions, i and j are two Mn sites and m and m' are two d orbitals. $\Delta_{m,m'}^{ij}$ is the energy-level difference, between m and m' orbitals at sites i and j and U is the Hubbard parameter. With a choice of $U = 4$ eV, the antiferromagnetic (AFM) exchange interactions in terms of the strongest Mn1-Mn1 NN interaction, J_1 , turned out be $J_2/J_1 = 0.12$,

Table 4.4: Effective hopping interactions (in eV) between two Mn sites which can be either Mn1 or Mn2 (see third column), connected through the connecting vector, as given in the first column, and separated by a distance, as given in the fourth column of the table. The number of neighbours for a given pair of Mn sites is indicated in the second column. Each hopping interaction is a 5×5 matrix, $h_{m,m'}$ with $m, m' = d_{xy}, d_{yz}, d_{3z^2-r^2}, d_{xz},$ and $d_{x^2-y^2}$.

Connecting vector hopping Int.	NN no.	Atoms	Distance (Å)		d_{xy}	d_{yz}	$d_{3z^2-r^2}$	d_{xz}	$d_{x^2-y^2}$
[0.58 0.00 - 0.04] t_1	3	Mn1	3.01	d_{xy}	-0.057	-0.033	0.009	0.045	0.007
				d_{yz}	0.033	0.048	-0.023	-0.032	-0.009
				$d_{3z^2-r^2}$	-0.009	-0.023	-0.154	-0.023	-0.101
				d_{xz}	0.045	0.032	0.023	0.282	0.004
				$d_{x^2-y^2}$	-0.007	-0.009	-0.101	-0.004	-0.270
[0.00 - 1.00 0.00] t_2	6	Mn1	5.20	d_{xy}	0.000	-0.014	-0.035	-0.015	0.047
				d_{yz}	-0.020	-0.016	0.013	-0.006	-0.028
				$d_{3z^2-r^2}$	0.026	-0.073	0.014	-0.012	-0.092
				d_{xz}	0.010	-0.003	-0.026	-0.003	-0.056
				$d_{x^2-y^2}$	-0.001	-0.001	0.016	-0.028	-0.014
[0.58 - 1.00 - 0.04] t_3	3	Mn1	6.01	d_{xy}	-0.004	0.007	-0.050	-0.035	-0.010
				d_{yz}	-0.007	0.009	-0.001	0.021	-0.004
				$d_{3z^2-r^2}$	0.050	-0.001	-0.007	0.025	-0.021
				d_{xz}	-0.035	-0.021	-0.025	0.008	-0.027
				$d_{x^2-y^2}$	0.010	-0.004	-0.021	0.027	0.000
[0.00 - 1.00 0.00] t_4	6	Mn2	5.20	d_{xy}	-0.003	0.000	-0.025	0.000	-0.040
				d_{yz}	0.000	0.010	0.000	-0.004	0.000
				$d_{3z^2-r^2}$	-0.037	0.000	-0.031	0.000	0.005
				d_{xz}	0.000	0.040	0.000	-0.005	0.000
				$d_{x^2-y^2}$	-0.069	0.000	-0.037	0.000	-0.020
[0.29 - 0.50 - 1.09] t_5	6	Mn1/Mn2	6.35	d_{xy}	0.003	0.010	0.007	-0.000	0.001
				d_{yz}	-0.006	0.018	-0.022	0.003	-0.023
				$d_{3z^2-r^2}$	0.021	0.013	-0.023	-0.001	-0.044
				d_{xz}	-0.009	-0.048	0.003	0.000	0.011
				$d_{x^2-y^2}$	0.000	-0.008	0.012	-0.002	0.012

$J_3/J_1 = 0.06$, $J_4/J_1 = 0.06$, $J_5/J_1 = 0.04$, where J_2, J_3, J_4 and J_5 represent second NN Mn1-Mn1, third NN Mn1-Mn1, NN Mn2-Mn2, and Mn1-Mn2 interactions, respectively.

Next, we plotted the Mn d Wannier functions, in order to probe the underlying superexchange pathways. In Fig. 4.8, we show the overlap of two Mn1 d Wannier functions placed at two nearest neighbour (NN) Mn1 sites, corresponding to strongest NN Mn1-Mn1 interaction t_1 . These two NN Mn1 being part of the neighbouring edge sharing octahedra, they are connected by two sharing oxygens. Additionally they are connected also through the path involving the V atom. The central part of the Wannier functions are shaped according to the active Mn d

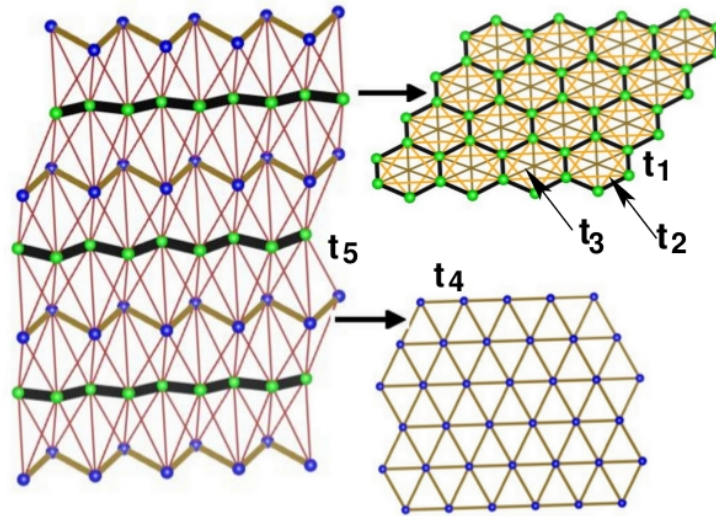


Figure 4.7: The dominant Mn-Mn effective hopping interactions, in the Mn1 layer (right top), Mn2 layer (right bottom), and that between Mn1 and Mn2 layers (left). The Mn1 and Mn2 sites are shown as green and blue balls, respectively. The fatness of the connecting bonds, connecting two sites, are proportional to the corresponding hopping strength.

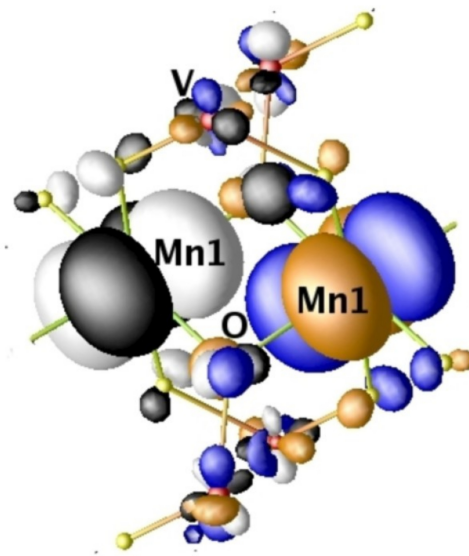


Figure 4.8: Plot of Wannier functions placed at two interacting nearest neighbour Mn1 sites, corresponding to strongest interaction t_1 . The two oppositely signed lobes of the wavefunctions at site $i(j)$ are coloured differently as black (blue) and white (orange).

symmetry while tail parts are shaped according to integrated out orbitals like O p and V d states. The presence of pronounced tail shaped of the two Mn1 Wannier functions at the O sites as well as at the V sites indicates that Mn1-Mn1 NN interaction (t_1) proceed not only through the edge-shared oxygens but also through the V sites, which contributes to Mn1-Mn1 interaction due to non negligible hybridization between V d and Mn d states.

Overlap of two Mn2 d Wannier functions placed at two NN Mn2 sites, corresponding to t_4 interaction and overlap of two Mn1 and Mn2 d Wannier function placed at two NN Mn1 and Mn2 sites, corresponding to t_5 interaction, are shown in Fig. 4.9(a) and 4.9(b). We find that Mn2-Mn2 interaction proceeds via the Mn-O-C-O-Mn super exchange paths, while the rather weak Mn1-Mn2 interaction between two adjacent layers proceeds via O-V-O path.

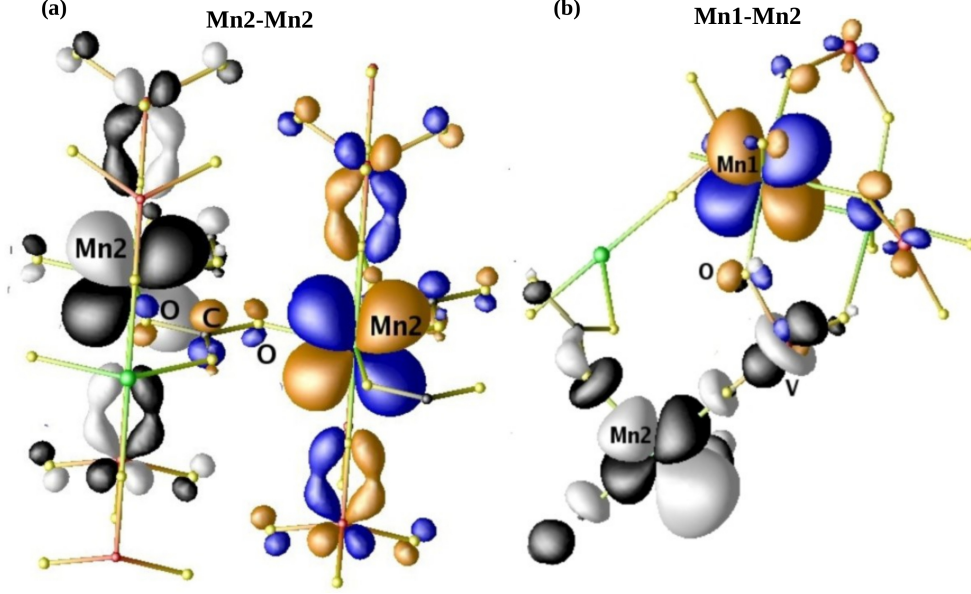


Figure 4.9: (a) Plot of Wannier functions placed at two interacting nearest neighbour Mn2 sites. (b) Plot of Wannier functions placed at two nearest neighbour Mn1 and Mn2 site, which connect the two layers. The two oppositely signed lobes of the wavefunctions at site $i(j)$ are coloured differently as black (blue) and white (orange).

Total energy calculation approach

The estimation of magnetic exchange interactions from the knowledge of computed hopping interactions, is based on the perturbative simple superexchange formula (Eq. 4.1). Therefore we followed an alternative more accurate approach where we carried out total energy calculation of different magnetic arrangement of Mn spins within the GGA+U scheme of calculation and mapped DFT total energy onto the underlying Ising model,

$$\begin{aligned}
 H = & J_1 \sum_{nn} S_{Mn1}^i S_{Mn1}^j + J_2 \sum_{2nn} S_{Mn1}^i S_{Mn1}^j + J_3 \sum_{3nn} S_{Mn1}^i S_{Mn1}^j \\
 & + J_4 \sum_{nn} S_{Mn2}^i S_{Mn2}^j + J_5 \sum_{nn} S_{Mn1}^i S_{Mn2}^j
 \end{aligned} \tag{4.2}$$

to extract dominant magnetic exchange J 's. The total-energy approach has been followed in

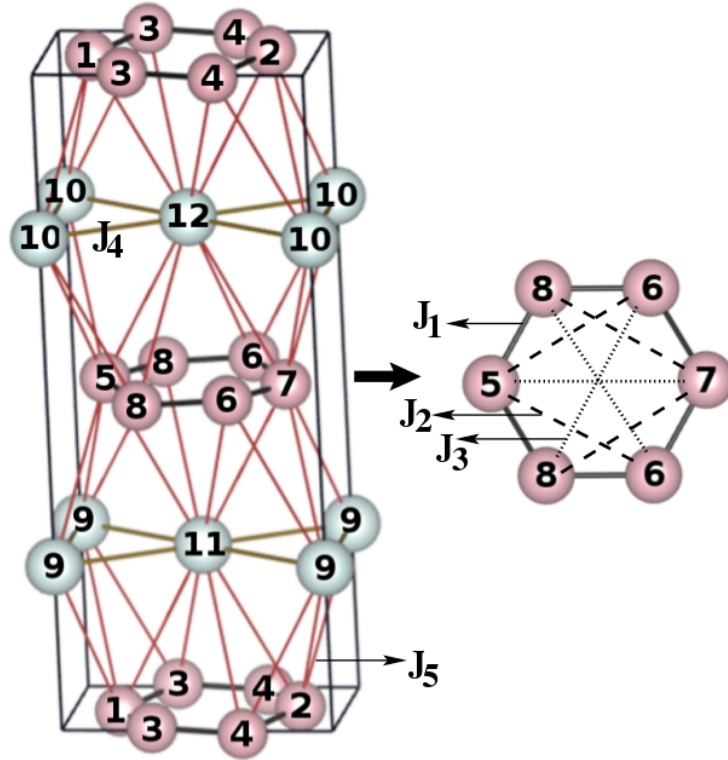


Figure 4.10: Labeling of Mn1 and Mn2 sites, forming alternate layers in the $1 \times 2 \times 1$ supercell, considered for total-energy calculations. The Mn1 and Mn2 atoms are coloured differently as pink and light gray, respectively. The connections corresponding to J_1 , J_2 , J_3 , J_4 and J_5 are indicated.

various studies in the literature [19] and found to be successful. For the total energy calculation, we constructed a supercell of dimension $1 \times 2 \times 1$ which gave rise 12 Mn atoms in the unit cell [cf. Fig. 4.10]. For the GGA+U [$U(\text{Mn})=4.0$ eV and $J_H=0.8$ eV] total-energy calculations, we considered sixteen different magnetic configurations of Mn spins. The energy differences of all the antiferromagnetic (or ferrimagnetic) configurations with respect to the ferromagnetic configuration turned out to be negative, as shown in Table 4.5, indicating the dominance of antiferromagnetic interaction. Exchange interactions are extracted by mapping these GGA+U energies of different spin configurations onto the above defined Ising Hamiltonian (Eq. 4.2). Estimated values of exchange interactions, J_1 , J_2 , J_3 , J_4 and J_5 are found to be -4.162 ± 0.033 meV, -0.242 ± 0.008 meV, -0.481 ± 0.130 meV, -0.123 ± 0.007 meV, and -0.005 ± 0.001 meV, respectively. Negative signs imply all interactions to be of antiferromagnetic nature. We find that total energy method gave rise to very similar description of the underlying spin model, as found in a super-exchange method, with a dominant J_1 in the Mn1 layer, small but nonnegligible

Table 4.5: Magnetic configurations of the Mn ions in the supercell for the states used to determine the magnetic interactions. The numbering of the Mn sites are as shown in Fig. 4.8. The last column gives the relative GGA+U energies in eV.

	1	2	3	4	5	6	7	8	9	10	11	12	ΔE
FM	+	+	+	+	+	+	+	+	+	+	+	+	0.000
AFM1	+	-	-	+	+	+	-	-	+	+	+	+	-0.629
AFM2	+	-	+	-	+	-	+	-	+	+	+	+	-0.365
AFM3	+	-	+	-	+	+	-	-	+	+	+	+	-0.445
AFM4	+	+	+	+	+	+	+	+	+	+	-	-	-0.013
AFM5	-	-	-	-	-	-	-	-	+	+	+	+	-0.003
AFM6	-	+	+	-	+	+	-	-	-	-	+	+	-0.641
AFM7	+	-	+	-	-	+	-	+	-	+	+	-	-0.377
AFM8	+	-	+	-	-	+	+	-	+	-	+	-	-0.262
AFM9	+	+	+	+	+	+	+	+	+	-	+	+	-0.006
AFM10	-	-	-	-	-	-	-	-	+	-	+	-	-0.002
AFM11	+	+	-	-	-	-	-	-	-	+	-	+	-0.236
AFM12	+	-	+	-	+	-	-	+	-	-	-	+	-0.268
AFM13	+	+	+	+	-	-	-	-	-	-	-	+	-0.007
AFM14	+	-	+	+	+	+	+	-	+	+	+	+	-0.340
AFM15	+	-	+	+	+	+	+	-	+	-	+	-	-0.342

values of J_2 and J_3 , an order of magnitude smaller value of J_4 in Mn2 layer compared to J_1 and a very small interlayer coupling, J_5 . In both the approaches, we find the value of J_5 to be smallest among all the interactions which indicates general agreement between the two approaches, although precise numerical values differ.

The above analysis suggests that $\text{K}_2\text{Mn}_3(\text{VO}_4)_2\text{CO}_3$ can be represented as a spin $S=5/2$, consisting of alternate layers of honeycomb and triangular lattices which are weakly connected.

4.2.4 Magnetic structure

The calculations, reported in the above, were carried out considering the collinear arrangement of the Mn spins. However, the frustration effect in the triangular geometry of the Mn2 spins due to the antiferromagnetic nature of NN Mn2-Mn2 interaction, is expected to lead to canting of the Mn spins with possible noncollinear arrangement. Considering the large S spin, J_1 - J_2 - J_3 model for a honeycomb lattice, classical phase diagram of possible ground state magnetic structure has been evaluated in Ref. [20, 21]. Following those structures, the lowest-energy structure, as computed within GGA+U, is found to be noncollinear with 120° canting of spins in Mn2 layer of

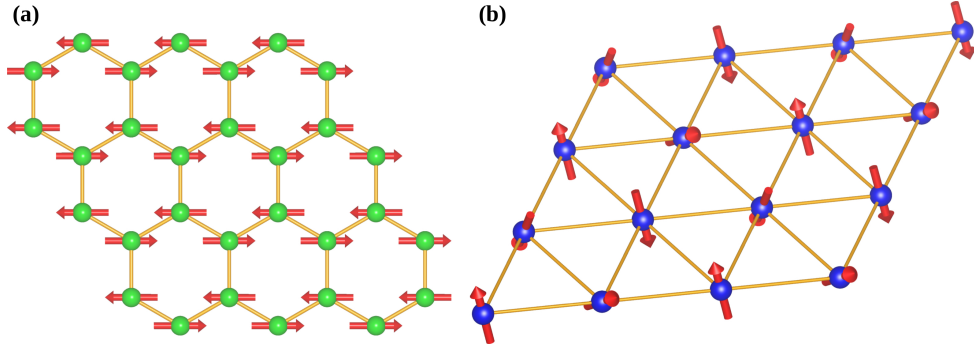


Figure 4.11: (a) The lowest-energy spin structure of Mn1 spins in Mn1 layer, as given in DFT calculation. (b) The lowest energy spin structure of Mn2 spins in Mn2 layer.

triangular lattice [cf. Fig. 4.11(b)], and that in Mn1 layer is found to be collinear with alternate pointing of spins along the hexagonal ring of the honeycomb lattice [cf. Fig. 4.11(a)]. The observed antiferromagnetic collinear magnetic structure in Mn1 layer is expected as the value of NN antiferromagnetic interaction J_1 in Mn1 layer, is an order of magnitude stronger compared to J_2 and J_3 interactions. The magnetic moments of the individual Mn spins in the noncollinear spin configuration are found in the range between 4.6 and 4.8 μ_B , which are in good agreement with results that were found considering the collinear spin arrangement.

4.2.5 Calculation of thermodynamic properties

Considering the ab-initio derived $S=5/2$ spin model of $\text{K}_2\text{Mn}_3(\text{VO}_4)_2\text{CO}_3$, we carried out the stochastic series expansion (SSE) technique of the quantum Monte Carlo (QMC) simulation [22–25] to compute the thermodynamic properties like magnetic susceptibility and field dependence magnetization. The tiny interlayer interaction J_5 is found to have negligible effect on the thermodynamic properties. Thus, the quantum Monte Carlo calculations are carried out considering J_1 - J_2 - J_3 - J_4 model. The reported thermodynamic properties like magnetic susceptibility and magnetization are computed on a lattice of dimension $20 \times 20 \times 10$. We checked our calculation with different lattice size also, but result was found to be remained unchanged.

In SSE-QMC, the spin susceptibility is measured as $\chi_{th} = \beta J_1 \langle S_z^2 - \langle S_z \rangle^2 \rangle$ where, $\beta = \frac{1}{k_B T}$. This is related to the experimentally observed molar susceptibility as follows,

$$\chi_{exp} = 0.50 \times S(S+1)g^2 \frac{\chi_{th}}{T_J}$$

Where T_J is the temperature corresponding to the strongest interaction, J_1 and g denotes the Lande g factor. The strongest interaction J_1 as well as the ratios of the other interactions to

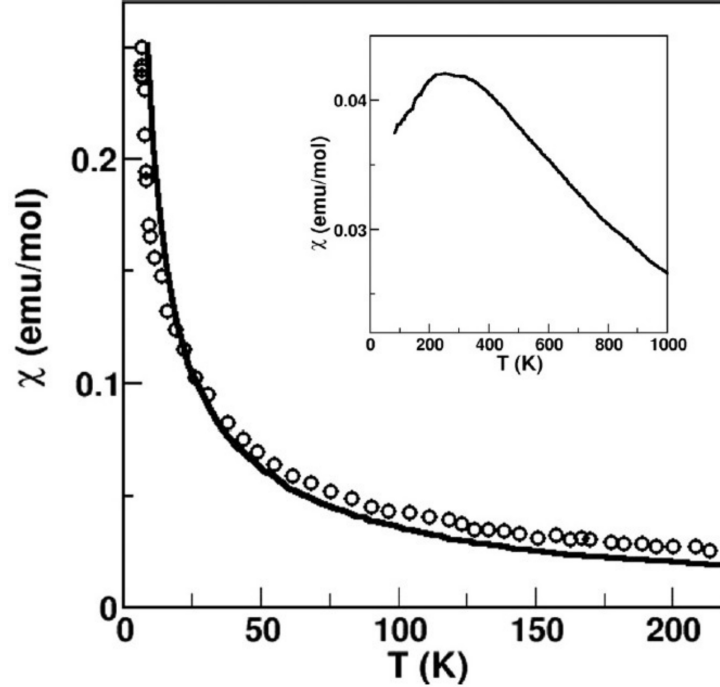


Figure 4.12: Temperature dependence of magnetic susceptibility. The solid line and circle correspond to calculated susceptibility based on ab initio-derived spin model and experimental data [6], respectively. Inset shows the calculated susceptibility based on only Mn1-Mn1 interactions *i.e.* J_1 - J_2 - J_3 .

J_1 are kept fixed at DFT estimated values and g is kept fixed at experimentally determined value of 1.978 [6]. The calculations are carried out in presence of magnetic field of 1 Tesla, the value which is used in the experiment [6]. The theoretical computed data and the experimental data for magnetic susceptibility are shown in Fig. 4.12. In the inset of Fig. 4.12, we show the calculated susceptibility considering only J_1 , J_2 and J_3 , *i.e.*, the interactions in Mn1-layer. In absence of interaction at the Mn2 layer, namely J_4 , the computed susceptibility shows a drop in low-temperature range, which changes drastically upon introduction of Mn2-Mn2 interaction. The overall agreement with the experimental data is reasonable. In Fig. 4.13 we show the computed the magnetization as a function of varying magnetic field, at a temperature of 3 K. The computed field dependence magnetization quite well reproduced the initial fast rise, with slow rise at intermediate field value as well as a fast upturn at higher field value as observed experimentally.

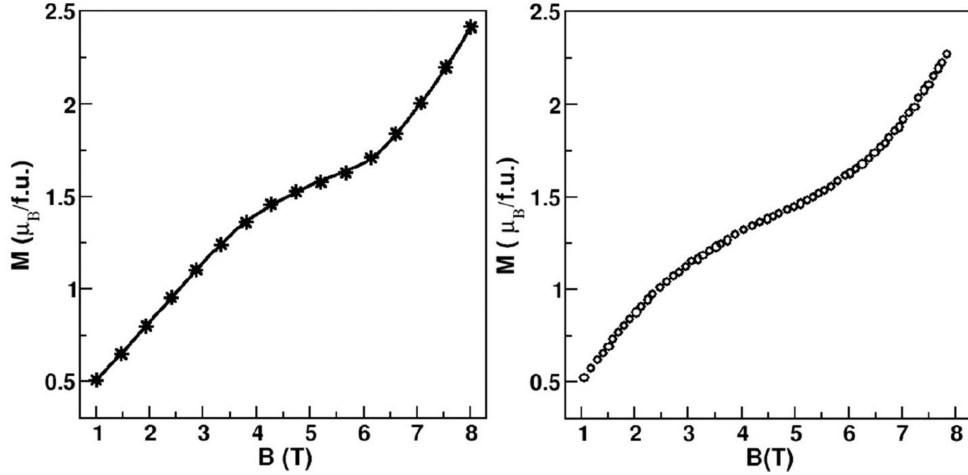


Figure 4.13: The magnetic-field dependence of magnetization. The left and right panels correspond to calculation based on ab initio-derived spin model and experimental data [6], respectively. In the left panel, the stars mark the calculated data while the line is a spline fit through the data points.

4.3 Summary and conclusions

Using first-principles density functional theory-based calculations, we investigated the experimental proposal of low-spin configuration of Mn^{2+} ion in $K_2Mn_3(VO_4)_2CO_3$. Site projected and spin projected DOS, estimated magnetic moment and fixed moment calculations confirmed the high spin state of both inequivalent Mn^{2+} ions, Mn1 and Mn2, one in octahedral and another in trigonal-bipyramidal coordination, contrary to the experimental suggestion that Mn1 is in the high spin state and Mn2 is in the low spin state [6]. The computed value of crystal field splitting (≈ 0.9 eV) at both inequivalent Mn sites, justified the high spin state of both the inequivalent Mn^{2+} ions. The estimated magnetic exchange interactions between Mn^{2+} ions from the knowledge of hopping parameters, employing super-exchange formula (Eq. 4.1), as well as from mapping of total energies of different magnetic arrangements to Ising Hamiltonian (Eq. 4.2), established that spin model of $K_2Mn_3(VO_4)_2CO_3$ to be an antiferromagnetic $S = 5/2$, with alternating layers of honeycomb and triangular lattices, which are coupled very weakly. We found the nearest-neighbour interaction in the honeycomb Mn1 layer to be the strongest interaction, followed by second- and third-neighbour interactions, in decreasing order, which are small but nonnegligible. The nearest-neighbour interaction in triangular Mn2 layer is found to be order of magnitude smaller compared to strongest nearest neighbour interaction in the honeycomb Mn1 layer, setting the low-energy scale at which ordering takes place. The connection

between Mn1 and Mn2 layers is very small and found to have negligible effect. The frustration effect in the triangular geometry of the Mn2 spins due to the antiferromagnetic nature of NN Mn2-Mn2 interaction, gave rise to canting of the spins in Mn2 layer with noncollinear arrangement. In the Mn1 layer spins arrangement is found to be collinear with alternate pointing of spins along the hexagonal ring of the honeycomb lattice, which is expected, as strongest nearest neighbour antiferromagnetic interaction is order of magnitude stronger compared to second- and third-nearest-neighbor interactions in the Mn1 layer [20,21]. Site projected density of state and Wannier function plot, revealed that nonmagnetic V atom plays a important role in mediating the super-exchange interactions between to nearest neighbour Mn1- Mn1 sites, corresponding to the strongest interaction J_1 . Finally, we solved the ab initio derived spin model using stochastic series expansion technique of QMC simulation to compute the thermodynamic quantities like static magnetic susceptibility and the magnetic-field dependence of the magnetization which are found to provide reasonable description of the experimental results. The difference in conclusion of the present study and the experimental study [6] concerning the spin state of Mn2 demands further experimental study on this interesting issue. Specifically, the suggestion [6] of the LS state of Mn2 should be reflected in its signature of Jahn-Teller activity, which has not been found in either crystal structure data or in specific heat data. We hope that our computational study will encourage experimental investigations on this compound.

Bibliography

- [1] H. L. Schlfer and G. Gliemann, "Basic Principles of Ligand Field Theory", Wiley Interscience, New York, (1969).
- [2] C. J. Ballhausen, "Crystal Field Theory", McGraw-Hill, New York, (1962).
- [3] D. Khomskii, "Transition Metal Compounds", Cambridge University Press, Cambridge, England, (2014).
- [4] D. Chernyshov *et al.*, *Angew. Chem. Int. Ed.* 42, 3825 (2003).
- [5] I. Krivokapic *et al.*, *Coord. Chem. Rev.* 251, 364 (2007).
- [6] O. V. Yakubovich, E. V. Yakovleva, A. N. Golovanov, A. S. Volkov, O. S. Volkova, E. A. Zvereva, O. V. Dimitrova, and A. N. Vasiliev, *Inorg. Chem.* 52, 1538 (2013).
- [7] Y. Jiang-Tsui, H. Ying-Sheng, and L. Shoei-Sheng, *J. Phys.: Condens. Matter* 2, 5587 (1990).
- [8] P. Basu and A. Chakravorty, *Inorg. Chem.* 31, 4980 (1992).
- [9] A. P. Ramirez, *Annu. Rev. Mater. Sci.* 24, 453 (1994).
- [10] R. Valent, T. Saha-Dasgupta, and C. Gros, *Phys. Rev. B* 66, 054426 (2002).
- [11] S. Derakhshan, H. L. Cuthbert, J. E. Greedan, B. Rahaman, and T. Saha-Dasgupta, *Phys. Rev. B* 76, 104403 (2007).
- [12] A. A. Tsirlin, A. Moller, B. Lorenz, Y. Skourski, and H. Rosner, *ibid.* 85, 014401 (2012).

-
- [13] O. Janson, A. A. Tsirlin, J. Sichelschmidt, Y. Skourski, F. Weickert, and H. Rosner, *ibid.* 83, 094435 (2011).
- [14] R. Valent and T. Saha-Dasgupta, *Phys. Rev. B* 65, 144445 (2002).
- [15] R. Valent, T. Saha-Dasgupta, J. V. Alvarez, K. Pozgajcic, and C. Gros, *Phys. Rev. Lett.* 86, 5381 (2001).
- [16] P. Lemmens, K. Y. Choi, R. Valent, T. Saha-Dasgupta, E. Abel, Y. S. Lee, and F. C. Chou, *New J. Phys.* 7, 74 (2005).
- [17] T. Saha-Dasgupta, R. Valenti, H. Rosner, and Claudius Gros, *Europhys. Lett.* 67, 63 (2004).
- [18] K. I. Kugel and D. I. Khomskii, *Sov. Phys. Usp.* 25, 231 (1982).
- [19] C. S. Hellberg, W. E. Pickett, L. L. Boyer, H. T. Stokes, and M. J. Mehl, *J. Phys. Soc. Jpn.* 68, 3489 (1999).
- [20] J. B. Fouet, P. Sindzingre, and C. Lhuillier, *Eur. Phys. J. B* 20, 241 (2001).
- [21] E. Rastelli, A. Tassi, and L. Reatto, *Physica B* 97, 1 (1979).
- [22] ALPS project (Algorithms and Libraries for Physics Simulations).
- [23] A. W. Sandvik, *Phys. Rev. B* 59, R14157(R) (1999).
- [24] F. Alet, S. Wessel, and M. Troyer, *Phys. Rev. E* 71, 036706 (2005).
- [25] L. Pollet, S. M. A. Rombouts, K. Van Houcke, and K. Heyde, *ibid.* 70, 056705 (2004).

Chapter 5

Rock-salt versus Layered Ordering in Double Perovskites: A Case Study with $\text{La}_2\text{CuSnO}_6$ and $\text{La}_2\text{CuIrO}_6^\dagger$

5.1 Introduction and motivation

Double perovskites with general formula $\text{A}_2\text{BB}'\text{O}_6$, have been studied intensively due to their diverse electric and magnetic properties [1,2], and they are found to be potential candidates for multiferroicity [3], spintronics [4], magnetocapacitive behavior [5,6], magneto-optic device materials [7]. Most properties of the double perovskite compounds crucially depend on the arrangement of B and B' cations. So arrangement of B and B' cations is an extremely important issue in the context of double perovskites. Apart from random arrangement of B and B' cations, which leads to disordered perovskite structure, three different possible arrangements of B and B' ordering are possible, namely columnar, layered and rock-salt [cf. Fig. 1.14 of chapter 1]. Till date, most synthesized double perovskites show order rock-salt arrangement of B and B'

[†]This chapter is based on publication, Kartik Samanta and T. Saha-Dasgupta, Phys. Rev. B 95, 235102 (2017).

cations, with very few examples of double perovskites having layered ordering of B and B' [8] cations. The main factors which have been identified as helpful for driving the ordering are following,

- (i) Large difference of valence of B and B' cations, at least two or more.
- (ii) Difference in ionic radius of B and B' cations.

It has been postulated that [8,9], having two different geometries of BO_6 and $\text{B}'\text{O}_6$ octahedra, *e.g.* the combination of an Jahn-Teller (JT) distorted B ion, like Cu and an undistorted B' ion, further stabilize the layer ordering over the rock-salt ordering. Following this idea, Anderson *et al.* [10] first synthesized the layer-ordered compound, $\text{La}_2\text{CuSnO}_6$ and later few more layer-ordered double perovskites R_2CuSnO_6 with smaller rare-earth cations, $\text{R}=\text{Nd}/\text{Pr}/\text{Sm}$ and $\text{La}_2\text{CuZnO}_6$ were synthesized using high pressure [11]. The presence of Jahn-Teller distorted Cu^{2+} ion appears to be necessary for stabilization of layer-ordering of B and B' cations but it is not sufficient. For example, $\text{La}_2\text{CuTiO}_6$ shows random arrangement [12], while $\text{La}_2\text{CuIrO}_6$ or $\text{La}_2\text{CuMnO}_6$ shows rock-salt ordering of B and B' cations [13]. For these cases, it has been suggested that cationic sizes are responsible for such behavior [11].

Arguments have been given in terms of geometric considerations for the stabilization of layered ordering over the rock-salt ordering [8,9] but to the best of our knowledge microscopic understanding has never been discussed. Therefore, in the present study we have addressed this issue by considering the examples of $\text{La}_2\text{CuSnO}_6$ (LCSO) and $\text{La}_2\text{CuIrO}_6$ (LCIO) compounds within the frame work of first-principles density functional theory calculations. Here we have studied the structural stability of LCIO and LCSO compounds between the layered and rock-salt ordering considering the following three effects,

- (a) band structure effect.
- (b) effect of magnetism.
- (c) effect of spin-orbit coupling (SOC).

Another aspect of present study is following. Ir is in the 4+ valence state in the LCIO and the physics of Ir 4+ is very rich due to the strong spin-orbit coupling (SOC) with an energy

scale comparable to that of electron correlation. Due to this interplay of strong SOC physics and Coulomb correlation effects, several different oxides containing the Ir^{4+} ion, have been studied heavily in the literature [14–16]. Most interesting manifestation of this strong SOC is the observation of novel quantum state, $j_{eff} = 1/2$ Mott insulating state in layered Sr_2IrO_4 oxide [17, 18]. This $j_{eff} = 1/2$ Mott picture is also observed in different double perovskites like $\text{La}_2\text{ZnIrO}_6$ or $\text{La}_2\text{MgIrO}_6$ [19]. Thus, it would be interesting to find out whether such scenario holds good for $\text{La}_2\text{CuIrO}_6$ or not, where B site (Cu) is magnetic as opposed to $\text{La}_2\text{ZnIrO}_6$ or $\text{La}_2\text{MgIrO}_6$ where B site is nonmagnetic.

5.2 Computational details

For the DFT based first principles calculations, we considered three different basis sets: a) the plane-wave based basis as implemented in the Vienna ab initio Simulation Package (VASP) b) the full potential linear augmented plane wave (FLAPW) basis as implemented in Wien2k code c) the muffin-tin orbital (MTO) based linear muffin-tin orbital (LMTO) method and the N^{th} order MTO method, namely, NMTO method as implemented in the STUTTGART code.

The structural optimization as well as total energy calculations were carried out using the plane wave basis with projector-augmented wave (PAW) potentials. During the structural optimization in the plane wave basis, keeping the symmetry of the crystal unchanged, the lattice parameters as well as atomic positions were relaxed completely towards equilibrium until the Hellmann-Feynman forces became less than $0.001 \text{ eV}/\text{\AA}$. Wave functions were expanded in the plane wave basis with a kinetic energy cut-off of 550 eV. Reciprocal space integration was carried out with Monkhorst-Pack k-point mesh of $6 \times 4 \times 6$ for $\text{P}\bar{1}$ and $4 \times 6 \times 6$ for $\text{P}2_1/\text{m}$ symmetry structure.

The total energy calculations of different structures as well as the calculations including spin-orbit coupling were carried out in all electron full potential method of LAPW. For the self-consistent calculation in LAPW, we used 168 k-points for $\text{P}\bar{1}$ symmetry and 147 k-points for $\text{P}2_1/\text{m}$ symmetry in the irreducible part of Brillouin zone. The wave functions were expanded in plane waves with a cut-off $R_{MT}k_{max} = 7.0$, where R_{MT} is the smallest muffin-tin sphere radius

and k_{max} is the magnitude of the largest k vector in the plane wave expansion. The chosen MT radii for La, Cu, Sn, Ir and O are 2.42, 2.02, 2.08, 2.09 and 1.71 Å, respectively. Spin-orbit coupling has been included in the calculation as a perturbation to the original Hamiltonian and was dealt using the second variational scheme. For extraction of a few-band, tight-binding Hamiltonian out of full DFT calculation we carried out muffin-tin orbital (MTO) based NMTO-downfolding calculations.

We considered the exchange correlation functional to be that of generalized gradient approximation (GGA), implemented following the Perdew-Burke-Ernzerhof (PBE) prescription. The missing strong electron-electron correlation at magnetic ions Cu and Ir, was taken into account through supplemented Hubbard U (GGA+U) calculation. We chose the typical U values for 3*d* (Cu) and 5*d* (Ir) transition metal ions. The results reported in this chapter have been obtained for $U(\text{Cu}) = 4.0$ eV and $U(\text{Os}) = 1.0$ eV, with Hund's coupling energy J_H of 0.8 eV. We have checked the validity of our results by varying U value by +/- 2 V at Cu site and by +/- 1.0 eV at Ir site. The trend of our result was found to remain unchanged. The consistency of the calculations in three different basis sets has been cross checked interms of density of states and band structure calculations.

5.3 Results and discussion

5.3.1 Crystal structure

Originally it was predicted that the LCIO crystallizes in a monoclinic $P2_1/n$ space group [20] with cell dimension, $\sqrt{2}a_p \times \sqrt{2}a_p \times 2a_p$, indicating rock-salt ordering of Cu and Ir ions, where a_p is the lattice parameter for the cubic perovskite structure. But very recent neutron diffraction as well as powder XRD measurement [21] confirmed the low-symmetry $P\bar{1}$ space group with two formula unit cell having two inequivalent Cu and Ir atoms. Basic structural units of this compound are CuO_6 and IrO_6 which alternate along three different crystallographic axis, as shown in Fig. 5.1(A). Both CuO_6 and IrO_6 are distorted, however CuO_6 is more distorted compared to IrO_6 .

The experimentally measured crystal structure of LCSO [11] has monoclinic $P2_1/m$ space group

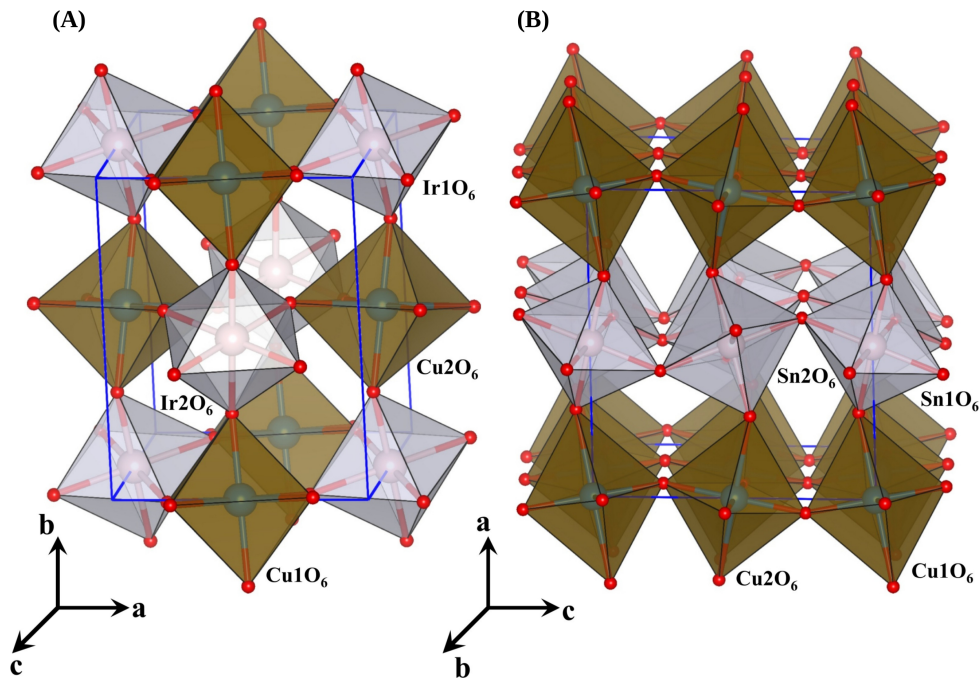


Figure 5.1: Panel (A): Crystal structures of $\text{La}_2\text{CuIrO}_6$ in $P\bar{1}$ space group, showing the rock-salt ordering of CuO_6 (brown color) and IrO_6 (light grey color) octahedra. Panel (B): Crystal structures of $\text{La}_2\text{CuSnO}_6$ in $P2_1/m$ space group, showing the layered ordering of CuO_6 (brown color) and SnO_6 (light grey color) octahedra. Two inequivalent CuO_6 , IrO_6 and SnO_6 octahedra are labelled in both the structures. The La ions sitting the void created by the corner-shared octahedra are not shown for clarity.

with four formula units having two inequivalent Cu atoms, two inequivalent Sn atoms and four

inequivalent La sites as shown in the Fig. 5.1(B). The cell size of LCSO is of dimension $2a_p \times 2a_p \times 2a_p$. Basically the structure consists of two kinds of 2D CuO_2 and SnO_2 layers which are strongly buckled with the tilting of JT distorted CuO_6 octahedron and that of SnO_6 octahedron.

5.3.2 Consideration of different structures to study structural stability

Table 5.1: Structural parameters and selected bond length for fully relaxed LCIO and LCSO structures in both rock-salt ordered $P\bar{1}$ and layered $P2_1/m$ symmetry.

	LCIO ($P\bar{1}$)	LCIO ($P2_1/m$)	LCSO ($P\bar{1}$)	LCSO ($P2_1/m$)
a(\AA)	6.021	8.655	6.090	8.706
b(\AA)	7.736	7.680	7.811	7.855
c(\AA)	5.588	7.716	5.793	7.862
Volume/f.u. (\AA^3)	130.12	128.12	136.94	134.35
α	90.58 ⁰	90.00 ⁰	89.68 ⁰	90.00 ⁰
β	91.16 ⁰	92.40 ⁰	96.39 ⁰	91.81 ⁰
γ	90.07 ⁰	90.00 ⁰	90.44 ⁰	90.00 ⁰
Cu1-O distance (\AA)				
Cu1-O ($\times 2$)	2.22	1.96	2.08	2.00
Cu1-O ($\times 2$)	2.32	1.97	1.98	2.00
Cu1-O ($\times 2$)	2.01	2.40	2.54	2.47
avg. Cu1-O distance (\AA)	2.18	2.11	2.20	2.16
Cu2-O distance (\AA)				
Cu2-O ($\times 2$)	2.24	1.94	2.03	1.98
Cu2-O ($\times 2$)	2.28	2.00	2.01	2.03
Cu2-O ($\times 2$)	2.02	2.40	2.54	2.47
avg. Cu2-O distance (\AA)	2.18	2.11	2.19	2.16
Ir1/Sn1-O distance (\AA)				
Ir1/Sn1-O ($\times 2$)	2.02	2.02	2.077	2.063
Ir1/Sn1-O ($\times 2$)	2.05	2.05	2.109	2.094
Ir1/Sn1-O ($\times 2$)	2.03	2.03	2.117	2.120
avg. Ir1/Sn1-O distance (\AA)	2.03	2.04	2.101	2.092
Ir2/Sn2-O distance (\AA)				
Ir2/Sn2-O ($\times 2$)	2.02	2.04	2.058	2.967
Ir2/Sn2-O ($\times 2$)	2.03	2.04	2.099	2.110
Ir2/Sn2-O ($\times 2$)	2.05	2.07	2.140	2.114
avg. Ir2/Sn2-O distance (\AA)	2.03	2.05	2.099	2.097

To study the relative structural stability of the rock-salt and layered ordering, we considered both LCIO and LCSO in their respective ground state structures with specific ordering type *i.e.* rock-salt or layered, as well as in the assumed structures with the other kind of ordering. In the literature, for all the double perovskites having layered-ordering, only reported space group is the monoclinic $P2_1/m$ space group. On the other hand, several different space groups,

namely cubic (Fm-3m), tetragonal (I2/m), rhombohedral ($R\bar{3}$), monoclinic ($P2_1/n$), have been reported for different double perovskites having rock-salt ordering [8]. From the knowledge of ionic radii [23], we have calculated tolerance factor, f for LCIO and LCSO compounds. The values of f turned out to be 0.945 for LCIO and 0.930 for LCSO. As discussed in the introductory chapter 1, generally for $f < 0.97$, the crystal structure is expected to be monoclinic ($P2_1/n$) with octahedral tilts [22]. In agreement with this expectation, the monoclinic structure is found to be lowest in energy compared to the tetragonal (I2/m), rhombohedral ($R\bar{3}$) structures for the assumed rock-salt ordering for both LCSO and LCIO compounds. Comparing the total energy for recently suggested $P\bar{1}$ space group with that of $P2_1/n$ structure, we found them to be comparable, with $P\bar{1}$ structure slightly lower in energy compared to $P2_1/n$. In the following sections, all the analysis have been presented considering $P2_1/m$ and $P\bar{1}$ symmetry structures.

To say it specifically, for further calculations, we considered LCIO in the experimentally measured symmetry of $P\bar{1}$ and in the $P2_1/m$ symmetry of layered ordered structure. Similarly, we considered LCSO in the experimentally measured symmetry of $P2_1/m$ and in the $P\bar{1}$ symmetry of rock-salt type ordered structure. Considering these four symmetry structures, we carried out structural optimization for each symmetry structure using the plane wave basis. Optimized lattice parameters and selected bond length for all four symmetry structures are shown in the Table 5.1. The DFT optimized crystal structure is found to be 1-2% larger volume compared to the experimentally determined volume. Its influence on octahedral rotations and JT distortions are found to be marginal (by less than 1° for rotation and by less than 0.1 \AA for distortion). The volume difference of LCIO or LCSO in the two symmetries are found to be less than 1% [cf. Table 5.1]. To check the effect of this volume difference in the structural stability, we did the enthalpy calculations but the trend of structural stability, is found to be the same as that from energy calculations.

5.3.3 Structural stability in terms of energetics

In order to find out the relative structural stability of LCIO and LCSO between the rock-salt and layered ordering of B and B' sites, we carried out total energy calculations in FLAPW basis.

Energetics within non spin-polarized scheme of calculation

In Fig. 5.2, we show comparison of energetics, calculated within non spin-polarized scheme of calculation, for both LCIO and LCSO compounds in two assumed symmetries ($P\bar{1}$ and $P2_1/m$) structure, where $\Delta E = E_{non}(P\bar{1}) - E_{non}(P2_1/m)$, $E_{non}(P\bar{1})$ and $E_{non}(P2_1/m)$ being the energies of the optimized nonmagnetic $P\bar{1}$ symmetry structure and $P2_1/m$ symmetry structure, respectively. The non spin-polarized scheme of calculation is expected to take into account primarily the band structure effect. Fig. 5.2 clearly shows that for both LCIO and LCSO

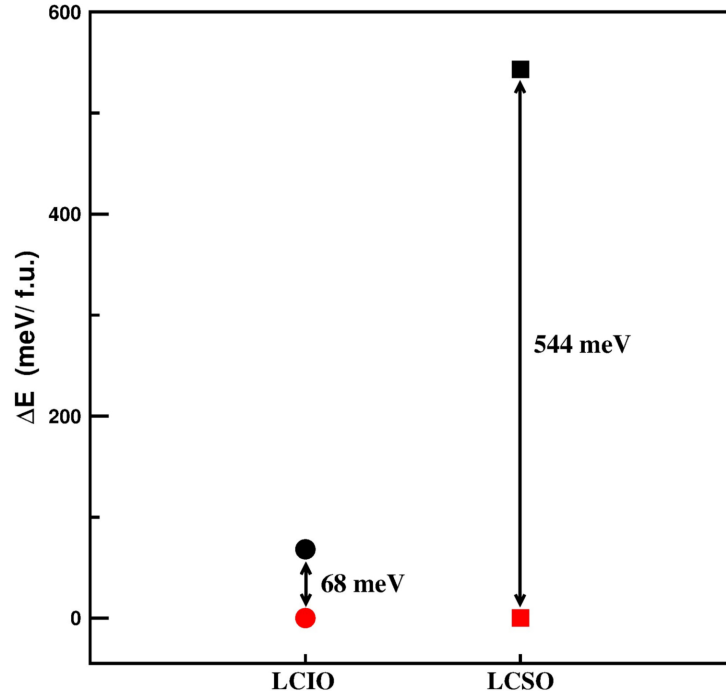


Figure 5.2: The non spin-polarized total energy of LCIO (circles) and LCSO (squares), in the optimized rock-salt ordered $P\bar{1}$ symmetry structure (black symbols) and layered ordered $P2_1/m$ symmetry (red symbols) structure. The positive value of ΔE indicates stability of $P2_1/m$ symmetry over $P\bar{1}$ symmetry.

compounds, the $P2_1/m$ symmetry (marked as red color) with layered ordering of B and B' sites is lower in energy compared to $P\bar{1}$ symmetry. For LCSO, the energy gain in layer-ordered structure is found to be ≈ 544 meV/f.u., while it is found to be an order of magnitude smaller for LCIO (≈ 68 meV/f.u.).

Energetics in presence of magnetism

To incorporate the effect of magnetic structure in the structural stability, we considered four different magnetic structures (FM, AFM-A, AFM-C, and AFM-G) for LCIO, possible within the unit cell of $P2_1/m$ and $P\bar{1}$ and three (FM, AFM-1D and AFM-2D) and two (FM and AFM-A) different magnetic structures for LCSO, possible within the unit cell of $P2_1/m$ and $P\bar{1}$. For both LCIO and LCSO, different considered magnetic structures except FM structure are shown in Fig. 5.3. We found, inclusion of supplemented Hubbard U correction is very important to stabilize the magnetic moments at Cu and Ir sites. Within the GGA+U scheme of calculation, calculated values of magnetic moment at Cu and Ir sites are presented in Table 5.2, for the choice of $U(\text{Cu})=4.0$, $U(\text{Ir})=1.0$ and $J_H=0.8$ eV. For LCIO, magnetic moments at Cu and Ir sites are about $0.5 \mu_B$ and $0.4-0.6 \mu_B$, respectively and for LCSO, it is about $0.6-0.7 \mu_B$ at Cu site. The energetics

Table 5.2: Calculated magnetic moments (in μ_B) of Cu, Ir in LCIO and of Cu, Sn in LCSO for the lowest energy magnetic structures within $P2_1/m$ and $P\bar{1}$ symmetry

LCIO	$P2_1/m$ (AFM-G)	$P\bar{1}$ (AFM-C)	LCSO	$P2_1/m$ (AFM-2d)	$P\bar{1}$ (AFM-A)
Sites	GGA+U	GGA+U	Sites	GGA+U	GGA+U
Cu1(1)	0.541	0.489	Cu1(1)	0.580	0.666
Cu1(2)	-0.539	-	Cu1(2)	-0.580	-
Cu2(1)	-0.546	-0.490	Cu2(1)	-0.582	-0.662
Cu2(2)	0.545	-	Cu2(2)	0.582	-
Ir1(1)	-0.417	-0.612	Sn	0.001	0.001
Ir1(2)	0.414	-			
Ir2(1)	0.420	0.612			
Ir2(2)	-0.425	-			

calculated within the GGA+U approach, are shown in Fig. 5.4 with solid lines where where for LCIO, $\Delta E = E - E_{FM}(P\bar{1})$, $E_{FM}(P\bar{1})$ and E being the energy of the optimized $P\bar{1}$ symmetry structure in FM phase and that of optimized $P\bar{1}$ or $P2_1/m$ symmetry structure in different magnetic structures, respectively. Similarly for LCSO, $\Delta E = E - E_{AFM-2D}(P2_1/m)$, $E_{AFM-2D}(P2_1/m)$ and E being the energy of the optimized $P2_1/m$ symmetry structure in AFM-2D phase and that of optimized $P\bar{1}$ or $P2_1/m$ symmetry structure in different magnetic structures, respectively. For LCIO, Fig. 5.4 shows that irrespective of considered magnetic structures, rock-salt ordered structure favoured compared to layered ordered structure in contrast with the result obtained within non-magnetic scheme of calculations. The lowest energy FM configuration in $P\bar{1}$

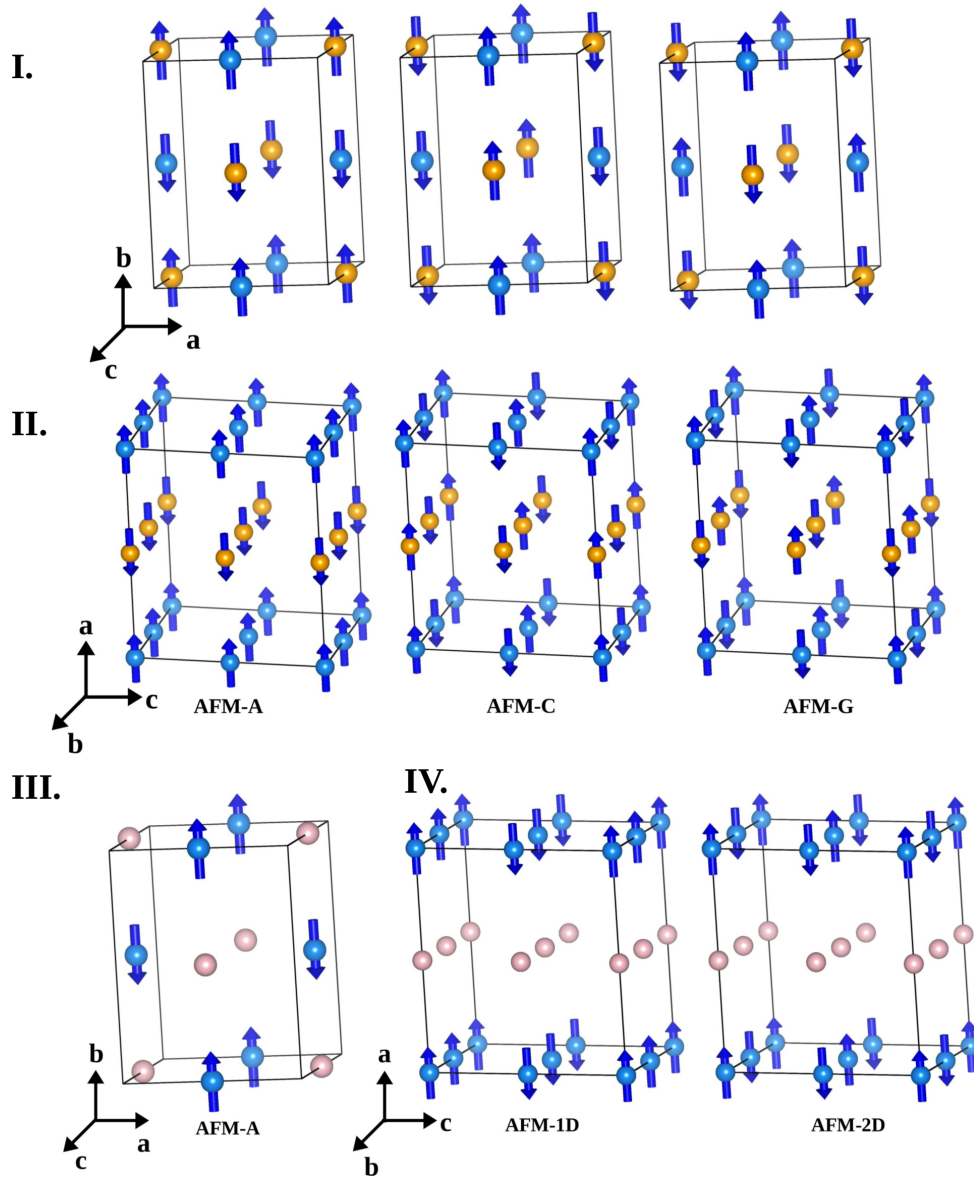


Figure 5.3: The various considered AFM magnetic structures. Panels I, II, are for rock-salt ordered, $P\bar{1}$ and layered ordered, $P2_1/m$ structured of LCIO, respectively while panels III and IV are for rock-salt ordered, $P\bar{1}$ and layered ordered, $P2_1/m$ structured of LCSO, respectively. The Cu and Ir sites are shown as blue and yellow coloured balls, while Sn sites are shown as pink coloured balls. The spins at Cu and Ir sites are as arrows.

symmetry is found to be lower than the lowest energy AFM-G configuration in $P2_1/m$ symmetry by ≈ 110 meV/f.u. While, effect of magnetism on structural stability of LCSO is found to be very small. The layered ordering continued to remain favoured over the rock-salt ordering for all different magnetic arrangements. Here, the lowest energy AFM-2D configuration in $P2_1/m$ symmetry is found to be lower than the lowest energy AFM-A configuration in $P\bar{1}$ symmetry by

≈ 596 meV/f.u., in the same order as the nonmagnetic stabilization of ≈ 544 meV/f.u.

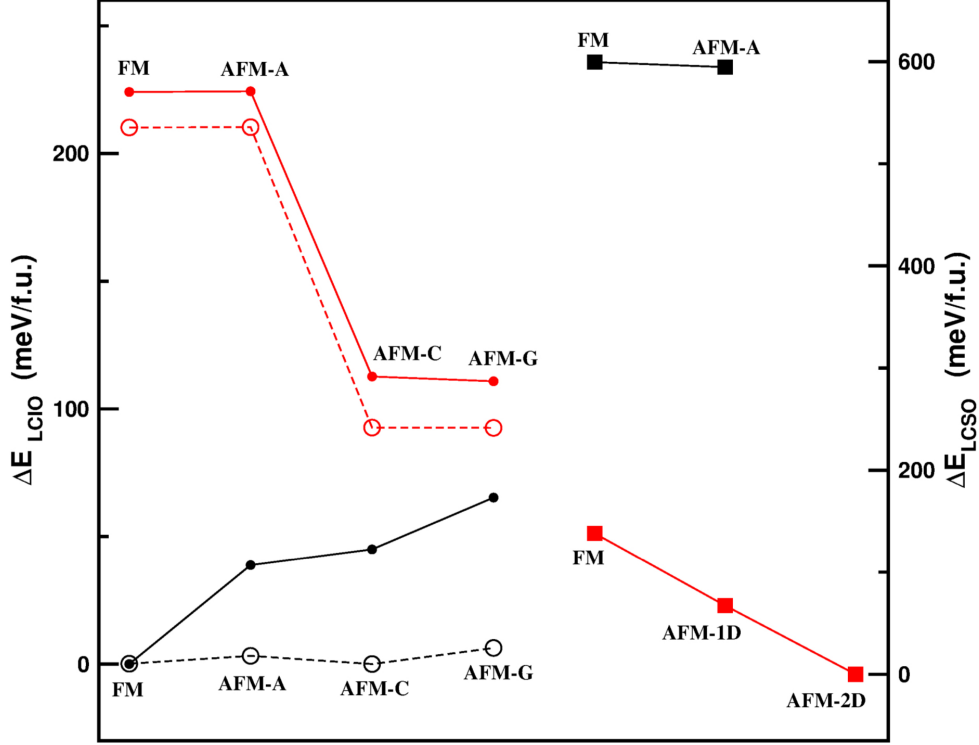


Figure 5.4: The comparison of GGA+U total energy of LCIO (circles) and LCSO (squares) between the rock-salt and layer ordered structures, considering different magnetic structures. See Fig. 5.3 for the considered magnetic structures. Plotted are the total energy differences (ΔE) for the optimized $P2_1/m$ symmetry (red symbols) structure and the $P\bar{1}$ symmetry structure (black symbols). See text for details. The positive value of ΔE for LCSO and LCIO indicates stability of $P2_1/m$ symmetry over $P\bar{1}$ symmetry, and of $P\bar{1}$ symmetry over $P2_1/m$ symmetry, respectively. The open symbols in case of LCIO represent results corresponding to GGA+U+SOC calculations

To check the effect of SOC, which is expected to be strong at Ir site, we calculated the energetics for LCIO within the GGA+U+SOC scheme of calculations as shown in Fig. 5.4 with dotted lines. From Fig. 5.4 one can see that, with inclusion of SOC general trend of structural stability remains unchanged as found within the GGA+U scheme of calculations. Calculated magneto-crystalline anisotropy energy showed the Ir moments to lie in-plane, in agreement with experimental observation [21]. Within the GGA+U+SOC scheme of calculations, we found AFM-C having Ir spins aligned in-plane as the lowest energy magnetic configuration among the other considered magnetic configurations within the unit cell of $P\bar{1}$.

5.3.4 Microscopic analysis

Analysis in terms of band structure effect

Next, we carried out electronic structure calculations for LCSO and LCIO, to gain a microscopic understanding of energetics, presented above. Fig. 5.5 shows the non spin-polarized band

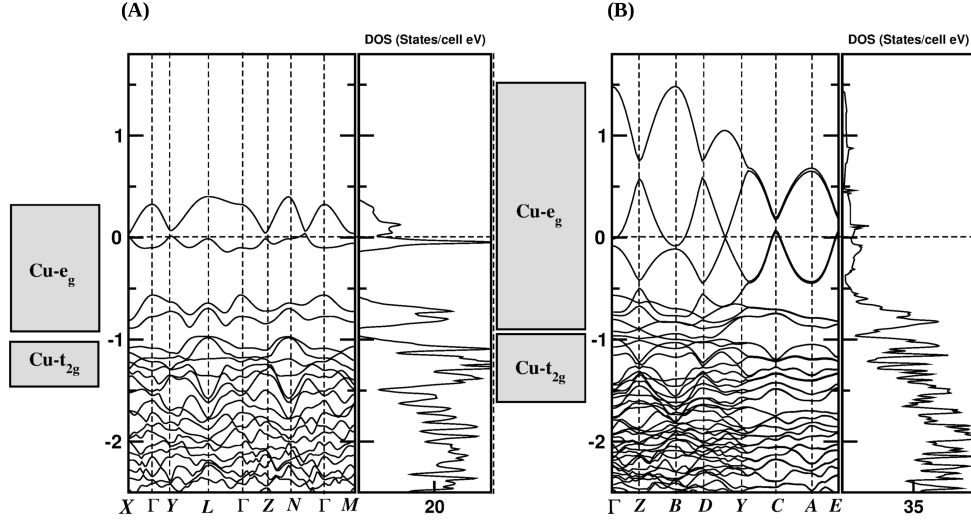


Figure 5.5: Panel (A): Non spin-polarized band structure and density of states of LCSO in the rock-salt ordered $P\bar{1}$ symmetry. Panel (B): Non spin-polarized band structure and density of states of LCSO in the layer ordered $P2_1/m$ symmetry. Band structure is plotted along the high-symmetry k-points of the triclinic (for $P\bar{1}$ symmetry) BZ and the monoclinic (for $P2_1/m$ symmetry) BZ. The zero of the energy is set at Fermi energy (E_F). The dominant orbital characters of the states are shown by side.

structure and density of states (DOS) of LCSO in the rock-salt ordered $P\bar{1}$ symmetry (left panel) and layered ordered $P2_1/m$ symmetry (right panel). Due to the octahedral crystal field, the d levels split into two main groups, t_{2g} and e_g . In LCSO compound, the JT distorted CuO_6 octahedron are elongated both in layer ordered $P2_1/m$ symmetry, and in rock-salt ordered $P\bar{1}$ symmetry [see Table 5.1]. As discussed in the introductory chapter, elongated octahedron will lead further splitting of Cu e_g states. With choice of local coordinate system having z -axis pointing along Cu to apical oxygen bond, Cu $d_{x^2-y^2}$ will lie above $d_{3z^2-r^2}$, for elongated octahedra. In the LCSO compound, Cu^{2+} is in d^9 configuration and Sn^{4+} is in d^{10} configuration. Thus, the states crossing the Fermi level (E_F) which is set at zero, are composed of Cu $d_{x^2-y^2}$ orbitals. In $P\bar{1}$ symmetry, there are two Cu $d_{x^2-y^2}$ orbitals corresponding two Cu atoms in the unit cell, crossing the E_F , while in $P2_1/m$ symmetry there are four such orbitals corresponding

four Cu atoms in the unit cell. From the Fig. 5.5 we find that band-width of the low-energy bands in layered ordered structure is significantly broader (by an amount of 75%) compared to the rock-salt ordered structure.

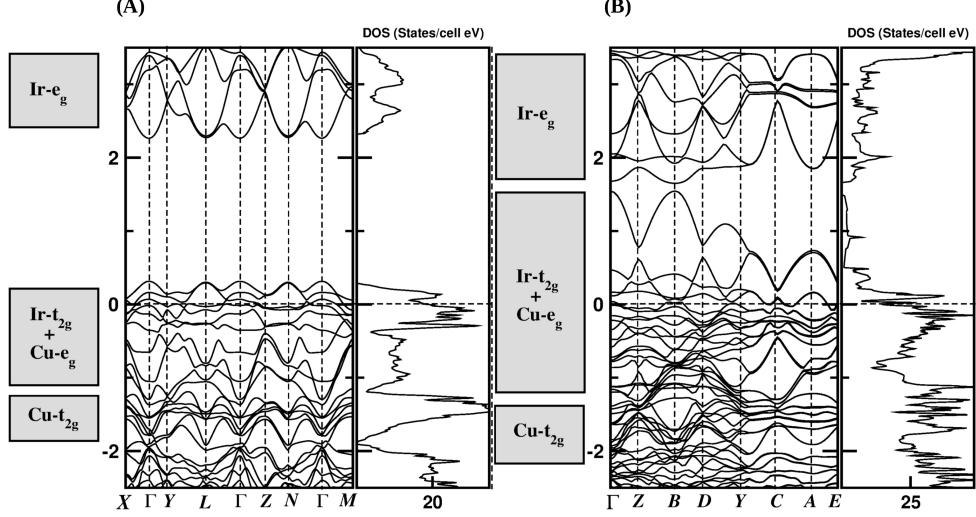


Figure 5.6: Panel (A): Non spin-polarized band structure and density of states of LCIO in the rock-salt ordered $P\bar{1}$ symmetry. Panel (B): Non spin-polarized band structure and density of states of LCIO in layer ordered $P2_1/m$ symmetry. Band structure is plotted along the high-symmetry k-points of the triclinic (for $P\bar{1}$ symmetry) BZ and the monoclinic (for $P2_1/m$ symmetry) BZ. The zero of the energy is set at Fermi energy (E_F). The dominant orbital characters of the states are shown by side.

In LCIO, Cu^{2+} is in high spin d^9 configuration, while due to the large crystal field splitting of Ir $5d$ orbital, $\text{Ir}^{4+}(d^5)$ ion is found to be stabilized in the low spin-state with one hole in the t_{2g} manifold. We note that the CuO_6 octahedra are elongated in $P2_1/m$ symmetry and compressed in $P\bar{1}$ symmetry [see Table 5.1]. Thus, the states crossing E_F in LCIO, are composed of Cu $d_{x^2-y^2}$ for $P2_1/m$ symmetry, Cu $d_{3z^2-r^2}$ for $P\bar{1}$ symmetry and the Ir t_{2g} states, as shown in Fig. 5.6. Considering the contribution of Cu $d_{x^2-y^2}$ or Cu $d_{3z^2-r^2}$, and Ir t_{2g} bands in LCIO, we found broadening of band-width in layered ordered structure compared to rock-salt ordered structure is only about 40%.

Analysis in terms of hopping parameters and Wannier functions: NMTO-downfolding calculations

We carried out NMTO-downfolding calculations to quantify the above-described band structure effect. We constructed Cu $d_{x^2-y^2}$ only low energy Hamiltonian by integrating out other degrees of freedom starting from the full non spin-polarized band structure for the ground state $P2_1/m$ symmetry as well as in the assumed $P\bar{1}$ symmetry structure of LCSO. Corresponding Wannier

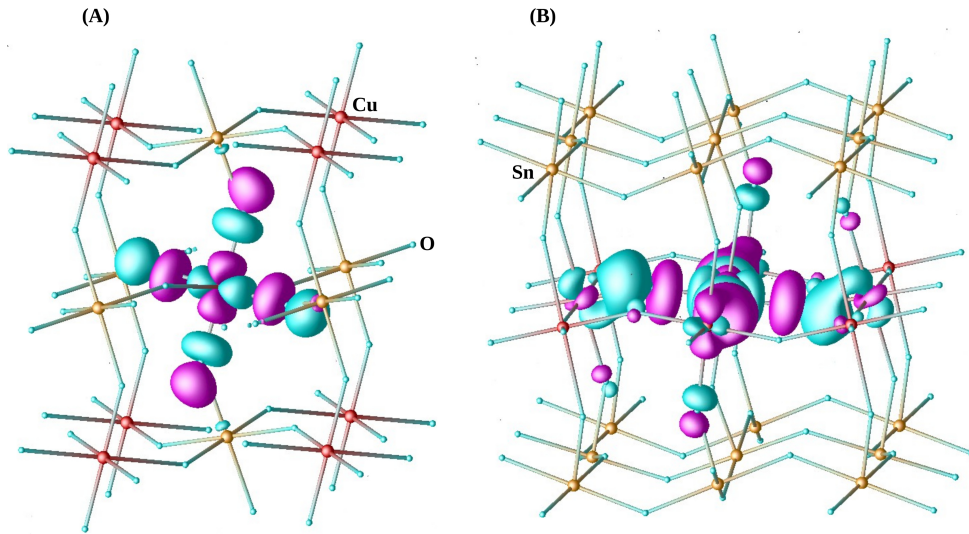


Figure 5.7: Wannier functions of effective Cu $d_{x^2-y^2}$ of LCSO for the rock-salt [panel (A)] and layer ordered [panel (B)] structures. Plotted are the constant value surfaces, with positive and negative lobes of the wavefunctions coloured differently.

functions for both the symmetries structure of LCSO are shown in Fig. 5.7. The central part of the Wannier function, positioned at Cu site, has the $d_{x^2-y^2}$ symmetry while the tails are shaped according to integrated out O-2p states. Significant weight at O sites, indicates the presence of strong antibonding Cu-O covalency. For the layered order $P2_1/m$ symmetry structure, the O-2p tails bend strongly toward the the Cu atoms [cf. Fig. 5.7(B)], indicating the strong hybridization of in plane Cu-Cu orbitals. From the real space representation of this low-energy Hamiltonian, we extracted various dominant effective Cu-Cu hopping interactions. Table 5.3 shows the various dominant effective Cu-Cu hopping interactions for both symmetries structures of LCSO. Dominant hopping paths are illustrated in Fig. 5.8, where B1(B2) is Sn1(Sn2) for LCSO and for LCIO it is Ir1(Ir2).

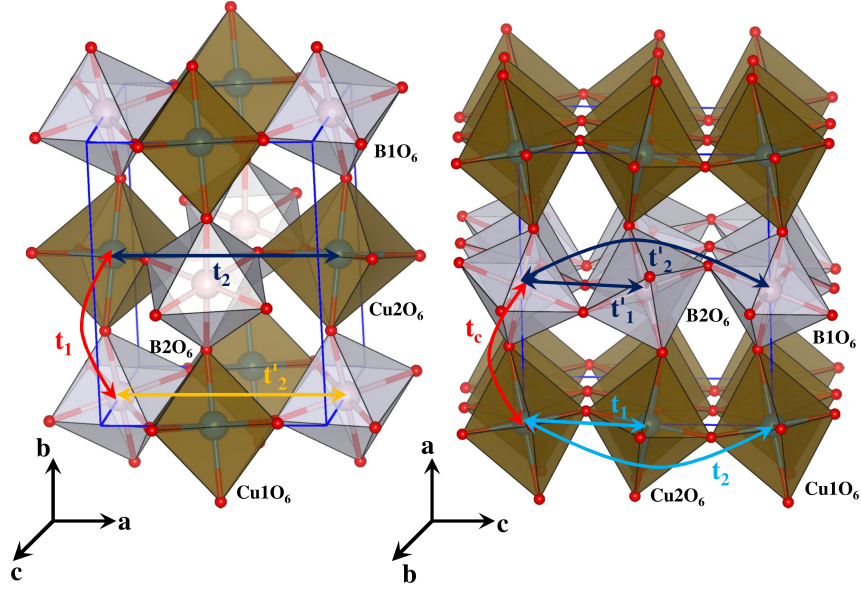


Figure 5.8: Left panel: dominant hopping path for rock-salt ordered $P\bar{1}$ symmetry structure. B1(B2) represent Ir1(Ir2) for LCIO and Sn1(Sn2) for LCSO. Right panel: dominant hopping path for layered ordered $P2_1/m$ symmetry structure.

Table 5.3: Dominant hopping integrals (in eV), as obtained from NMTO-downfolding calculation, for LCSO in $P\bar{1}$ and $P2_1/m$ symmetry. The large hoppings are marked in bold.

Compound	Connecting vector Hopping Int.	N_n	Atoms	$d_{x^2-y^2}$
LCSO ($P\bar{1}$)	$[-0.775 \ 0.004 \ 0.087]$ t_2	4	Cu1-Cu1/ Cu2-Cu2	$d_{x^2-y^2}$ -0.021
	$[0.000 \ 0.000 \ -0.501]$ t_1	4	Cu1-Cu1/Cu2	$d_{x^2-y^2}$ 0.330
LCSO ($P2_1/m$)	$[0.000 \ 0.000 \ 1.001]$ t_2	4	Cu1-Cu1 Cu2-Cu2	$d_{x^2-y^2}$ -0.015

The dominant hopping paths for the layered ordering in LCSO, are t_1 (in-plane nearest neighbour (NN) Cu-Cu) t_2 (in-plane second NN Cu-Cu) while for rock-salt ordering it is only t_2 (second NN Cu-Cu) [cf. Fig. 5.8] as Sn in the d^{10} configuration. From the Table 5.3 one can see that dominant hopping interaction t_2 in the layered structure is order of magnitude stronger than the dominant hopping interaction t_2 in the rock-salt ordered structure. This explains the stabilization of the layered structure over the rock-salt structure supporting the conclusion obtained from band structure and energetics.

Table 5.4: Dominant hopping integrals (in eV), as obtained from NMTO-downfolding calculation, for LCIO in $P\bar{1}$ and $P2_1/m$ symmetry. The large hoppings are marked in bold

Compound	Connecting vector Hopping Int.	N_n	Atoms		d_{xy}	d_{yz}	d_{xz}
LCIO ($P\bar{1}$)	$[0.000 \ 0.500 \ 0.000]$ t_1	6	Cu1-Ir2/Ir1	$d_{3z^2-r^2}$	-0.116	-0.014	-0.130
	$[-0.778 \ 0.001 \ 0.016]$ t_2	4	Cu1-Cu1 Cu2-Cu2	$d_{3z^2-r^2}$	$d_{3z^2-r^2}$ 0.017		
	$[-0.778 \ 0.001 \ 0.016]$ t'_2	4	Ir1-Ir1 Ir2-Ir2	d_{xy} d_{yz} d_{xz}	-0.002 0.008 -0.025	0.008 0.006 -0.060	-0.025 -0.060 0.016
LCIO ($P2_1/m$)	$[0.563 \ 0.000 \ -0.024]$ t_c	2	Cu1-Ir1 Cu2-Ir2	$d_{x^2-y^2}$	d_{xy} 0.005	d_{yz} 0.007	d_{xz} -0.008
	$[0.000 \ 0.000 \ 0.502]$ t_1	4	Cu1-Cu1/Cu2	$d_{x^2-y^2}$	$d_{x^2-y^2}$ -0.326		
	$[0.000 \ 0.000 \ 1.005]$ t_2	4	Cu1-Cu1	$d_{x^2-y^2}$	-0.013		
	$[0.000 \ 0.000 \ 0.502]$ t'_1	4	Ir1-Ir1/Ir2	d_{xy} d_{yz} d_{xz}	-0.029 -0.102 0.252	-0.001 -0.045 -0.061	0.009 -0.013 0.021
	$[0.000 \ 0.000 \ 1.005]$ t'_2	4	Ir1-Ir1 Ir2-Ir2	d_{xy} d_{yz} d_{xz}	-0.003 -0.002 -0.002	-0.002 -0.018 -0.033	-0.002 -0.033 -0.034

The dominant orbital characters close to E_F in the rock-salt ordered $P\bar{1}$ structure of LCIO, are Cu $d_{3z^2-r^2}$ - Ir t_{2g} states, while for layered ordering it is Cu $d_{x^2-y^2}$ - Ir t_{2g} states [cf. Fig. 5.6] Thus, for LCIO, we constructed Cu $d_{3z^2-r^2}$ - Ir t_{2g} only low energy Hamiltonian for rock-salt ordered $P\bar{1}$ symmetry and Cu $d_{x^2-y^2}$ - Ir t_{2g} only low energy Hamiltonian for layered ordered $P2_1/m$ symmetry by integrating out other degrees of freedom starting from the full non spin-polarized band structure. The dominant hopping paths for the rock-salt ordered $P\bar{1}$ structure are t_1 (NN Cu-Ir), t_2 (second NN Cu-Cu) and t'_2 (second NN Ir-Ir) while for layered ordered $P2_1/m$ structure these are t_1 (in plane NN Cu-Cu), t_2 (in plane second NN Cu-Cu), t'_1 (

in plane NN Cu-Cu) and t'_2 (in plane second NN Cu-Cu) [cf. Fig. 5.8]. Table 5.4 shows the dominant hopping integrals for both the symmetries structure of LCIO. The combined effect of large t_1 and t'_1 hopping in the layered structure is found to be more stronger than the t_1 in the rock-salt ordered structure. This explains the stabilization of the layered structure over the rock-salt structure for the non-magnetic LCIO in agreement with the conclusion from non-magnetic energetics calculations [cf. Fig. 5.2]. For the Wannier function plot, we carried out

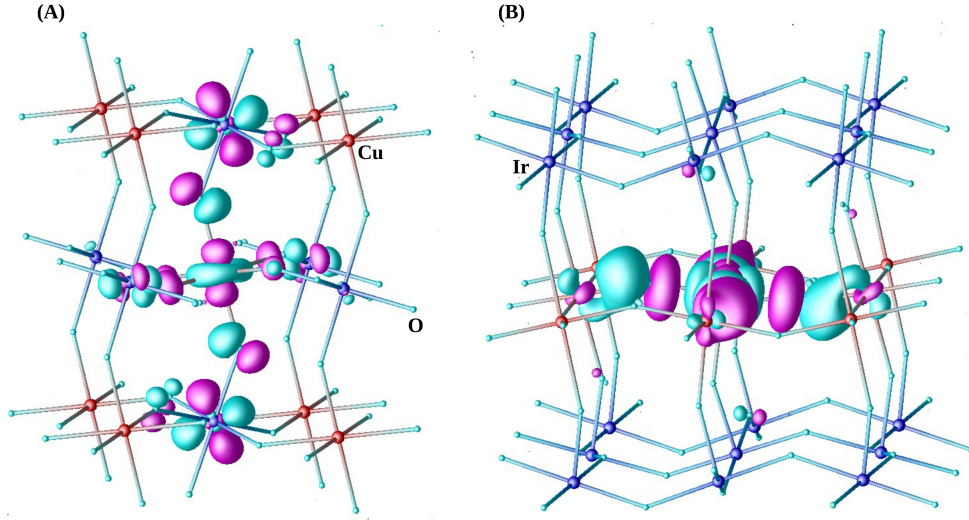


Figure 5.9: Wannier functions of effective Cu $d_{3z^2-r^2}$ for the rock-salt [panel (A)] and Cu $d_{3z^2-r^2}$ for layer ordered [panel (B)] structures of LCIO. Plotted are the constant value surfaces, with positive and negative lobes of the wavefunctions coloured differently

massive downfolding, where we kept only Cu $d_{3z^2-r^2}$ (for rock-salt ordered $P\bar{1}$) or $d_{x^2-y^2}$ (for layer ordered $P2_1/m$) active and integrated the rest. The corresponding Wannier functions for both the symmetries structure of LCIO are shown in Fig. 5.9. The central part of the Wannier function, positioned at Cu site, has the $d_{3z^2-r^2}$ or $d_{x^2-y^2}$ symmetry while the tails are shaped according to integrated out O- $2p$ or Ir- t_{2g} states. Significant weight at O sites, indicates the presence of strong anti-bonding Cu-O covalency. In the rock-salt ordered $P\bar{1}$ symmetry structure, Wannier function shows appreciable weight at neighbouring Ir [cf. Fig. 5.9(A)], indicating well defined Cu-O-Ir super-exchange path. On the other hand, in the layered ordered structure, the weight at the out-of plane Ir site is comparatively negligible [cf. Fig. 5.9(B)]. This super-exchange driven Cu-Ir magnetism contributes to a large extent in lowering the energy of the rock-salt ordering compared to layered ordering.

5.3.5 Electronic structure of magnetic $\text{La}_2\text{CuSnO}_6$

From the total energy calculations of different considered magnetic structure, we found AFM-2D (antiferromagnetic ordering of in plane Cu^{2+} spins) to be the lowest energy magnetic configuration in the ground state $\text{P2}_1/\text{m}$ symmetry [cf. Fig. 5.4], in agreement with experimental prediction based on temperature dependent susceptibility measurement [10]. Fig. 5.10 shows

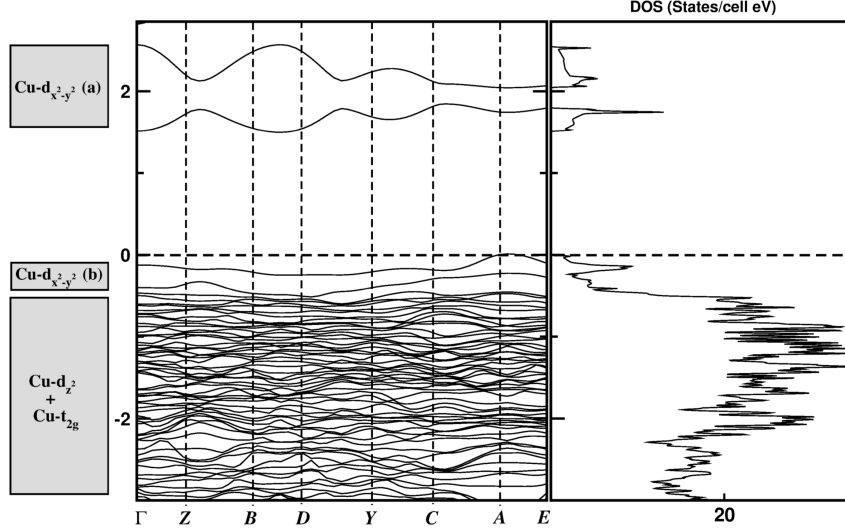


Figure 5.10: The band structure and density of states of LCSO in magnetically ordered ground state of AFM-2D in layer ordered $\text{P2}_1/\text{m}$ symmetry within GGA+U scheme of calculation. Band structure is plotted along the high-symmetry k-points of the monoclinic BZ. The zero of the energy is set at E_F . The dominant orbital characters of the states are shown by side, with $\text{Cu } d_{x^2-y^2}$ (a)/(b) denoting the minority/majority spin bands.

band structure and density of states (DOS) corresponding to AFM-2D magnetic ground state, calculated within GGA+U approach for layer-ordered $\text{P2}_1/\text{m}$ structure of LCSO. Note that, for AFM magnetic structure up and down spin channels are completely identical and thus we showed only one spin channel in the Fig. 5.10. Upon introduction of 2D antiferromagnetism and correlation effect within the framework of GGA+U, $\text{Cu } d_{x^2-y^2}$ became completely filled in majority spin channel while completely empty in minority spin channel, making magnetic ground state insulating, in agreement with experimental observation based on conductivity measurement [10].

5.3.6 Electronic structure of magnetic $\text{La}_2\text{CuIrO}_6$

In Fig. 5.11, we show, band structure and DOS of LCIO, considering the AFM-C magnetic structure which is found to be lowest in energy in the rock-salt ordered structure, within the GGA+U and GGA+U+SOC scheme of calculation.

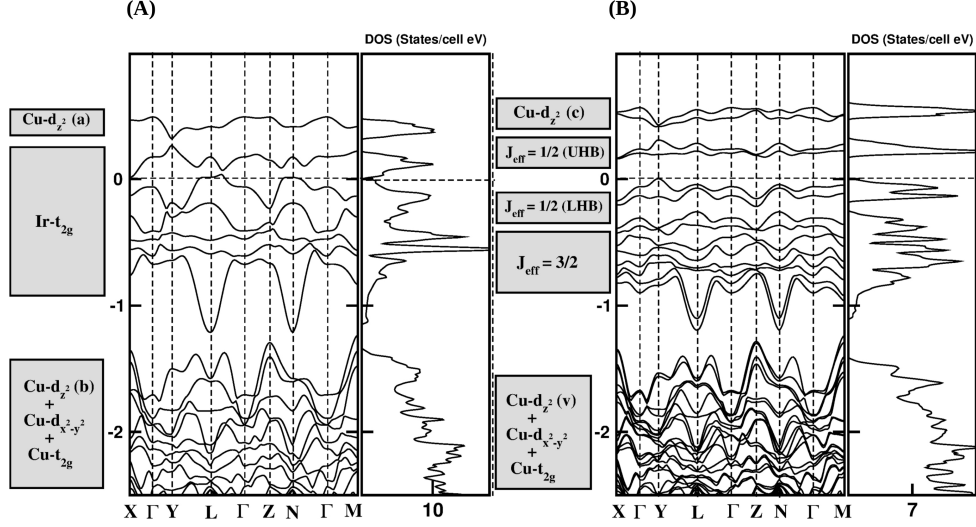


Figure 5.11: The band structure and density of states of LCIO in magnetically ordered state of AFM-C in rock-salt ordered $P\bar{1}$ symmetry within GGA+U [panel (A)] and GGA+U+SOC [panel (B)] scheme of calculations. Band structure is plotted along the high-symmetry k-points of the triclinic BZ. The zero of the energy is set at E_F . The dominant orbital characters of the states are shown by side. Cu $d_{x^2-y^2}$ (a)/(b) denotes the minority/majority spin bands, while Cu- d_{z^2} (c)/(v) denotes the UHB and LHB bands of Cu $d_{3z^2-r^2}$

Introduction of large U , together with large spin-splitting at Cu site, make Cu $d_{z^2-r^2}$ completely filled in majority spin channel while empty in minority spin channel. Ir- t_{2g} dominated six bands corresponding two Ir atom in the unit cell, appear in between the spin-split levels of Cu $d_{z^2-r^2}$. These Ir t_{2g} bands span in the energy range between 0.1 –1.20 eV, which are 5/6 filled, making the magnetic ground state metallic [cf. Fig. 5.11(A)]. We found, the nature of magnetic ground state remained unchanged for increase of U value within 0.5-1.0 eV.

A significant change is observed in the band structure upon inclusion of SOC. From the Fig. 5.11(B), one can see that inclusion of SOC together with Hubbard U , split the Ir t_{2g} manifold into group of 8, 2 and 2 bands. In the limit of strong SOC the t_{2g} states (with an effective quantum state $l_{eff} = 1$ [24]) of Ir^{4+} can split into $j_{eff} = 1/2$ doublet and $j_{eff} = 3/2$ quartet as disused initially in the context of layered Sr_2IrO_6 compound [17,18]. $j_{eff} = 1/2$ doublet would

be higher in energy compared to $j_{eff} = 3/2$ quartet, since j_{eff} is produced from $j_{5/2}$ manifold due to the large crystal field splitting. Therefore the branch of total eight bands of two Ir in the unit cell correspond to $j_{eff} = 3/2$ quartet while remaining four bands of two Ir around E_F belong to the $j_{eff} = 1/2$ doublet. Among the total 10 Ir- d electrons in the unit cell, $j_{eff} = 3/2$ contains 8 electrons being completely filled and remaining 2 electrons occupy $j_{eff} = 1/2$, making $j_{eff} = 1/2$ bands half-filled. Upon inclusion of small but finite U , splits the $j_{eff} = 1/2$ bands into completely filled lower Hubbard band (LHB) and completely empty upper Hubbard band (UHB). This results into a semiconducting solution with a gap of ≈ 0.3 eV, in agreement with findings of recent study [25]. This confirms LCIO to be a $j_{eff} = 1/2$ Mott insulator.

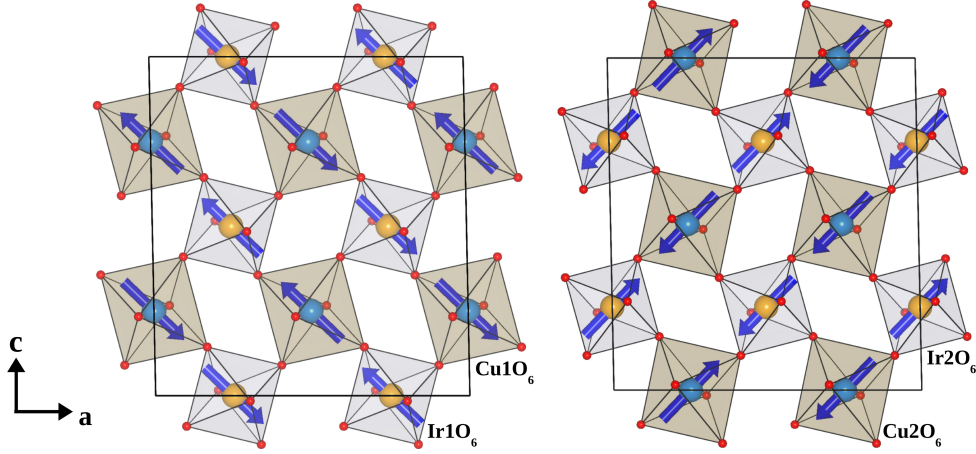


Figure 5.12: experimental determined magnetic structure of LCIO, stabilized in a $2 \times 1 \times 2$ supercell of $P\bar{1}$ symmetry. The Cu and Ir sites are shown as blue and yellow coloured balls.

Fig. 5.12 shows very recently proposed magnetic structure of LCIO, based on low-temperature neutron diffraction data [21]. To realize this magnetic structure (*i.e.* collinear AFM spin arrangement in every ac plane and mutually orthogonal spin orientations in neighbouring planes) we constructed $2 \times 1 \times 2$ supercell of $P\bar{1}$ triclinic cell. Comparing the energy of this magnetic structure with the lowest energy magnetic structure realized within the unit cell of $P\bar{1}$ *i.e.* AFM-C, we found that the former is lower in energy by about 15 meV/f.u. The calculated band structure and DOS corresponding this magnetic arrangement shows similar features as shown in the Fig. 5.11(B), with a SOC assisted Mott gap. In Table 5.5, we show calculated spin and orbital moment at different Cu and Ir site corresponding to the experimentally suggested magnetic ground state. The orbital moment at Cu sites is found to be very large (by an amount

$\approx 0.32 \mu_B$) pointing parallel to the spin moment due to the more than half-filled nature of Ir- t_{2g} occupancies.

Table 5.5: Calculated magnetic (spin and orbital) moments (in μ_B) of Cu and Ir in LCIO for experimentally determined magnetic structure of $P\bar{1}$

Site	S_x	S_y	S_z	L_x	L_y	L_z	M_x	M_y	M_z
Cu1(1)	-0.548	0.003	0.215	-0.039	0.017	0.097	-0.587	0.020	0.312
Cu1(2)	0.552	-0.004	-0.209	0.040	-0.017	-0.098	0.592	-0.021	-0.307
Cu1(3)	0.549	-0.011	-0.215	0.039	-0.017	-0.098	0.588	-0.028	-0.313
Cu1(4)	-0.543	-0.011	0.227	-0.038	0.017	0.098	-0.581	0.006	0.325
Cu2(1)	0.398	-0.091	0.421	0.085	-0.007	-0.014	0.483	-0.098	0.407
Cu2(2)	-0.393	0.085	-0.429	-0.085	0.007	0.012	-0.478	0.092	-0.417
Cu2(3)	-0.406	0.081	-0.417	-0.085	0.008	0.014	-0.491	0.089	-0.403
Cu2(4)	0.395	-0.080	0.428	0.085	-0.007	-0.013	0.480	-0.087	0.415
Ir1(1)	-0.175	-0.024	0.065	-0.299	-0.077	0.125	-0.474	-0.101	0.190
Ir1(2)	0.182	0.022	-0.065	0.297	0.073	-0.136	0.479	0.095	-0.201
Ir1(3)	0.177	0.016	-0.061	0.300	0.068	-0.128	0.477	0.084	-0.189
Ir1(4)	-0.178	-0.030	0.069	-0.296	-0.084	0.132	-0.474	-0.114	0.201
Ir2(1)	-0.183	-0.002	0.319	0.142	0.039	0.351	-0.041	0.037	0.670
Ir2(2)	0.181	-0.003	-0.318	-0.146	-0.044	-0.348	0.035	-0.047	-0.666
Ir2(3)	0.182	-0.002	-0.319	-0.144	-0.042	-0.349	0.038	-0.044	-0.668
Ir2(4)	-0.183	-0.002	0.318	0.134	0.045	0.353	-0.049	0.043	0.671

5.4 Summary and conclusions

Considering the examples of $\text{La}_2\text{CuIrO}_6$ and $\text{La}_2\text{CuSnO}_6$, we have carried out DFT-based first principles calculation to gain microscopic understanding on the issue of B-cation arrangements in double perovskites. Calculations of energetics considering non spin-polarized scheme of calculation which is expected to take primarily band structure effect, showed stabilization of layered structure in both LCSO and LCIO compounds. From the calculation of hopping interactions we found that presence of large in plane nearest neighbour Cu $d_{x^2-y^2}$ - Cu $d_{x^2-y^2}$ hopping favoured the layered ordering over the rock-salt ordering. Introduction of magnetic interaction is found to be crucial in LCIO compound to stabilize layered ordering over rock-salt ordering while it's effect is found to be minimal in the structural stability of LCSO. This reversing in relative structural stability (*i.e.* stability of rock-salt ordering over layered ordering) is found to be driven by the strong Cu-Ir super-exchange interaction. Presence of SOC at Ir site kept the stability of

rock-salt ordering over layered ordering unperturbed. We found Consideration of enthalpy does not effect the general trend of structural stability as obtained from energetics for both LCIO and LCIO. Our rigorous study interms of energetics, electronic structure calculation and NMTO downfolding calculation showed that presence of magnetic ion at B' site of double perovskite $\text{A}_2\text{BB}'\text{O}_6$, is extremely important in order to maintain the magnetism driven stability of rock-salt ordered structure over layered ordered structure. In order to confirm the rigorousness of our conclusion, we have further carried out calculations on $\text{La}_2\text{CuMnO}_6$ (LCMO) compound. The details of the results are given in the section 5.5. We found that following our prediction, while in absence of magnetism the layered ordering is favoured over rock- salt, turning on magnetism reverses the stability, making rock-salt favored over layered, in conformity with experimental observation [11]. We hope that our findings will shed more light on the problem of cation ordering in double perovskites.

We also found presence of strong SOC coupling at Ir site which splits the Ir- t_{2g} bands into $j_{eff} = 1/2$ doublet and $j_{eff} = 3/2$ quartet. Calculated band structure and DOS with the scheme of GGA+U+SOC calculation, showed, LCIO to be a $j_{eff} = 1/2$ Mott insulator in agreement with finding of recent literature [25].

5.5 Structural stability of $\text{La}_2\text{CuMnO}_6$ (LCMO)

Experimentally measured crystal structure of LCMO is reported to be that of cubic Fm-3m space group [8] with rock-salt ordering of CuO_6 and MnO_6 octahedra [cf. Fig. 5.13(I)]. To study the relative structural stability of LCMO, between rock-salt and layered ordering of Cu and Mn sites, we considered LCMO in the experimentally measured Fm-3m symmetry of rock-salt ordered structure as well as in the $\text{P2}_1/\text{m}$ symmetry of layer ordered structure. For both the symmetry structures, the lattice parameters as well as the internal coordinates are relaxed completely. Within the non-spin polarized scheme of calculation, the relative structural stability of LCMO, between rock-salt ordering and layered ordering, in terms of energetics, is shown in left side of Fig. 5.13(II), where $\Delta E_{non} = E_{non}(\text{Fm-3m}) - E_{non}(\text{P2}_1/\text{m})$, $E_{non}(\text{Fm-3m})$ and $E_{non}(\text{P2}_1/\text{m})$ being the energies of the optimized nonmagnetic Fm-3m symmetry and $\text{P2}_1/\text{m}$ symmetry structure, respectively. We found that the $\text{P2}_1/\text{m}$ symmetry structure with layered

ordering of Cu and Mn sites, is favoured compared to Fm-3m symmetry structure. The energy gain in the layer ordered structure is found to be around 115 meV/f.u. Next, we compared

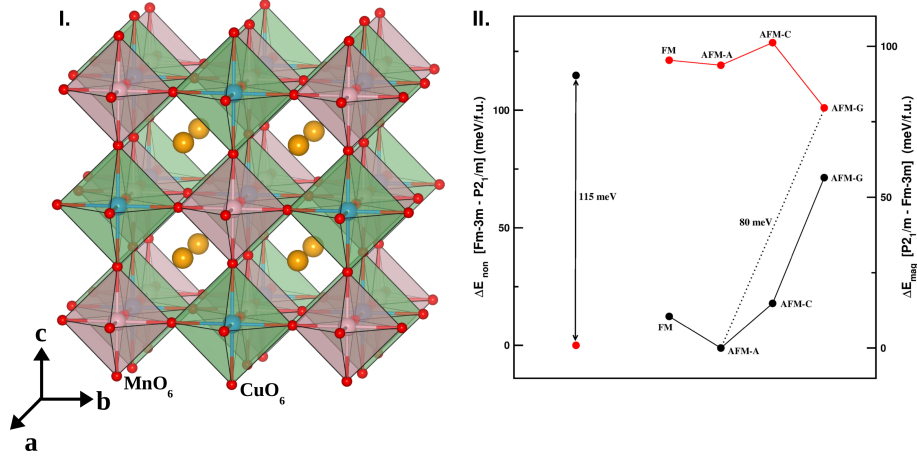


Figure 5.13: Panel I: Crystal structure of Fm-3m space group of LCMO, showing the rock-salt ordering of CuO_6 (green color) and MnO_6 (pink color) octahedra. Panel II: (left side) The non spin-polarized total energy difference (ΔE) of LCMO between the optimized Fm-3m symmetry structure (black symbol) and P2₁/m symmetry (red symbol) structure. The positive value of ΔE indicates stability of P2₁/m symmetry over Fm-3m symmetry. Right side: The comparison of GGA+U total energy between the rock-salt and layer ordered structures, considering different magnetic structures. Plotted are the total energy differences (ΔE) for the optimized P2₁/m symmetry (red symbols) structure and the Fm-3m symmetry structure (black symbols). The positive value of ΔE indicates stability of Fm-3m symmetry over P2₁/m symmetry.

the total energies of rock-salt and layer-ordered structures, considering the effect of magnetism. To do so, apart from ferromagnetic (FM) structure with parallel alignment of Cu and Mn, we considered three different antiferromagnetic (AFM) structures (AFM-A, AFM-C, AFM-G), possible within the unit cell of rock-salt ordered Fm-3m symmetry structure [cf. Fig. 5.3(I)] and layer-ordered P2₁/m symmetry structure [cf. Fig. 5.3(II)]. Considering different magnetic structures, the DFT calculated energetics within GGA+U scheme of calculation are shown in right side of Fig. 5.13(II), where $\Delta E_{\text{mag}} = E(\text{P2}_{1/m}) - E_{\text{AFM-A}}(\text{Fm-3m})$, $E_{\text{AFM-A}}(\text{Fm-3m})$ and $E(\text{P2}_{1/m})$ being the energies of the optimized Fm-3m symmetry structure in AFM-A phase and that of optimized P2₁/m symmetry structure in different magnetic structures, respectively. As clearly seen from Fig 5.13(II), magnetism helps to stabilize the rock-salt ordering over the layer ordering, irrespective of the considered magnetic structures, as found in the case of LCIO. The lowest energy AFM-A configuration in the rock-salt ordered Fm-3m symmetry structure is found to be lower in energy compared to the lowest energy AFM-G configuration in P2₁/m symmetry structure by an amount ≈ 80 meV/f.u.

Bibliography

- [1] J. B. Philipp, P. Majewski, L. Alff, A. Erb, R. Gross, T. Graf, M. S. Brandt, J. Simon, T. Walther, W. Mader, D. Topwal, and D. D. Sarma, Phys. Rev. B 68, 144431 (2003).
- [2] S. Vasala and M. Karppinen, Prog. Solid State Chem. 43, 1-36 (2015).
- [3] M. Azuma *et al.*, J. Am. Chem. Soc. 127, 8889 (2005).
- [4] K. I. Kobayashi, T. Kimura, H. Sawada, K. Terakura, and Y. Tokura, Nature 395, 677 (1998)
- [5] N. S. Rogado, J. Li, A. W. Sleight, and M. A. Subramanian, Adv. Mater. 17, 2225 (2005).
- [6] Hena Das, Umesh V. Waghmare, T. Saha-Dasgupta, and D. D. Sarma, Phys. Rev. Lett. 100, 186402 (2008).
- [7] Hena Das, Molly De Raychaudhury, and T. Saha- Dasgupta, Appl. Phys. Lett. 92, 201912 (2008).
- [8] Mark T. Anderson, Kevin B. Greenwood, Gregg A. Taylor, and Kenneth R. Poeppelmeier, Prog Solid State Chem. 22, 197 (1993)
- [9] M. W. Lufaso , P. M. Woodward, Acta Crystallogr Sect B Struct. Sci. 60, 10 (2004).
- [10] Mark T. Anderson and Kenneth R. Poeppelmeier, J. Solid State Chem. 102, 164 (1993).
- [11] Masaki Azuma, Shingo Kaimori, and Mikio Takano, Chem. Mater. 10, 3124 (1998).
- [12] N. Ramadass, J. Gopalakrishnan, M. V. C. J. Sastri, Inorg. Nucl. Chem. 40, 1453 (1978).
- [13] G. J. Blasse, Inorg. Nucl. Chem. 27, 993 (1965)

-
- [14] F. Wang and T. Senthil, Phys. Rev. Lett. 106 136402 (2011)
- [15] X. Wan *et al.* Phys. Rev. B 83 205101 (2011)
- [16] G. Jackeli and G. Khaliullin, Phys. Rev. Lett. 102 017205 (2009).
- [17] B. J. Kim, H. Jin, S. J. Moon, J. Y. Kim, B. G. Park, C. S. Leem, J. Yu, T. W. Noh, C. Kim, S. J. Oh, J. H. Park, V. Durairaj, G. Cao, E. Rotenberg, Phys. Rev. Lett. 101, 076402 (2008).
- [18] B. J. Kim, H. Ohsumi, T. Komesu, S. Sakai, T. Morita, H. Takagi, T. Arima, Science, 323, 1329 (2009).
- [19] G. Cao, A. Subedi, S. Calder, J. Q. Yan, J. Yi, Z. Gai, L. Poudel, D. J. Singh, M. D. Lumsden, A. D. Christianson, B. C. Sales, D. Mandrus, Phys. Rev. B 87, 155136 (2013).
- [20] A. V. Powell, J. G. Gore and P. D. Battle, Journal of Alloys and Compounds, 201 73 (1993).
- [21] Kaustuv Manna *et al.*, Phys. Rev. B 94, 144437 (2016).
- [22] R. D. Shannon, Acta. Crystallogr. A 32 751 (1976).
- [23] D. Serrate, J.M. De Teresa, and M. R. Ibarra, J. Phys.: Condens. Matter 19, 023201 (2007).
- [24] Daniel H. Khomskii, Transition Metal Compounds, Cambridge University Press, (2014).
- [25] W. K. Zhu, J.-C. Tung, W. Tong, L. Ling, M. Starr, J. M. Wang, W. C. Yang, Y. Losovyj, H. D. Zhou, Y. Q. Wang, P.-H. Lee, Y.-K. Wang, Chi-Ken Lu, and S. X. Zhang, arXiv:1608.07763.

Chapter 6

Half-Metallic Behavior in Doped $\text{Sr}_2\text{CrOsO}_6$ Double Perovskite with High Transition Temperature[†]

6.1 Introduction and motivation

Half-metals having metallic behavior in one spin channel and insulating behavior in opposite spin channel, are typically characterized by metallic conductivity with an integer spin moment at $T = 0\text{K}$ [1, 2]. Half-metals have potential application possibility in the field of spintronic as they allow spin-polarized current to flow without any external operation [3]. Ordered double perovskites ($\text{A}_2\text{BB}'\text{O}_6$) consisting of alkaline-earth or rare-earth metal ion at A site and two different transition metal ions at B and B' sites, are potential candidates showing half-metallic character. Observation of half-metallicity as well as large low-field tunneling magnetoresistance (TMR) at room temperature in double perovskite $\text{Sr}_2\text{FeMoO}_6$ with fairly high transition temperature (T_c) $\approx 410\text{K}$ [4] indicated promise in double perovskite compound [5]. Later few

[†] This chapter is based on publication: Kartik Samanta, Prabuddha Sanyal and T. Saha-Dasgupta, Sci. Rep. 5, 15010 (2015).

more double perovskite compounds have been identified showing half-metallic behaviour such as Sr_2CrWO_6 with transition temperature $T_c \approx 458$ K [6] and $\text{Sr}_2\text{CrMoO}_6$ with transition temperature $T_c \approx 450$ K [7,8]. Operating temperature of half-metallic magnetic materials, needs to be sufficiently below the T_c for the full moment to develop and also to avoid the demagnetization effect. This suggests the need of half-metallic magnetic materials with T_c as much higher than room temperature as possible, so that room temperature applications can be made. As, in the literature there exists very few half-metallic double perovskite compounds with high T_c , it is therefore very important to search and understand the occurrence of half-metallic magnetic materials with high T_c .

In search of such materials, we considered Cr-based double perovskite $\text{Sr}_2\text{CrOsO}_6$ for investigation. This material is very important in the sense that compound has spectacular high T_c of 725 K [9], highest ever known in the oxide family with a finite net moment in the ground state. In its ground state, $\text{Sr}_2\text{CrOsO}_6$ is a ferrimagnetic insulator [9] with a large band gap. Our aim is to drive the half-metallic state in $\text{Sr}_2\text{CrOsO}_6$, maintaining the high magnetic transition temperature T_c . Previous study [10] of partial doping of La at Sr site of $\text{Sr}_2\text{FeMoO}_6$ showed an increase of T_c of about 70 K and also observation of novel state has been reported for large La doping [11–13]. A very recent theoretical work [14] based on dynamical mean field theory calculations, proposed that starting from half-filled antiferromagnetic correlated band insulator, in which up and down spins are at two inequivalent sites, one can obtain a half-metallic ferrimagnet. These findings and observations strongly motivated us to study the effect of doping in $\text{Sr}_2\text{CrOsO}_6$. In this present study we have explored the possibility of driving half-metallicity in $\text{Sr}_2\text{CrOsO}_6$ by La and Na doping at Sr site.

To explore this possibility we have carried out DFT based first-principles calculations together with exact diagonalization of Cr-Os model Hamiltonian constructed in a first-principles derived Wannier function basis.

6.2 Computational details

The first-principles DFT calculations were carried out using full potential linear augmented plane wave (FLAPW) basis as implemented in the Wien2k code. For the self-consistent calculation in LAPW, we used 108 k-points in the irreducible part of Brillouin zone. The wave functions were expanded in plane waves with a cut-off $R_{MT}k_{max} = 7.0$, where R_{MT} is the smallest muffin-tin sphere radius and k_{max} is the magnitude of the largest k vector in the plane wave expansion. Spin-orbit coupling has been included in the calculation as a perturbation to the original Hamiltonian and was dealt using the second variational scheme. We considered the exchange correlation functional to be that of generalized gradient approximation (GGA), implemented following the Perdew-Burke-Ernzerhof (PBE) prescription. The missing strong electron-electron correlation at magnetic ions Cr and Os was taken into account through supplemented Hubbard U (GGA+U) calculation. We chose the typical U values for 3d (Cr) and 5d (Os) transition metal ions. The results reported in this chapter have been obtained for $U(\text{Cr}) = 4.8$ eV and $U(\text{Os}) = 1.8$ eV, with Hund's coupling energy J_H of 0.8 eV. We have checked the validity of our results by varying U value by +/- 1 V at Cr site and by +/- 0.5 eV at Os site. The trend of our result was found to remain unchanged.

For extraction of a few-band, tight-binding Hamiltonian out of full DFT calculation which has been used as input to multi-orbital, low energy Hamiltonian based calculations, we have carried out muffin-tin orbital (MTO) based NMTO-downfolding calculations. The constructed multi-orbital low energy Hamiltonian has been solved by means of real space based exact diagonalization technique on a lattice of finite dimensions $8 \times 8 \times 8$. Calculations have been checked as well for lattices of different size but trend was found to remain unchanged. The consistency of the calculations in different basis sets has been cross checked interms of density of states and band structure calculations.

6.3 Results and discussion

6.3.1 Results for parent compound $\text{Sr}_2\text{CrOsO}_6$

We considered parent compound $\text{Sr}_2\text{CrOsO}_6$, in its cubic Fm-3m space group with lattice constant 7.82 \AA [9]. Basic structural units of this compound are corner sharing two regular octahe-

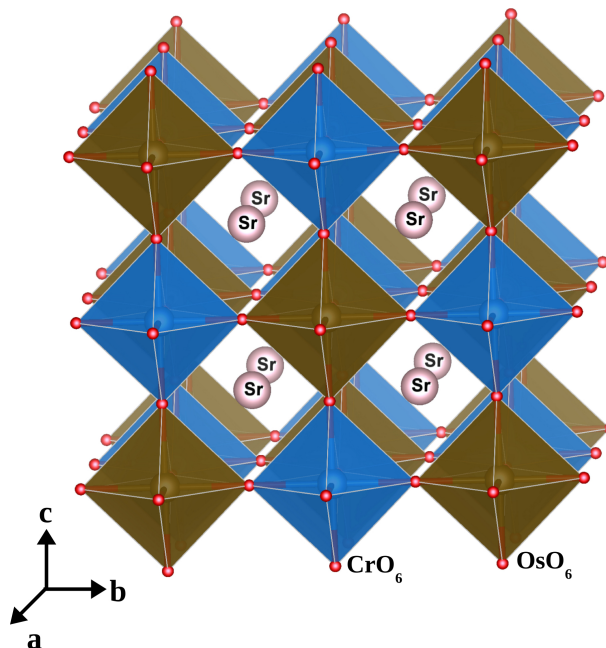


Figure 6.1: The cubic structure of $\text{Sr}_2\text{CrOsO}_6$ in Fm-3m space group. The small red balls represent O atoms.

drons (CrO_6 and OsO_6) which alternate along three crystallographic axis, creating rock-salt like arrangement [cf. Fig. 6.1]. Selected bond lengths for the parent compound are listed in Table 6.1.

Table 6.1: Structural parameters and selected bond lengths of experimentally measured parent compound $\text{Sr}_2\text{CrOsO}_6$.

Unit	description	bond length (\AA)
	Cr-O distance	
CrO_6	Cr-O \times 6	1.948
	Os-O distance	
OsO_6	Os-O \times 6	1.965

DFT calculated magnetic moments for the parent compound are shown in Table 6.2. Table 6.2 shows that in absence of spin-orbit coupling (SOC), within the GGA+U scheme of calculation, the parent compound is a compensated ferrimagnet with zero net moment. The calculation converges to antiparallel alignment of the Cr and Os spins with spin moment $+2.36$ and $-1.57 \mu_B$, respectively within GGA+U scheme of calculation, giving rise to a ferrimagnetic ground state in agreement with experimental observation [9]. Calculated values of spin moments at Cr and Os sites indicate that both the Cr and Os are in d^3 configuration. In the simplest approximation

Table 6.2: Calculated magnetic moments (in μ_B) of parent compound $\text{Sr}_2\text{CrOsO}_6$

$\text{Sr}_2\text{CrOsO}_6$ sites	GGA+U	GGA+U+SOC		
	spin (M_s)	spin (M_s)	orbital (M_L)	total (M_{tot})
Cr	2.36	2.39	-0.04	2.35
Os	-1.57	-1.49	0.13	-1.36
O	-0.10	-0.10	-	-0.10
Total/f.u.	0.00			0.25

one would expect the spin moments M_s to be equal to the number of unpaired electrons, namely, 3 for Cr(III) and 3 for Os(V). The calculated value of M_s is 21% smaller than the nominal value for Cr(III) and 48% smaller for Os(V). This reduction is predominantly due to covalency with the surrounding oxygen ions which is expected to be higher for highly delocalized $5d$ orbitals of Os(V). Inclusion of SOC gives rise to finite orbital moment at Os site which points opposite to that of spin moments. This makes the parent compound an uncompensated ferrimagnet with a net moment, in agreement with experimental observation [9]. Thus presence of SOC is very important to get the net moment in the ground state.

Therefore to understand the electronic structure of parent compound, we calculated spin-polarized density of states (DOS) within GGA+U+SOC scheme of calculation, which is shown in Fig 6.2. As is evidenced from Fig 6.2, the states close to Fermi level (E_F) are dominated by Cr and Os d states hybridized with O p states, while the O p dominated states are separated from Cr and Os d dominated states occupy the energy range far below E_F . Sr s and d dominated states remain far above E_F . The d states of Cr and Os ions are exchange split as well as crystal field split. Both the Cr and Os are in the regular octahedron environment of oxygen ions. Within the crystal field of regular octahedron, d levels split into t_{2g} and e_g states. From the Fig. 6.2

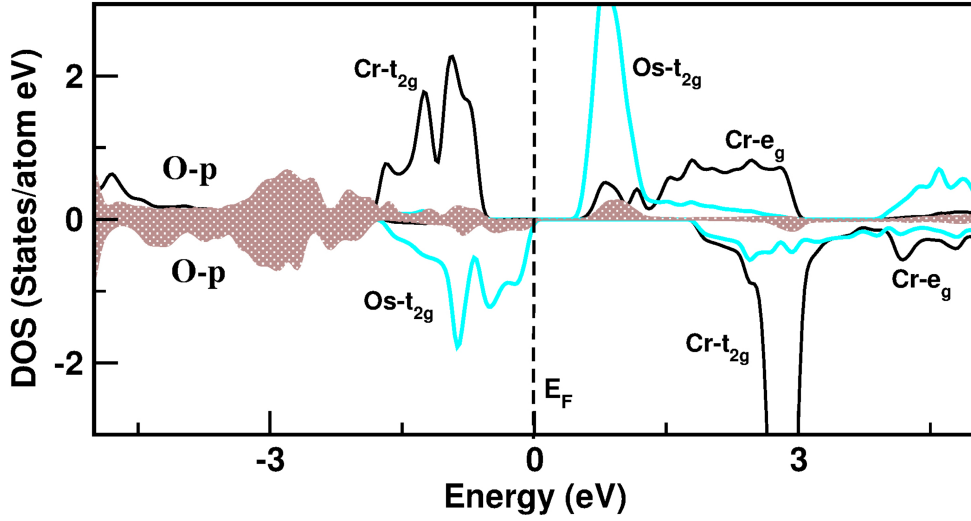


Figure 6.2: GGA+U+SOC density states of parent compound, $\text{Sr}_2\text{CrOsO}_6$, projected onto Cr d (black solid lines), Os d (cyan solid lines) and O p (brown shaded area). Zero of the energy is set at E_F .

one can see that in the majority spin channel, Cr t_{2g} states are completely filled while the Cr e_g states remain empty with the empty Os t_{2g} states lying in between Cr t_{2g} and Cr e_g states. In the minority spin channel, the Os t_{2g} states are completely filled which are separated from empty Cr t_{2g} , Cr e_g and Os e_g states. This gives rise to an insulating solution with a gap in both spin channels. We notice finite hybridization of Os t_{2g} states with Cr t_{2g} states. Previous study [15] on parent compound $\text{Sr}_2\text{CrOsO}_6$ showed that magnetism arises due to interplay of both hybridization driven mechanism and super-exchange mechanism which help to stabilize the high T_c (725 K) of parent compound.

6.3.2 DFT electronic and magnetic structure of doped compounds

In order to study the doping effect of La and Na at the Sr site of $\text{Sr}_2\text{CrOsO}_6$, we first constructed a supercell which is 4 times larger than that of the Fm-3m primitive unit cell. This created eight Sr sites in the supercell. Out of this eight Sr atoms, one, two and three Sr atoms were replaced by La/Na. For the case of two and three atom substitutions, we considered different inequivalent configurations. Due to the cubic symmetry of the cell, we found only three inequivalent configurations are possible for the case of two and three atom substitutions which are shown in Fig. 6.3. After substitution of Sr by La/Na, the structures were optimized completely both in terms of volume and atomic positions.

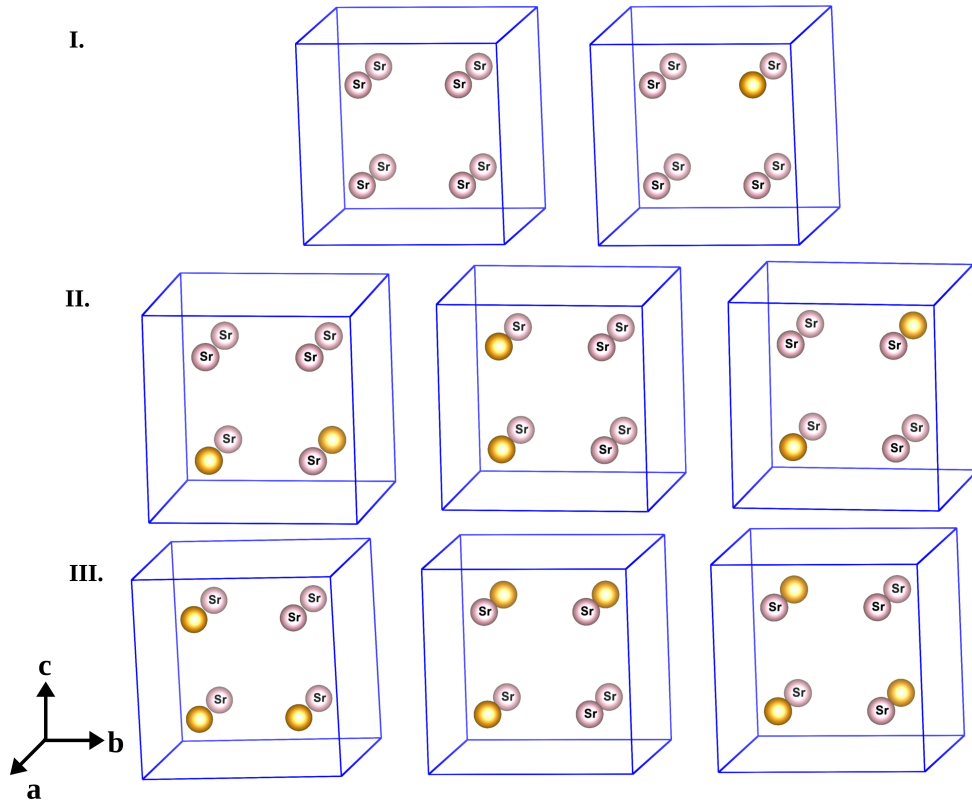


Figure 6.3: Panel I: left side shows the A sublattice with eight Sr atoms. Right side shows the A sublattice with one of eight Sr atoms substituted by La/Na. The substituted atom is shown as yellow ball. Panel II.: The A sublattice with two out of eight Sr atoms substituted by Na/La, in various inequivalent positions. Panel III.: The A sublattice with three out of eight Sr atoms substituted by Na/La, in various inequivalent positions.

For the case of La doping at the Sr sites, we considered three different doped compounds, $\text{Sr}_{1.875}\text{La}_{0.125}\text{CrOsO}_6$, $\text{Sr}_{1.75}\text{La}_{0.25}\text{CrOsO}_6$, $\text{Sr}_{1.625}\text{La}_{0.375}\text{CrOsO}_6$, and for Na doping we also considered three doped compounds $\text{Sr}_{1.875}\text{Na}_{0.125}\text{CrOsO}_6$, $\text{Sr}_{1.75}\text{Na}_{0.25}\text{CrOsO}_6$, $\text{Sr}_{1.625}\text{Na}_{0.375}\text{CrOsO}_6$. In Fig. 6.4, we show spin-polarized density of states (DOS) for both La and Na doped compounds along with parent compound, as obtained in DFT calculation within GGA+U+SOC scheme of calculation. DOS of two and three atom substituted cases are averaged over different inequivalent configurations. Left panel of Fig. 6.4 shows the DOS for Na doped compounds while right panel for La doped compounds. One can find that substitution of divalent Sr^{2+} by trivalent La^{3+} amounts to electron doping in the system while substitution of divalent Sr^{2+} by monovalent Na^{1+} amounts to hole doping in the system. Cr being $3d$ transition metal and Os being $5d$ transition metal with wider bands compared to Cr, electron-electron correlation is expected to be stronger in Cr compared to Os. Therefore it is energetically favourable

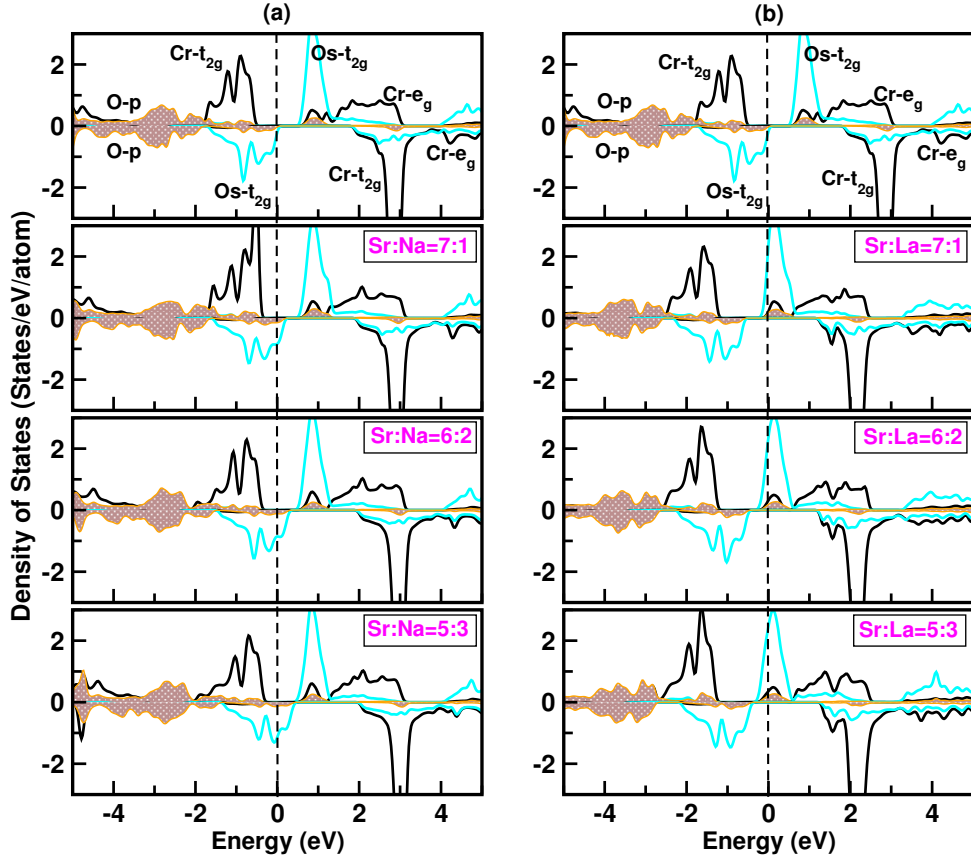


Figure 6.4: Left panel: GGA+U+SOC density of states of the parent compound, and the Na doped compounds. From top to bottom, the various panels refer to parent compound, $\text{Sr}_{1.875}\text{Na}_{0.125}\text{CrOsO}_6$, $\text{Sr}_{1.75}\text{Na}_{0.25}\text{CrOsO}_6$, $\text{Sr}_{1.625}\text{Na}_{0.375}\text{CrOsO}_6$ compounds respectively. The zero of the energy is set at E_F . The black, cyan, orange shaded area represent the states projected onto Cr d , Os d and O p states, respectively. Right panel: Same as left panel, but shown for parent and La doped compounds. From top to bottom, the various panels refer to parent compound, $\text{Sr}_{1.875}\text{La}_{0.125}\text{CrOsO}_6$, $\text{Sr}_{1.75}\text{La}_{0.25}\text{CrOsO}_6$, $\text{Sr}_{1.625}\text{La}_{0.375}\text{CrOsO}_6$ compounds respectively. The dashed, vertical lines in each panel mark the positions of Fermi level.

for doped carriers to go in Os site rather than Cr site. Thus, Na doping creates hole in the filled Os t_{2g} states. As number of electron in the Os t_{2g} states decreases upon increasing Na doping, absolute value of E_F decreases progressively with respect to the parent compound. Thus upon increasing Na doping, E_F level progressively depleted toward the valence band, making minority spin channel conducting while majority spin channel remains insulating. This leads to a half-metallic solution with finite density of states at E_F in the minority spin channel and a gap in the majority spin channel. On the other hand, La doping creates extra electron in the majority spin Os t_{2g} states which happened to be empty in the parent compound. Thus upon increasing La doping progressively fill up the majority spin Os t_{2g} states, making majority

spin channel conducting while minority spin channel remains insulating. This again gives rise to half-metallic solution with finite density of states at E_F in the majority spin channel and a gap in the minority spin channel. As is evidenced from Fig. 6.4, relative position of Cr t_{2g} and Os t_{2g} states remains almost unchanged upon La or Na doping, only E_F shifts toward valence band for Na (hole) doped case while toward conduction band for La (electron) doped case, like a rigid band picture. From the DOS calculated at $T = 0$ K, the value of the gap in the insulating

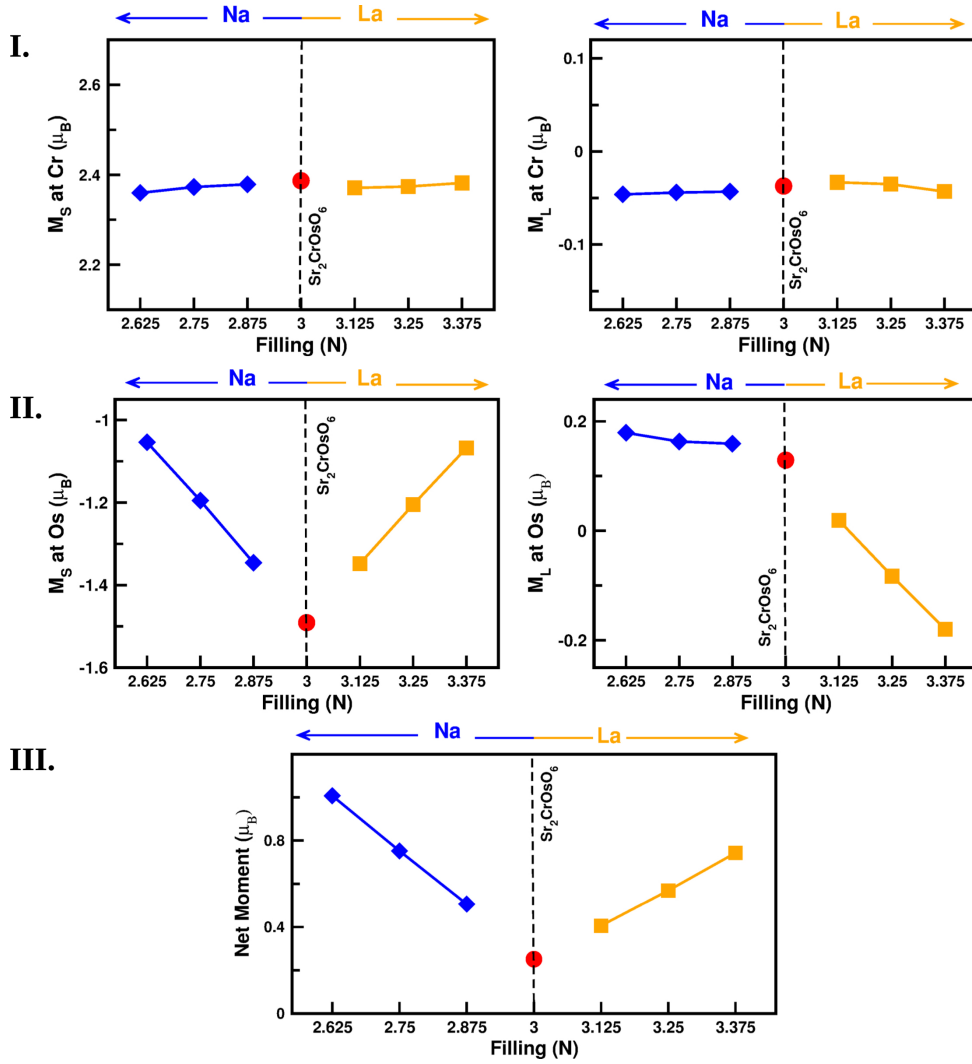


Figure 6.5: Panel I: Calculated M_S and M_L at Cr site for the parent and six different doped compounds as a function of Os t_{2g} filling (N). The circle denotes the parent compound, while the diamond and squares represent Na doped and La doped compounds. Panel II: Same as panel I, but shown for that at Os site. Panel III: The net magnetic moment per formula unit plotted as a function of Os t_{2g} filling

spin channel turned out to be about 0.6-0.7 eV for Na doped compounds, and about 1.5-1.6 eV for La doped compounds. This suggests that half-metallic character as obtained for La or Na

doping will retain even at significantly high temperature below T_c . It is to be noted that for Na (hole) doped case the carriers belong to Os-Cr hybridization derived broad t_{2g} bands having a band width of about 2 eV, while for La (electron) doped case they belong to sharply peaked Os t_{2g} majority bands having a width of about 0.5 eV. Thus effective mass of the carriers in electron and hole doping cases is expected to be different and should be reflected in transport measurement. In the context of spin-polarization calculation, this effect is discussed in section 6.3.3. We found the half-metallicity achieved by Na/La doping is robust upon the inclusion of SOC, unlike the case of $\text{Sr}_2\text{CrReO}_6$ where it was reported that presence of strong SOC at Re site destroyed the half-metallicity [16]. In Fig. 6.5 we show, variation of spin (M_s) and orbital moments (M_L) as a function of the nominal electron count at Os site, calculated within the GGA+U+SOC scheme of calculation. We find that both spin and orbital moments at Cr site remain more or less unchanged upon doping Na or La, as the doped carriers go to Os rather than to Cr. Orbital moment at Cr site is negligibly small which points in the opposite direction to that of spin moment, in agreement with half-filled nature of Cr t_{2g} states. Absolute value of the spin moment at Os site decreases systematically from that of the parent compound as number of unpaired Os t_{2g} electrons decreases upon La or Na doping. While orbital moment at Os site increases from that of parent compound as valence of Os shifts away from half-filled t_{2g}^3 configuration upon both La and Na doping. Taking into account both spin and orbital contribution, the total moment at Cr site remains unchanged while it decreases at Os site for both Na and La doping and this combined effect helps net moment to grow sharply ($1 \mu_B$ and $0.7 \mu_B$ for 18.75% Na and La doping, maximum doping considered in our calculation) due to antiferromagnetic nature of coupling between Os and Cr. Thus from electronic structure calculation, we find that upon Na (hole) and La (electron) doping, half-metallic ferrimagnetic state is achievable with reasonably large net magnetic moment.

6.3.3 Exact diagonalization study of DFT derived model Hamiltonian

From the knowledge of magnetic exchanges, which can be obtained from total energy calculations of different spin configurations, one can estimate the magnetic T_c using mean-field formula [17]. In the context of $\text{Sr}_2\text{CrOsO}_6$, this approach faces difficulties. In Ref. 15 it was explained that magnetism in $\text{Sr}_2\text{CrOsO}_6$ arises due to interplay of the hybridization driven mechanism and

super-exchange mechanism. Presence of this two mechanisms leads to strong frustration effect in some of spin configurations where consideration of different possible non-collinear, canted spin configurations are very important as shown in Ref. 18, based on Monte Carlo simulation of a classical spin Hamiltonian. Within full blown DFT scheme, it is extremely difficult to handle such cases. Such calculations are much more easier to handle within a model Hamiltonian approach. The model Hamiltonian, describing the interplay of the hybridization and super-exchange mechanism can be written as,

$$\begin{aligned}
H = & \epsilon_{Cr} \sum_{i \in B} f_{i\sigma\alpha}^\dagger f_{i\sigma\alpha} + \epsilon_{Os} \sum_{i \in B'} m_{i\sigma\alpha}^\dagger m_{i\sigma\alpha} - t_{Cr-Os} \sum_{\langle ij \rangle_{\sigma,\alpha}} f_{i\sigma\alpha}^\dagger m_{j\sigma\alpha} \\
& - t_{Os-Os} \sum_{\langle ij \rangle_{\sigma,\alpha}} m_{i\sigma\alpha}^\dagger m_{j\sigma\alpha} - t_{Cr-Cr} \sum_{\langle ij \rangle_{\sigma,\alpha}} f_{i\sigma\alpha}^\dagger f_{j\sigma\alpha} \\
& + J \sum_{i \in Cr} S_i \cdot f_{i\alpha}^\dagger \vec{\sigma}_{\alpha\beta} m_{i\beta} + J_2 \sum_{i \in Cr, j \in Os} S_i \cdot s_j
\end{aligned} \tag{6.1}$$

where the f 's and m 's refer to the Cr t_{2g} and Os t_{2g} degrees of freedoms. t_{Cr-Os} , t_{Os-Os} , t_{Cr-Cr} represent the nearest neighbour Cr-Os, second nearest neighbour Os-Os and Cr-Cr hopping respectively. σ is the spin index and α is the orbital index that spans the t_{2g} manifold. The difference between the ionic levels, $\Delta = \epsilon_{Cr} - \epsilon_{Os}$, defines the on-site energy difference between Cr t_{2g} and Os t_{2g} levels. s_j is the intrinsic moment at the Os site. The first six terms of the Hamiltonian describe the hybridization mechanism, or equivalently a double-exchange like mechanism which consist of a large core spin at the Cr site (S_i) and the coupling between the core spin and the itinerant electron delocalized over the Cr-Os network. The last term represents the super-exchange mechanism that consists of coupling between Cr spin and the intrinsic moment at Os site. In order to extract the parameters of this model Hamiltonian we have carried out NMTO downfolding calculation. Through NMTO downfolding technique we constructed Cr t_{2g} - Os t_{2g} only low energy Hamiltonian by integrating out O and Sr as well as Cr and Os e_g degrees of freedom starting from the full non spin-polarized band structure. From the real space representation of this Hamiltonian, onsite energy ϵ 's and hopping parameters t 's are estimated. The comparison of constructed real space bands and the full DFT bands are shown in Fig. 6.6. The DFT estimated value of Δ , t_{Cr-Os} , t_{Os-Os} and t_{Cr-Cr} turned out to be 0.26 eV,

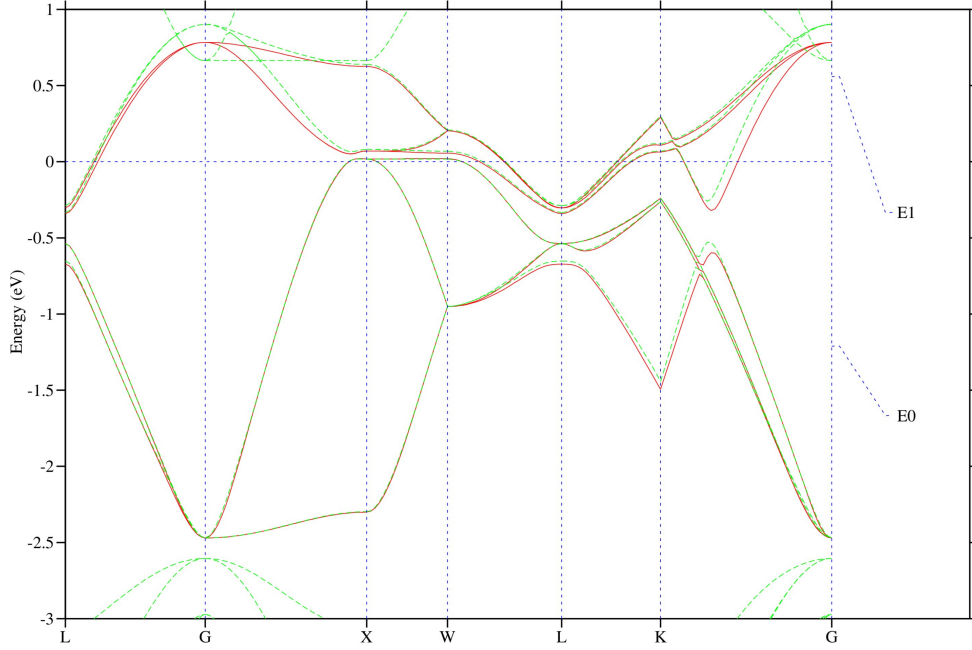


Figure 6.6: The downfolded, tight-binding band structure of $\text{Sr}_2\text{CrOsO}_6$ in effective Cr-Os t_{2g} basis (in red lines) in comparison with full band structure (in green lines). Zero of the energy is set at Fermi energy. The energies, E0 and E1 represent the energy points about the expansion were carried out in NMTO calculation.

-0.35 eV, -0.12 eV and -0.08 eV respectively, with little variation between the parent and doped compounds. J parameter is estimated from the spin splitting at Cr site. The estimation of J_2 parameter is little bit tricky. Comparing the extra spin splitting at Os site than that expected from solely hybridization mechanism [15], the parameter J_2 is extracted.

Cr being $3d$ transition metal ion, the spin splitting at Cr site (which provides the estimate of J) is found to be very large compared to the $t_{\text{Cr-Os}}$ *i.e.* $J \gg t_{\text{Cr-Os}}$. In this limit Hamiltonian of Eq. 6.1 can be cast into form appropriate for $J \rightarrow \infty$. This has been done by performing a rotation to the local S_i axis at each Cr site, and retaining only the electron state oriented antiparallel to S_i at that site. This gives the Hamiltonian, with spin-less Cr conduction electrons while Os electrons having both spin states. Thus the number of degrees of freedom reduced to three per Cr site and six per Os, compared to original problem with six degrees of freedom at both the sites. This is the lowest energy Hamiltonian and there is no longer any large coupling in the model. Since the spin S is large quantum effect is expected to be very small and it can be considered as classical spin. Therefore one can consider different spin configurations (ferro,

antiferro, canted and disordered) and diagonalize the system in real space, to obtain variational estimates of the ground state and its stability.

Calculation of magnetic transition temperature

We solved this DFT derived model Hamiltonian (Eq. 6.1) using exact diagonalization [19] on an lattice of dimension $8 \times 8 \times 8$ for the ferromagnetic (FM) and paramagnetic (PM) configurations of Cr spins. To simulate the PM phase we have considered several (≈ 50) disordered

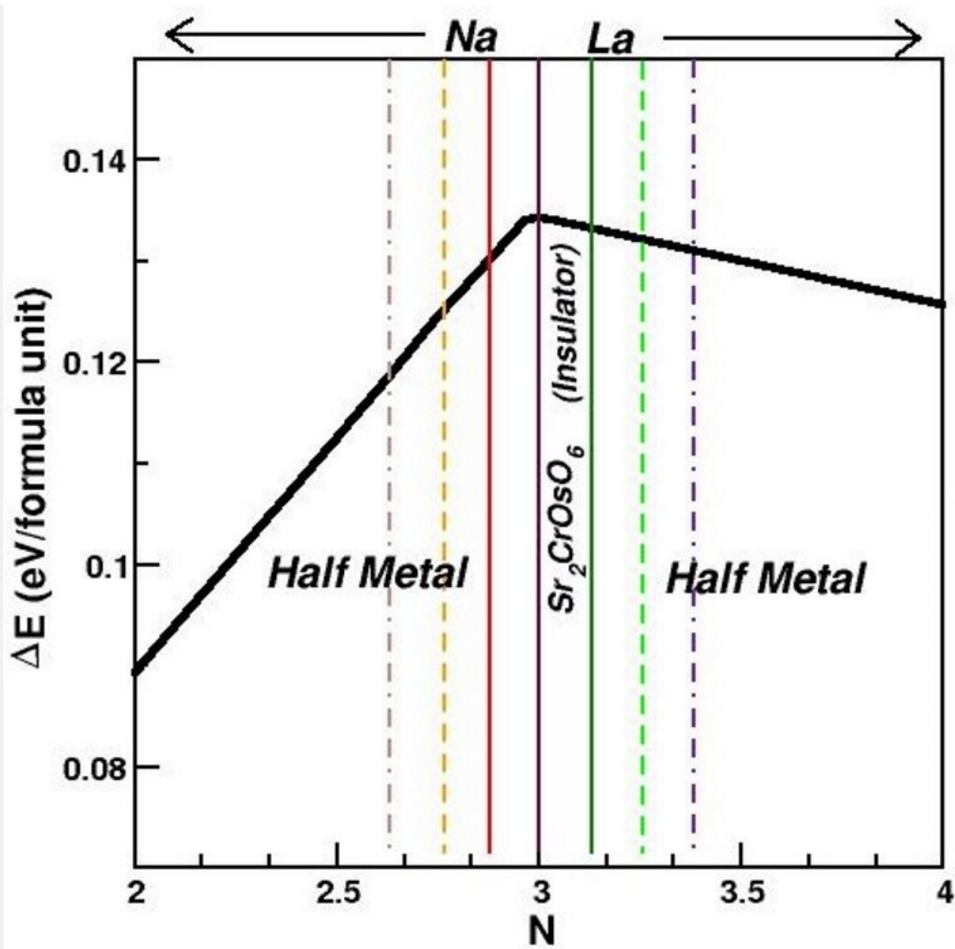


Figure 6.7: The energy difference between PM and FM arrangement of Cr spins, plotted as a function of Os t_{2g} filling (N), shown as black solid line. The vertical lines mark the filling corresponding to the parent (solid, magenta) and various Na (red-solid, orange-dashed and brown- dot-dashed for $\text{Sr}_{1.875}\text{Na}_{0.125}\text{CrOsO}_6$, $\text{Sr}_{1.75}\text{Na}_{0.25}\text{CrOsO}_6$, $\text{Sr}_{1.625}\text{Na}_{0.375}\text{CrOsO}_6$, respectively) and La doped compounds (green-solid, green-dashed and indigo-dot-dashed for $\text{Sr}_{1.875}\text{La}_{0.125}\text{CrOsO}_6$, $\text{Sr}_{1.75}\text{La}_{0.25}\text{CrOsO}_6$, $\text{Sr}_{1.625}\text{La}_{0.375}\text{CrOsO}_6$, respectively) studied in present work. Both the Na-doped and La-doped compounds are half-metallic, while the parent compound with electron count of three, is insulating.

configurations of Cr spin and averaging over this several configurations we have calculated the energy for paramagnetic phase. In Fig. 6.7, we show the energy difference between FM and PM configuration of Cr spins for the parent as well as doped compounds as a function of Os t_{2g} filling (N). From Fig. 6.7 one can see that, the energy difference is maximum for the undoped compound and it is decreasing for both electron doping and hole doping while for hole doping, decrease is found to be more rapid compared to electron doping. Due to decrease of delocalized carriers by hole doping the hybridization driven mechanism becomes weaker, which reduces the PM-FM energy difference. If we extrapolate the data for $N = 0$, the PM-FM energy difference should be zero, as for $N = 0$ there is no delocalized carrier to support the magnetism. Upon electron doping, due to the competing antiferromagnetic (AFM) ordering of B-site spins [20,21] as discussed for La doped $\text{Sr}_2\text{FeMoO}_6$ [11], the PM-FM energy difference decreases. We estimated

Table 6.3: Model Hamiltonian estimated transition temperature T_c of six doped compounds with respect to parent compound

$\frac{T_c^{La0.125}}{T_c^{parent}} = 0.99$	$\frac{T_c^{Na0.125}}{T_c^{parent}} = 0.96$
$\frac{T_c^{La0.25}}{T_c^{parent}} = 0.98$	$\frac{T_c^{Na0.25}}{T_c^{parent}} = 0.92$
$\frac{T_c^{La0.375}}{T_c^{parent}} = 0.97$	$\frac{T_c^{Na0.375}}{T_c^{parent}} = 0.87$

T_c for parent as well as for doped compounds by mapping the PM and FM energy difference to the mean field formula. Though, it is well known fact that the mean field approximation overestimate the T_c significantly [17], but the ratio's of T_c 's are expected to reproduce rather well, as demonstrated in Ref. 15. Table 6.3 shows the estimated T_c for doped compounds with respect to the parent compound. We find, for moderate doping the T_c of doped compounds are nearly as high as the parent compound.

Calculation of spin polarization

In the context of half-metallic state the degree of spin polarization is an important issue. The most popular definition is given by

$$P = (N_{\uparrow} - N_{\downarrow}) / (N_{\uparrow} + N_{\downarrow}) \quad (6.2)$$

where $N_{\uparrow(\downarrow)}$ is the value of the density of states in two spin channels. The spin polarization is 100% for any half-metal according this definition. A more suitable definition where velocity of charge carriers are taken into account (important for transport measurement) is given by [22],

$$P_{Nv^2} = \left(\langle Nv^2 \rangle_{\uparrow} - \langle Nv^2 \rangle_{\downarrow} \right) / \left(\langle Nv^2 \rangle_{\uparrow} + \langle Nv^2 \rangle_{\downarrow} \right) \quad (6.3)$$

with $\langle Nv^2 \rangle_{\sigma=\uparrow\downarrow} = \sum_k v_{k\sigma}^2 \delta(E - \epsilon_{k\sigma})$, where $\epsilon_{k\sigma}$ is the band energy and $v_{k\sigma}^2$ is the corresponding velocity at wave vector k . We calculated the spin polarization from model Hamiltonian calculations. It is to be noted however that spin-orbit effect can change the degree of spin-polarization as discussed in Ref. 23. However, we have not considered it in the calculation of polarization (P) because in this present study configuration of Os is d^3 or close to d^3 which leads to a rather small effect of spin-orbit coupling, with M_L/M_S values much less than 1 [cf. Fig. 6.5]. Using Eq. 6.3, we calculated spin-polarization from model Hamiltonian calculation which is shown in Fig. 6.8 where spin polarization is plotted as a function of the Os t_{2g} fillings (N). The signs of the spin polarizations are opposite for La and Na doping, as carriers are generated from the two different spin channels in two cases. We find that the degree of spin polarization is larger for hole doping compared to electron doping. This arises due to the fact that, for Na (hole) doping carriers are generated in the broad Os t_{2g} -Cr t_{2g} hybridized bands in the minority spin channel which produces light carriers with faster speed. While for La (electron) carriers are generated in the relatively narrow Os t_{2g} bands in the majority spin channel [cf. Fig. 6.4] which produces heavier carriers with slower speed.

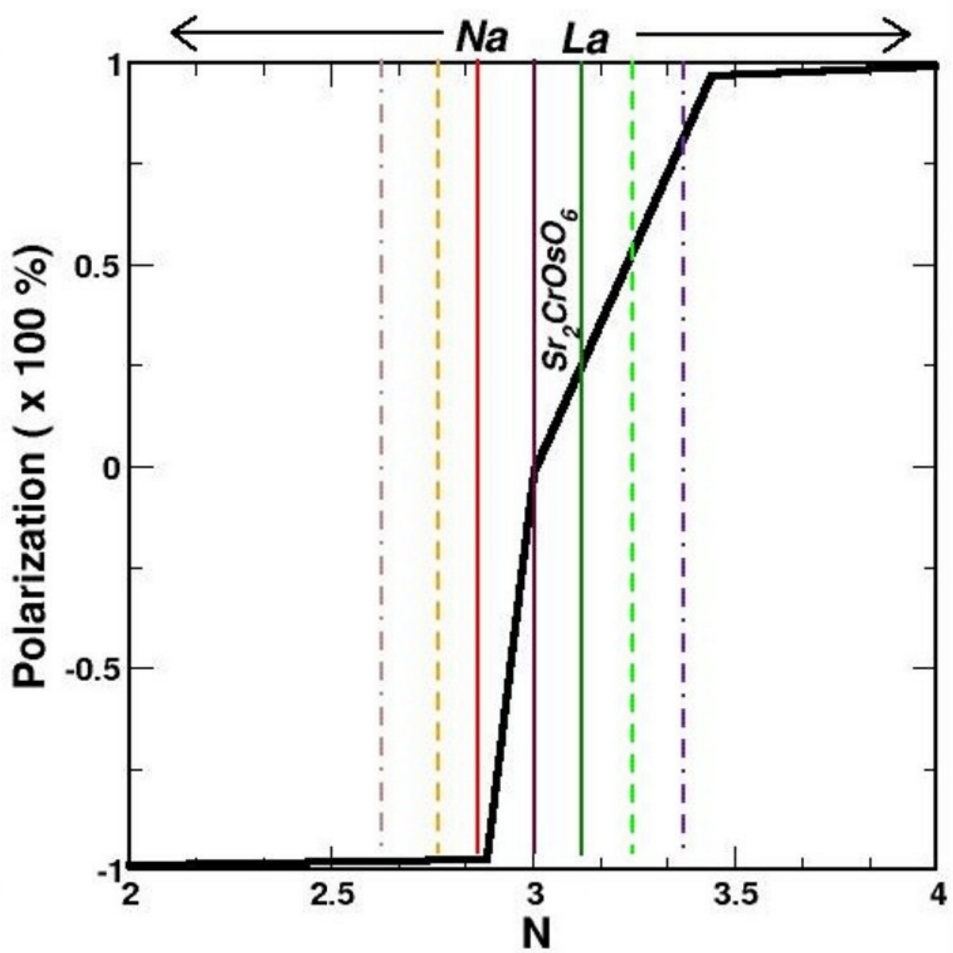


Figure 6.8: The spin polarization, plotted as a function of Os t_{2g} filling (N), shown as black solid line. The vertical lines mark the filling corresponding to the parent (solid, magenta) and various Na (red-solid, orange-dashed and brown- dot-dashed for $\text{Sr}_{1.875}\text{Na}_{0.125}\text{CrOsO}_6$, $\text{Sr}_{1.75}\text{Na}_{0.25}\text{CrOsO}_6$, $\text{Sr}_{1.625}\text{Na}_{0.375}\text{CrOsO}_6$, respectively) and La doped compounds (green-solid, green-dashed and indigo-dot-dashed for $\text{Sr}_{1.875}\text{La}_{0.125}\text{CrOsO}_6$, $\text{Sr}_{1.75}\text{La}_{0.25}\text{CrOsO}_6$, $\text{Sr}_{1.625}\text{La}_{0.375}\text{CrOsO}_6$, respectively) studied in present work. Both the Na-doped and La-doped compounds are half-metallic, while the parent compound with electron count of three, is insulating

6.4 Summary and conclusions

Our DFT calculations together with exact diagonalization of the low energy model Hamiltonian consisting of Cr and Os t_{2g} degrees of freedom showed that upon moderate Na (hole) or La (electron) doping of about 10 to 20% at the Sr site of $\text{Sr}_2\text{CrOsO}_6$ half-metallic ferrimagnetic state is achievable with high transition temperature which is estimated to be 87 to 99% of the T_c of the parent compound (725 K [9]). We found that the effect of doping is not symmetric with respect to La (electron) and Na (hole) doping. For Na doping broad Os t_{2g} -Cr t_{2g} hybridized bands in

the minority spin channel became conducting while majority spin channel remained insulating. On the other hand narrow Os t_{2g} bands in the majority spin channel became conducting while minority spin channel remained insulating for La doping. Due to this asymmetry, the degree of spin polarization is found to be higher in Na doped compounds compared to La doped compounds while magnetic transition temperature is found to be higher for La doped compounds compared to Na doped compounds. It is to be noted that La doping reduces the valence difference between Cr and Os compared to the parent compound which may lead to increased antisite disorder [see Table 1.1 of chapter 1] while for Na doping the situation is expected to be opposite which increases the valence difference between Cr and Os. Therefore it will be a good choice to consider the Na doping of about 10% which has both high T_c and high degree of spin polarization for driving half-metallicity in $\text{Sr}_2\text{CrOsO}_6$.

We noted that finding the half-metallicity by La/Na doping in $\text{Sr}_2\text{CrOsO}_6$ is very similar to what proposed in Ref. 14, in the context of 2 band model Hamiltonian study based on dynamical mean field theory calculation. In absence of SOC, $\text{Sr}_2\text{CrOsO}_6$ is similar to the model study of Ref. 14, where the role of two inequivalent sites is played by Cr and Os sites. In presence of SOC the undoped $\text{Sr}_2\text{CrOsO}_6$ is an uncompensated ferrimagnet with a net magnetic moment, rather than a compensated ferrimagnet with zero magnetic moment [cf. Table 6.2]. Though in this respect, $\text{Sr}_2\text{CrOsO}_6$ differed from the model study in Ref. 14 but the essential physics upon doping is found to be similar to that described in Ref. 14. Thus our study is realization of the model study proposed in Ref. 14 which can be validated experimentally. We hope that our computational study will encourage experimental investigations in this direction.

Bibliography

- [1] J. M. D Coey, M. Venkatesan, J. Appl. Phys. 91, 8345 (2002).
- [2] W. E. Pickett, and J. S. Moodera, Physics Today 54, 39 (2001)
- [3] S. A. Wolf, D. D. Awschalom, R. A. Buhrman, J. M. Daughton, S. von Molnar, M. L. Roukes, A. Y. Chtchelka- nova, and D. M. Treger, Science 294, 1488 (2001).
- [4] K. -I. Kobayashi, T. Kimura, H. Sawada, K. Terakura, and Y. Tokura, Nature (London) 395, 677 (1998).
- [5] J. M. D. Coey. In Lecture Notes in Physics 569, (edn M. J. Thornton and M. Ziese), Ch 12, 277-297 (Springer, Berlin, New york, 2001).
- [6] J. B. Philipp, P. Majewski, L. Alff, A. Erb, R. Gross, T. Graf, M. S. Brandt, J. Simon, T. Walther, W. Mader, D. Topwal, and D. D. Sarma, Phys. Rev. B 68, 144431 (2003).
- [7] A. Arulraj, K. Ramesha, J. Gopalakrishnan, and C. N. R. Rao, J. Solid State Chem. 155, 233 (2000).
- [8] P. Sanyal, A. Halder, Liang Si, M. Wallerberger, K. Held and T. Saha-Dasgupta, Phys. Rev. B. 94, 035132 (2016).
- [9] Y. Krockenberger, K. Mogare, M. Reehuis, M. Tovar, M. Jansen, G. Vaitheeswaran, V. Kanchana, F. Bultmark, A. Delin, F. Wilhelm, A. Rogalev, A. Winkler, and L. Alff, Phys. Rev. B 75, 020404 (2007).
- [10] J. navarro, C. Frontera, L. I. Balcells, B. Martinez, and J. Fontcuberta, Phys. Rev. B 64, 092411 (2001).

-
- [11] P. Sanyal, H. Das and T. Saha-Dasgupta, Phys. Rev. B 80, 224412 (2009).
- [12] L. Brey, M. J. Caldern, S. Das Sarma and F. Guinea, Phys. Rev. B 74, 094429 (2006).
- [13] S. Jana, C. Meneghini, P. Sanyal, S. Sarkar, T. Saha-Dasgupta, O. Karis, and S. Ray, Phys. Rev. B 86, 054433 (2012).
- [14] A. Garg, H. R. Krishnamurthy and M. Randeria, Phys. Rev. Lett. 112, 106406 (2014).
- [15] H. Das, P. Sanyal, T. Saha-Dasgupta and D. D. Sarma, Phys. Rev. B 83, 104418 (2011).
- [16] G. Vaitheeswaran, V. Kanchana and A. Delin, J. Phys. Conf. Ser. 29, 50 (2006).
- [17] C. Kittel, Introduction to Solid State physics, 8th ed. (Wiley, Hoboken, 2005).
- [18] O. N. Meetei, O. Erten, M. Randeria, N. Trivedi and P. Woodward, Phys. Rev. Lett. 110, 087203 (2013).
- [19] A. Weie and H. Fehske. In Lecture Notes in Physics 739, (eds H. Fehske *et al.*), Ch. 18, 529-544 (Springer, Berlin, Heidelber, 2008).
- [20] P. Sanyal, Phys. Rev. B 89, 115129 (2014).
- [21] P. Sanyal and P. Majumdar, Phys. Rev. B 80, 054411 (2009).
- [22] I. I. Mazin, Phys. Rev. Lett. 83, 1427 (1999).
- [23] A. Cook and A. Paramekanti, Phys. Rev. B 88, 235102 (2013)

Chapter 7

Magnetism in $\text{Ca}_2\text{CoOsO}_6$ and $\text{Ca}_2\text{NiOsO}_6$: Unraveling the Mystery of Superexchange Interactions between $3d$ and $5d$ Ions[†]

7.1 Introduction and motivation

Double perovskite compounds having $3d$ transition metal ion at B and $4d/5d$ transition metal ion B' site need special attention. It has been observed that double perovskites having most intriguing electrical and magnetic properties are tend to be those containing mixed $3d$ and $5d$ elements at B and B' sites [1]. Thus, recent research has been devoted for understanding the electronic and magnetic properties in mixed $3d$ - $5d$ double perovskites.

[†] This Chapter is based on publication, Ryan Morrow, Kartik Samanta, Tanusri Saha Dasgupta, Jie Xiong, John W. Freeland, Daniel Haskel, and Patrick M. Woodward, Chem. Mater. 28, 3666-3675 (2016).

The electrical and magnetic properties of oxides containing $5d$ transition metals (TMs) are significantly different from compounds containing $3d$ TMs, in many ways. There are some notable differences between $3d$ and $5d$ transition metal elements which have been discussed more elaborately in the introductory chapter 1. Here we only briefly mentioned them. Due to larger spatial extent of the $5d$ orbitals, it hybridizes more strongly with oxygens compared to $3d$ orbitals, resulting in large crystal field splitting of $5d$ orbitals. Also presence of strong spin-orbit coupling (SOC) can lead to interesting and unexpected magnetic behavior [2]. In order to rationalize and predict the electric and magnetic properties of mixed $3d$ - $5d$ oxides, an understanding of the local moment formed at $5d$ site and the sign and strength of superexchange interactions between $3d$ and $5d$ ions are necessary. The venerable Goodenough-Kanamori (G-K) rules [3, 4] are useful to predict the superexchange interactions in a qualitative sense. However the G-K rules are often found to fail to predict even the sign of the superexchange coupling between $3d$ ions and $5d$ ions where a mismatch in the energies of the d -orbitals is pronounced, making the situation complicated. The shortcomings of the G-K rules have been observed in mixed $3d$ - $5d$ double perovskites, $\text{Sr}_2\text{FeOsO}_6$ and $\text{Ca}_2\text{FeOsO}_6$, both of which contain Os(V) and Fe(III). According to G-K rules, the super-exchange interaction between d^3 orbitals and one with high-spin d^5 should be ferromagnetic. In spite of this, $\text{Sr}_2\text{FeOsO}_6$ orders antiferromagnetically [5, 6], while the ground state of $\text{Ca}_2\text{FeOsO}_6$ is ferrimagnetic [7, 8]. In $\text{Sr}_2\text{FeOsO}_6$, the Os-O-Fe bonds are bent in the ab plane and linear along c -direction, while in $\text{Ca}_2\text{FeOsO}_6$, additional tilting of the octahedra due to smaller Ca^{2+} ions in place of Sr^{2+} ions, lowers the symmetry to monoclinic. For $\text{Ca}_2\text{FeOsO}_6$, this leads to bending of Os-O-Fe bonds (151 - 153°) in all three crystallographic directions and magnetic ground state becomes ferrimagnetic. A similar crossover from antiferromagnetism to ferrimagnetism has also observed in A_2CoOsO_6 , A_2NiOsO_6 , and A_2CuOsO_6 ($\text{A} = \text{Sr}$ or Ca), as tolerance factor decreases [9–14]. This behaviour indicates that there are competing super-exchange interactions and some or all of those interactions are highly sensitive to distortion of the structure [15].

In this chapter, we studied the electronic structure, magnetic, and electrical properties of two mixed $3d$ - $5d$ ferrimagnetic double perovskites, $\text{Ca}_2\text{CoOsO}_6$ ($T_c = 145$ K) and $\text{Ca}_2\text{NiOsO}_6$ ($T_c = 175$ K) [12, 13] to provide critical insight on the above mention issues. Understanding of local moment at Os site and magnetism of these two compounds are one of the main aim

of this present study. Neutron diffraction is most straightforward experimental technique for determining local moments but in the literature there are no known example of double perovskites, containing Os(VI) the only magnetic ion where researchers have been able to measure the moment using neutron diffraction [16–19]. So, we have carried out DFT based first principles calculations to develop a comprehensive picture of the local magnetism and magnetic coupling in these two compounds. The theoretical results based on DFT calculations have been further corroborated by experimental measurements like dc conductivity, magnetization, X-ray absorption spectroscopy (XAS) and X-ray magnetic circular dichroism (XMCD).

7.2 Results

7.2.1 Crystal structure

Both $\text{Ca}_2\text{CoOsO}_6$ and $\text{Ca}_2\text{NiOsO}_6$ crystallize in monoclinic space group with $P2_1/n$ symmetry [12,13]. Main structural units of these two double perovskites are corner sharing Co/NiO_6 and OsO_6 octahedrons which alternate along all three crystallographic axis, creating rock-salt like arrangement [cf. Fig. 7.1]. Due to size mismatch between the radius of the Ca^{2+} ion and the corner sharing octahedral framework, the Co/NiO_6 and OsO_6 octahedrons are found to be tilted. Lattice parameters, selected bond lengths and angles of these two double perovskites are

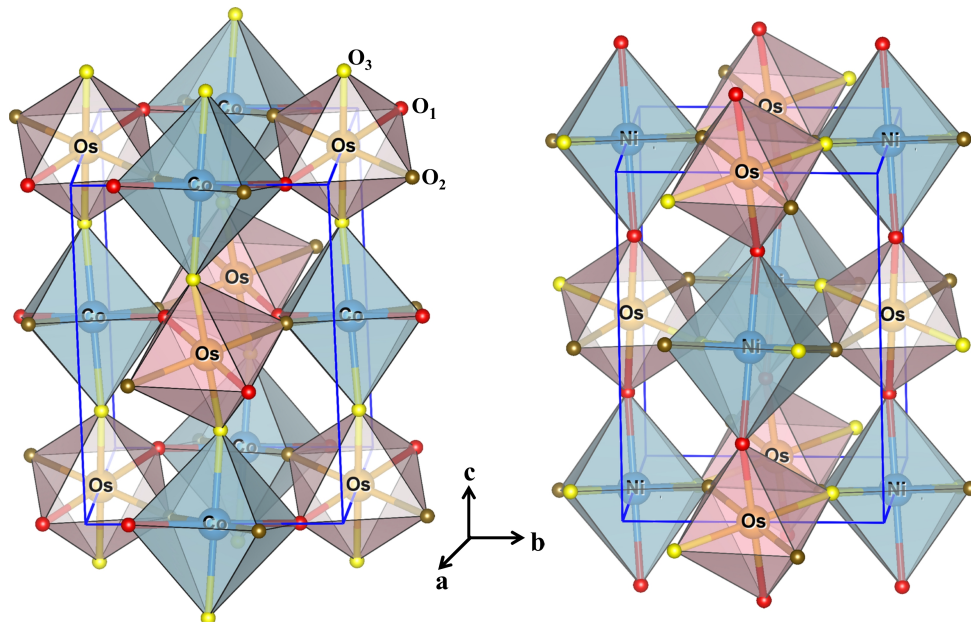


Figure 7.1: Crystal structure of $\text{Ca}_2\text{CoOsO}_6$ (left panel) and $\text{Ca}_2\text{NiOsO}_6$ (right panel), showing the three dimensional network. Various atoms including the inequivalent oxygens are marked. Ca atoms are not shown for clarity.

summarized in Table 7.1. Table 7.1 shows that the $\text{Os-O-Co}/\text{Ni}$ bond angles in both the double perovskites are significantly bent ($151 \pm 2^\circ$) in all three crystallographic axis which have strong effect on the magnetic ground state, as will be discussed in section 7.2.4.

Table 7.1: Structural parameters, selected bond lengths and bond angles of experimentally measured $\text{Ca}_2\text{CoOsO}_6$ and $\text{Ca}_2\text{NiOsO}_6$ double perovskites.

	$\text{Ca}_2\text{CoOsO}_6$	$\text{Ca}_2\text{NiOsO}_6$
reference	12	13
a(\AA)	5.375	5.361
b(\AA)	5.568	5.543
c(\AA)	7.636	7.618
β	89.75 ⁰	90.29 ⁰
Co/Ni-O distance (\AA)		
Co/Ni-O1 ($\times 2$)	2.080	2.038
Co/Ni-O2 ($\times 2$)	2.072	2.065
Co/Ni-O3 ($\times 2$)	2.032	2.071
avg. Co/Ni-O distance (\AA)	2.061	2.058
Os-O distance (\AA)		
Os-O1 ($\times 2$)	1.935	1.911
Os-O2 ($\times 2$)	1.932	1.921
Os-O3 ($\times 2$)	1.922	1.920
avg. Os-O distance (\AA)	1.930	1.917
Os-O-Co/Ni angles		
Os-O1-Co/Ni	150.29 ⁰	149.34 ⁰
Os-O2-Co/Ni	149.86 ⁰	150.58 ⁰
Os-O3-Co/Ni	149.07 ⁰	150.01 ⁰

7.2.2 DFT electronic structure calculation

In order to understand the electronic properties of these two compounds, we carried out DFT based calculations using the full potential linear augmented plane wave (FLAPW) basis as implemented in Wien2k code. For the self-consistent calculation in LAPW, we used 160 k-points in the irreducible part of Brillouin zone. The wave functions were expanded in plane waves with a cut-off $R_{MT}k_{max} = 7.0$ where R_{MT} is the smallest muffin-tin sphere radius and k_{max} is the magnitude of the largest k vector in the plane wave expansion. Spin-orbit coupling has been included in the calculation as a perturbation to the original Hamiltonian and was dealt using the second variational scheme. We considered the exchange correlation functional to be that of generalized gradient approximation(GGA), implemented following the Perdew-Burke-Ernzerhof (PBE) prescription. The missing strong electron-electron correlation at magnetic ions Co, Ni and Os was taken into account through supplemented Hubbard U (GGA+U) calculation. We chose the typical U values for 3d (Co and Ni) and 5d (Os) transition metal ions. The results reported in this chapter have been obtained for $U(\text{Co/Ni}) = 4.0$ eV and $U(\text{Os}) = 2$ eV, with

Hund's coupling energy J_H of 0.8 eV. We have checked the validity of our results by varying U value by ± 2 eV at Co/Ni site and by ± 1.0 eV at Os site. The trend of our result was found to remain unchanged.

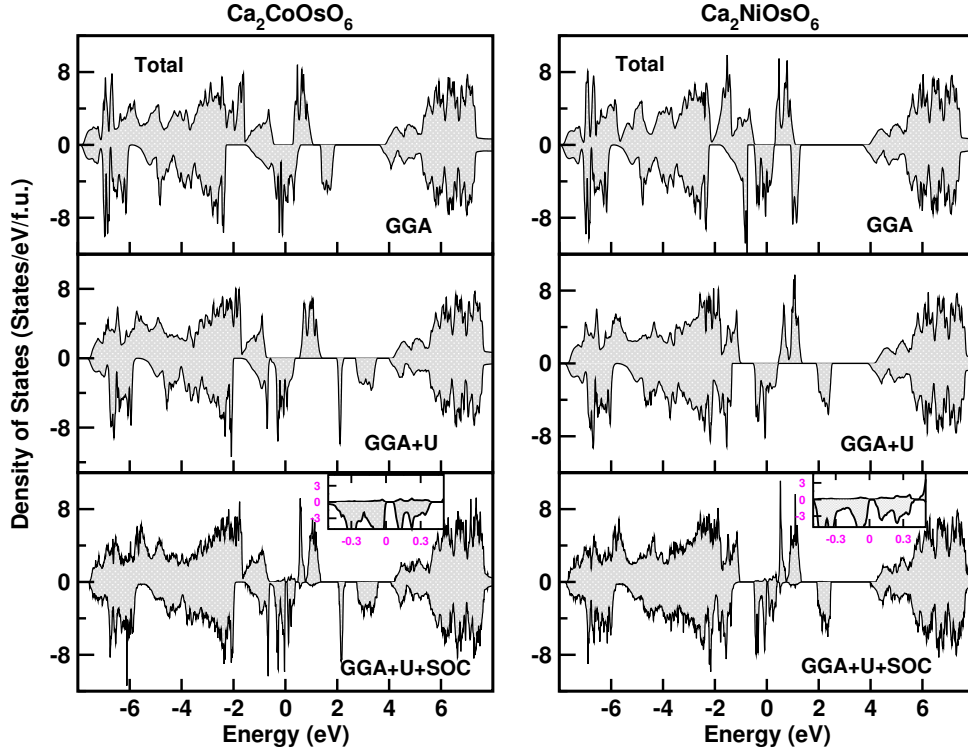


Figure 7.2: Total density of states of $\text{Ca}_2\text{CoOsO}_6$ and $\text{Ca}_2\text{NiOsO}_6$ as obtained within GGA, GGA+U and GGA+U+SOC scheme of calculations. The zero of the energy in each panel is set at Fermi energy. The insets in the bottom panels highlights the region near the Fermi energy revealing a small gap.

Fig. 7.2 shows the total density of states (DOS) for $\text{Ca}_2\text{CoOsO}_6$ and $\text{Ca}_2\text{NiOsO}_6$ as obtained in three different schemes of calculation, GGA, GGA+U, and GGA+U+SOC. Within GGA and GGA+U scheme of calculation, both the compounds are found to be half-metal with zero density of states in the majority spin channel, and finite density of states in the minority spin channel. For both the compounds, we find spin-orbit coupling (SOC) has strong effect in electronic structure. Inclusion of SOC, together with supplemented Hubbard U helps to open a small gap also in the minority spin channel, making both the compounds insulator. Thus, DFT calculations suggest that both the compounds are spin-orbit coupling driven Mott insulator.

To understand the electronic structure in more detail, we calculated DOS within GGA, GGA+U and GGA+U+SOC scheme of calculation, for $\text{Ca}_2\text{CoOsO}_6$ and $\text{Ca}_2\text{NiOsO}_6$ projected

onto the Co/Ni, Os d states as shown in Fig. 7.3. The states close to Fermi level (E_F) which is set at zero, are dominated by Co/Ni $3d$ states and Os $5d$ states. The calculations converge to antiparallel alignment of the Co/Ni and Os spins which indicates ferrimagnetic nature of ground state. The d states of Co, Ni and Os ions are exchange split as well as crystal field split. Co, Ni and Os are in the octahedral environment of oxygen ions. Within the crystal field of octahedral, d levels split into approximately degenerate t_{2g} and e_g states. Form the left panel of

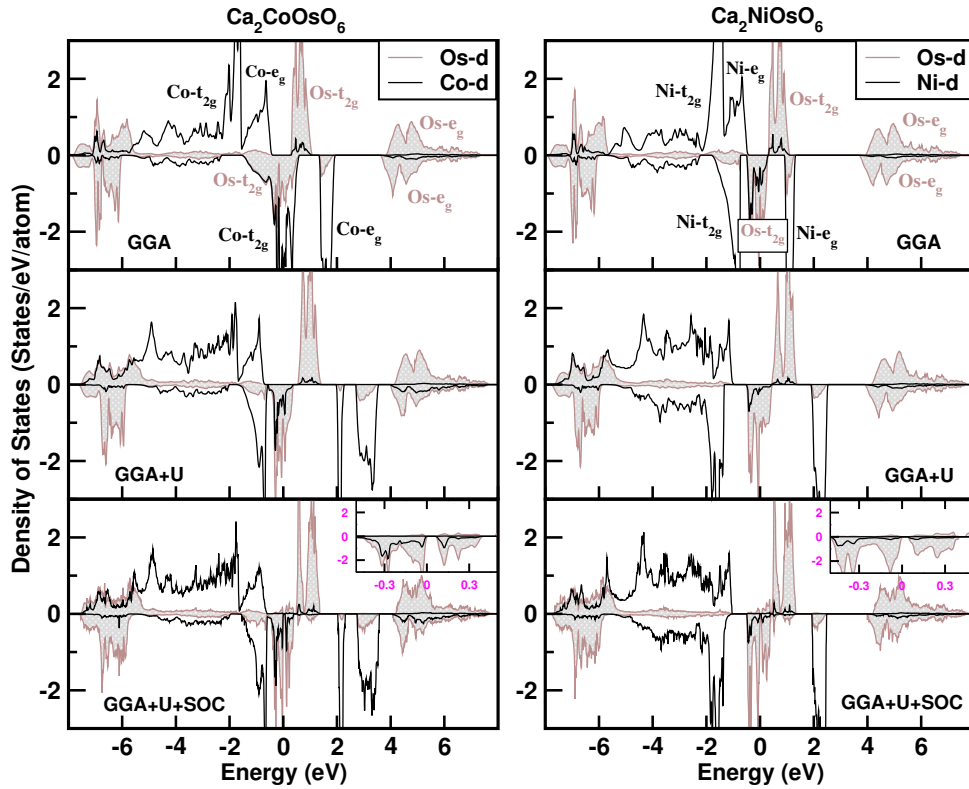


Figure 7.3: Density of states of $\text{Ca}_2\text{CoOsO}_6$ and $\text{Ca}_2\text{NiOsO}_6$ projected onto the Co/Ni (black line) and Os- d (brown shaded area) states, as obtained within GGA, GGA+U and GGA+U+SOC scheme of calculations. The zero of the energy in each panel is set at Fermi energy. The insets in the bottom panels highlights the region near the Fermi energy revealing a small gap.

Fig. 7.3, one can see that within GGA scheme of calculation, Co d states are completely filled in the majority spin channel while the Co t_{2g} are partially filled in the minority spin channel, suggesting Co^{2+} ion to be in a d^7 high spin state. In the minority spin channel, Os t_{2g} states are partially filled while majority t_{2g} channel is completely empty, suggesting nominal occupancy to be d^2 which corresponds to an oxidation state of Os(VI). Due to large Os t_{2g} - e_g crystal field splitting (about 4 eV), the Os e_g states located far above the Fermi level which show minimal

mixing with the Co $3d$ states. The t_{2g} states of both Co and Os cross the Fermi level in the minority spin channel which makes the minority spin channel conducting while there is a clear gap in the majority spin channel. This leads to a half-metallic solution. The bands close to E_F show a pronounced admixture of Os and Co t_{2g} character in the minority spin channel with GGA scheme of calculations. Partial DOS is found to remain unchanged with application of Hubbard U, only the spin-splitting gets renormalized in effect of Hubbard U, as expected. On the other hand, introduction of spin-orbit coupling reconstructs the t_{2g} states and split them which helps to open up a very small gap in the minority spin channel making the system insulating, as shown in the inset to the lowest panel of Fig. 7.5. Thus we find that both correlations and SOC are necessary to explain the insulating nature of $\text{Ca}_2\text{CoOsO}_6$. Similar behavior was also found in the $\text{La}_2\text{CoMnO}_6$ [20].

Right panel of Fig. 7.3, shows partial DOS for $\text{Ca}_2\text{NiOsO}_6$, calculated within GGA, GGA+U and GGA+U+SOC scheme of calculation. Partial DOS plots are qualitatively similar to $\text{Ca}_2\text{CoOsO}_6$, except the fact that now Ni t_{2g} states become completely filled in the minority spin channel, as expected for a d^8 Ni(II) ion. We also find, close to the E_F , contribution of the Ni t_{2g} bands to the minority spin Os t_{2g} bands is significantly smaller than it was in the case of $\text{Ca}_2\text{CoOsO}_6$. This may help to explain why the conductivity of $\text{Ca}_2\text{NiOsO}_6$ is roughly 2 orders of magnitude smaller than that of $\text{Ca}_2\text{CoOsO}_6$ as found in experimentally measured dc conductivities.

7.2.3 DFT calculated local moments

DFT electronic structure calculations show that both $\text{Ca}_2\text{CoOsO}_6$ and $\text{Ca}_2\text{NiOsO}_6$ contain localized electrons. Thus next we calculated magnitude of local moments which are given in Table 7.2, as obtained within GGA+U+SOC scheme of calculation. In atomic limit, one would expect the spin moments m_s to be equal to the number of unpaired electrons in magnetic ions. Therefore m_s would be 3 for Co(II), 2 for Ni(II) and 2 for Os(VI). Table 7.2 shows calculated m_s values are 10-20% smaller than the nominal values for Co(II) and Ni(II) and 70% smaller for Os(VI). This reduction is predominantly due to covalency with the surrounding oxygen ions which is expected to be higher for highly delocalized $5d$ orbitals of Os(VI). As both the Co(II)

Table 7.2: DFT calculated the spin (m_s), orbital (m_l) and total (m_{tot}) magnetic moments within GGA+U+SOC.

	Ca ₂ CoOsO ₆	Ca ₂ NiOsO ₆
m_s (Co/Ni)	+2.62 μ_B	+1.61 μ_B
m_l (Co/Ni)	+0.13 μ_B	+0.16 μ_B
m_{tot} (Co/Ni)	+2.75 μ_B	+1.76 μ_B
m_l/m_s (Co/Ni)	4.9%	9.8%
m_s (Os)	-1.05 μ_B	-0.98 μ_B
m_l (Os)	+0.34 μ_B	+0.34 μ_B
m_{tot} (Os)	-0.71 μ_B	-0.64 μ_B
m_l/m_s (Os)	33%	35%
m_{tot} (O)	-0.04 μ_B	-0.04 μ_B
net magnetization	+1.57 μ_B /fu	+0.61 μ_B /fu

and Ni(II) are in the more than half-filled d -states, small orbital moment at Co and Ni site, points parallel to the spin moments. On the other hand, large orbital moment m_l which is approximately one-third as large as the spin moment m_s at Os(VI) site, points opposite to the spin moment due to less than half-filled Os- t_{2g} occupancies.

The net magnetization values given in Table 7.2, are calculated by summing over all atoms and interstitial space in the unit cell. In absence of SOC, the net magnetization is found to be exactly 1 μ_B /formula unit (f.u.) for Ca₂CoOsO₆ where the Co(II) ion has one more unpaired electron than the Os(VI) ion, and 0 μ_B /f.u. for Ca₂NiOsO₆ where both ions have two unpaired electrons. Presence of SOC coupling increases the Co(II)/Ni(II) moment and decreases the Os(VI) moment, both of which thus lead to an increase in the net magnetization. In presence of SOC, along with supplemented Hubbard U, we find values of net magnetization to be 1.57 μ_B /f.u. for Ca₂CoOsO₆ and 0.61 μ_B /f.u. for Ca₂NiOsO₆, in good agreement with experimentally estimated values from magnetic hysteresis loop measurements.

7.2.4 Calculation of magnetic exchange interaction

As discussed in the introduction, tetragonal Sr₂BOsO₆ (B= Fe, Co, Ni and Cu) double perovskites are antiferromagnets while the monoclinic Ca₂BOsO₆ analogues are ferrimagnets. This behaviour indicates that there are competing super-exchange interactions and some or all of those interactions are highly sensitive to distortions of the structure.

We note that, the Co/Ni-O-Os bond angles in $\text{Ca}_2\text{CoOsO}_6$ and $\text{Ca}_2\text{NiOsO}_6$ are bent quite strongly away from the linear geometry of the aristotype cubic structure, to average values of 151° and 150° , respectively [cf. Table 7.1]. To see effect of this bond bending in the magnetic ground state, estimation of sign and relative strength of various coupling constants are very important. Due to the lack of large single crystals, estimation of sign and strength of the various coupling constants can not be obtained from experimental probes like inelastic neutron scattering. Therefore, to extract various coupling constants we carried out DFT total energy calculations of different spin configurations. By mapping total energy of five different collinear spin configurations of Co/Ni and Os onto an underlying spin model, various coupling constants are estimated. DFT estimated various coupling constants are summarized in Table 7.3 and the exchange path ways corresponding to each coupling constants are illustrated in Fig. 7.4. In the Table 7.4, NN signifies nearest neighbours and NNN signifies next nearest neighbours. Negative values of J signify antiferromagnetic coupling while positive values signify ferromagnetic coupling. Calculations were also carried out considering nine different spin configurations where we assumed the in plane and out-of-plane couplings to be different. But the difference between in-plane and out-of-plane couplings was estimated to be small due to nearly equal value of all three crystallographically distinct bond angles [cf. Table 7.1]. Table 7.3 shows that the Co/Ni-Os

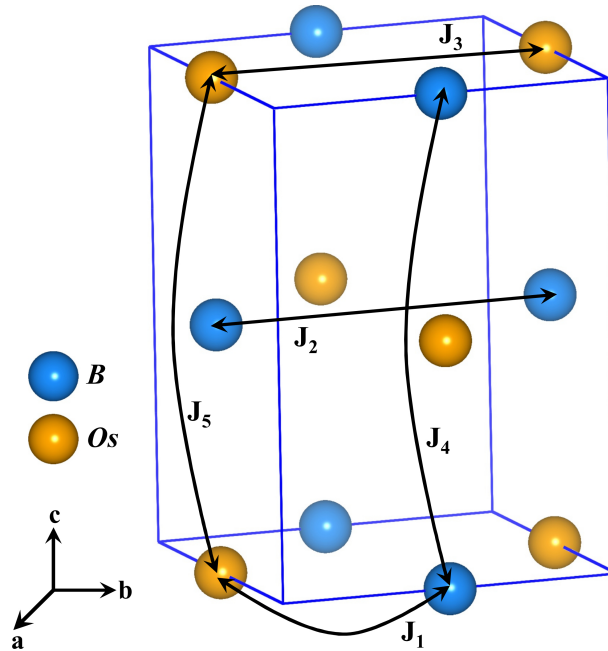


Figure 7.4: The relevant magnetic exchange pathways.

Table 7.3: Computed values of the relevant magnetic exchange interactions in meV unit. Negative and positive values of J signify, anti-ferromagnetic and ferromagnetic coupling respectively.

exchange	description	neighbours	Ca ₂ CoOsO ₆	Ca ₂ NiOsO ₆
J_1	Co/Ni-Os	6	-8.39	-10.82
J_2	Co-Co/Ni-Ni(NN)	12	-0.11	-0.08
J_3	Os-Os(NN)	12	+2.03	+2.72
J_4	Co-Co/Ni-Ni(NNN)	6	-0.37	-1.21
J_5	Os-Os (NNN)	6	+0.97	+0.29

interaction J_1 is the strongest interaction. This observation is not surprising because this is the shortest distance between magnetic ions. The negative sign indicates antiferromagnetic coupling between Co/Ni-Os which is consistent with experimentally observed ferrimagnetic ground state of these two compounds [12, 13]. The relative magnitudes of the homonuclear Co-Co or Ni-Ni coupling constants J_2 and J_4 are found to be consistent with the behaviour of other double perovskites containing a single late 3d transition metal ion [21–24]. Observation of ferromagnetic Os-Os coupling constants, J_3 and J_5 , is unexpected as there are no known examples of double perovskites where the only magnetic ion is a $5d^2$ (or $4d^2$) ion which are known to be a ferromagnet. Antiferromagnetic behavior was observed in double perovskites like Ba₂CaOsO₆, Ca₂CaOsO₆ and Sr₂MgOsO₆ containing Os(VI) [16–19]. Thus, the calculation have been cross checked in different basis set and different choice of U parameter over a reasonable range but the observation of the ferromagnetic Os-Os coupling constants, J_3 and J_5 was found to be robust output of the calculations. It is to be noted that the J_5 pathway was experimentally found to be ferromagnetic in the antiferromagnet Sr₂CoOsO₆ (or at least the moments connected by that pathway are aligned parallel) [9]. This partially support our findings. Though presence of ferromagnetic Os-Os coupling is unexpected but it works cooperatively with the antiferromagnetic Os-Co/Ni coupling to stabilize the ferrimagnetic state. We argued that Os-O-O-Os dihedral angles play a crucial role for this observation of ferromagnetic Os-Os coupling. We will discuss this issue in more details in the discussion section.

Considering the pseudo sum, defined as $\sum J_k \cdot Z_k \cdot S_i \cdot S_j$, over the dominant magnetic interactions listed in Table 7.3, we calculated the Curie temperature (T_c) for both Ca₂CoOsO₆ and Ca₂NiOsO₆ using mean field equation. In the pseudo sum formula, Z_k is the number of neighbours for the k^{th} magnetic interaction and S_i and S_j are the spin values of the magnetic sites

at i and j defining the magnetic interactions. To calculate the T_c , spin values of Co(II), Ni(II) and Os(VI) are taken as 3/2, 1 and 1, respectively. The ratio of Curie temperature ($T_c^{Ni}/T_c^{Co} = 1.13$) is found to be in good agreement with experimentally observed ratio ($T_c^{Ni}/T_c^{Co} = 175 \text{ K}/145 \text{ K} = 1.2$) [12, 13].

7.3 Experimental results

The theoretical results based on DFT calculations are further corroborated by experimental measurements like dc conductivity, magnetization, X-ray absorption spectroscopy (XAS) and X-ray magnetic circular dichroism (XMCD). The brief description of experimental results are given below. For details see the Ref [25].

7.3.1 DC electrical conductivity measurements

The dc electrical conductivity measurement was made using the 4-point probe method on sintered polycrystalline pellets for both the compounds $\text{Ca}_2\text{CoOsO}_6$ and $\text{Ca}_2\text{NiOsO}_6$ to confirm the insulating behaviour of the ground state. Fig. 7.5 shows the measured dc electrical con-

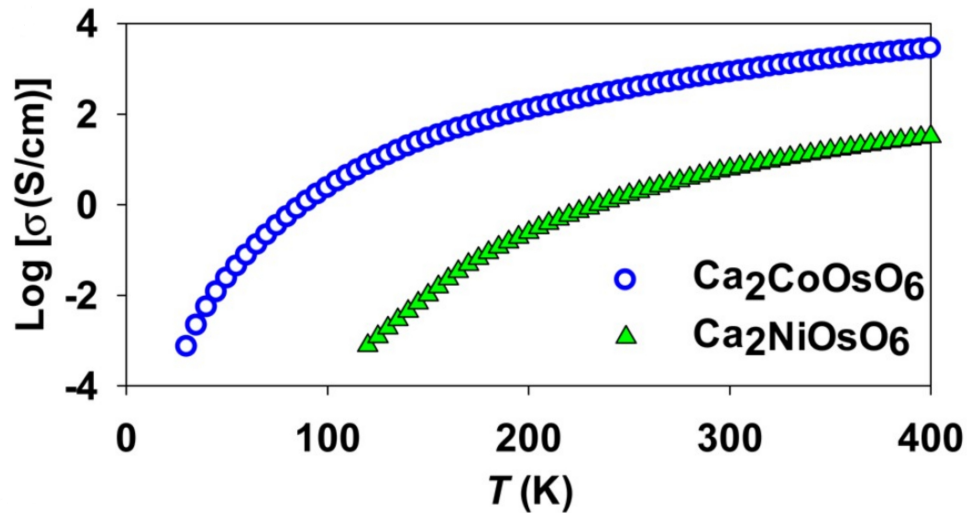


Figure 7.5: Temperature dependence of the electrical conductivity of $\text{Ca}_2\text{CoOsO}_6$ and $\text{Ca}_2\text{NiOsO}_6$ shown on a linear temperature scale. (reproduced from Ref. [25]).

ductivities which clearly indicate that both the $\text{Ca}_2\text{CoOsO}_6$ and $\text{Ca}_2\text{NiOsO}_6$ exhibit insulating

behaviour, in agreement with DFT obtained result. The conductivity of $\text{Ca}_2\text{NiOsO}_6$ is found to be roughly 2 orders of magnitude smaller than that of $\text{Ca}_2\text{CoOsO}_6$.

7.3.2 Magnetic hysteresis loop measurements

Fig. 7.6 shows the experimentally measured magnetic hysteresis loops for each compound. From

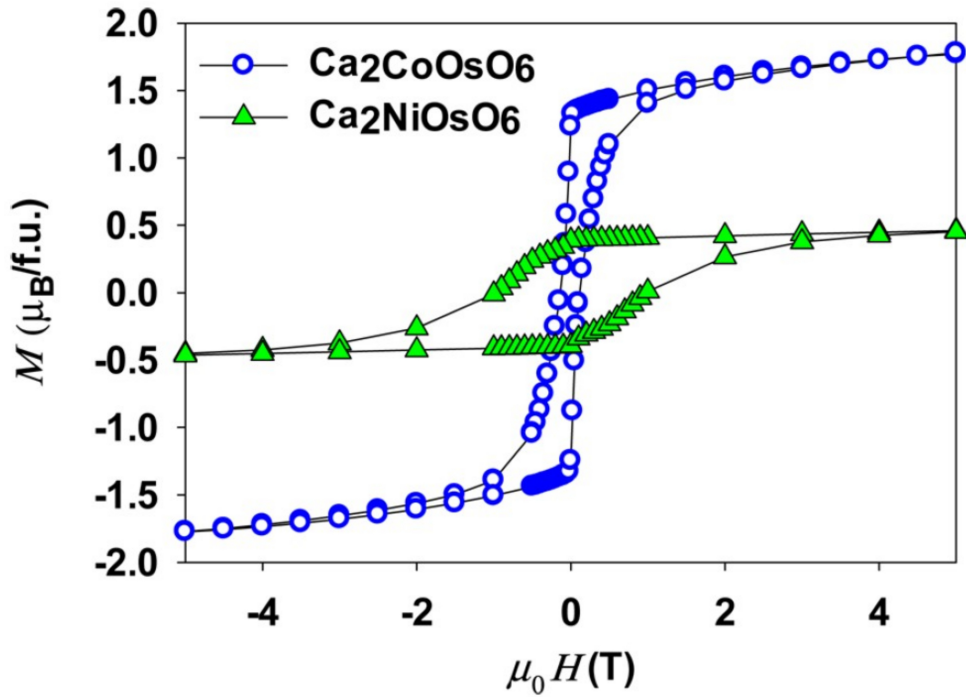


Figure 7.6: Field dependence of the magnetization measured at 5 K. (reproduced from Ref. [25]).

these plots, saturation magnetization values were estimated to be $1.77 \mu_B/\text{f.u.}$ for $\text{Ca}_2\text{CoOsO}_6$ and $0.48 \mu_B/\text{f.u.}$ for $\text{Ca}_2\text{NiOsO}_6$ in good agreement with DFT obtained values.

7.3.3 XAS and XMCD measurements

To confirm the oxidation state of transition metal ions (Co, Ni and Os), X-ray absorption spectroscopy (XAS) as well as X-ray magnetic circular dichroism (XMCD), measurements were made at the $L_{3,2}$ edges of the Co and Ni ions at 10 K and at the $L_{3,2}$ edges of Os at 5 K. These measured XAS and XMCD data are shown in Fig. 7.7. From the observed XAS L_3 and L_2 peak shapes and energies, oxidation states were assigned to be high spin Co(II) and Ni(II), in complete agreement with DFT assigned oxidation state. Due to the closeness in L edge

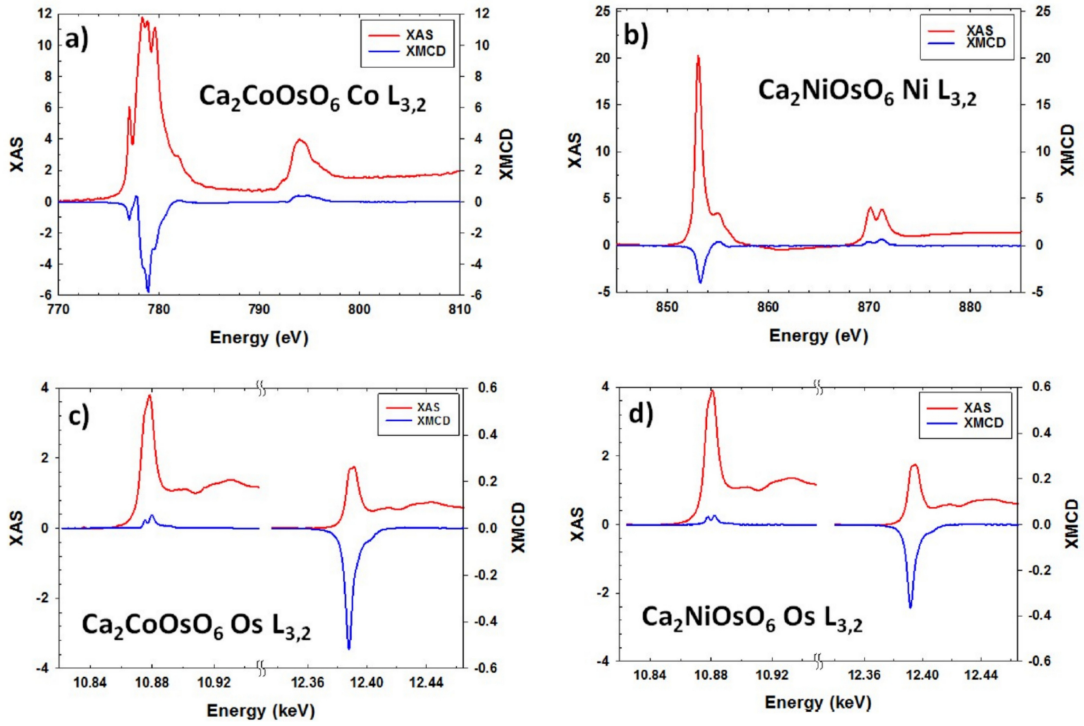


Figure 7.7: XAS and XMCD spectra of $\text{Ca}_2\text{CoOsO}_6$ (a, c) and $\text{Ca}_2\text{NiOsO}_6$ (b, d). The data have been normalized to a 2:1 L_3 to L_2 step size. Arbitrary y-axis units are used for all spectra. (reproduced from Ref. [25]).

XAS peak shape and position for the different valencies [26, 27], assignment of oxidation state for $5d$ cations are less straightforward. In the absence of large concentrations of defects (*e.g.*, oxygen vacancies) the oxidation state was assigned to be Os(VI) from the stoichiometry and the oxidation state of the $3d$ ion. These assigned oxidation state *i.e.* high-spin Co(II), Ni(II) and Os(VI), from XAS measurement are in agreement with the DFT obtained results.

Using X-ray magnetic circular dichroism (XMCD) sum rules [28], spin, orbital and total moments were estimated for Co, Ni and Os ions. These values are given in Table 7.4.

Table 7.4: The spin (m_s) and orbital (m_l) moments obtained from X-ray magnetic circular dichroism measurements (XMCD)

	$\text{Ca}_2\text{CoOsO}_6$		$\text{Ca}_2\text{NiOsO}_6$	
	Co	Os	Ni	Os
m_s	+1.80	-1.97	0.90	-1.20
m_l	+0.80	0.56	+0.27	+0.34
m_{tot}	+2.60	-1.41	+1.17	-0.86
m_l/m_s	44%	-29%	29%	-28%

Fig. 7.7 and Table 7.4 show that the magnetic moment of each $3d$ transition metal is oppositely aligned to the Os moment. From this observation, together with the absence of (purely) magnetic diffraction peaks in the neutron diffraction data, and the observed values of net magnetization, experimentally predicted that magnetic ground state to be ferrimagnetic in nature. This observation is found to be consistent with DFT obtained results. The total moments obtained from XMCD measurements for the $3d$ ions are found to be much smaller than the DFT calculated values of $2.75 \mu_B$ (Co) and $1.76 \mu_B$ (Ni). Conversely, the value of the Os moments obtained from XMCD is found to be larger compared to the DFT calculated values [see Tables 7.2 and 7.4]. Experimentally suggested possible reasons for this discrepancy are,

- (i) exclusion of the magnetic dipole term in the spin sum rule. For example, in $\text{Sr}_2\text{FeOsO}_6$ it contributes a 20% correction to the Os spin moment [7].
- (ii) exclusion of core level mixing in $3d$ cations, such as Co(II) and Ni(II).

The m_l/m_s ratio obtained from XMCD is in reasonable agreement with the DFT calculated values for Os(VI).

7.4 Discussion

Among the Os based double perovskites, $\text{Ca}_2\text{CoOsO}_6$ can be considered as one of the best candidate to be a half metallic conductor due to the following facts:

- (i) the t_{2g} orbitals of both Os and Co are partially filled.
- (ii) antisite disorder of Co/Os is very small.
- (iii) and the ferrimagnetic ordering is ideal for delocalization of the electrons in the Os $5d$ orbitals.

But, conductivity measurement of $\text{Ca}_2\text{CoOsO}_6$ ruled out metallic conductivity. The DFT obtained DOS within GGA scheme of calculation, showed considerable hybridization between Os and Co t_{2g} orbitals at the Fermi level (E_F) which led the compound to a half metallic conductor. Nevertheless, we found presence of spin-orbit coupling (SOC) together with supplemented Hubbard U, reduced that hybridization and opened up a small gap at E_F which made $\text{Ca}_2\text{CoOsO}_6$

a SOC assisted Mott insulator. $\text{Ca}_2\text{NiOsO}_6$ is also SOC assisted Mott insulator but the conductivity is found to be dropped by 2-3 orders of magnitude compared to that of $\text{Ca}_2\text{CoOsO}_6$. From the partial DOS plots [cf. Fig. 7.3] we found a much smaller contribution of the Ni $3d$ orbitals to the minority spin Os t_{2g} bands of $\text{Ca}_2\text{NiOsO}_6$ than the Co $3d$ orbital contribution to those same bands in $\text{Ca}_2\text{CoOsO}_6$. The decreased conductivity likely originates from the above mentioned effect.

One of the main motivation behind this present study was to estimate the size of the local moment on the Os(VI) ion. Though there is some spread in the exact value of the Os moment but XMCD measurements and first-principles based DFT calculations pointed to a finite local moment on Os(VI). Neutron diffraction is most straightforward technique for determining local moments but in the literature there are no known example of double perovskites containing Os(VI) the only magnetic ion where researchers have been able to measure the moment using neutron diffraction [16–19]. However, in perovskites containing the d^3 Os(V) ion, such as Sr_2BOsO_6 (B = Sc, In, Y) and Ba_2YOsO_6 , using neutron diffraction technique the local moment at Os(V) has been found to be in the range 1.6-1.9 μ_B [29–31]. One can expect that going from the Os(VI) $5d^3$ configuration to Os(V) $5d^2$ spin moment should be reduced by a factor of 1/3. The increase in oxidation state should also increase covalency with oxygen which will further reduce the Os moment and also the SOC, will further reduce the Os moment which is expected to be much higher for the d^2 configuration compared to d^3 configuration. Considering all these factors, it seems that DFT calculated Os(VI) moment of 0.6-0.7 μ_B [cf. Table 7.2] are a reasonable estimation.

DFT estimated magnetic exchange interactions pointed out two key things:

- (i) the failure of the Goodenough-Kanamori rules [3, 4] to predict the sign of the Os-Co/Ni super-exchange coupling.
- (ii) and the unexpected observation of ferromagnetic Os-Os coupling.

According to Goodenough-Kanamori prescription, the super-exchange interaction between a half-filled e_g orbitals (Co(II)/Ni(II)) and one with empty e_g orbitals (Os(VI) in the present case) should be ferromagnetic, as observed in $\text{La}_2\text{NiMnO}_6$ [32, 33] or $\text{La}_2\text{CoMnO}_6$ [20]. This

prediction is in disagreement with both DFT calculations and experimental observations. However, Os being a $5d$ transition metal ion, its t_{2g} - e_g crystal-field splitting is large (about 4 eV). This makes negligible hybridization of Co/Ni e_g states with empty Os e_g states via oxygen, thus making e_g states out of the picture. Therefore, general question arises is that if Os e_g -Co/Ni e_g interactions are not playing an important role what types of orbital interactions are leading to the strong antiferromagnetic coupling of the ions. In $\text{Ca}_2\text{NiOsO}_6$, Os t_{2g} -Ni t_{2g} hopping interactions are not possible as Ni t_{2g} orbitals are completely filled. The only possible realistic super-exchange interaction can occur between the Ni(II) half-filled e_g orbitals and Os(VI) partially filled t_{2g} . In the cubic double perovskite structure these two sets of orbitals are orthogonal which will hinder the hopping interaction between them. But this is not the case in the monoclinic structures that $\text{Ca}_2\text{NiOsO}_6$ and $\text{Ca}_2\text{CoOsO}_6$ adopt. In order to rationalize the sign of the net magnetic interaction between Co(II)/Ni(II) and Os(VI) we considered simple electron exchange pathways, as shown in Fig. 7.8. It shows the presence of both ferromagnetic

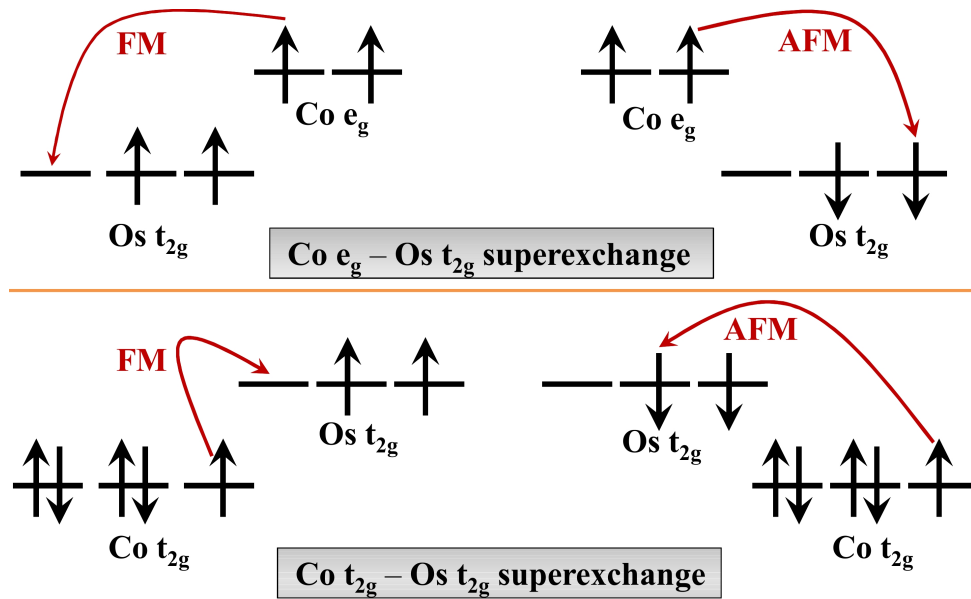


Figure 7.8: Potential superexchange interactions between the Os t_{2g} orbitals and the Co e_g orbitals (upper row), and the Co t_{2g} orbitals (lower row).

and antiferromagnetic contributions from different channels. The virtual exchange between the half-filled Co(II)/Ni(II) e_g orbitals and the two half-filled Os t_{2g} orbitals, leads antiferromagnetic contribution, while the ferromagnetic contribution is due to virtual exchange between the half-filled Co(II)/Ni(II) e_g orbitals and the single empty Os t_{2g} orbital. As there are two half-filled Os t_{2g} orbitals and only one empty Os t_{2g} orbital, the number of antiferromagnetic

interactions is double than the number of ferromagnetic interactions (see the upper panel of Fig. 7.8). This leads antiferromagnetic Os-O-Ni/Co coupling, in spite of the Hund's energy gain that accompanies the ferromagnetic exchange pathway. In $\text{Ca}_2\text{CoOsO}_6$ two additional interaction channels open up which are shown in the lower panel of Fig 7.8. Once again, the number of antiferromagnetic channels is found to be greater than that of the ferromagnetic channels which favoured net antiferromagnetic Co-Os interaction. Following the above discussion, we can now understand why the magnetic ground states of $\text{Sr}_{2-x}\text{Ca}_x\text{BOsO}_6$ ($B = \text{Co}, \text{Ni}$) double perovskites are so sensitive to Os-O-B bond angles. As mentioned above, the antiferromagnetic coupling of Os-O-B (J_1) involves virtual hopping between e_g and t_{2g} orbitals. Thus J_1 term should be smaller as the bonds become more linear, as is the case in $\text{Sr}_2\text{CoOsO}_6$ and $\text{Sr}_2\text{NiOsO}_6$. As the Os-O-B bond angle approaches 180° , not only the strength of J_1 will decrease but it is expected the longer range antiferromagnetic Co-Co and Ni-Ni exchange interactions, J_4 [cf. Fig. 7.4] to be stronger. Thus, this effect can lead formation of anti-ferromagnetic state.

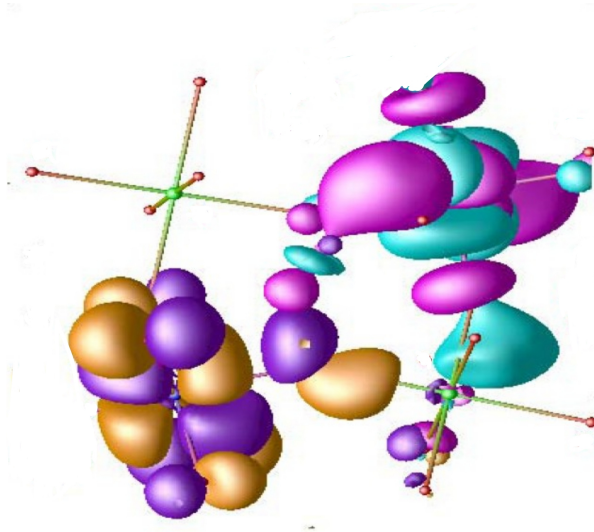


Figure 7.9: Overlap of the Os xy effective Wannier functions in $\text{Ca}_2\text{CoOsO}_6$ obtained from NMTO-downfolding calculations, keeping active only the Os t_{2g} states in the basis. The plot shows the overlap of Wannier functions at two Os sites connected through diagonal hopping. Plotted are the constant value surfaces with positive and negative lobes of the wavefunctions coloured differently at two different Os sites. The red small and green medium balls denote the positions of the O and Co. The Ca atom sits in the middle of the square, covered by the lobes of the Wannier functions.

Observation of Os-Os ferromagnetic coupling, as obtained from DFT calculation, is interesting and demands attention. Primarily to understand this ferromagnetic nature of coupling,

we calculated effective Os t_{2g} Wannier function from NMTO downfolding calculation keeping only Os t_{2g} states active and integrating out all other degrees of freedom. Fig. 7.9 shows the overlap of two Os xy Wannier function placed at diagonal position. The central part of the wannier function follows the xy symmetry while tail parts are shaped according to integrated out orbitals. Presence of pronounced tail shaped at O site and negligibly small at Co site indicates that the Os-O-O-Os exchange pathway is the dominant exchange pathway. Therefore, the dihedral angle involving Os-O-O-Os atoms should be important, especially for the NN Os-Os interaction for which the value of the exchange interaction is found to be substantial [see Table 7.3]. In $\text{Ca}_2\text{CoOsO}_6$ and $\text{Ca}_2\text{NiOsO}_6$ this dihedral angle is small ($\approx 30^\circ$ - 35°) compared to antiferromagnet $\text{Ca}_2\text{CaOsO}_6$ in which it is 60.4° [16]. Further studies are needed to confirm or refute this observation of the effect of the Os-O-O-Os dihedral angle on Os-Os superexchange coupling.

7.5 Conclusions

We have studied magnetic properties of two ferrimagnetic double perovskites $\text{Ca}_2\text{CoOsO}_6$ and $\text{Ca}_2\text{NiOsO}_6$ by calculating the magnetic moment and super-exchange couplings from DFT based first principles calculations. From the DFT calculation, we found, inclusion of spin-orbit coupling together with electron correlations led to a localized electron insulator instead of a half metallic conductor, in agreement with experimentally observed insulating nature of ground state from dc conductivity measurement. From the DFT calculations the local moment on the d^2 Os(VI) ion is found to be around 0.6 - $0.7 \mu_B$. The moment is reduced by approximately 50% due to strong covalency with the surrounding oxygens and by another 30% due strong spin-orbit coupling. DFT estimated magnetic exchange interactions suggested ground state to be ferrimagnetic in nature, in agreement with experimental observation. The ferrimagnetism is found to be driven by antiferromagnetic Os-O-Co/Ni super-exchange coupling, which arises from half-filled e_g orbitals of the $3d$ Co/Ni ion and partially filled t_{2g} orbitals of the $5d$ Os ion. Our DFT obtained results are further corroborated by experimental measurements like magnetization, X-ray absorption spectroscopy (XAS) and X-ray magnetic circular dichroism (XMCD). XMCD measurements confirmed the presence of strong spin-orbit coupling at Os site.

Bibliography

- [1] D. Serrate, J. M. De Teresa, M. R. Ibarra, *J. Phys. Condens. Matter.* 19, 023201 (2007).
- [2] W. Witczak-Krempa, G. Chen, Y. B. Kim, L. Balents, *Annu. Rev. Condens. Matter Phys.* 5, 57-82 (2014).
- [3] J. B. Goodenough, *Phys. Rev.* 100, 564-573 (1955).
- [4] J. Kanamori, *J. Phys. Chem. Solids* 10, 87-98 (1959).
- [5] A. K. Paul, M. Reehuis, V. Ksenofontov, B. Yan, A. Hoser, D. M. Tobbens, P. M. Abdala, M. Jansen, C. Felser, P. Adler, *Phys. Rev. Lett.* 111, 167205 (2013).
- [6] R. Morrow, J. W. Freeland, P. M. Woodward, *Inorg. Chem.* 53, 7983-7992 (2014).
- [7] L. S. I. Veiga,; G. Fabbris, M. van Veenendaal, N. M. Souza-NEto, H. L. Feng, K. Yamaura, D. Haskel, *Phys. Rev. B*, 91, 235135 (2015).
- [8] L. H. Feng, M. Arai, Y. Matsushita, Y. Tsujimoto, Y. Guo, C. I. Sathish, X. Wang, Y. Yuan, M. Tanaka, K. Yamaura, *J. Am. Chem. Soc.* 136, 3326-3329 (2014).
- [9] R. Morrow, R. Mishra, O. R. Restrepo, R. M. Ball, W. Windl, S. Wurmehl, U. Stockert, B. Buchner, P. M. Woodward, *J. Am. Chem. Soc.* 135, 18824-18830 (2013).
- [10] B. Yan, A. K. Paul, S. Kanungo, M. Reehuis, A. Hoser, D. M. Tobbens, W. Schnelle, R. C. Williams, T. Lancaster, F. Xiao, J. S. Moller, S. J. Blundell, W. Hayes, C. Felser, M. Jansen, *Phys. Rev. Lett.* 112, 147202 (2014).
- [11] A. K. Paul, M. Reehuis, C. Felser, P. M. Abdala, M. Jansen, *Z. Anorg. Allg. Chem.* 639, 2421-2425 (2013).

- [12] R. Morrow, J. Q. Yan, M. A. McGuire, J. W. Freeland, D. Haskel, P.M. Woodward, *Phys. Rev. B*, 2015, 92, 094435 (2015).
- [13] R. Macquart, S. J. Kim, W. R. Gemmill, J. K. Stalick, Y. Lee, T. Vogt, H. C. Zur Loye, *Inorg. Chem.* 44, 9676-9683 (2005).
- [14] M. W. Lufaso, W. R. Gemmill, S. J. Mugavero, S. J. Kim, Y. Lee, T. Vogt, H. C. zur Loye, *J. Solid State Chem.* 181, 623-627 (2008).
- [15] K. J. Yamaura, *Solid State Chem.* 236, 45-54(2016).
- [16] C. M. Thompson, J. P. Carlo, R. Flacau, T. Aharen, I. A. Leahy, J. R. Pollicemi, T. J. S. Munsie, T. Medina, G. M. Luke, J. Munevar, S. Cheung, T. Goko, Y. J. Uemura, J.E. Greedan, *J. Phys.: Condens. Matter* 26, 306003 (2014).
- [17] H. L. Feng, Y. Shi, Y. Guo, J. Li, A. Sato, Y. Sun, X. Wang, S. Yu, C. I. Sathish, K. Yamaura, *J. Solid State Chem.* 201, 186-190 (2013).
- [18] A. Sarapulova, P. Adler, W. Schnelle, D. Mikhailova, C. Felser, L. H. Tjeng, M. Jansen, *Anorg. Allg. Chem.* 641, 769-771 (2015).
- [19] Y. Yuan, H. L. Feng, M. P. Ghimire, Y. Matsushita, y. Tsujimoto, J. He, M. Tanaka, Y. Katsuya, K. Yamaura, *Inorg. Chem.* 54, 3422-3431 (2015).
- [20] S. Baidya, T. Saha-dasgupta, *Phys. Rev. B*, 84, 035131 (2011).
- [21] C. A. Lopez, M. E. Saleta, J. Curiale, R. D. Sanchez, *Mater. Res. Bull.* 47, 1158-1163 (2012).
- [22] M. C. Viola, M. J. Martinez-Lope, J. A. Alonso, J. M. De Paoli, S. Pagola, J. C. Pedregosa, M. T. Fernandez-Diaz, R. E. Carbonio, *Chem. Mater.* 15 (8), 1655-1663 (2003).
- [23] C. G. F. Blum, A. Holcombe, M. Gellesch, S. Rodan, R. Morrow, A. Maljuk, P. M. Woodward, P. Morris, A. U. B. Wolter, B. Buchner, S. J. Wurmehl, *Cryst. Growth*, 421, 39-44 (2015).
- [24] K. R. Chakraborty, A. Das, P.S. R. Krishna, S. M. Yusuf, S. J. Patwe, S. N. Achary, A. K. Tyagi, *J. Alloy Compd.* 457, 15-18 (2008).

- [25] Ryan Morrow, Kartik Samanta, Tanusri Saha Dasgupta, Jie Xiong, John W. Freeland, Daniel Haskel, and Patrick M. Woodward, *Chem. Mater.* 28, 3666-3675 (2016).
- [26] J. H. Choy, D. K. Kim, J. Y. Kim, *Solid State Ionics* 108, 159-163 (1998).
- [27] M. A. Laguna-Marco, P. Kayser, J. A. Alonso, M. J. Martinez-Lope, m. van Veenendaal, Y. Choi, D. Haskel, *Phys. Rev. B*, Phys. 91, 214433 (2015).
- [28] C. T. Chen, Y. U. Idzerda, H. J. Lin, N. V. Smith, G. Meigs, E. Chaban, G. H. Ho, G. E. Pellegrin, F. Sette, *Phys. Rev. Lett.* 75, 152-15 (1995).
- [29] E. Kermarrec, C. A. Marjerrison, C. M. Thompson, D. D. Maharaj, K. Levin, S. Kroeker, G. E. Granroth, R. Flacau, Z. Yamani, G. E. Greedan, B. D. Gaulin, *Phys. Rev. B: Condens. Matter Mater. Phys.* 91, 075133 (2015).
- [30] A. E. Taylor, R. Morrow, D. J. Singh, S. Calder, M. D. Lumsden, P. M. Woodward, A. D. Christianson, *Phys. Rev. B*, 91, R100406 (2015).
- [31] A. K. Paul, A. Sarapulova, P. Adler, M. Reehuis, S. Kanungo, D. Mikhailova, W. Schnelle, Z. Hu, C. Kuo, V. Siruguri, S. Rayaprol, Y. Soo, B. Yan, C. Felser, L. Hao Tjeng, M. Z. Jansen, *Anorg. Allg. Chem.* 641, 197-205 (2015).
- [32] D. Haskel, G. Fabbri, N. M. Souza-Neto, M. van Veenendaal, G. Shen, A. E. Smith, M. A. Subramanian, *Phys. Rev. B*, 84, 100403 (2011).
- [33] H. Das, U. V. Waghmare, T. Saha-Dasgupta, D. D. Sarma, *Phys. Rev. B*, 79, 144403 (2008).

Chapter 8

Conclusion and outlook

8.1 Conclusion

Interplay between charge, orbital and spin degrees of freedom in transition metal compounds give rise to many novel physical phenomena which are appealing both from application as well as fundamental science aspect. Understanding of this complex interplay is a great challenge for modern day research. The aim of this thesis was to the investigation of microscopic origin of many exciting and intriguing physical properties as well as improve physical properties of different transition metal compounds. As presented in chapters 3-7, we have studied different transition metal compounds belonging two broad categories, namely i) low dimensional quantum spin systems ii) double perovskite compounds, using density functional theory (DFT) as well first principles derived model Hamiltonian approach combined with many body techniques like quantum Monte Carlo (QMC) method and exact diagonalization (ED). At the end of each chapter summary of result and discussion have been presented in that particular chapter. In this chapter we enlist the main findings of this thesis in a concise manner.

chapter3 :Magnetic modeling and effect of biaxial strain on the Haldane chain compound $\text{SrNi}_2\text{V}_2\text{O}_8$

- DFT based parameter-free first-principles calculation suggested that S=1 Haldane spin chain compound SrNi₂V₂O₈ can be described by a coupled spin chain J_1 - J_2 - J_3 - J_4 model, together with easy axis single-ion anisotropy, where J_1 is the strongest nearest neighbour intrachain coupling, J_2 is the next-nearest-neighbour intrachain coupling, and J_3 and J_4 are two interchain couplings.
- Site projected density of states and Wannier function plots revealed that nonmagnetic V (V^{5+} ; $3d^0$; S=0) atom plays a crucial role in mediating the super-exchange interactions between two nearest neighbour Ni sites (J_1) along the chain direction.
- The computed thermodynamic properties like static susceptibility and high field magnetization for proposed spin model by performing the quantum Monte Carlo (QMC) simulations (stochastic series expansion) showed good agreement with experimental observation.
- The estimated spin gap ($0.32J_1$) from the estimate of the critical field was found to be much reduced compared to $0.41J_1$ value of an ideal 1D Haldane chain. The next-nearest-neighbour intrachain coupling J_2 was found to have the strongest effect in this reduction.
- With an application of 2% biaxial compressive strain, spin gap was found to be increased compared to its value in unstrained condition due to the significant change in the J_2/J_1 ratio. On the other hand, upon application of 2% biaxial tensile strain, the spin gap was found to be reduced compared to its value in unstrained condition due to the reduction on the strength of strongest coupling J_1 . Thus, a monotonic decrease of the absolute value of the spin gap, upon changing lattice constant, as obtained in our study, suggests that a tensile strain of 7-8% may enable a closure of spin-gap, thereby driving quantum phase transition from spin-gapped ground state to an ordered one.

chapter 4: Spin state of Mn²⁺ and magnetism in vanadate-carbonate compound, K₂Mn₃(VO₄)₂CO₃

- The high spin state of two inequivalent Mn²⁺ ions, Mn1 and Mn2, one in octahedral and another in trigonal-bipyramidal coordination in K₂Mn₃(VO₄)₂CO₃ compound was confirmed from site, spin projected density of states, calculated magnetic moment and

fixed moment calculations. This finding contradicts the experimental suggestion that Mn1 is in the high spin state and Mn2 is in the low spin state. The similar values of crystal field splitting (≈ 0.9 eV) at both inequivalent Mn sites as given in DFT calculation, further justified the high spin state of both the inequivalent Mn^{2+} ions.

- The estimated magnetic exchange interactions between Mn^{2+} ions obtained from the knowledge of hopping parameters, employing super-exchange formula, as well as from mapping of total energies of different magnetic arrangements to Ising Hamiltonian, established that spin model of vanadate-carbonate compound to be a antiferromagnetic $S = 5/2$ model, with weakly coupled alternating layers of honeycomb and triangular lattices.
- Nearest-neighbour (NN) interaction in the honeycomb Mn1 layer was found to be the strongest interaction, followed by second and third-neighbour interactions which were found to be small but nonnegligible. The nearest-neighbour interaction in triangular Mn2 layer was found to be order of magnitude smaller compared to strongest nearest neighbour interaction in the honeycomb Mn1 layer.
- The frustration effect in the triangular geometry of the Mn2 spins due to the antiferromagnetic nature of NN Mn2-Mn2 interaction, gave rise to canting of the spins in Mn2 layer with noncollinear arrangement. In the Mn1 layer spins arrangement was found to be collinear with alternate pointing of spins along the hexagonal ring of the honeycomb lattice.
- Computed static magnetic susceptibility and the magnetic-field dependence of the magnetization for proposed spin model, using QMC simulation were found to provide reasonable description of the experimental results.

chapter 5: Rocksalt versus layered ordering in double perovskites: A case study with $\text{La}_2\text{CuSnO}_6$ (LCIO) and $\text{La}_2\text{CuIrO}_6$ (LCSO)

- Layered structure in both LCIO and LCSO was found to be stabilized within non-spin polarised scheme of calculation which is expected to take primarily the band structure

effect. We found presence of large in plane nearest neighbour Cu-Cu hopping drives the layered ordering over the rock-salt ordering.

- In presence of magnetism, structural stability of LCSO was found to be maintained but effect of magnetism was found to be dramatic for LCIO, making layered ordering favourable compared to layered. This reversing in relative structural stability (*i.e.* stability of rock-salt ordering over layered ordering) was found to be driven by the strong Cu-Ir super-exchange interaction. The magnetism driven stability of rock-salt ordering over layered ordering in LCIO was found to hold good also in presence of spin orbit coupling.
- In order to confirm the rigorousness of our conclusion, we further studied the structural stability of $\text{La}_2\text{CuMnO}_6$ compound. In absence of magnetism the layered ordering was found to be favoured over rock-salt, which turning on magnetism reversed the stability, making rock-salt favoured over layered. Our rigorous studies in terms of energetics, electronic structure calculation and NMTO downfolding calculation showed that presence of magnetic ion at B' site of double perovskite $\text{A}_2\text{BB}'\text{O}_6$, is extremely important in order to maintain the magnetism driven stability of rock-salt ordered structure over layered ordered structure.
- We also found presence of strong SOC coupling at Ir (Ir^{4+} ; d^5 ; $S=1/2$) site which splits the Ir- t_{2g} bands into $j_{eff} = 1/2$ doublet and $j_{eff} = 3/2$ quartet. Calculated band structure and density of states within the scheme of GGA+U+SOC calculation showed LCIO to be a $j_{eff} = 1/2$ Mott insulator in agreement with finding of recent literature.

chapter 6: Half-Metallic Behaviour in Doped $\text{Sr}_2\text{CrOsO}_6$ Double Perovskite with High Transition Temperature

- From DFT calculations together with exact diagonalization of the low energy model Hamiltonian consisting of Cr and Os t_{2g} degrees of freedom, we found that upon moderate Na (hole) or La (electron) doping of about 10 to 20% at the Sr site of $\text{Sr}_2\text{CrOsO}_6$, half-metallic ferrimagnetic state is achievable with high transition temperature which was estimated to be 87 to 99% of the T_c of the parent compound (725 K).

- For Na doping broad Os t_{2g} - Cr t_{2g} hybridized bands in the minority spin channel became conducting while majority spin channel remained insulating. On the other hand narrow Os t_{2g} bands in the majority spin channel became conducting while minority spin channel remained insulating for La doping. Due to this asymmetry, the degree of spin polarization was found to be higher in Na doped compounds compared to La doped compounds while magnetic transition temperature was found to be higher for La doped compounds compared to Na doped compounds. Considering different doping levels of both Na and La doping, our study suggests that 10% of Na doping at Sr site would be a good choice which has both high T_c and high degree of spin polarization.
- We further noticed that finding of the half-metallicity by La/Na doping in $\text{Sr}_2\text{CrOsO}_6$ is very similar to that proposed in recent literature, in the context of 2 band model Hamiltonian study based on dynamical mean field theory calculation. Our study in this sense was realization of the model study proposed in Ref.[Phys. Rev. Lett. 112, 106406 (2014)] which can be validated experimentally.

chapter 7: Magnetism in $\text{Ca}_2\text{CoOsO}_6$ and $\text{Ca}_2\text{NiOsO}_6$: Unraveling the Mystery of Superexchange Interactions between $3d$ and $5d$ Ions

- From the DFT calculations both the compounds were found to be spin-orbit coupling assisted Mott insulators instead of a half metallic conductors.
- DFT calculated local moment at the d^2 Os(VI) ion was found to be around $0.6-0.7 \mu_B$. The calculated moment is reduced compared to moment expected from nominal value by about 50% due to strong covalency with oxygen owing to larger spatial extension of $5d$ orbital and by another 30% due to presence of strong spin-orbit coupling at Os site.
- DFT estimated magnetic exchange interactions suggested ground state to be ferrimagnetic in nature. The ferrimagnetism was found to be driven by antiferromagnetic Os-O-Co/Ni super-exchange coupling, which arises from half-filled e_g orbitals of the $3d$ Co/Ni ion and partially filled t_{2g} orbitals of the $5d$ Os ion.
- Our DFT calculated result were further corroborated by experiments. Experimentally measured dc conductivities measurements for both compounds confirmed the insulating

nature of ground state. XMCD measurements confirmed the presence of strong spin-orbit coupling at the Os site. The neutron diffraction data and measured saturation magnetization values from field dependence of the magnetization of $\text{Ca}_2\text{CoOsO}_6$ and $\text{Ca}_2\text{NiOsO}_6$ provided the validation of the ferrimagnetic ground state.

8.2 Outlook

In this present thesis, out of vast field of transition metal compounds, we studied few of the relevant transition compounds belonging two broad categories, namely (i) low dimensional quantum spin system, (ii) double perovskite compounds. This thesis covers very little, yet important part of this vast field. There are few issues in connections to the transition metal compounds that we have studied which can be taken up for further studies. Here we list few such possibilities which can be considered as a future continuation of the present study.

- Our conjecture of closing of spin-gap value by application of tensile biaxial strain of 7-8% in $\text{SrNi}_2\text{V}_2\text{O}_8$ can be validated experimentally by considering a film of $\text{SrNi}_2\text{V}_2\text{O}_8$, grown along the (001) direction and placed on a piezoelectric substrate to tune the biaxial strain. This should enable experimental realization of quantum phase transition from spin-gapped ground state to an ordered state.

The almost 90° Ni-O-Ni superexchange pathways between two intrachain nearest neighbour (NN) Ni ions in $\text{SrNi}_2\text{V}_2\text{O}_8$ should prefer a weak ferromagnetic interaction according to Goodenough-Kanamori rules. However we found the presence of empty V d orbitals play a crucial role in making this magnetic interactions strong and antiferromagnetic. This phenomena of strong super-exchangeexchange paths involving empty d orbitals are quite common in V^{5+} systems. Therefore if one replaces the d element V in $\text{SrNi}_2\text{V}_2\text{O}_8$ with a p element, such as P and As, it may drastically affect the nearest neighbours magnetic coupling. This could be a interesting route to modulate the magnetic properties of this $S=1$, nickelate system.

- The magnetic properties of $\text{K}_2\text{Mn}_3(\text{VO}_4)_2\text{CO}_3$ has been discussed experimentally in terms of unusual low-spin configuration of Mn2, while our present theoretical study established

that Mn²⁺ is in high spin state. This difference in conclusion of our present theoretical study and the experimental study concerning the spin state of Mn²⁺ demands further experimental study of this interesting issue, which should use direct probe of the spin state of specific atom.

- Our theoretical prediction of driving half-metallicity in ferrimagnetic insulator Sr₂CrOsO₆, by moderate La/Na doping of about 10 to 20 % at the Sr site maintaining the high T_c of parent compound (725 K) can stimulate experimental investigation in this direction.

It is well known fact that antisite disordered can lower the magnetic transition temperature, even can destroy the half-metallicity. As La doping reduces the valence difference between Cr and Os, it may lead to increased antisite disorder. Thus consideration of antisite disorder effect in calculating the magnetic transition temperature can be taken up as a future project.

With increasing filling in Sr₂CrOsO₆ from 2 (Na-doped) to 4 (La-doped) one can expect enigmatic re-entrant metal insulator transition which could be an another interesting topic for future project.

- The observation of ferromagnetic nature of Os-Os interaction in Ca₂CoOsO₆ and Ca₂NiOsO₆ compounds is interesting and demands further attention. In our theoretical studies, we argued dihedral angle involving Os-O-O-Os atoms should be important for this observation. To confirm or refute this conjecture of the effect of the dihedral angle involving Os-O-O-Os atom, one should study other Os based double perovskites in future.

The tetragonal Sr₂BOsO₆ (B = Fe, Co, Ni and Cu) double perovskites are antiferromagnetic while the monoclinic Ca₂BOsO₆ analogues are ferrimagnetic. In order to understand the sensitivity of magnetic ground state to relative subtle change in B-O-Os (B= Fe, Co, Ni and Cu) bond angle in osmate double perovskite, different tetragonal osmate double perovskite can be studied by changing c/a ratio, and comparing their bond angle (B-O-Os) and hopping strength with that of monoclinic analogue of osmate double perovskites.